Alma Mater Studiorum
Università degli Studi di Bologna

Facoltá di Scienze Matematiche, Fisiche e Naturali

Dipartimento di Astronomia

DOTTORATO DI RICERCA IN ASTRONOMIA

Ciclo XXII

MAGNETIC FIELDS IN GALAXY CLUSTERS:

FARADAY ROTATION AND NON THERMAL EMISSION

Dottoranda:

ANNALISA BONAFEDE

Coordinatore:
Chiar.mo Prof.
LAURO MOSCARDINI

Relatore:
Chiar.mo Prof.
GABRIELE GIOVANNINI

Co-relatore:
Dr. **LUIGINA FERETTI**

Settore Scientifico Disciplinare: Area 02 - Scienze Fisiche

FIS/05 Astronomia e Astrofisica

Esame Finale Anno 2010

QUESTA TESI E' STATA SVOLTA

NELL'AMBITO DELLE ATTIVITA' DI RICERCA

DELL' ISTITUTO DI RADIOASTRONOMIA

DELL' ISTITUTO NAZIONALE DI ASTROFISICA

(BOLOGNA)

Contents

Abstract

In this thesis we study the magnetic field in galaxy clusters and their connection with thermal and non-thermal phenomena in the Intra Cluster Medium. These topics are investigated through the analysis of the polarization properties of sources located behind and inside galaxy clusters as well as through MHD cosmological simulation. To this aim we have obtained observations at the Very Large Array (VLA) radio telescope (New Mexico USA) and we have investigated the magnetic field properties through different methods. We used the numerical code *Faraday* to interpret our results. We also used the brand new implementation within the *Gadget3* code to investigate the properties of massive simulated galaxy clusters.
The chapters of this thesis are organized as follows:

- In Chap. 1 we give a brief review of the established picture concerning the physical processes taking place in the ICM of galaxy clusters, and present a summary of the problematics related to non-thermal phenomena. In Chap. 2 different methods to analyze the magnetic field in galaxy clusters are presented, and a concise review regarding the problem of the origin of magnetic fields is also presented.

- In Chap. 3 we present the analysis of polarization data for seven radio sources in the Coma cluster field observed with the Very Large Array at 3.6, 6 and 20 cm, The Faraday Rotation measures for each source in the sample is derived with kpc-scale resolution. We have used the *Pacerman* code (Dolag et al. 2005c) that allows a better fit over low signal-to-noise regions. Results from the RM distribution of these sources as well as from their polarization properties are presented. The main results from this chapter can also be found in Bonafede et al. (2010).

- In Chap. 4 the magnetic field strength, structure and power spectrum in

the Coma cluster is constrained. We have derived the magnetic field power spectrum model that best fits the auto-correlation function and the structure function of the RM images obtained for the source sample presented in Chap. 3. We have then simulated different magnetic field models by varying the central intensity and the radial slope of the magnetic field and derived the central magnetic field strength , and radial profile values that best reproduce the RM observations. The main results from this chapter can also be found in Bonafede et al.(2010).

- In Chap. 5 we present the study at multiple frequencies of the emission arising from the massive galaxy cluster MACS J0717.5+3745 (z=0.55). Known to be an extremely complex cluster merger, the system is uniquely suited for an investigation of the phenomena at work in the intra-cluster medium (ICM) during cluster collisions. We use multi-frequency and multi-resolution data obtained with the Very Large Array radio telescope, and X-ray features revealed by Chandra, to probe the non-thermal and thermal components of the ICM, their relations and interactions. The cluster shows highly complex radio emission. A bright, giant radio halo is detected at frequencies as high as 4.8 GHz. MACS J0717.5+3745 is the most distant cluster currently known to host a radio halo. This radio halo is also the most powerful ever observed, and the second case for which polarized radio emission has been detected, indicating that the magnetic field is ordered on large scales. The main results from this chapter can also be found in Bonafede et al. (2009b).

- In Chap. 6 the study of the magnetic field at the periphery of two galaxy clusters is performed, thanks to the presence of double radio relics in Abell 1240 and Abell 2345. New Very Large Array observations at 20 and 90 cm for these two clusters are presented. We performed spectral index, and polarization analysis and compared our results with expectations from theoretical models. The main results from this chapter can also be found in Bonafede et al. (2009a).

- In Chap. 7 we present preliminary results from a study of the magnetic field in a sample of simulated massive galaxy clusters. We selected the most massive clusters from a pre-existing large cosmological simulation. The sample is called *Dianoga* and consists of 20 galaxy clusters with $M > 10^{15}$ $M_{\odot}$/h. We have

resimulated each of this massive clusters at high resolution in order to reach length scale comparable to observations. We used the *Gadget3* code (Springel in prep.) with the MHD implementation by Dolag & Stasyszyn (2009). Moreover, we extended the ideal MHD implementation by including a spatially constant dissipation η_m. Clusters are evolved with different values of η_m, in order to achieve the dissipation value that best reproduces the magnetic field properties of the Coma cluster, as obtained from the analysis performed in Chap. 2 and 3. The preliminary results obtained in this chapter will be presented in Bonafede & Dolag, in preparation.

- In Chap. 8 we present the main results from two projects that we have collaborated to: a statistical study on nearby radio halos and the study of radio emission in the intergalactic filament in the ZwCl 2341.1+0000 region.

- The results presented in the previous chapters are summarized in the Conclusions, where they are discussed together with other literature results obtained in the last three years. We show the impact that this thesis has on the study of the magnetic fields in galaxy clusters and on the origin of the non-thermal radio emission. Finally, we discuss how future radio telescopes will be able to shed light on these topics.

Chapter 1

Galaxy clusters

1.1 Introduction

The hierarchical model of structure formation predicts that clusters of galaxies form at the over-density peaks of a continue distribution of baryonic and dark matter components. The evolution of these components is described by the Friedman metric in a Universe that is represented by a ΛCDM cosmological model, with Λ referring to the cosmological constant and DM referring to Cold Dark Matter. The energy in these components is dominated at the present epoch by the cosmological constant, while baryons (b) and radiation (R) are less relevant: $\Omega_\Lambda < \Omega_{DM} < \Omega_b < \Omega_R$.
All of these components are fundamental ingredients in the physics and evolution of galaxy clusters. Galaxy clusters are self-gravitating systems, containing typically hundreds of galaxies, spread over a region of $\sim 1 - 3h^{-1}$ Mpc size. In 1966 X-ray emission was detected from the region around the galaxy M87 in the center of the Virgo cluster, (Byram et al. 1966) thus proving that hot gas permeates the space among the cluster member galaxies, the so called Intra Cluster Medium (ICM). Afterwards, the discovery of radio diffuse emission arising from the ICM of the Coma cluster (Willson 1970) proved the presence of magnetic fields and relativistic particles in the ICM. Galaxy clusters were then revealed to be complex systems, where different components co-exist and interact, giving rise to a variety of phenomena.
The ensemble of phenomena in galaxy clusters can be distinguished in *thermal* and *non-thermal*: the main properties of the radiation arising from galaxy clusters depends on the properties of baryons in approximate thermal equilibrium within the gravitational potential well; on the other hand, a considerable number of

observations in radio, soft and Hard-x energy bands, have shown that a number of phenomena in the ICM cannot be explained without considering the existence and evolution of a population of relativistic baryons. Although the observed scaling relations between different quantities like mass, galaxy velocity dispersion, X-ray luminosity and temperature, indicate that cluster components are in approximate dynamical equilibrium within the gravitational potential well, observations of spatially inhomogeneous thermal and non-thermal emissions of the ICM reveal signatures of non gravitational processes and interactions taking place at several different physical scales. Moreover, both the fraction of clusters with these features, and the correlation between the dynamical and morphological properties of irregular clusters and the surrounding large-scale structure are found to be increasing with redshift (*e.g.* Diaferio et al. 2008 for a review). Therefore understanding in detail most of the long standing, or new questions arisen by observations, should involve the study of the interplay between thermal and non-thermal components.

1.2 The Thermal component of the ICM

Clusters of galaxies are beside quasars, the most powerful X-ray sources in the sky, with typical luminosity of the order of 10^{43}– 10^{45} erg/s. When clusters of galaxies were found to be an important class of X-ray sources, there were a number of suggestions as to the primary X-ray mechanism. Felten et al. (1966) first suggested that this emission was due to diffuse intra-cluster gas at a temperature $T \approx 10^8$ K and an atomic density $n \approx 10^{-3} cm^{-3}$. In these conditions the primary emission process for a gas composed mainly by hydrogen is thermal bremsstrahlung optically thin emission. The X-ray Luminosity can thus be expressed as :

$$L_X = \int n_{\rm e}(\mathbf{r}) n_{\rm ions}(\mathbf{r}) \Lambda[T(\mathbf{r})] {\rm d}^3\mathbf{r} \ , \tag{1.1}$$

where $n_{\rm e}$ and $n_{\rm ions}$ are the electron and ion number densities in the ICM and $\Lambda(T)$ is the cooling function. When $k_B T > 2$ keV, the ICM is almost fully ionized, and $\Lambda(T) \propto T^{1/2}$. The emissivity at the frequency ν is then given by:

$$J_X(\nu) = 5.4 \times 10^{-39} \frac{Z^2 n_{\rm e} n_{\rm ions} g_{\rm ff}}{T^{1/2}} \exp^{-h\nu/K_B T} \, ergs^{-1} cm^{-3} Hz^{-1} Sr^{-1} \tag{1.2}$$

with Z being the charge of the ions, and $g_{\rm ff}$ is the Gaunt factor, a slowly varying function of temperature and energy that is ≈ 1, and corrects for quantum mechanical

effects and for distant collisions effect.
The collision time between protons, electrons and ions is $< 10^9$ yr, that is much shorter then the cluster life time. A first approximation, the ICM can then be assumed to be mainly at a single temperature. In this case, Eq. 1.1 indicates that the X-ray spectrum should be close to an exponential of the frequency, with a cut-off close to the region of the spectrum where $h\nu \sim k_B T$. In fact the continuum X-ray emission of galaxy clusters is generally well described, at first approximation, by this equation, with typical temperature of 2-10 keV (see also 1.2.2).

The presence of hot diffuse X-ray emitting gas implies the presence of a deep gravitational potential well that maintains the gas confined in the cluster. By assuming hydrostatic equilibrium and spherical symmetry, the cumulative mass within radius r is given by:

$$M(< r) = -\frac{k_B T r^2}{G\mu m_{\rm p}} \left(\frac{{\rm d}\,\ln \rho_{\rm gas}}{{\rm d}\,\ln r} + \frac{{\rm d}\,\ln T}{{\rm d}\,\ln r} \right) , \tag{1.3}$$

where $\rho_{\rm gas}$ is the gas mass density, μ is the mean molecular weight in a atomic mass unit, and m_p indicates the proton mass. The total mass of a galaxy cluster can also be estimated from the velocity dispersion of the member galaxies. If the cluster is in equilibrium, the virial theorem gives:

$$M = \frac{3\sigma_v^2 R}{G}; \tag{1.4}$$

here G is the gravitational constant, σ_v is the dispersion of the galaxy velocities along the line of sight, and R is the cluster size.
More recently, other approaches have been proposed and applied to derive estimates of the total mass: weak and strong gravitational lensing analysis (*e.g.* Schneider 2006), the caustic technique (Diaferio et al. 1999), that is based on the analysis of the galaxy distribution in redshifts space, and the measure of the Sunayaev-Zeldovich (SZ) effect (*e.g.* Bartlett 2006).
These methods indicate that galaxy clusters contain $\sim 10^{14}$–10^{15} $M_\odot$, that is mainly contributed by Dark Matter ($\sim$80%), while the ICM contributes $\sim$ 18%, and the galaxies contribute less than a few percent.

Distribution of the gas in the ICM

In the physical conditions typical of the ICM the cooling time due to thermal bremsstrahlung is $\sim 10^{10} - 10^{11}$ yr, that is much longer that the sound crossing time. The same condition is also verified for time-scales for heating by in-fall and compression of the gas, ejection from galaxies and galaxy motions. Thus the gas distribution is usually assumed to be hydrostatic. An additional assumption regards the spherically symmetry of the gas. Isothermal models have been derived from these assumptions (Cavaliere & Fusco Femiano 1976; 1978):

$$n_e(r) = n_e(0) \left[1 + \frac{r^2}{r_c^2}\right]^{-3/2\beta} . \tag{1.5}$$

This is the so called "β-model" (Cavaliere & Fusco-Femiano, 1976). $n_e(0)$ is the central electron density, that is typically $\approx 10^{-3}$ cm^{-3}, $\beta = \frac{\mu m_p \sigma_r^2}{k_B T}$, where σ_r is the one dimensional velocity dispersion of the galaxies. In this model both the galaxies and the intra-cluster gas are assumed to be isothermal, bound to the cluster and in equilibrium, and the galaxies are assumed to have an isotropic velocity dispersion. While none of the assumptions underlying this self-consistent isothermal model can be strictly verified, and the gas is probably not generally isothermal, the expression for the projected surface brightness derived from Eq. 1.5 is:

$$S(r) = S(0) \left[1 + \frac{r^2}{r_c^2}\right]^{-3\beta+1/2} \tag{1.6}$$

where $S(0)$ is the central surface brightness. With exception of the central cusps found in some clusters this expression has been found to be an adequate description of the gas distribution to the extent that the gas has been traced in clusters.

Under the virial equilibrium assumption, simple relations between the global properties of galaxy clusters can be derived. Namely: mass, galaxy velocity dispersion, number of galaxies, X-ray luminosity, ICM temperature.

The simplest model to predict observable properties of the ICM assumes that gravity alone determines the thermodynamical properties of the hot diffuse plasma (Kaiser 1986). By considering the virial relation $3k_BT/(2\mu m_{\rm p}) = GM/R$, one can derive the scaling relation between the total mass M and the gas temperature k_BT:

$$k_BT = 3.229 \left(\frac{\mu}{0.6}\right) \left(\frac{\delta}{500}\right)^{1/3} \left(\frac{M}{10^{14} h^{-1} {\rm M}_\odot}\right)^{2/3} {\rm keV} \tag{1.7}$$

Here δ indicates the average cluster over-density with respect to the critical density ρ_{cr} of the Universe. ρ_{cr} is defined as $\rho_{cr} \equiv 3H_0^2/(8\pi G)$, with $H_0 = 100h$ km s^{-1} Mpc^{-1} being the Hubble constant at the present time. Quantities in equation (1.7) are normalized to typical observed cluster values. L_X can be written in a similar way as:

$$\begin{aligned} L_X &= 1.327 \times 10^{43} \left(\frac{f_{\rm gas}}{0.1h^{-3/2}}\right)^2 \left(\frac{0.6}{\mu}\right) \left(\frac{n}{10^{-3}h^2\,{\rm cm}^{-3}}\right) \left(\frac{T}{\rm keV}\right)^{0.4} \times \\ &\times \left(\frac{M}{10^{14}h^{-1}{\rm M}_\odot}\right) h^{-2}\,{\rm erg\,s}^{-1}\,, \end{aligned} \tag{1.8}$$

where the cooling function Λ can be approximated as $\Lambda(T) = 0.843 \times 10^{-23}(k_BT/{\rm keV})^{0.4}$ erg cm^3 s^{-1} at $k_BT \geq 1$ keV, which holds for gas with poor metallicity, and $n_{\rm e} = n_{\rm ions} \equiv n = f_{\rm gas}\rho/(\mu m_{\rm p})$, where $f_{\rm gas}$ is the fraction of the cluster total mass in the ICM and ρ is the cluster total mass density.

In addition, a scaling law between an X-ray observable related to pressure and the cluster mass has been recently proposed by Kravtsov et al. (2006). They defined the quantity $Y_X = M_{\rm gas}T$, where both $M_{\rm gas}$ and T are measured within a given aperture. It is worth noting that Y_X represents the X–ray counterpart of the Compton-y parameter, measured from the SZ effect. By computing Y_X for a set of simulated clusters and for a sample of nearby clusters observed with Chandra, Kravtsov et al. (2006) showed that Y_X has a very tight correlation with the cluster mass, with a remarkably small scatter of only 8 per cent.

All the above scaling relations are based on the assumption of dynamical equilibrium. Even if quantities related to X-ray observations are robust and relatively simple to correlate (Rosati et al. 2002), a number of observational facts from X–ray, optical and radio data, points against the simple self–similar picture, indicating that more complicated frameworks need to be considered.

1.2.1 The inner thermal profiles of galaxy clusters

Despite their relatively modest spatial resolution, early ASCA observations established that most of the clusters show significant departures from an isothermal profile, with negative temperature gradients characterized by a remarkable degree of similarity, out to the largest sampled radii (*e.g.* Markevitch et al. 1998). The observation of strong central peak in the X-ray surface brightness of many clusters and the negative temperature gradients where then initially interpreted as signature

of a cooling flow (Cowie & Binney 1977, Fabian 1994).
Beppo–SAX observations showed afterwards that the above gradients do not extend towards the innermost cluster central regions, where instead an isothermal profile is observed, and more recent Chandra and XMM-Newton observations basically confirmed this picture, providing more detailed picture of the central temperature profile for a number of galaxy clusters (Pratt et al. 2007). Relaxed clusters are generally shown to have a smoothly declining profile toward the center, with values about half of the overall virial cluster temperature in the innermost sampled regions. The emerging picture suggests that gas cooling is responsible for the decline of the temperature in the central regions, while some still unknown mechanism of energy feedback should be responsible for preventing overcooling, thereby suppressing the mass deposition rate and the resulting star formation.
On the other hand, including gas cooling has the effect of steepening the T– profiles in the core regions, in clear disagreement with observations. The problem of the central temperature profiles in radiative simulations has been consistently found by several independent analyzes (*e.g.* Valdarnini 2003; Borgani et al. 2004; Nagai et al. 2007; Burns et al. 2007) and is likely due to the difficulty of implementing feedback schemes which balance the cooling runaway in a stable fashion. Resolving this would require that simulations are able to produce the correct thermal structure of the observed "cool cores", meaning that a suitable feedback should compensate the radiative losses of the gas at the cluster center, while keeping it at about $\sim 1/3$ of the virial temperature. AGN might represent the natural solution to this problem, even if only quite recently these studies have been extended to clusters forming in a fully cosmological context (Heinz et al. 2006; Sijacki et al. 2007).

1.2.2 Evidences of non equilibrium and formation process

In the current bottom-up scenario for the formation of cosmic structure, where tiny fluctuations of the primordial density field are amplified by gravity, clusters are the most massive nodes of the filamentary large-scale structure of the cosmic web. Since they form by anisotropic and episodic accretion of mass, it is expected that a fraction of them shows deviations from the spherical symmetry and that signatures of these phenomena are visible in X-ray and optical data. A large fraction of clusters, indeed, shows the presence of sub-structures both in their galaxy distribution and

in their X-ray emission morphology. The fraction of clusters with these irregular X-ray features is in the range 30-80 % depending on the cluster sample and on the cluster identification technique (see Ramella et al. 2007), and increases with redshift (Jeltema et al. 2005). Where the angular resolution of X-ray observations is high enough to resolve the internal structure of clusters, more detailed information about the ICM can be obtained, and the equilibrium assumptions can be tested. Clusters show typically patchy temperatures (Belsole et al. 2005; Gitti & Schindler 2004; Ma et al. 2008) and metallicity gradients (e. g. Hayakawa et al. 2006, Finoguenov et al. 2006, Werner et al. 2008). Also, where the angular resolution is too low and detailed maps of the X-ray surface brightness cannot be obtained, indications that some clusters are out of equilibrium come from Hard-X observations. In some cases in fact a high energy excess appears in the X-ray spectrum when it is fitted assuming a plasma with single temperature and metallicity. In these cases, two or more temperatures are required to yield a reasonable fit. All these pieces of evidence suggest that in agreement with the standard scenario clusters accrete matter from the surrounding regions. One of the most spectacular examples of merging clusters at intermediate redshift is the so-called "bullet cluster", namely 1ES 0657-55.8 (Markevitch et al. 2002) at z=0.296. At low redshift there are many other examples of merging clusters and galaxy groups falling onto clusters along intergalatic filaments: the Coma cluster (Colless & Dunn, 1966), Abell 521 (Ferrari et al. 2003), Abell 754 (Henry et al. 2004) are among the most famous, but many other have been studied in detail (see Diaferio et al. 2008 and references therein). At high redshift the number of irregular and merging clusters increases. On of the most spectacular example of interacting system is the cluster MACS J0717+3745, at z=0.55, where a triple ongoing merger has been observed (Ebeling et al. 2004). The above mentioned results indicate that merging episodes are common phenomena in clusters, and signatures of them can be studied through optical and X-ray observations. Other indications of these energetic phenomena can bee derived from radio emission, and will be presented in the following Sections.

1.3 The Non-thermal components

Radio observations of galaxy clusters have shown that the ICM is not only composed by hot gas. Magnetic fields and relativistic particles are present in the ICM, and

are key ingredients for understanding the physical processes at work in clusters of galaxies. They reveal themselves through non-thermal mechanisms and are thus referred to as non-thermal components of the ICM.
The energetic events that galaxy clusters undergo during the process of structure formation, are expected to generate turbulent motions and shock waves in the ICM (see *e.g.* the recent review by Bykov et al. 2008). The amount of energy that is released during these processes is the major source of energy for the ICM non-thermal components: a fraction of this energy could be channeled into the amplification of the magnetic fields (*e.g.* . Dolag et al. 2008 and references therein) and into the acceleration of high energy Cosmic Rays particles via stochastic mechanism (see Petrosian et al. 2008 for a review).
The presence of non-thermal components is proved by different observational evidences:

- Since the last twenty years radio observations have discovered the the presence of radio emission arising from the ICM and not connected to the emission of the individual galaxies in the clusters. These radio sources are called Radio Halos Radio Relics, and Mini Halos, depending on their position and observational properties. The emission mechanism is synchrotron from ultra relativistic electrons diffusing in a turbulent magnetic field at μG level. (see Ferrari et al. 2008 for a review).

- The Faraday Rotation Measures of sources located behind and inside galaxy clusters have shown an enhancement with respect to field sources (Clarke et al. 2001, 2004; Johnston-Holitt 2004), testifying that the ICM is magnetized.

- The Hard-X ray emission observed in some galaxy clusters has been interpreted by several authors as inverse Compton scattering of cosmic microwave background photons by relativistic electrons (*e.g.* Rephaeli 1999; Sarazin 1999; Fusco Femiano et al. 2007).

Yet, the last point is debated, and other mechanisms have been proposed in the literature, as non-thermal bremsstrahlung and synchrotron emission from ultra-relativistic electrons; some authors suggested that the emitting electrons originate from a population of point sources, as AGN, merger shocks, dark matter bow-shocks (see Rephaeli et al. 2008 for a review).

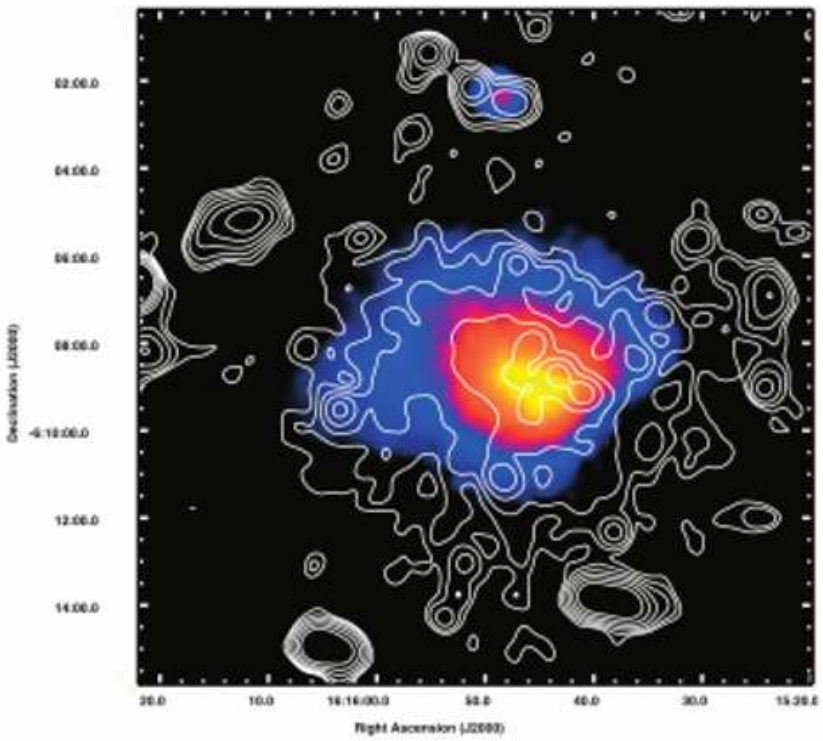

Figure 1.1: Abell 2163: the isocontour map at 1.4 GHz of the central region of A2163 is overlaid on the X-ray image in the 0.8-6.5 Kev energy band (colors). The radio image has a FWHM of $30'' \times 30''$. The contour levels are 0.1, 0.2, 0.4, 0.8, 1.6, and 3.2 mJy/beam. From Govoni et al. (2004), Feretti et al. (2001)

Thermal and non-thermal components living in the ICM are expected to mix, and they may drive still unexplored physical processes modifying our simplified view of the Inter-galactic medium (IGM) itself (Schekochihin et al. 2007; Subramanian et al. 2006; Brunetti & Lazarian 2007; Guo et al. 2008).

1.3.1 Radio Halos

Radio Halos are the most spectacular expression of cluster non-thermal emission. They are wide ($\sim$ 1 Mpc) diffuse radio sources with no connection with individual galaxies, and are characterized by low surface brightness ($\sim 10^{-6}$ Jy/arcsec^2 at 1.4 GHz) and steep spectra ($\alpha \geq 1$, with $S(\nu) \propto \nu^{-\alpha}$).

They have a quite regular morphology, similar to the clusters X-ray morphology, and are located at the center of clusters with a disturbed dynamical state and without a cooling core. In Fig. 1.1 the radio halo in the cluster Abell 2163 is shown (from Govoni et al. 2004). This can be considered one of the prototypes of the low surface

brightness and extended radio halos.

No polarized flux has been detected usually in radio halos. In the Coma cluster upper limits to the fractional polarization is ∼10% at 1.4 GHz, and lower values (∼6% and 4%) have been found for two other powerful halos in Abell 2219 and Abell2163 (see Govoni & Feretti 2004 and references therein). The only exception is the clusters Abell 2255 (Govoni et al. 2005) where polarized filaments have been observed; in this thesis we will present the second case where polarized emission has been detected in the cluster MACS J0717+3745 (see Chap. 5).

Apart from these cases, the low upper limits on the polarized emission indicate that significant depolarization occurs. This could be both *internal i.e.* due to the presence of thermal gas mixed with the relativistic plasma, and *external*, due to the spatial resolution of the observations (see Chap. 2). Due to their low surface brightness, in fact, the emission from radio halos requires low spatial resolution to be properly revealed.

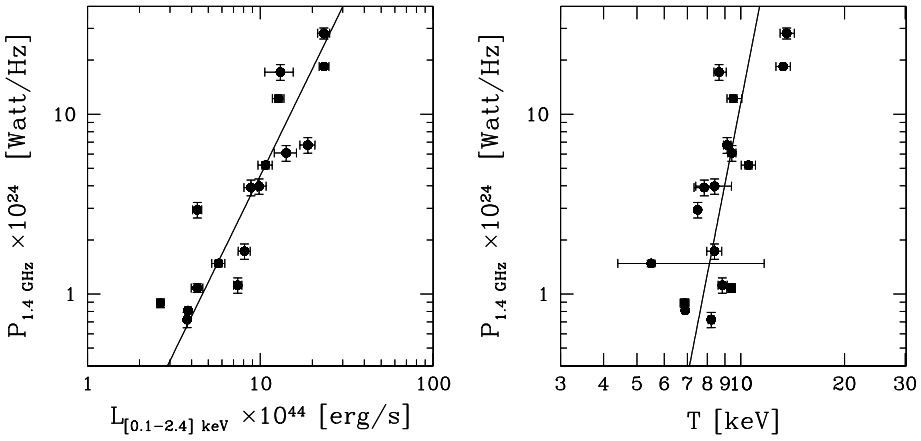

Figure 1.2: Radio power at 1.4 GHz of radio halos with size >1 Mpc versus cluster X-ray Luminosity in the energy band [0.1-2.4] keV (left) and versus cluster Temperature. (From Ferrari et al. 2008; adapted from Cassano et al. 2006)

Connections between radio and - X-ray emission

In recent years, many observational efforts have been devoted to multi-frequency observations of radio halos, in order to get more and more accurate determinations of their radio properties and of their connection with the hot thermal gas in galaxy clusters. These studies are limited however by the capability of current instruments

to perform multi-frequency observations at the sensitivity required for studying radio halos. Nonetheless, it is now possible to draw some of the general characteristics of radio halos and derive correlations with cluster properties:

1. Halos are typically found in clusters with significant substructures and disturbed X-ray morphology and temperature gradients (Feretti, 1999, Buote, 2001) that are clear signs of recent or ongoing merger event.

2. Not all merging clusters host a radio halo and indeed they are *rare* phenomena, found only in a fraction of X-ray luminous galaxy clusters. Their detection rate is 5% in a complete cluster sample at the detection limit of the NVSS, and grows to ∼35% when only clusters with L_X [0.12.4 keV]$> 0.6 \times 10^{45} h_{70}^2$ erg s^{-1} are considered. (Giovannini et al. 1999). In a complete sample selected on the basis of the X-ray luminosity, the detection rate is $\sim$ 30% (Venturi et al. 2008).

3. In a number of well resolved clusters a point-to-point spatial correlation is observed between the radio brightness of the radio halo and the X-ray brightness (*e.g.* Kempner & David 2004; Govoni et al. 2001), indicating an interaction between the two components.

4. A strong correlation has been pointed out between the radio power ($P(\nu)$) of halos and the X-ray luminosity of their host clusters (*e.g.* Liang et al. 2000; Giovannini & Feretti 2002; Enßlin & Röttgering 2002; Cassano et al. 2006). A relation with a much larger scatter between $P(\nu)$ and X-ray temperature of the ICM (T_x) has also been suggested (*e.g.* Liang et al. 2000). Since both the X-ray luminosity and temperature of clusters correlate with mass (*e.g.* Neumann & Arnaud 1999; 2001), the observed $P(\nu)$ - L_X and $P(\nu)$ - T_X relations could reflect a dependence of the radio halo luminosity on the cluster mass (see Fig. 1.2). The above correlations have been studied in this thesis by considering all the radio halos known to date at $z < 0.4$ (Chap. 8).

5. In addition Feretti et al. (2004) investigated the existence of a possible correlation between the spectral index of radio halos and the cluster temperature, finding a marginal evidence that clusters at higher temperature tend to host halos with flatter spectrum. In the cluster Abell 2744, it was

indeed found that flatter radio spectral indexes regions are associated with regions of high temperature of X-ray emitting gas (Orrú et al. 2007). This study has been extended in this thesis (Chap. 8) by considering all nearby radio halos ($z < 0.4$).

These correlations have interesting implications on the theoretical models of cosmic ray production, since they are suggesting that gravity, that drives the thermal properties of the galaxy clusters on large scales, is also responsible for the observed non–thermal phenomena (see Cassano 2009 for a review).

Formation Scenarios for Radio Halos

The presence of Mpc-size diffuse emission in clusters poses some questions about the origin of the relativistic emitting particles, that are subject to energy losses. Relativistic electrons with momentum $p_e = m_e c\gamma$ lose energy through ionization losses and Coulomb collisions, which dominate for $\gamma < 100$, and via synchrotron and IC scattering off the Cosmic Microwave Background photons, which dominate at higher energies (*e.g.* Sarazin 1999). On the other hand relativistic protons lose energy mainly through proton–proton inelastic scattering, while Coulomb losses become important at lower energies. Thus relativistic protons are long living ($> 10^9$ yr) and accumulate in the ICM, while relativistic electrons are short living particles that radiate their energy in the region where they are produced (*e.g.* Jaffe 1977). The radiative lifetime of a particle with a Lorentz factor $\gamma_L < 10^8$ is given by (e. g. Longair 1981):

$$\tau \approx \frac{2 \times 10^{12}}{\gamma_L} \left[(1+z)^4 + \left(\frac{B^2}{(3.25\mu G)^2} \right) \right]^{-1} y. \tag{1.9}$$

For instance, electrons emitting synchrotron radiation around ~ 1 GHz have an energy of the order of $\approx 7\, B_{\mu G}^{1/2}$ GeV and a life-time of $\approx 10^8$ yr. During this timescale electrons can only diffuse for a few tens of kpc, which is very small compared with the observed $\sim$ Mpc scale common for Radio Halos. This lead to the requirement that the electrons responsible for the radio emission in Radio Halo must be generated or accelerated everywhere in the cluster. Indeed, the observed connection between the non–thermal emissions in galaxy clusters and cluster mergers suggests that a fraction of the energy dissipated during these mergers is channeled in non–thermal components of the ICM. Two main classes of models have been proposed to explain the origin of the emitting particles:

- *primary models*: in which electrons are re-accelerated *in situ* through second-order Fermi mechanism by ICM turbulence developing during cluster mergers (Brunetti et al. 2001; Petrosian 2001);

- *secondary models*: in which electrons originate from hadronic collisions between the long-living relativistic protons in the ICM and thermal ions (Dennison 1980; Blasi & Colafrancesco 1999).

Present observations disfavour the second scenario. The strongest problem related to these models is the fact that radio halos are *rare* phenomena. Recently, from the non-detection of diffuse emission in a sample of clusters, upper limits have been put to cosmic ray hadrons in these galaxy clusters (Brunetti et al. 2007), indicating that either the magnetic field is dramatically different in clusters with and without radio halos, or the contribution of the secondary particles is insufficient to explain the observed radio emission. Furthermore, steep radio spectra ($\alpha \geq 1.5$) have been observed in some clusters, that would require an unrealistic energy budget in terms of relativistic protons in order to explain radio halos with secondary models (Brunetti et al. 2008). Gamma-ray emission is also predicted in this context from the π_0 decay generated from hadron collisions.
In the second scenario the statistical properties of radio halos depend on the interplay between the rate of cluster-cluster mergers and the fraction of the energy that is channeled into MHD turbulence and in the re-accelerating of high energy particles, and thus the correlations between thermal and non-thermal properties of galaxy clusters can be explained. Despite the wide range on uncertainty, this model predicts some basic features of the statistical properties of radio halos (Cassano et al. 2006; Cassano 2009) that are in line with present observations.
Observations from the new generation of high energy experiments (*e.g.* FERMI/GLAST and Cherenkov telescopes) are likely going to provide much more stringent constraints to the energy budget stored by relativistic hadrons, thus improving the theoretical understanding of this complex picture.

1.3.2 Radio Relics

Radio relics have observational properties similar to radio halos: they are wide (≈ 1 Mpc) diffuse, radio sources associated to the ICM and characterized by a steep radio spectrum. Differently from radio halos, they have usually an elongated morphology,

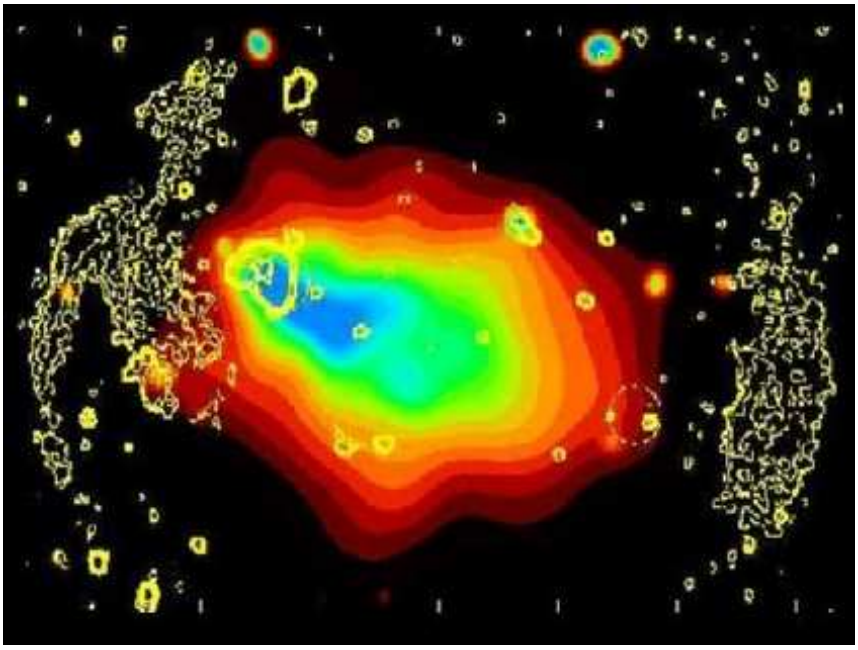

Figure 1.3: Colors: X-ray emission of A 3376 in the energy band 0.14-2 keV from from ROSAT PSPC observations. Contours: radio emission at 1.4 GHz. The beam width is $20''$ FWHM Gaussian. Contour levels are at 0.12, 0.24, 0.48 and 1 mJy/beam. Taken from Bacghi et al. 2006.

are located at the outskirts of the host galaxy clusters, usually at the boundary of the X-ray emission, and are strongly polarized, with linear fractional polarization at 1.4 GHz of 10-30 %, reaching values up to 50 % in some regions (see *e.g.* Govoni & Feretti 2004; Ferrari et al. 2008). So far, there are $\sim$ 20 clusters of galaxies where at least one radio relic is present. Their radio morphology and location are quite varied, and could reflect different physical origin or ICM conditions (Kempner et al. 2004; Giovannini & Feretti 2004). Some of the most extended and powerful giant relics are located in clusters with central radio halos (*e.g.* A2256: Clarke & Ensslin 2006), and in a few cases two symmetric relics have been detected within the same clusters (*e.g.* Rottgering et al. 1997; Bagchi et al. 2006).

Their origin is uncertain. There is a general consensus that it is related to phenomena occurring in the ICM during merging events. Radio relics in fact are always observed in clusters that have a signature of recent merger. Yet, due to low X-ray brightness at the cluster periphery, a comparison of relic properties with the surrounding medium (*i.e.* temperature and brightness gradient induced by shock waves) is not obvious. For instance, Feretti & Neumann (2006) did not find any

evidence of a temperature jump nearby the Coma cluster relic. In the case of A520, instead, a spatial correlation with shocks in the thermal gas has been suggested (Markevitch et al. 2005).

Formation scenario for radio relics

Several models have been proposed to explain the origin of radio relics. They can be divided into two classes:

1. Re-acceleration of emitting particles due to adiabatic compression of fossil radio plasma (Ensslin & Gopal-Krishna 2001).

2. Diffusive Shock Acceleration by Fermi-I process (Ensslin et al. 1998; Roettiger et al. 1999; Hoeft & Brüggen 2007).

In both of these models the presence of a shock within the gas is required. The first one also requires the presence of a nearby radio source to provide the fossil radio plasma which can be re-energized by the shock wave. Simulations of cluster mergers show indeed that the merging of two sub-clusters leads to the formation of shocks in the cluster outskirts (Ryu et al. 2003).
In favor of the first scenario there is the observational evidence that relics resemble individual objects and do not trace the entire shock front (Hoeft et al. 2004). Moreover, when a radio ghost is passed by a shock wave with typical velocity of 10^3 km/s, it is adiabatically compressed because of the higher value of the sound speed in the radio ghost (Ensslin & Brüggen 2002). Hoeft et al. (2004) investigated the Ensslin & Gopal-Krishna (2001) model by using the SPH code *GADGET* to simulate a merging galaxy cluster within a cosmological environment. This work showed that the probability for a shock wave to flare the ghost radio plasma is reduced in the central regions of galaxy clusters, where the radio plasma ages much faster due to the pressure of the radio plasma, kept higher by the external medium, and the higher values of the magnetic field. Moreover, the compression ratio of the shock wave is much higher in the low-density peripheral regions than in the cluster center and this would explain why radio relics are more common in these regions. It is worth reminding, however, that the equation of state of the radio emitting plasma is still poorly known, and that ghost radio plasma should be well confined into the

ICM to keep the internal sound speed at the level of the speed of light, in order to experience adiabatic compression and not shock acceleration. As soon as the ghost relativistic component is mixed with the ICM, diffusive shock acceleration come into play as leading mechanism for the acceleration of particles.
In the framework of the "Diffusive Shock Acceleration" scenario two main categories of shocks could be responsible of the acceleration of the emitting particles. Several independent cosmological simulations in fact have identified two main categories of cosmological shocks:

(i) "accretion shocks" resulting from accretion of cold gas onto already formed structure, characterized by high Mach numbers;

(ii) "merging" or "internal" shocks due to merging of substructures such as galaxy clusters or groups, with moderate Mach numbers: $2 \leq M \leq 4$ (see review by Bykov et al. 2008 and references therein).

The presence of double relics is particularly interesting in this scenario since the shape, morphology and properties of these extended structures strongly suggest the presence of shock waves propagating from the cluster center to the peripheral regions. Because of the short radiative lifetime of relativistic electrons, radio emission is produced close to the location of the shock waves. These models predict that the magnetic field is aligned with the shock front and that the radio spectrum is flatter at the shock edge, where the radio brightness is expected to decline sharply. Roettiger et al. (1999) were able to reproduce the main features of the relic radio emission in Abell 3667, by combining a single merger simulations with a model for shock acceleration. Relativistic electrons were injected with a power-law spectrum with slope dependent on the shock Mach number, and the aging of the radio plasma were included in their simulation. They found that the observed distribution of the spectral index of the relic were reproduced by adopting a shock velocity of the order of $v_{\rm s} \approx 700 - 1000$ km s^{-1} and a magnetic field of $\approx 0.6\mu$G at the position of the radio relic.

1.3.3 Radio mini halos

A few "cooling-core" clusters exhibit signs of diffuse synchrotron emission that cannot be entirely attributed to the central dominant radio galaxy. These sources

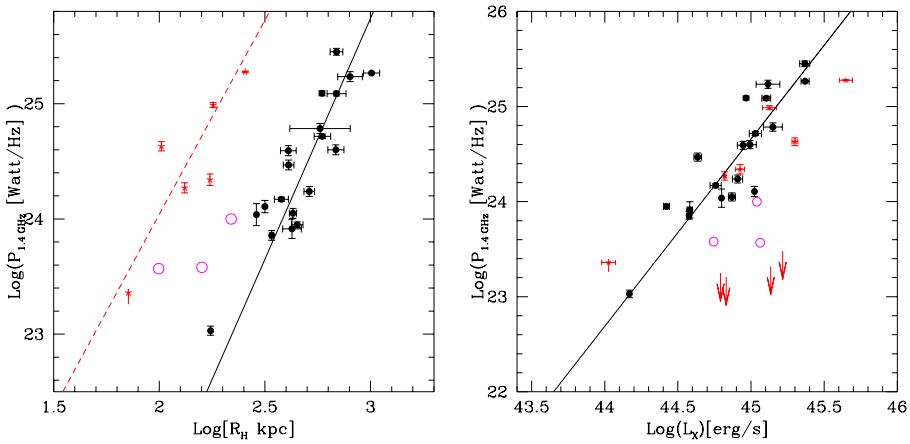

Figure 1.4: Left: Radio power at 1.4 GHz versus radio size of GHs (black circles) and MHs (red asterisks), and small-scale radio emissions (magenta open circles). The black solid line and the red dashed line are the best-fit correlations for GHs ($P_{1.4} \propto R_{\rm H}^{4.18}$), and for MHs ($P_{1.4} \propto R_{\rm H}^{3.4}$), respectively. Right: Radio power at 1.4 GHz versus L_X in the [0.1-2.4] keV band. Arrows are upper limits to the radio power of Cluster cool cores without radio halos. Other symbols are as in the left panel. The line is the best fit correlation for Giant Radio Halos. Taken from Cassano et al. (2008).

are called "mini radio-halos". They are diffuse radio sources, with typical size of $\sim$ 500 kpc, and in common with radio halos they are characterized by steep spectrum and very low surface brightness.

The detection of radio mini halos is further complicated by the combination of small angular size and strong radio emission of the central radio galaxy, that require high dynamic range and resolution data to disentangle the different contributions t the radio emission. As a consequence, our current observational knowledge on mini-halos is limited to less than ten known sources (*e.g.* , Perseus: Burns et al. 1992; A2390: Bacchi et al. 2003; RXJ1347.5-1145: Gitti et al. 2007, A1835, A2029, Ophiucus: Govoni et al. 2009).

Major mergers are thought to be powerful enough to disrupt cluster cooling flows (*e.g.* Buote & Tsai 1996), thus they cannot play a major role in the origin of mini halos. On the other hand, when analyzed in detail they sometimes reveal peculiar X-ray features in the cluster center which may indicate a possible link between the mini-halo emission and some minor merger activity. (see *e.g.* , Gitti et al. 2007, Mazzotta & Giacintucci 2008, Govoni et al. 2009).

Gitti et al. (2002) suggested that the mini-halo emission is due to a relic population

of relativistic electrons re-accelerated by MHD turbulence via Fermi-like processes, the necessary energetics being supplied by the cooling flow. In agreement with this hypothesis, Gitti et al. (2004) found a trend between the radio power of mini-halos and the cooling flow power. Recently, Cassano et al. (2008) suggested a possible connection between mini halos and "moderate" merger events in the host cool-core clusters. In this work, evidences were also shown for a P_ν-$L_{\rm X}$ and P_ν-$R_{\rm H}$ (where R_H is the radio halo radius) trends for mini-halos. Mini–halo clusters share the same region of giant halo clusters in the $(P_{1.4}; L_X)$ plane, whereas they are clearly separated in the $(P_{1.4}; R_H)$ plane (see Fig.1.4). Compared to radio halos, a more efficient source of injection of particles, (likely connected with the central radio galaxy) which takes part in the re-acceleration process, is required in mini-halos, that indeed have a synchrotron emissivity much larger than that of giant halos. Accordingly, Murgia et al. (2009) have shown that while radio halos have a similar emissivity, mini-halos span a wide range of radio emissivity. They also found that some of them have a radio emissivity which is much more typical of halos in merging clusters rather than similar to that of the other mini-halos previously known.
Alternatively, Pfrommer & Enßlin (2004) proposed that relativistic electrons in mini-halos are of secondary origin, continuously produced by the interaction of cosmic ray protons with the ambient, thermal protons.

Chapter 2

Magnetic fields in galaxy clusters

2.1 Introduction

In recent years the presence of magnetic field in astronomical objects, going from stars to galaxies and galaxy clusters has been unambiguously proved. These magnetic fields are thought to play an important role in different astrophysical environments (Valleé et al. 2004) going from small to large scales. The magnetic fields that we observe in the local Universe probably owe their strength to dynamo amplification of an initial seed. The smaller the object is the shorter is the time required for the dynamo to amplify the original seed. The magnetic fields on large scales are thus the most challenging. In fact, the dynamical scale for large objects are long, and the amplification is correspondingly slow. This indicates the need for additional amplification mechanisms (see *e.g.* Rees, 2006).
Galaxy clusters host the largest scale magnetic field observed so far. The presence of magnetic fields on such large scales poses questions about its origin and evolution, and its properties have a number of fundamental implications in order to understand the processes at work in the ICM.

2.2 Magnetic field origin

From a theoretical point of view, the magnetic field is believed to be injected in galaxy clusters and amplified in a second phase by mechanisms probably connected with the formation process of galaxy clusters (e.g. Dolag et al. 2008 for a review). Several models have been proposed to explain the origin of magnetic field. They can be divided into three main classes:

- **Low redshift models (z $\sim$ 2-3):** galactic winds and AGN ejecta produce magnetic field within the proto-cluster region (Völk & Atoyan 2000, Enßlin et al. 1997, Furlanetto & Loeb 2001).

- **High redshift models (z > 4):** the magnetic field is produced by and early population of stars and dwarf star-burst galaxies before clusters start to form a gravitationally bound system.

- **Cosmological origin:** the magnetic field has a primordial origin, generated in the early universe before the epoch recombination. In this case, magnetic fields would be already present at the onset of structure formation, and would be a remnant of the early Universe.

One of the main arguments in favour of the low-redshift models is the chemically enrichment occurred in the ICM. The high metallicity observed in the ICM, in fact, suggests an important enrichment operated in the past by galactic winds and AGNs, that are expected to carry magnetic fields together with the processed matter. It has been shown that magnetic fields produced by the ejecta of star-burst galaxies can be as large as $0.1\,\mu$G. One of the main expectation of these models is that magnetic fields should be mainly concentrated around galaxies and within galaxy clusters. In this class of models magnetic fields could be amplified also by the action of turbulent motions, shear flows and merging events, provided that the injection process happened early enough. In addition, during the non-linear stage of the Large Scale Structure formation, shocks are expected to occur. During their propagation specific instabilities driven by energetic accelerated particles could result in a strong non-adiabatic amplification of an up-stream magnetic field seed (Bell & Lueck 2001; Vladimirov 2006).
The "high-redshift" class of models differ by the "low-redshift" ones only in the time when the magnetic pollution is assumed to take place, predicting that the magnetic pollution happened by an early population of star-burst galaxies at $4<z<6$ (Kronberg et al. 1999). The magnetic field seed is smaller, but the subsequent amplification can be more significant.
The third scenario includes a number of different models for the origin of the magnetic fields. These models for the cosmological origin of the magnetic field are supported by the evidence that magnetic fields are present everywhere in the

universe. The magnetic field seed could be generated during inflation, or at neutrino and photon decoupling, or during phase transitions, or by small thermo-ionic electric currents (Biermann-Battery effect) generated by merger/accretion shocks related to the hierarchical structure formation process (see Grasso & Rubinstein, 2001 for a review).

Despite the different assumed origin for the magnetic field seed, both the 'high-redshift' models and the 'primordial' models expect the strength of the seed field to be considerably smaller than the first scenario. In this context the amplification due to the adiabatic compression of the gas and the shear flows driven by the accretion of structures has to give rise to a significant amplification of the magnetic field, in order to reconcile the weak seed fields proposed by these models with present observations.

2.3 Cosmological MHD simulations

It is commonly expected that merger events and accretion of materials onto galaxy clusters will drive significant shear flows within the ICM. The Kelvin-Helmholtz instabilities driven by these motions represent a mechanism for the magnetic field amplification during the process of structure formation. Early extensive numerical simulations following the generation and evolution of magnetic field during single merger events were presented in Roettiger et al. (1999) by using the Eulerian code ZEUS. These authors demonstrated that the field initially becomes quite filamentary, as a result of stretching and compression by shocks and bulk flows during infall. Then when the bulk flow is replaced by turbulent motions, the field amplification is more rapid and located in particular regions (Fig. 2.1). The magnetic field energy increases of a factor 3 with respect to a non-merging cluster, and in localized regions it can increase of a factor 20 or more.

Cosmological simulations performed with different codes (Dolag et al. 1999, 2002 using *GrapeMSPH*, Dolag et al. 2004; 2005b using the MHD implementation in the *GADGET2* code; Brueggen et al. 2005 using *FLASH*; Dubois & Teyssier, 2008 using *RAMSES*; Collins et al. 2009 using *ENZO*) and assuming that a seed magnetic field exists before structure formation, have shown that the amplification of the magnetic field during the process of cluster formation is highly non linear. The contribution of shear-flows and of the induced turbulence, in fact causes the

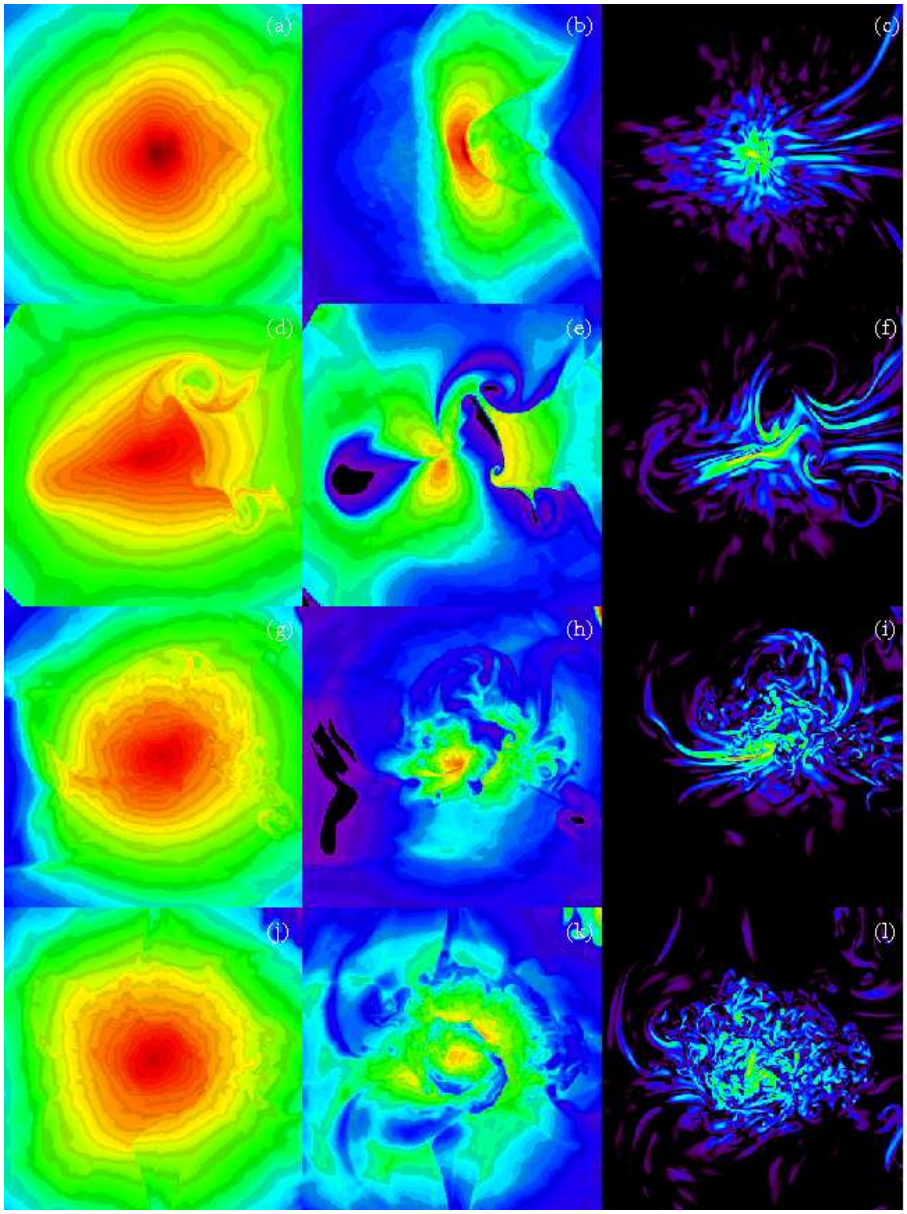

Figure 2.1: From left to Right: the evolution of the gas density,gas temperature and magnetic field pressure in logarithmic scale in two dimensional slices through the core of a cluster undergoing a major merger in the plane of the merger. The merging subcluster enter from right. From top to bottom different epochs are shown: t=0 (time of core coincidence), t=1.3, 3.4 and 5 Gyr. Each panel is 3.75×3.75 Mpc. Figure taken by Roettiger et al. (1999).

magnetic field amplification to deviate from the predictions made by purely adiabatic compression (see Fig. 2.2). It results that the magnetic field strength and structure in cluster environments reflects the process of structure formation, and no memory of the initial magnetic field configuration survives. Thus, studying the magnetic field in galaxy clusters means to study how the magnetic field is built-up during the process of cluster formation.

2.3.1 The magnetic field structure

Another interesting quantity to look at is the magnetic field power spectrum:

$$|B_k|^2 \propto k^{-\eta}, \tag{2.1}$$

with k being the wave vector). Several independent simulations performed with different codes found that the magnetic field power spectrum in galaxy clusters can be well represented by a Kolmogorov-like power spectrum. This result is not obvious, since even in the ideal MHD hypothesis, galaxy clusters have a density profile, so that the Kolmogorov theory cannot be strictly applied. Nonetheless, η is predicted by cosmological MHD simulations (Dolag et al. 2002; Rordorf et al. 2004) to be slightly lower but still very close to 11/3, which is expected for a Kolmogorov like power spectrum. Also Adaptive Mesh Refinement (AMR) simulations by Brüggen et al. (2005) nearly perfectly match the Kolmogorov slope.

2.3.2 The magnetic field profile

A simple energetic argument proves that the magnetic field strength cannot be constant through the whole cluster volume: if the field values detected at the cluster centers would extend over several core radii, up to distances of the order of $\sim$ Mpc, the magnetic pressure would exceed the thermal pressure in the outer parts of the clusters. Jaffe (1980) first suggested that the magnetic field distribution in a cluster would depend on the thermal gas density and on the distribution of massive galaxies and therefore would decline with the cluster radius. Cosmological MHD simulations (Dolag et al. 2008 and references therein) found that the μG level field presently observed in clusters can be reproduced by the evolution of the magnetic field starting from an initial field of $\sim 10^{-9}$ G at redshift 15. One of their results is that the magnetic field strength at any point within galaxy clusters is proportional

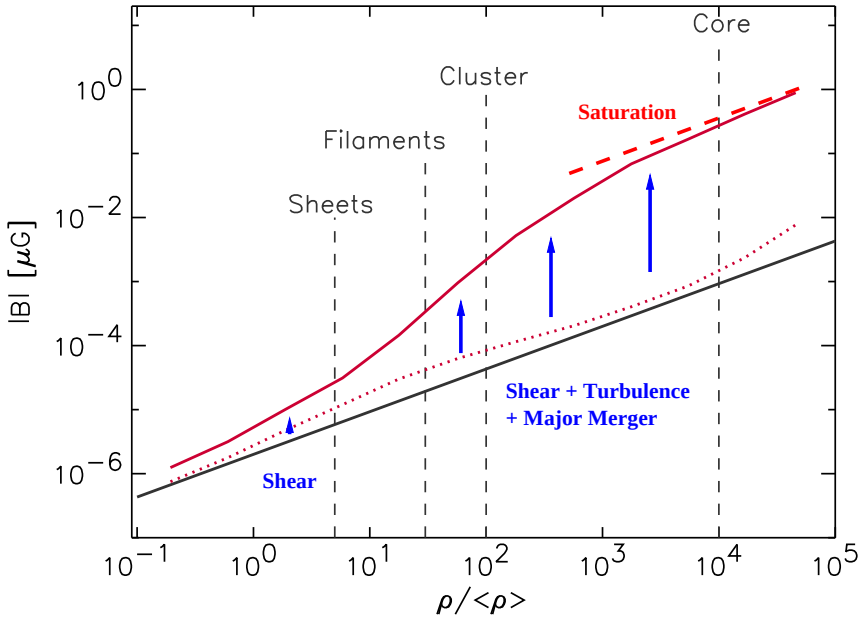

Figure 2.2: Mean strength of the magnetic fields as a function of baryionic overdensity within a cosmological simulation (solid line). The straight line shows the evolution for a purely adiabatic amplification. It is possible to note the amplification due to shear flows and turbulence in denser regions, and the saturation in cluster cores. The dotted line refers to the median of the magnetic field strength, indicating that a large fraction of the particles remain close to the adiabatic expectation. Figure taken from Dolag et al. (2008).

to the gas density. In the simplest case of adiabatic compression during the cluster gravitational collapse, one may assume that the magnetic field lines are frozen into the plasma, so that compression of the plasma results is compression of flux lines. The expected growth of the magnetic field intensity in then $B \propto \rho^{2/3}$, and since ρ decreases with the distance from the cluster center the magnetic field intensity will decrease accordingly.

2.4 Observations of magnetic field in galaxy clusters

The presence of magnetic field from the observational point of view has been performed so far through three different methods:

- Study of the synchrotron emission from diffuse radio sources in the ICM (radio halos and relics).

- Study of the Faraday Rotation of sources embedded and behind the cluster.

- Hard X-ray emission from clusters containing radio halos and relics.

In the following sections, we will show the methods used to derive estimates of the magnetic field strength and the results obtained until 2006, *i.e.* before the work that we present in this thesis.

2.5 Total intensity synchrotron emission and magnetic fields

As previously stated (Chap. 1) in some galaxy clusters diffuse and wide radio sources have been observed, whose emission arises from the ICM itself. The emission is generated by relativistic electrons girating the intra cluster magnetic field, and is thus the most direct evidence that the ICM is magnetized. From the synchrotron emissivity alone it is not possible to derive unambiguously the magnetic field value, since the synchrotron emission depends on both the magnetic field strength and the energy spectrum of the emitting particles. In order to derive an estimate of the magnetic field from the synchrotron emission it is necessary to make some assumptions and to infer some unknown quantities. The usual way to estimate the magnetic field strength in a radio source is to minimize its total energy content E_{tot}. The total energy in a synchrotron emitting source is contributed by three terms: the energy in relativistic electrons (E_e), in protons (E_p) plus the energy in magnetic fields (E_B). It is common to assume that the protons energy is proportional to the electron energy: $E_p = kE_e$, while the magnetic field energy in a source of volume $V$is given by:

$$E_B = \int_V \frac{B^2}{8\pi} dV. \tag{2.2}$$

In order to properly compute the integral one should know how the magnetic field is distributed inside the source, and what is its strength over different spatial scales *i.e.* what is the magnetic field power spectrum. However, the expression above is usually written as $E_B = V\Phi B^2/8\pi$, with Φ being the so-called "filling factor", that should account for non-uniformity of the magnetic field inside the source. The electron total energy in the energy range $\epsilon_1 - \epsilon_2$, assuming a power-law distribution

of the electron energy spectrum: $N(E) = N_0 E^{-\delta}$, is given by:

$$E_e = V \times \int_{\epsilon_1}^{\epsilon_2} N(E) E dE = V N_0 \times \int_{\epsilon_1}^{\epsilon_2} E^{-\delta+1} dE. \tag{2.3}$$

The synchrotron luminosity is given by:

$$L_s = V \times \int_{\epsilon_1}^{\epsilon_2} -\frac{dE}{dt} N(E) dE = N_0 V B_\perp^2 c_2 \times \int_{\epsilon_1}^{\epsilon_2} E^{-\delta+2} dE \tag{2.4}$$

where $c_2 = \frac{2e^4}{3m_0^4 c^7}$ and $B_\perp$is the component of the magnetic field in the direction perpendicular to that of the velocity of the emitting particle. It is reasonable to assume that $B_\perp = B$, *i.e.* the radiation that we observe, being highly relativistic, is emitted by particles that have velocity along the line of sight. Eliminating $N_0 V$ from Eq. 2.3 and 2.4 and writing ϵ_1 and ϵ_2 as a function of the corresponding frequencies ν_1 and ν_2 at which each particle emits most of its radiated energy ($\nu = \frac{3eB_\perp E^2}{4\pi m_0^3 c^5}$), E_e can be written as a function of L_S:

$$E_e = C(\delta, \nu_1, \nu_2) B^{-3/2} L_S \tag{2.5}$$

where all physical constants and expressions depending on δ, ν_1 and ν_2 have been enclosed in $C(\delta, \nu_1, \nu_2)$. The total energy can thus be obtained as a function of L_s and B:

$$E_{tot} = C(\delta, \nu_1, \nu_2)(1+k) E_e + \frac{B^2}{8\pi} \Phi V. \tag{2.6}$$

It is thus not possible to obtain an estimate for the magnetic field without making some further assumptions on the energy distribution between magnetic field and particles. If one assumes that the total energy E_{tot} is minimum, it results that the energy is almost equally distributed between magnetic field and particles:

$$E_{tot}(min) = \frac{7}{4}(1+k) E_{el} = \frac{7}{3} E_B. \tag{2.7}$$

It is now possible to derive an estimate of the magnetic field B (*equipartition estimate*):

$$B_{eq} = \left(\frac{6\pi(1+k) C(\delta, \nu_1, \nu_2) L_S}{\Phi V} \right)^{2/7}. \tag{2.8}$$

It has been noted (Brunetti et al. 1997; Beck and Krause 2005) that the integration limits (Eq. 2.4) are variable in terms of the energy of the radiating electrons. The lower limit is particularly relevant, owing to the power-law shape of the electron

energy distribution and to the fact that electrons of very low energy are expected to be present. If a low-energy cutoff in the particle energy distribution is assumed, rather than a low-frequency cut-off in the synchrotron spectrum, it is possible to derive a more consistent estimate of the magnetic field under the mentioned assumptions. It results that if the integral is computed in terms of the energy γ of the emitting electrons, and $\gamma_{min} << \gamma_{max}$

$$B'_{eq} = 1.1\gamma_{min}^{\frac{1-2\alpha}{3+\alpha}} B_{eq}^{\frac{7}{2(3+\alpha)}} \tag{2.9}$$

with $\alpha = \frac{\delta-1}{2}$.

2.5.1 Current results from radio equipartition

Magnetic field estimate derived under the equipartition assumption can be obtained in clusters where radio diffuse emission is detected. Typical equipartition estimate are in the range $B'_{eq} \sim$ 0.1-2 μG (see Ferrari 2008 and references therein). It is worth mentioning the strong assumptions and uncertainties that this approach requires, especially in the case of cluster halos and relics. K depends on the the mechanism of generation of relativistic electrons, which is so far poorly known; assumptions on Φ are needed, and on the geometry of the source in order to compute V; other critical assumptions regard the energy distribution of the emitting particles: radio halos and relics, in fact, have been observed so far only in a small portion of the radio spectrum, so that the particle spectrum is poorly constrained, and could be different from a simple power-law, as also suggested by some models for halos and relics. The lower limit of the integral is particularly relevant, owing to the steep spectrum observed. Small changes in γ_{min} have a huge impact on the determination of the magnetic field. Furthermore, the conditions of particles and magnetic field in ICM are very different from those in radiogalaxies, and there is no reason to assume that these two components should be in equipartition. Thus, because of the many assumptions until at least a precise knowledge of the low energy spectrum of the emitting electrons in radio halo can be reached, this estimate should be used with caution. It must also be noted that the magnetic field estimates regard average value of the magnetic field strength over the radio emitting volume.

2.6 The Faraday Rotation

2.6.1 Polarized emission and Faraday Rotation measures

Polarization observations of synchrotron emission are important diagnostic tool in the study of the extragalactic magnetic fields. When linearly polarized waves, as synchrotron radiation, propagates through a magneto-ionic medium, as the ICM, its polarization properties change. Due to the birefringence of the medium, in fact, the polarization plane of the radiation is rotated as a function of frequency. This effect is called Faraday rotation. Following Burn & Sciama (1964), we define the complex linear polarization $P = pe^{2i\Psi}$, where p and Ψ are the degree and angle of polarization. If we indicate with Ψ_{int} the intrinsic polarization angle, the effect of the Faraday rotation can be parametrized by:

$$\Psi_{obs}(\lambda) = \Psi_{int} + C_{RM}\phi(z)\lambda^2 \tag{2.10}$$

where $C_{RM} = \frac{e^3}{2\pi m_e c^4}$, $\phi(z)$ is the Faraday depth of the point z with respect to an observer that is in $z = 0$

$$\phi(z) = \int_0^{z_s} n_e \mathbf{B} \cdot \hat{\mathbf{z}} dz \tag{2.11}$$

where $\mathbf{z}$ is a unit vector in the z direction. For Faraday-thin objects, *i.e.* when the Faraday screen is external to the source of linearly polarized emission, the observed polarization angle Ψ_{obs} is a linear function of λ^2, and the Faraday Rotation Measure can be introduced by $\Psi_{obs} = \Psi_{int} + RM\lambda^2$, with

$$RM = C_{RM} \int_0^{z_s} n_e \mathbf{B} \cdot \hat{\mathbf{z}} dz \tag{2.12}$$

that can be better expressed in practical units as:

$$RM[rad/m^2] = 812 \int_0^{z_s} n_e[cm^{-3}]\mathbf{B}[\mu G] \cdot \hat{\mathbf{z}} dz[kpc] \tag{2.13}$$

By definition the RM is positive when the magnetic field direction points toward the observer and is negative when pointing in the opposite direction.
The real and imaginary parts of P are observable quantities, and are related to the Stokes parameters I, Q, and U through:

$$\begin{aligned} p_\lambda &= \sqrt{U_\lambda^2 + Q_\lambda^2}/I_\lambda \\ \Psi_\lambda &= \frac{1}{2} tan^{-1}\left(\frac{U_\lambda}{Q_\lambda}\right) \end{aligned} \tag{2.14}$$

Ψ_{obs} at several wavelengths can be obtained by multi-frequency radio observations, so that the RM of radio sources can be obtained by a linear fit of Eq. 2.10. To determine RM accurately and remove the $\Psi_{obs} = \Psi_{obs} + n\pi$ ambiguity the value of Ψ_{obs} has to be measured at least at three different wavelengths. In the last years different algorithms have been implemented in order to better recover the RM from radio data. In this thesis I have used the *Pacerman* algorithm developed by Dolag et al. (2005c), that will be briefly described in 3.5.

2.6.2 Faraday rotation and depolarization

Eq. 2.12 holds if the Faraday screen is external to the emitting source. In many cases Ψ is not a linear function of λ^2, indicating that the source that is radiating is not Faraday-thin. In the Faraday-thick regime it is still possible ti define the RM as:

$$RM(\lambda^2) = \frac{d\Psi}{d\lambda^2} \tag{2.15}$$

being aware that this is function of λ^2. In these cases it is not possible to derive information about the properties of the magneto ionic medium by studying the Faraday effect unless the dependence of Ψ_{obs} from λ is known. This happens only in very simplified cases (see *e.g.* . Burn 1966; Sokoloff et al. 1998).
When the Faraday effect originates entirely in the source, in a very simplified geometry in which the source consists of synchrotron emitting slab with with a purely regular magnetic field $\mathbf{B}= \mathbf{B}'$, containing thermal gas with constant volume density n_e Burn (1966) showed that:

$$p(\lambda) = p_{int}\frac{sin(RM'\lambda^2)}{RM'\lambda^2}\Psi_{obs} = \Psi_{int} + \frac{1}{2}RM'\lambda^2, 0 \leq RM'\lambda^2 \leq \frac{\pi}{2} \tag{2.16}$$

where $RM' = C_{RM}n_eB'_z$ is called the *internal Faraday RM*, or the Faraday depth of the source. In this case Ψ_{obs} is a linear function of λ^2 and the observable Faraday RM is equal to $\frac{1}{2}RM'$ only in a range of wavelengths between any two zero points of $p(\lambda)$.
In other more realistic geometries Ψ_{obs} will not obey the λ^2-*law* even in a small range of wavelengths (see Burns et al. 1966; Solokoloff et al. 1998 and references therein).

Internal Depolarization

Assuming that the radiation is due to synchrotron emission by relativistic electrons whose energy distribution follows a power-law: $N(E) \propto E^{-\delta}$, the intrinsic degree of polarization is (Burn 1966):

$$p_i(\delta) = \frac{3\delta + 3}{3\delta + 7}. \tag{2.17}$$

When synchrotron emission originates in a magneto-ionic medium containing a magnetic field that is randomly fluctuating (*e.g.* because of turbulent motions of the plasma where the magnetic field is frozen-in), the polarization plane of the radiation produced at different depth is rotated over different angles. This results in a decrease of the degree of polarization (differential Faraday Rotation). If the rotation is significant, this will lead to severe depolarization. This is called *internal depolarization* since it is due to intrinsic properties of the emitting source. We define as depolarization (DP) the ratio between the polarization obtained after the rotation of the plane of polarization and the intrinsic polarization at a given wavelength:

$$DP = \frac{p_{obs}(\lambda)}{p_i(\lambda)} \tag{2.18}$$

Another useful definition is the depolarization between two wavelengths λ_1 and λ_2 ($\lambda_1 < \lambda_2$) :

$$DP_{\lambda_2}^{\lambda_1} = \frac{p_{obs}(\lambda_2)}{p_{obs}(\lambda_1)} \tag{2.19}$$

that is the quantity accessible from observations. If λ_1 is small, one can assume that $p(\lambda_1) \sim p_i$ and thus Eq. 2.19 allows to estimate the intrinsic DP.
If the magnetic field consists of two components, one uniform ($B_u = (B_x^u, B_y^u, B_z^u)$) and one random and isotropic, that can be represented by a Gaussian function with variance= $\frac{2}{3}B_r^2$, Burn (1966) has shown that the intrinsic polarization is related to the observed one through:

$$p_{obs} = p_i \frac{B_u^2}{B_u^2 + B_r^2}, \tag{2.20}$$

If $B_x^u \approx B_y^u \approx B_z^u$, Eq. 2.20 gives the ratio of the energy in the uniform field over the energy in the total field.

External depolarization and instrumental effects

Another mechanism that leads to a decrement of the observed degree of polarization is the depolarization in an external Faraday screen. The effect of Faraday screen

with tangled magnetic field has been analyzed by several authors (*e.g.* Lawler & Dennison 1982; Tribble 1991). Due to the Faraday rotation by a random magnetic field, the polarization plane suffers a random walk that causes depolarization as long as different turbulent cells are averaged within the observing beam.

It is worth noting the differences between this *external depolarization* with respect to the internal effect discussed above. Here depolarization occurs at a position where synchrotron emission has vanished, and this is essentially an instrumental effect, that occurs if there are structure of the magnetic field on scales smaller the beam resolution. A key difference between *external* and *internal depolarization* is that the internal depolarization, in regions where RM follows Eq. 2.16 should be correlated with the RM. Regions of small RM should in fact exhibit little if no depolarization. The *external* depolarization is instead correlated with the gradient of the RM. Large gradient will cause in fact a strong decrement of the observed degree of polarization when averaged within the observing beam.

Another instrumental effect arises from the finite bandwidth of the receiving system. The angle of polarization will vary across the receiving band by an amount:

$$\Delta\Psi = -2RM\lambda^2\frac{\Delta\nu}{\nu} \tag{2.21}$$

where $\Delta\nu$ is the bandwidth and ν is the central frequency. This will reduce the observed polarization degree by a quantity $sin(\Delta\Psi)/\Delta\Psi$ below that for monochromatic radiation.

An important peculiarity of a Faraday screen is that the mean degree of polarization decreases with λ as:

$$p(\lambda^2) \propto \exp -k\lambda^4 \tag{2.22}$$

with k depending on the morphology of the random magnetic field. Burn (1966) has shown for instance that in the case of a Faraday screen extending for a distance R from the observer, and a Gaussian random field with variance $C_{RM}^2 B_z^2 n_e^2 dR$, where d is the typical fluctuation scale of the magnetic field, Eq. 2.22 becomes $p(\lambda^2) = p_i \exp(-2C_{RM}^2 B_z^2 n_e^2 dR\lambda^4)$.

2.6.3 Current results from Faraday RM

In the last decade increasing attention has been devoted to the study of the magnetic field in galaxy clusters through the analysis of the RM of sources located inside or

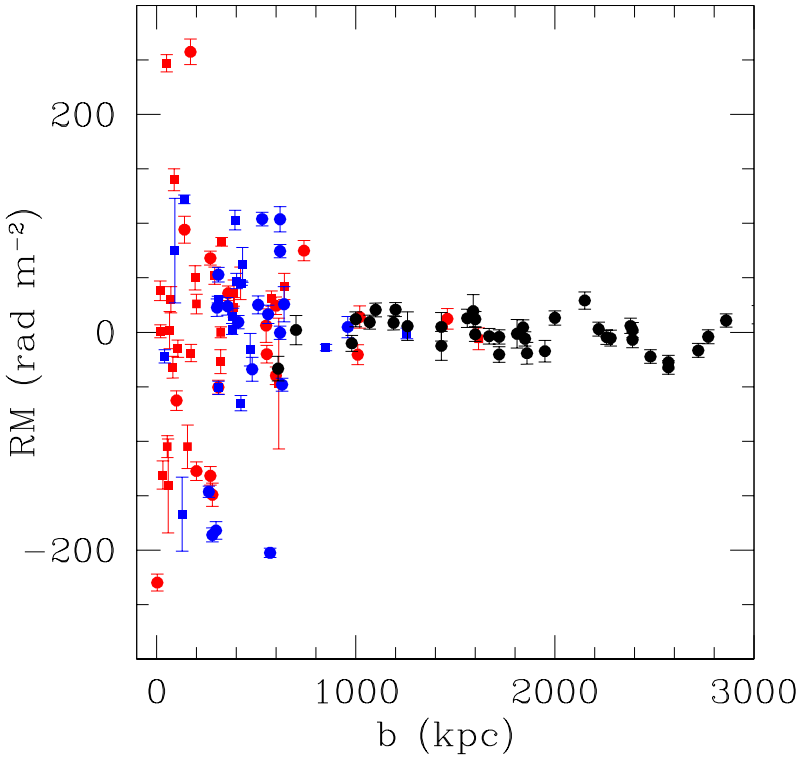

Figure 2.3: Rotation Measure (corrected for the Galactic contribution) plotted as a function of source impact parameter separated in embedded (red), background (blue), and control (black) samples. Figure taken by Clarke 2004.

behind the cluster.

One of the observing strategies to have information on the cluster magnetic field intensity and structure is to obtain high resolution RM images of sources located at different impact parameters of a cluster, then derive the average value of the rotation measure: $\langle RM \rangle$ and the value of its dispersion σ_{RM}. These information, combined with measurements of the thermal gas density distribution and with assumptions on the magnetic field morphology, allow to estimate the cluster magnetic field along the line of sight. Such studies have been carried out on both statistical samples and on individual objects.

In order to derive the magnetic field from RM observations, the integral in Eq. 2.12 must be solved. Analytical solutions of the integral require some assumptions on the magnetic field morphology along the line of sight. A solution that is widely used in the literature is based on the assumption that the magnetic field is tangled on a single scale Λ_{MF}. In this case, if the density distribution follows a β-profile (Eq. 1.5), the following relation for the RM dispersion can be obtained by integrating Eq. 2.12

$$\sigma_{RM}(r_\perp) = \frac{K_F B n_0 r_c^{1/2} \Lambda_{MF}^{1/2}}{(1+\frac{r_\perp}{r_c})^{(6\beta-1)/4})} \sqrt{\Gamma(3\beta-0.5)}\Gamma(3\beta) \qquad (2.23)$$

where Γ is the Gamma function, $r_\perp$ is the projected distance from the cluster center, an K_f depends on the integration path along the gas density distribution. On the basis of this formula, statistical study of RMs have been performed by Clarke (2004), who analyzed the RMs for a representative sample of 27 cluster sources, plus a control sample. The author found a statistically significant broadening of the RM distribution in the cluster sample, and a clear increase in the width of the RM distribution toward smaller impact parameters. Their estimates give a magnetic field of 4- 8 μG, assuming a magnetic field tangled on a single scale of $\sim$ 15 kpc. (Fig. 2.3). Polarization data from sources at different cluster locations have been obtained in clusters without cooling cores, *i.e.* Coma (Feretti et al. 1995), A119 (Feretti et al. 1999), A514 (Govoni et al. 2001), 3C129 (Taylor et al. 2001) , A400 and A2634 (Eilek & Owen 2002).

Extreme values of RMs are found to be associated with radiogalaxies at the center of cooling-core clusters, with the magnitude of the RMs roughly proportional to the cooling rate (Taylor et al. 2002) Magnetic fields, from $\sim$ 5 μG up to the values of $\sim$ 30 μG are deduced in the innermost regions of these clusters, *e.g.* Hydra A (Taylor

& Perley 1993) and 3C295 (Perley & Taylor 1991).

Overall, the data are consistent with magnetic field of the order of μG over the central Mpc of non-relaxed clusters, and with extreme field values in cluster cooling cores.

These estimates of the magnetic field strength from RM data crucially depend on the geometry of the magnetic field. RM images of sources located within and behind galaxy clusters show a RM distribution that is generally patchy, indicating that large-scale magnetic fields are not regularly ordered on cluster scales, but have structures on scales as low as 10 kpc or less. In many cases, high resolution RM images show a nearly Gaussian RM distribution, suggesting an isotropic distribution of the field component along the line-of-sight. However, many RM distributions show clear evidence for a non-zero mean RM if averaged over areas comparable with the radio source size, even after the Galactic contribution is subtracted. These RM offsets are interpreted as due to fluctuations of the cluster magnetic fields on scales greater than the typical source size, *i.e.* . considerably larger than those responsible for the RM dispersion. A realistic model of the magnetic field must comprise both small and large scale fluctuations, *i.e.* the magnetic field power spectrum must be considered. Small scales are necessary to produce the smallest structures observed in the RM images and larger scales are required to account for the non-zero RM average. At the purpose of investigating the magnetic field power spectrum in the ICM, Murgia et al. (2004) have developed a code: *Faraday* that allows to obtain simulated RM images starting from realistic 3-D multi-scale magnetic field models. When the results of the simulations performed by Murgia et al. are compared to those obtained by using Eq. 2.23, it results that Eq. 2.23 can lead to reliable estimate for the average magnetic field strength once the value of Λ_{RM} is equal to the magnetic field correlation length. However, since the auto-correlation length depends on the slope of the power spectrum, it turns out that, in any case, the magnetic field power spectrum must be estimated (Murgia et al. 2004).

This approach has been used in order to derive the magnetic field in the cluster Abell 2255 (Govoni et al. 2006) and Abell 119 (Murgia et al. 2004). Because of the degeneracies in the magnetic field power spectrum and radial profile, several power spectrum models have been investigated, while the radial slope of the magnetic field has been fixed. In Abell 119 the best magnetic field model is the one with

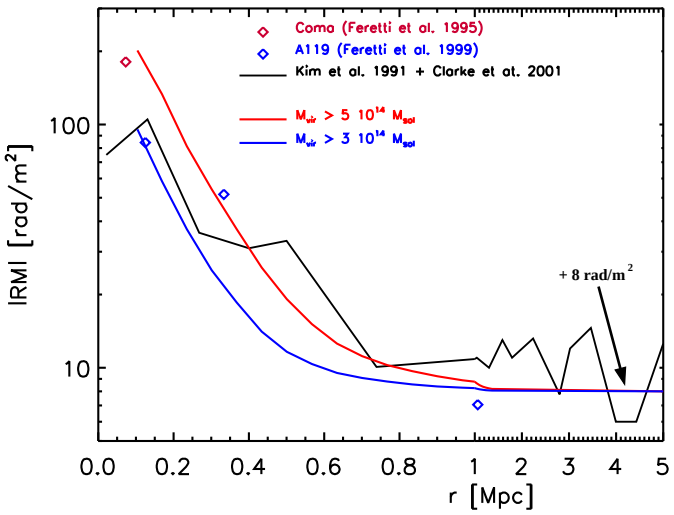

Figure 2.4: Comparison of RMs in simulations with observations of Abell clusters, as a function of the distance from the cluster center. The smooth lines refer to the median values of $|RM$ produced by simulated clusters with masses above 5×10^{14} $M_{\odot}$(upper line) and 3×10^{14} $M_{\odot}$(lower line). The broken line refers to the median of combined data taken from the independent samples in Kim et al. (1991) and Clarke et al. (2001). Diamonds refer to the sources in Abell 119 (Feretti et al. 1999) and to the source 5C4.81 in the Coma cluster (Feretti et al. 1995).Figure taken from Dolag et al. (2008)

central intensity of $\sim$5 μG, and with a power spectrum characterized by n=2, with maximum and minimum scale of 12 and $\sim$1500 kpc respectively. In Abell 2255 the best fit between data and simulations is obtained for a power spectrum model with n=2 in the center and 4 at the cluster periphery and the central intensity results $\sim$ 3μG (Govoni et al. 2006).

An alternative approach has been proposed by Enßlin & Vogt (2003). By using a semi-analytic technique, they showed that the magnetic field power spectrum can be estimated by Fourier transforming RM maps if very detailed RM images are available. Moreover, they derived that the auto-correlation length of the RM fluctuations is in general larger than the magnetic field auto-correlation length.

2.7 Magnetic field from Hard-X and radio emission

Another method to obtain a volume-averaged estimate of the magnetic field strength in clusters hosting radio halos, consists in comparing the Hard-X non-thermal emission with the radio emission. The Hard-X emission originates from the Inverse-

Compton scattering of the CMB photons with a population of relativistic electrons that fill the cluster volume and generate the radio emission. The non-thermal Hard-X ray emission was predicted by Rephaeli (1977) and detected in several systems (see Rephaeli et al. 2008; Fusco Femiano et al. 2007 and references therein).
The detection of non-thermal Hard-X ray emission produced by the same population of relativistic electrons, allows to determine the volume-average ICM magnetic field. The exact derivation of the equations for the synchrotron flux f_{sin} at the frequency ν_R and the and the Compton X-ray flux f_C at the frequency ν_X can be find in Blumenthal & Gould (1970). It results that

$$B \propto \left(\frac{f_{syn(\nu_R)}}{f_C(\nu_X)}\right)^{\frac{2}{\delta+1}} \left(\frac{\nu_R}{\nu_X}\right)^{\frac{\delta-1}{\delta+1}} \tag{2.24}$$

Typical magnetic field values of $\sim$ 0.1-0.3 μG are obtained through this method. (Rephaeli et al. 1999; Fusco-Femiano et al. 1999, 2000, 2001; Rephaeli & Gruber 2003; Rephaeli et al. 2006). Compared to equipartition measures, this method has the great advantage of using only observables.
The new generation of Hard X-ray satellites (*Suzaku, INTEGRAL*) failed in some cases in founding the Hard-X ray excess with respect to the thermal emission (see e.g. Ajello 2009). It must be noted however, as reported by several authors, that the Hard-X ray emission could originate in regions that are more extended than the field of view of these new instruments.

2.8 Current knowledge on cluster magnetic fields and open questions

In the literature there is a long-standing debate about the different magnetic field estimates derived from equipartition, Inverse-Compton emission and Faraday RM. As shown in the previous sections, in fact, equipartition and IC estimates, being sensitive to volume averages magnetic field strength, are or the order of 0.1-1μG, while RM studies, frequently performed in single central sources, give higher estimates. These different methods are sensitive on magnetic field strength on different scales, so that the discrepancies are not surprising and can be alleviated by considering realistic models for the ICM magnetic fields. As suggested by Goldshmidt and Rapheali (1993) and by simulations performed by Murgia et al.

(2004), once the radial decline of the magnetic field is considered, it is possible to obtain magnetic field models that are able to produce both the observed values of the Faraday RM and, when averaged over the cluster volume, the values derived from equipartition and Hard-X ray emission. It is thus fundamental to constrain the radial profile of the magnetic field from observational point of view, and to obtain information on the magnetic field structure at the center and at the outskirts of galaxy clusters. In the next chapters, different methods to estimate the magnetic field in the ICM fom radio observations will be analyzed and applied to single clusters. We will then use these results to analyze the magnetic field evolution in cosmological MHD simulations.

Chapter 3

Faraday Rotation Measures in the Coma cluster*

3.1 Introduction

A discussed in Chap. 2, the presence of magnetized plasma in the ICM affects the polarization properties of sources located either inside or behind the cluster. Therefore, polarization studies of clusters containing extended radio sources, provide valuable information about the intra-cluster magnetic field properties.
In this Chapter and in the following, we will present the analysis of the magnetic field in the Coma cluster. Here we present the analysis of a sample of extended sources selected in the Coma cluster field, and observed with the Very Large Array (VLA) at 3.6, 6 and 20 cm. The Faraday Rotation Measures have been derived with kiloparsec scale resolution. The Coma cluster is an important target for a detailed study of cluster magnetic fields. It is a nearby cluster (z=0.023), it hosts large scale radio emission (radio halo, radio relic, bridge) and a wealth of data are available at different energy bands, from radio to hard X-rays. Given the assumed cosmology, at the Coma redshift $1''$ corresponds to 0.46 kpc

3.2 Previous works on the Coma cluster magnetic field

The first investigation of the magnetic field in the Coma cluster was performed by Kim et al. (1990). They analyzed 18 bright radio-sources in the Coma cluster region, obtaining RM maps at $\sim 20''$ (~ 9.2 kpc) resolution and found a significant

*Bonafede et al. 2010, A&A in press

enhancement of the RM in the inner parts of the cluster. Assuming a simple model for the magnetic field reversal length, they derived a field strength of $\sim$ 2 μG. A complementary study was performed by Feretti et al. (1995) studying the polarization properties of the extended radio galaxy NGC 4869. From the average value of RM and its dispersion across the source, they deduced a magnetic field of $\sim$6 μG tangled on scales of $\sim$ 1 kpc, in addition to a weaker magnetic field component of $\sim$0.2 μG , uniform on a cluster core radius scale.
From the Coma radio halo, assuming equipartition, a magnetic field estimate of $\sim 0.7 - 1.9$ μG, averaged over the radio emitting volume, is derived (Thierbach et al. 2003), while from the Inverse Compton Hard X-ray emission an average value of $\sim$0.2 μG has been derived by Fusco Femiano et al. (2004), although new hard X-ray observations performed with the new generation of satellites did not find such evidence of non-thermal emission (Wik et al. 2009 using XMM and Suzaku data; Lutovinov et al. 2008 using ROSAT, RXTE and INTEGRAL data; Ajello et al. 2009 using XMM-Newton, Swift/XRT, Chandra and BAT data). However, the discrepancy between these values is not surprising: equipartition estimates, in fact, rely on several assumptions, and refer to the cluster volume; IC measurements refer to cluster volume averaged estimates as well, while the RM is sensitive to the local structures of both the thermal plasma and the cluster magnetic field component that is parallel to the line of sight. Furthermore, the equipartition estimate should be used with caution, given the number of underlying assumptions. For example, it depends on the poorly known particle energy distribution, and in particular on the low energy cut-off of the emitting electrons.

3.3 Thermal emission from X-ray observations

The study of the magnetic field through the Faraday RM requires knowledge of the properties of the thermal gas (see Eq. 2.12). This information can be derived from X-ray observations. In Fig. 3.1 the X-ray emission of the Coma cluster is shown in colors. X-ray observations in the energy band $0.1-2.4$ keV have been retrieved from the ROSAT All Sky Survey data archive. After background subtraction the image has been divided by the exposure map and smoothed with a Gaussian of $\sigma = 60''$.
The radio contours of the NVSS (NRAO VLA Sky Survey) at 1.4 GHz are overlaid onto the X-ray emission and shown in contours in Fig. 3.1. The location of the

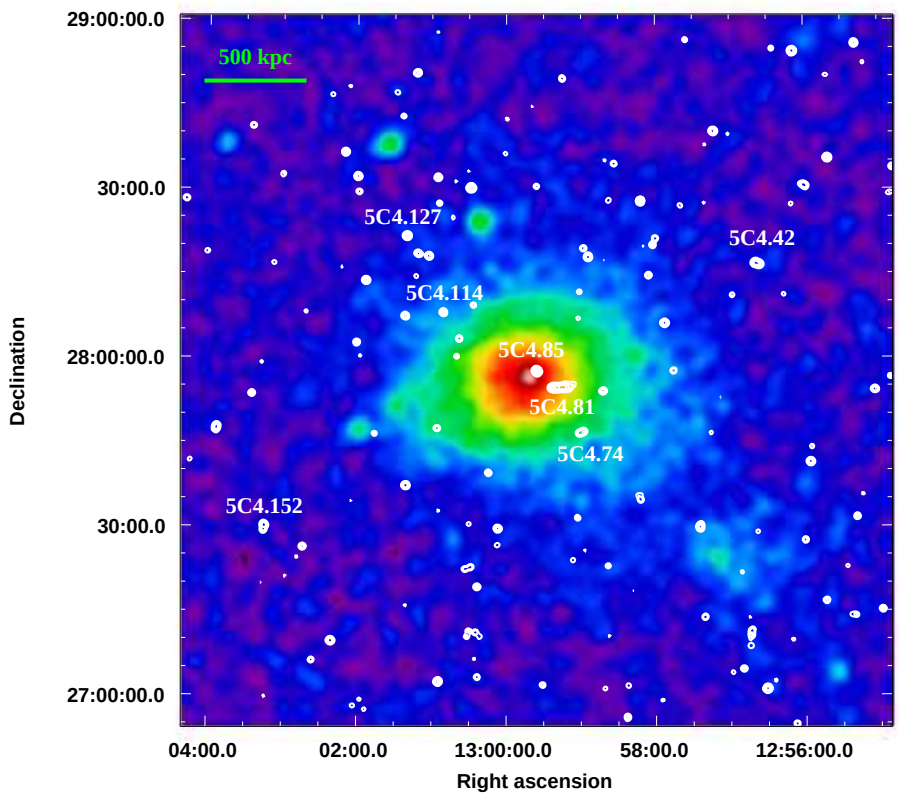

Figure 3.1: Colors: Coma X-ray emission from the ROSAT All Sky Survey in the energy band [0.1, 2.4] kev. Contours: Coma radio emission at 1.4 GHz from the NVSS. The beam FWHM is $45'' \times 45''$, contours start from 1.5 mJy/beam and are spaced by a factor of 2. The observed sources are labelled.

observed sources is marked with crosses together with their names. Note that the extended radio emission of the radio halo, relic and bridge are completely resolved out in the NVSS image due to the lack of very short baselines and sensitivity limits. The X-ray emission is from thermal bremsstrahlung, and can be used to trace the thermal particle distribution in the ICM. The distribution of the gas is well reproduced by the "β-model" (Cavaliere & Fusco Femiano, 1976), reported in Eq. 1.5. The cluster center is RA = 12h 59m 41.5s; DEC = 27° 56′ 20″. We use the values derived by Briel et al. (1992), corrected for the cosmology adopted in this thesis. They found :

- β =0.75±0.03;
- r_c =291±17 kpc;

- n_0 =3.44±0.04 10^{-3} cm^{-3}.

3.4 Radio observations and images

3.4.1 VLA observations and data reduction

We selected from NVSS a sample of sources having a peak flux density larger than 45 mJy, located in a radius of 1^o from the cluster X-ray center center ($\simeq 5r_c$), and which have indication of polarization from Kim et al. (1990). A further selection was performed on the basis of the position of the sources. Observations have been performed at the VLA on 7 sources: 5C4.85 (NGC 4874), 5C4.81 (NGC 4869), 5C4.74, 5C4.114, 5C4.127, 5C4.42, and 5C4.152. Radio observations were performed using the 6 cm and 3.6 cm bands for all of the source except 5C4.114. This source being weaker, was observed at 20 cm and 6 cm. The sources were observed at two frequencies within each band, in order to have 4 frequency observations: 4.535 GHz, 4.935 GHz, 8.085 GHz, and 8.465 GHz. In addition 4.735 GHz observations were performed on sources 5C4.85 and 5C4.74. Due to technical issues, the observing time for the source 5C4.152 was reduced, and it was necessary to increase the signal-to-noise ratio in the 3.6 cm band. To increase the signal-to-noise ratio, the data at 8.085 and 8.465 GHz were averaged together and a single image at 8.275 GHz was obtained. For the source 5C4.114 we have observations at 1.365 GHz, 1.516 GHz, 4.535 GHz and 4.935 GHz. Details of the observations are reported in Table 6.1. The source 3C286 was used as both primary flux density calibrator[1] and as absolute reference for the electric vector polarization angle. The source 1310+323 was observed as both a phase and parallactic angle calibrator.

We performed standard calibration and imaging using the NRAO Astronomical Imaging Processing Systems (*AIPS*). Several cycles of phase self-calibration were performed to refine antenna phase solutions on target sources, followed by a final amplitude and gain self-calibration cycle in order to remove minor residual gain variations. Total intensity, I, and Stokes parameter Q and U images have been obtained for each frequency separately. After cleaning, radio images were restored with a naturally weighted beam. The final images were then convolved with a Gaussian beam having FWHM = $1.5''\times1.5''$ ($\sim 0.7\times0.7$ kpc). Polarization intensity $P = \sqrt{U^2+Q^2}$, Polarization angle $\Psi = \frac{1}{2}atan(U,Q)$ and fractional polarization

[1] we refer to the flux density scale by Baars et al. (1990)

Table 3.1: VLA observations of radio galaxies in the Coma cluster field.

Source	RA (J2000)	DEC (J2000)	ν (GHz)	Bandwidth (MHz)	Config.	Date	Time on Source (Hours)
5C4.85	12 59 35.3	+27 57 36	8.085 - 8.465	50	B	Jul 06	2.6
			4.535 - 4.935	50	B	Oct 07	2.6
			4.735	50	B	May 09	2.6
5C4.81	12 59 22.8	+27 54 40	8.085 - 8.465	50	B	Jul 06	2.6
			4.535 - 4.935	50	B	Jul 06	2.7
			8.465	50	C	Nov 90	3.8
5C4.74	12 58 59.4	+27 46 46	8.085 - 8.465	50	B	Jul 06	2.7
			8.085 - 8.465	50	C	Apr 08	5.4
			4.535 - 4.935	50	B	Jul 06	2.7
			4.735	50	B	May 09	2.6
5C4.114	13 00 50.6	+28 08 03	1.365 - 1.515	25	A	Dec 08	4.6
			4.535 - 4.935	50	B	Apr 09	5.1
5C4.127	13 01 20.1	+28 21 38	8.085 - 8.465	50	B	Jul 06	2.6
			4.535 - 4.935	50	B	Oct 07	2.9
5C4.42	12 56 38.2	+28 16 43	8.085 - 8.465	50	B	Jul 06	2.5
			4.535 - 4.935	50	B	Jul 06	2.6
5C4.152	13 03 14.4	+27 30 06	8.085 - 8.465	50	B	Aug 06	1.2
			4.535 - 4.935	50	B	Aug 06	1.5

Col. 1: Source name; Col. 2, Col. 3: Pointing position (RA, DEC); Col. 4: Observing frequency;
Col 5: Observing bandwidth; Col. 6: VLA configuration; Col. 7: Dates of observation;
Col. 8: Time on source (flags taken into account).

$FPOL = \frac{P}{I}$ images were obtained from the I, Q and U images. Polarization intensity images have been corrected for a positive bias. The calibration errors on the measured fluxes are $\sim 5\%$.

3.4.2 Radio properties of the observed sources

In this section the radio properties of the observed sources are briefly presented, and further details are reported in Table 3.2.

Redshift information is available for three out of the seven observed radio sources. Two of them (5C4.85 and 5C4.81) are well studied Coma cluster members, while the third one (5C4.127) is associated with a background source. Although the redshift

Table 3.2: Total and polarization intensity radio images. Images are restored with a beam of $1.5'' \times 1.5''$

Source name	ν (GHz)	σ(I) (mJy/beam)	σ(Q) (mJy/beam)	σ(U) (mJy/beam)	Peak brightness (mJy/beam)	S (mJy)	P (mJy)
5C4.85	4.535	0.018	0.015	0.015	5.8	75.7	7.5
	4.735	0.017	0.016	0.016	5.7	75.6	7.6
	4.935	0.019	0.017	0.017	5.8	75.2	7.5
	8.085	0.032	0.021	0.023	3.3	38.6	4.2
	8.465	0.034	0.022	0.022	3.1	36.4	4.0
5C4.81	4.535	0.025	0.022	0.024	2.7	66.7	12.1
	4.935	0.025	0.022	0.022	2.7	58.2	10.5
	8.085	0.022	0.019	0.021	2.4	25.2	5.5
	8.465	0.015	0.014	0.014	2.3	54.0*	11.3
5C4.74	4.535	0.025	0.023	0.023	2.7	17.0	3.4
	4.735	0.019	0.016	0.016	2.3	13.4	2.7
	4.935	0.023	0.021	0.021	2.6	15.6	3.1
	8.085	0.015	0.013	0.013	1.7	9.1	2.2
	8.465	0.014	0.013	0.013	1.6	8.6	2.1
5C4.114	1.365	0.040	0.027	0.027	11.3	47.0	5.9
	1.516	0.034	0.021	0.022	10.4	42.6	5.5
	4.535	0.014	0.013	0.013	4.2	16.4	3.0
	4.935	0.014	0.013	0.013	3.8	14.9	2.8
5C4.127	4.535	0.028	0.019	0.017	56.3	72.5	3.9
	4.935	0.024	0.020	0.017	56.4	72.9	3.9
	8.085	0.023	0.021	0.022	52.2	62.3	3.4
	8.465	0.025	0.021	0.023	51.6	61.4	3.3
5C4.42	4.535	0.023	0.022	0.022	7.2	63.2	8.0
	4.935	0.023	0.022	0.022	6.5	57.8	7.3
	8.085	0.022	0.020	0.020	3.8	33.2	4.1
	8.465	0.021	0.020	0.019	3.6	31.0	4.0
5C4.152	4.535	0.026	0.024	0.025	7.0	22.7	2.9
	4.935	0.026	0.025	0.025	6.4	20.3	2.4
	8.275	0.021	0.019	0.019	4.1	12.3	1.8

Col. 1: Source name; Col. 2: Observation frequency; Col. 3, 4, 5: RMS noise of the I, Q, U images;

Col. 7: Peak brightness; Col. 8: Flux density; Col. 9: Polarized flux density.

*The higher flux measured at 8.465 GHz is derived by combining together B and C array observations.

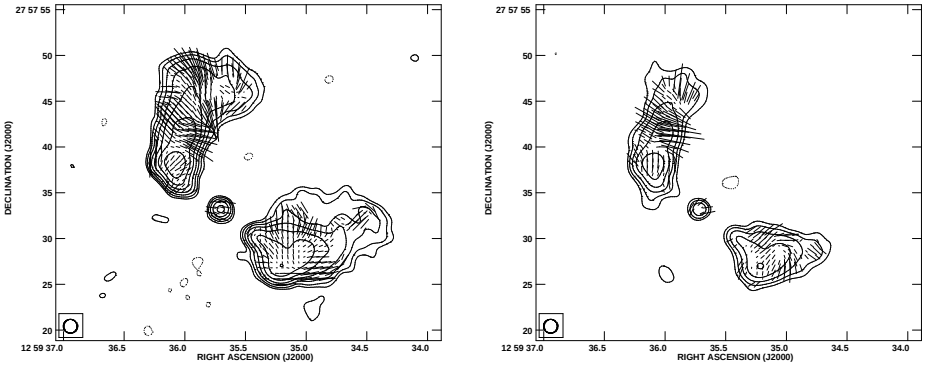

Figure 3.2: Source 5C4.85. Total intensity radio contours and polarization vectors at 4.535 GHz (left) and 8.465 GHz (right). The bottom contour corresponds to a 3σ noise level, contours are then spaced by a factor of 2. E vectors are superimposed: the orientation indicates the direction of the E field, while the line length is proportional to the fractional polarization intensity ($1''$ corresponding to 10%).

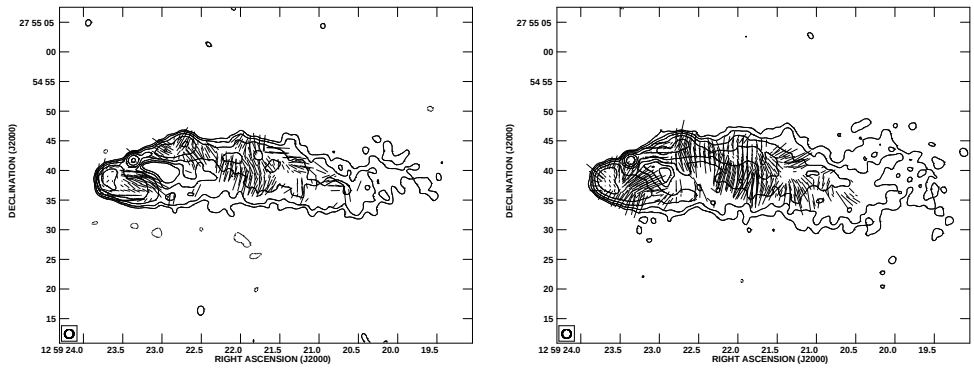

Figure 3.3: Source 5C4.81. Total intensity radio contours and polarization vectors at 4.535 GHz (left) and 8.465 GHz (right). The bottom contour corresponds to a 3σ noise level, and contours are then spaced by a factor of 2. E vectors are superimposed: orientation indicates the direction of the E field, while line length is proportional to the fractional polarization intensity ($1''$ corresponding to 10%).

is not known for the other four radio sources, they have not been identified with any cluster member down to very faint optical magnitudes: $M_r \geq$ -15 (see Miller et al. 2009). This indicates that they are background radio sources, seen in projection through the cluster. In the following the radio emission arising from the selected sample of sources is described together with their main polarization properties. In the fractional polarization images (from Fig. 3.2 to 3.8) pixels with errors larger than 10% were blanked.

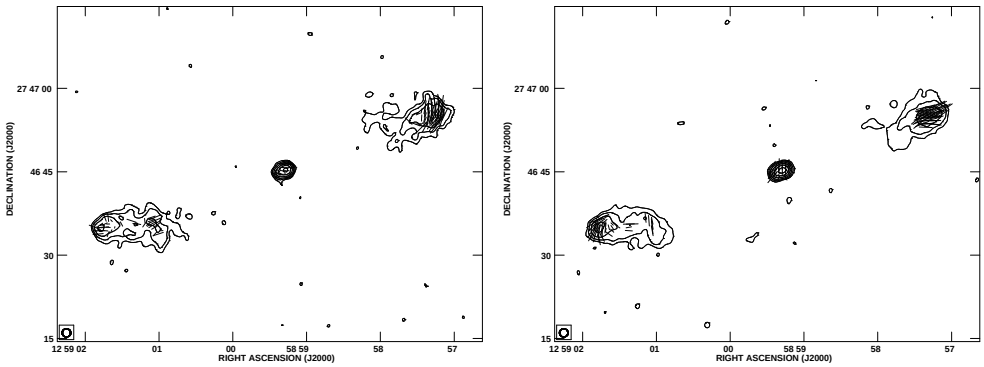

Figure 3.4: Source 5C4.74. Total intensity radio contours and polarization vectors at 4.535 GHz (left) and 8.465 GHz (right). The bottom contour corresponds to a 3σ noise level, contours are then spaced by a factor of 2. E vectors are superimposed: the orientation indicates the direction of the E field, while the line length is proportional to the fractional polarization intensity ($1''$ corresponding to 10%).

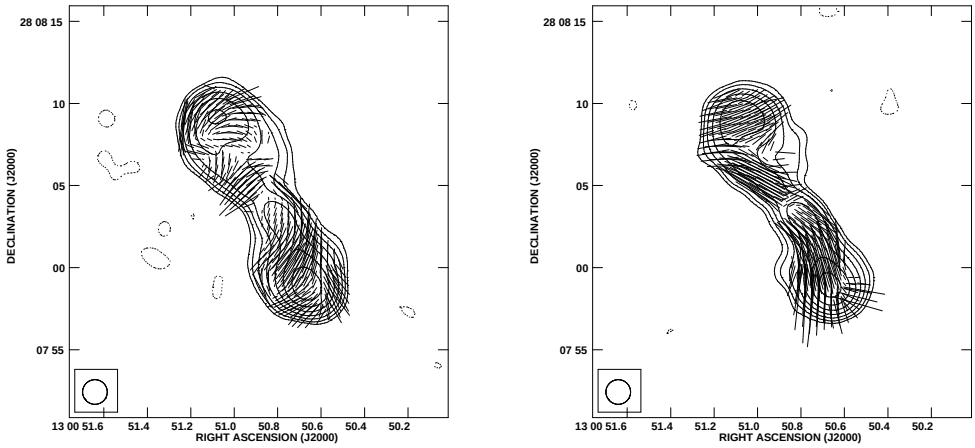

Figure 3.5: Source 5C4.114. Total intensity radio contours and polarization vectors at 1.365 GHz (left) and 4.935 GHz (right). The bottom contour corresponds to a 3σ noise level, contours are then spaced by a factor of 2. E vectors are superimposed: the orientation indicates the direction of the E field, while the line length is proportional to the fractional polarization intensity ($1''$ corresponding to 10%).

5C4.85 - NGC 4874

This a cluster source, optically identified with the Coma central cD galaxy NGC 4874 (see *e.g.* Mehlert et al. 2000). It is a Wide Angle Tail radio galaxy, whose maximum angular extension is $\sim 30''$, corresponding to ~ 15 kpc. The angular extension of the two lobes individually is larger at the lowest frequency. The northern lobe shows a mean fractional polarization of 10% and 11% at 4.535 and 8.465 GHz respectively, while the western lobe is less polarized ($\sim$7% at both frequencies). In Fig. 3.2 the radio emission is shown at 4.535 and 8.465 GHz.

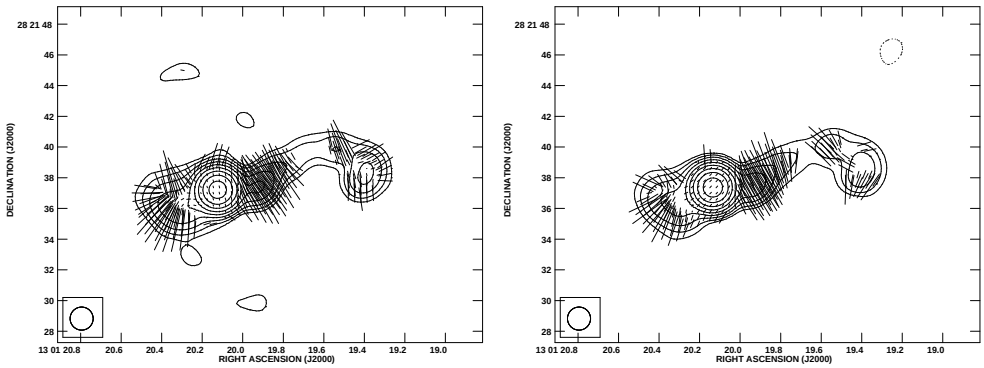

Figure 3.6: Source 5C4.127. Total intensity radio contours and polarization vectors at 4.535 GHz (left) and 8.465 GHz (right). The bottom contour corresponds to a 3σ noise level, contours are then spaced by a factor of 2. E vectors are superimposed: the orientation indicates the direction of the E field, while the line length is proportional to the fractional polarization intensity ($1''$ corresponding to 10%).

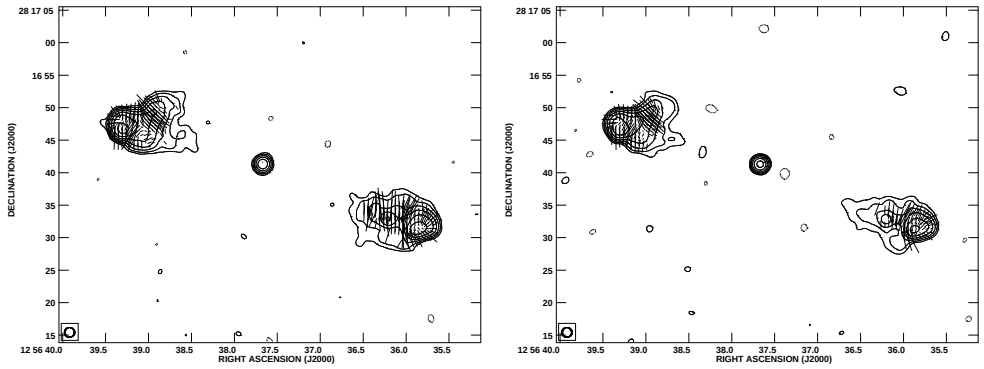

Figure 3.7: Source 5C4.42. Total intensity radio contours and polarization vectors at 4.535 GHz (left) and 8.465 GHz (right). The bottom contour corresponds to a 3σ noise level, contours are then spaced by a factor of 2. E vectors are superimposed: the orientation indicates the direction of the E field, while the line length is proportional to the fractional polarization intensity ($1''$ corresponding to 10%).

5C4.81 - NGC 4869

This source has been studied in detail by Dallacasa et al. (1989) and Feretti et al. (1995). It is associated with the giant elliptical galaxy NGC4869. 5C4.81 has a Narrow Angle Tail radio morphology, and its angular size in the images obtained here is $55''$ (25 kpc). The mean fractional polarization in the tail is 18% at 4.535 GHz and 21% at 8.465 GHz. In Fig. 3.3 the radio emission is shown at 4.535 and 8.465 GHz.

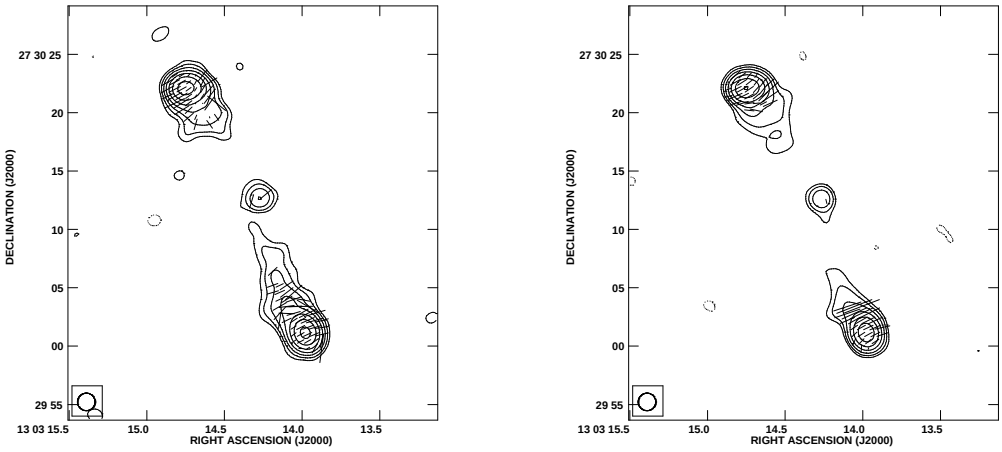

Figure 3.8: Source 5C4.152. Total intensity radio contours and polarization vectors at 4.535 GHz (left) and 8.465 GHz (right). The bottom contour corresponds to a 3σ noise level, contours are then spaced by a factor of 2. E vectors are superimposed: the orientation indicates the direction of the E field, while the line length is proportional to the fractional polarization intensity ($1''$ corresponding to 10%).

5C4.74

The source 5C4.74 consists of 5C4.74a and 5C4.74b, the two radio lobes of a FRII radio source. Its redshift is unknown, and no optical identification has been found, either with a Coma cluster member (Miller et al. 2009) nor with a background radio source. From this we conclude that it is a distant background source. The northeastern lobe has a fractional polarization of ∼28% and 35% respectively at 4.535 and 8.465 GHz, while the southwestern lobe is less polarized (∼ 19% at 4.535 GHz and ∼ 23% at 8.465 GHz).

In Fig. 3.4 the radio emission is shown at 4.535 and 8.465 GHz.

5C4.114

5C4.114 is a FRI radio source, with angular size of ∼ $15''$. Its redshift is unknown, and no optical identification either with a Coma cluster galaxy (Miller et al. 2009) nor with a background galaxy has been found, indicating that 5C4.114 has a redshift greater than 0.023. The southern lobe appears brighter than the northern one. The source fractional polarization is ∼ 13% at 1.365 GHz and ∼ 19% at 4.935 GHz. In Fig. 3.5 the radio emission is shown at 1.365 and 4.935 GHz.

5C4.127

5C4.127 is a QSO located at z=1.374 (Veron-Cetty & Veron, 2001). Observations presented here show that in addition to a bright nucleus the source has a weak extension in the E-W direction of $\sim 16\ ''$ ($\sim$ 136 kpc) at both of the observing frequency bands. The extended component has a mean fractional polarization of 13% at 4.535 GHz and 14% at 8.465 GHz, while the nucleus is polarized at the 3% level. In Fig. 3.6 radio contours of the source and polarization vector images are shown.

5C4.42

5C4.42 is a FRII-type radio source. Redshift information is not available in the literature and no optical identification has been found. The same arguments explained above for the source 5C4.74 let us conclude that it is a background radio source. The source is composed by a weakly polarized core and two lobes that extend for $\sim 25''$ in the southwest and northeast directions. The lobes show a mean fractional polarization of $\sim$ 13% at both 4.535 GHz and 8.465 GHz. In Fig. 3.7 radio contours and vector polarization images of the source are shown.

5C4.152

5C4.152 is a FRII type Radio Galaxy. No redshift is available in the literature for this source. The same arguments explained above for the source 5C4.74 let us conclude that it is a background radio source. It is composed of a core having a fractional polarization of a few percent and two lobes that extend for $\sim 28''$ north-south. The lobes show a mean fractional polarization of $\sim \sim$ 13% 4.535 GHz and 15% at 8.275 GHz. In Fig. 3.8 radio contours and vector polarization images of the source are shown.

3.5 RM: fits and errors

The multifrequency observations described in the previous section allow a precise determination of the Faraday RM. There are however some additional complications in the determination of the RM, that require an accurate evaluation of the observed polarization plane orientation. In fact, since the measured polarization angle Ψ_{obs} is constrained only to values between 0 and π leaving the freedom of additions of nπ,

with n being an integer, the determination of RM and $\Psi_\circ$ is ambiguous, causing the so-called nπ-ambiguity. As a consequence, the least square fits has to be applied to all possible nπ combinations of the polarization angle data at each data point of the polarised radio source while searching for the nπ combination for which the χ^2 is minimal. A further complication derives from the fact that in pronciple χ^2 can be decreased to infinitely small values by increasing RM substantially (Vallèe & Kronberg, 1975). Several approaches have been proposed to overcome this issue: Vallé & Kronberg (1975) suggested to perform the fit introducing an artificial upper limit in the $|RM|$ value, Ruzmaikin & Sokoloff (1979) proposed to infer the nπ ambiguity from observations of two closely spaced frequencies, that is the algorithm that is currently implemented in the *AIPS RM* task. Other approaches have been proposed by Sarala & Jain (2001), that take into account the circular nature of the polarization angle and apply a maximum likelihood method to spectral polarization data, and by Brentjens & De Bruyn (2005), who proposed the RM-synthesys method via wide band low frequency polarimetry. A different approach, that is based on a "global" fit of the RM, has been suggested by Dolag et al. (2005c) and implemented in the *Pacerman* algorithm. This algorithm is based on the assumption that if small gradients exist in the polarization angle between neighbouruing pixels in all the observed frequencies simultaneously, then these pixels can be considered as connected and define a patch. Inside each patch, the pixel that shows the higher signal-to noise ratio is selected, and it is defined to have a unique absolute polarization angle. The algorithm will start from this pixel to assigne absolute polarization angle to the pixel inside the same patch. It is thus sufficient to solve the nπ ambiguity for a small number of pixels simultaneously within the same area, and this solution is used for all the spatially connected pixels. Pixels with low signal-to-noise will profit from their neighbouring pixels allowing a relicable detremination of the RM and Ψ_i.

We used the *Pacerman* algorithm to derive the RM from the observed Ψ_{obs}. We considered as reference pixel those with a polarization angle uncertainty less than 7 degrees, and fixed the gradient threshold to consider pixels as belonging to the same patch, to 15 degrees. An error of 7 degrees in the polarization angle corresponds to 3σ level in both U and Q polarization maps simultaneously. We allowed *Pacerman* to perform the RM fit if at least in 3 frequency maps the above mentioned conditions

were satisfied. The resulting RM images are shown in Fig. 3.9, 3.10, 3.11, 3.12, 3.13, 3.14 and 3.15 overlaid on the total intensity contours at 4.935 GHz. In the same figures we also provide the RM distribution histograms and the RM fits for selected pixels in the map. The linear trend of Ψ versus λ^2 and the good fits obtained clearly indicate that the Faraday rotation is occurring in a screen external to the emitting source. From the RM images we computed the RM mean ($\langle RM \rangle$) and its dispersion ($\sigma_{RM,obs}$).

There are two different types of errors that we have to account for: the statistical error and the fit error. The statistical errors for $\langle RM \rangle$ and for $\sigma_{RM,obs}$ is given by $\sigma_{RM,obs}/\sqrt{n_b}$ and $\sigma_{RM,obs}/\sqrt{2n_b}$ respectively, where n_b is the number of beams over which the RM has been computed. The statistical error is the dominant one, while the error of the fit has the effect of increasing the *real* value of σ_{RM}. Thus, in order to recover the *real* standard deviation of the observed RM distribution we have computed the $\sigma_{RM,dec}$ as $\sqrt{\sigma^2_{RM,obs} - Median(Err_{fit})^2}$. with $Median(Err_{fit})$ being the median of the error distribution. The fit error has been estimated with Monte Carlo simulations. We have extracted n_B values, from a random Gaussian distribution having $\sigma = \sigma_{RM,obs}$ and mean = $\langle RM \rangle$, we have then added to the extracted values a Gaussian noise having $\sigma_{noise} = Err_{fit}$, in order to mimic the effect of the noise in the observed RM images. We have computed the mean and the dispersion (σ_{sim}) of these simulated quantities and then subtracted the noise from the dispersion obtaining $\sigma_{sim,dec} = \sqrt{\sigma^2_{sim} - \sigma^2_{noise}}$. We have thus obtained a distribution of $\sigma_{sim,dec}$ and means. The standard deviation of the $\sigma_{sim,dec}$ distribution is then the fit error on $\sigma_{RM,dec}$ while the standard deviation of the mean distribution is the fit error on $\langle RM \rangle$. We checked that the mean of both distributions recover the corresponding observed values. In Table 3.3 we report the RM mean, the observed RM dispersion ($\sigma_{RM,obs}$), the value of $\sigma_{RM,dec}$ (hereafter simply σ_{RM}), with the respective errors, the average fit error (Err_{fit}), and the number of beam over which the RM statistic is computed (n_b).

The source 5C4.74

The value of $\langle RM \rangle$ that we have derived for the source 5C4.74 is quite high compared with the values found for the other sources in this cluster and it is also higher than the values obtained in other clusters for sources at similar distances from the cluster

center (*e.g.* Clarke et al. 2004). The level of polarization of this source is also quite high compared to the other sources (see Sec. 3.4.2). We note its position southwest of the cluster core, in the direction of the sub-group NGC4839 that is currently merging with the Coma cluster (Feretti & Neumann 2006). One possibility is that the magnetic field and/or the thermal gas has been compressed and ordered in this region, increasing the observed polarization flux and making $\langle RM \rangle$ peculiar in this position. This might imply that more sophisticated models, that include deviations from a spherical symmetry, could give a better representation of the gas density profile. We note however that the X-ray analysis performed in the literature by Briel et al. (1992) shows that the spherical $\beta-$model is a good representation of the cluster X-ray surface brightness, indicating that deviations from spherical symmetry are small. The σ_{RM} value is fully compatible with the trend suggested by the other sources. This could be explained in the proposed scenario, if the magnetic field has been compressed and ordered. In the following analysis we will use mainly the σ_{RM} to infer the magnetic field strength. Nonetheless, results will also be presented excluding this source from our analysis.

3.5.1 Galactic contribution

The contribution to the Faraday RM from our Galaxy may introduce an offset in the Faraday rotation that must be removed. This contribution depends on the galactic positions of the observed sources. The Coma cluster Galactic coordinates are $l = 58^\circ$ and $b = 88^\circ$. The cluster is close to the galactic north pole, so that Galactic contribution to the observed RM is likely negligible. However, in order to estimate this contribution the average RM for extragalactic sources located in projection nearby the Coma cluster region has been computed using the catalogue by Simard-Normadin et al. (1981). The RM from each source has been weighted by the inverse of its distance from the Coma cluster center. It results that in a region of 25×25 degrees^2 centered on the cluster, the Galactic contribution is $\sim$ -0.15 rad/m^2. This small contribution is thus completely negligible and has been ignored in the following analysis.

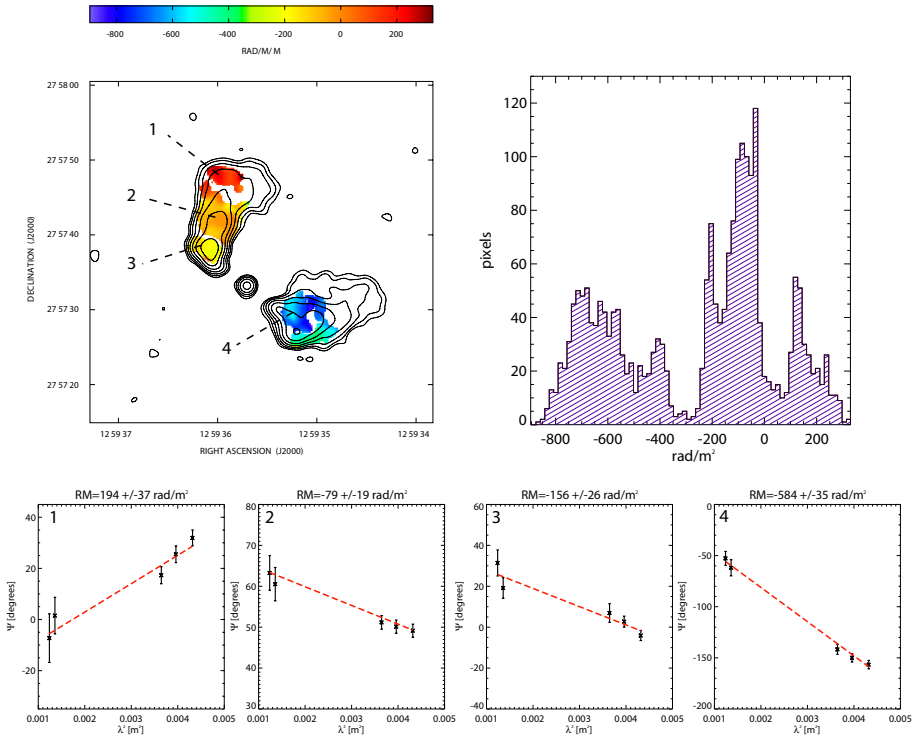

Figure 3.9: **5C4.85:** *Top left:* The *RM* fit is shown in color along with total intensity radio contours 4.935 GHz. The bottom contour correspond to the 3σ noise level and contours are then spaced by a factor of 2.*Top right* distribution histogram of the *RM* values. *Bottom:* fits of polarization angle versus λ^2 in four representative pixels.

Table 3.3: Rotation Measures values of the observed sources

Source	Projected distance kpc	n. of beams	$\langle RM \rangle$ rad/m^2	$\sigma_{RM,obs}$ rad/m^2	Err$_{fit}$ rad/m^2	σ_{RM} rad/m^2
5C4.85	51	35	-256±50	303	46	299±36
5C4.81	124	56	-120±22	166	48	159±17
5C4.74	372	10	372±51	154	44	148±41
5C4.114	532	16	51±4	16	2	16±3
5C4.127	919	7	21±30	65	36	54±26
5C4.42	1250	33	6±12	56	43	36±11
5C4.152	1489	4	32±27	37	28	24±21

Col. 1: Source name Col. 2: Source projected distance from the X-ray cluster center;

Col. 3: number of beams over which *RM*s are computed;

Col. 4: Mean value of the observed *RM* distribution;

Col. 5: Dispersion of the observed *RM* distribution;

Col. 6: Median of the *RM* fit error; Col 7: Dispersion of the *RM* distribution after noise deconvolution.

3.5.2 *RM* local contribution

We discuss here the possibility that the *RM* observed in radio galaxies are not associated with the foreground ICM but may arise locally to the radio source, as

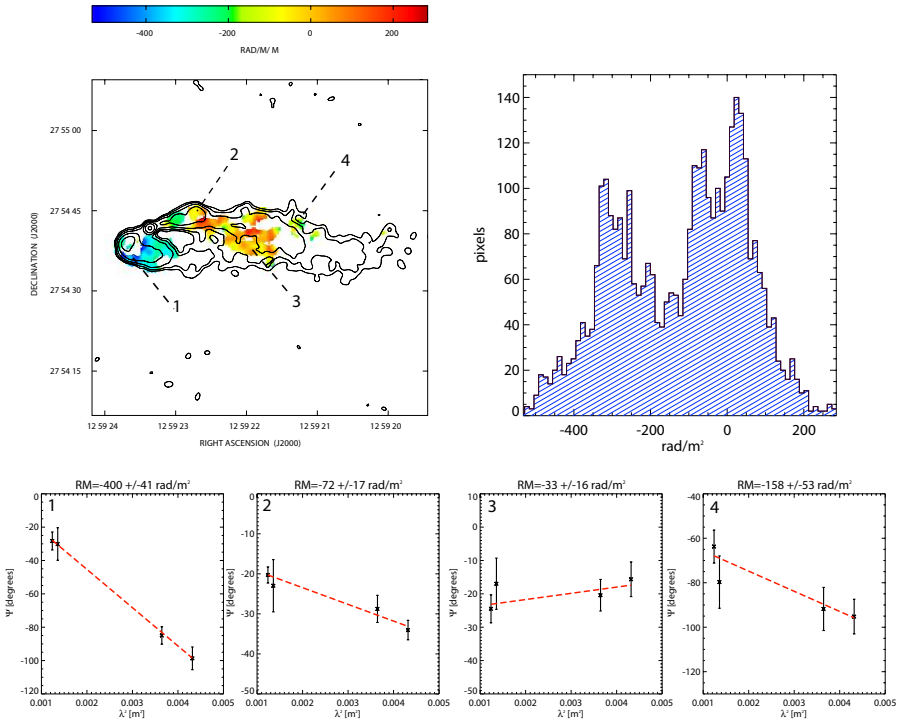

Figure 3.10: **5C4.81:** *Top left:* The *RM* image is shown in color along with total intensity radio contours at 4.935 GHz. Contours start at 3σ and increase by factors of 2. *Top right* distribution histogram of the *RM* values. *Bottom:* fits of polarization angle versus λ^2 in four representative pixels.

suggested by Bicknell et al. (1990), Rudnick & Blundell (2003), either in a thin layer of dense warm gas mixed along the edge of the radio emitting plasma, or in its immediate surroundings. There are several arguments against this interpretation:

- the trend of *RM* versus the cluster impact parameter in both statistical studies and individual cluster investigations (Clarke et al. 2001, 2004; Feretti et al. 1999; Govoni et al. 2005);

- the Laing-Garrington effect (Laing 1988; Garrington et al. 1988; Garrington & Conway 1991). This effect consists of an asymmetry in the polarization properties of the lobes of bright radio sources with one-sided, large scale jets. The lobe associated with the jet that is beamed toward the observer is more polarized than the one associated with the counter-jet that points away from the observer. This effect can be explained if we assume that the radio emission from the two lobes cross different distances through the ICM, and therefore

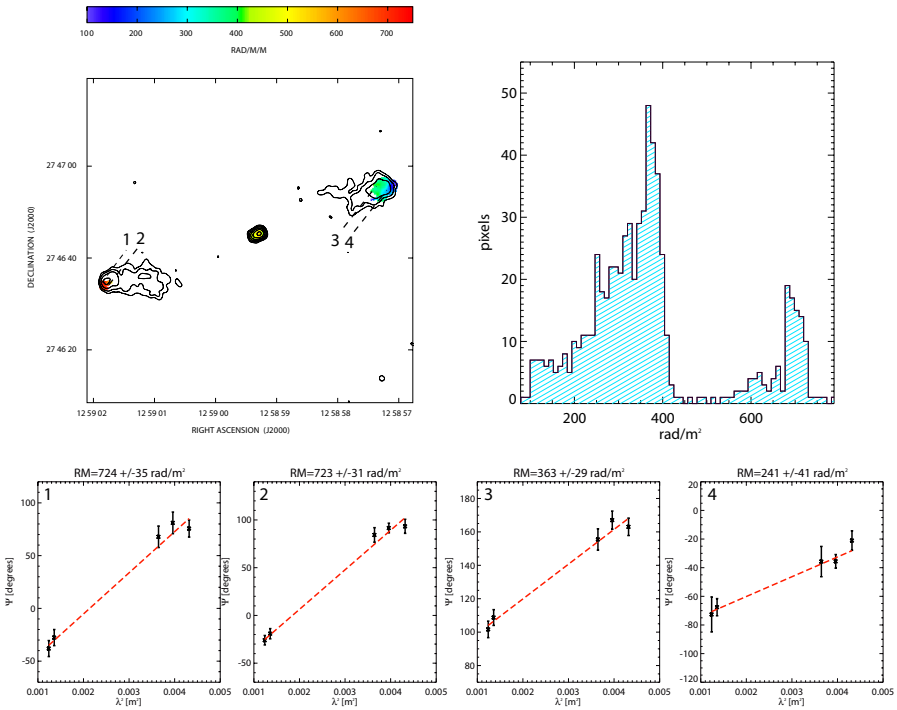

Figure 3.11: **5C4.74:** *Top left:* The *RM* image is shown in color along with total intensity radio contours at 4.935 GHz. Contours start at 3σ and increase by factors of 2. *Top right* distribution histogram of the *RM* values. *Bottom:* fits of polarization angle versus λ^2 in four representative pixels.

the emission from the counter-lobe is seen through a greater Faraday depth, causing greater depolarization. This means also that the observed polarization properties of the source are strongly influenced by the ICM.

- statistical tests on the scatter plot of *RM* versus polarization angle for the radio galaxy PKS1246-410 (Ensslin et al. 2003);

- the relation between the *RM* and the cooling flow rate in relaxed clusters (Taylor et al. 2002).

This observational evidence allows us to conclude that the main contribution to the *RM* occurs in a Faraday screen located outside the radio sources. The only contribution that could contaminate the cluster Faraday screen is the contribution

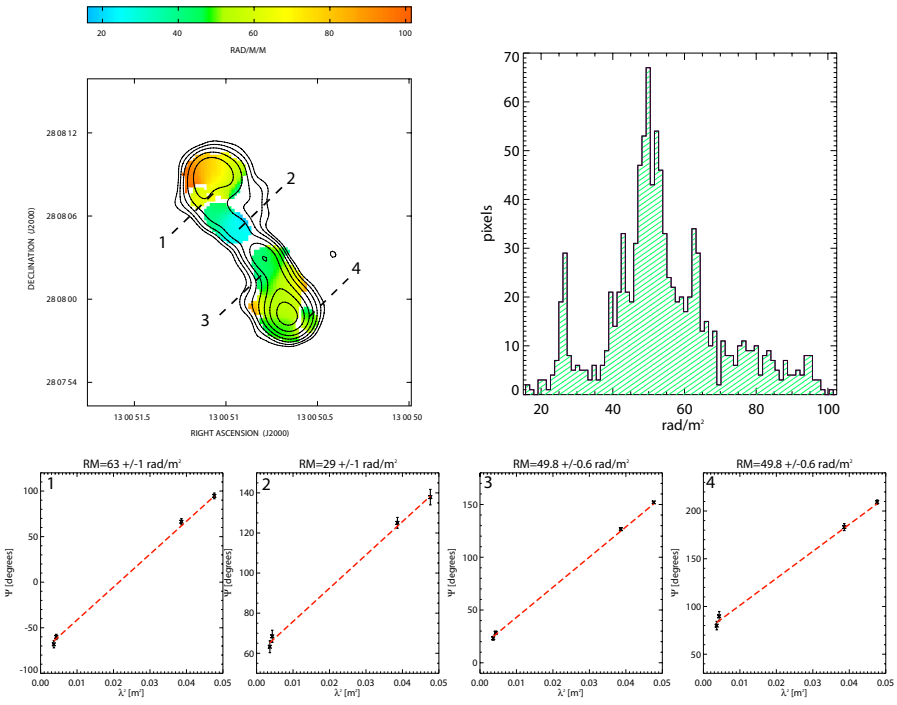

Figure 3.12: **5C4.114:** *Top left:* The RM image is shown in colors along with total intensity radio contours at 4.935 GHz. Contours start at 3σ and increase by factors of 2. *Top right* distribution histogram of the RM values. *Bottom:* fits of polarization angle versus λ^2 in four representative pixels.

from the disturbed ISM in the central parsecs of the host elliptical galaxy where the inner jet has been found to have RMs up to thousands of radians per square meter (Zavala & Taylor 2004). We removed the core from the RM analysis in order to avoid any contribution of this kind (out to a distance of $\sim 5''$ from the core).

The ICM origin of the observed RM is also confirmed by the data presented here (Tab. 3.3): the trend of σ_{RM} exhibits a decrease with increasing cluster impact parameter. Values of $\langle RM \rangle \neq 0$ and different values of $\langle RM \rangle \neq$ for sources located at different projected distances to the cluster center indicate that the magnetic field substantially changes on scales larger than the source size, while small RM fluctuation can be explained by magnetic field fluctuation on scales smaller than the source size. Thus in order to interpret correctly the RM data we have to take into account magnetic field fluctuations over a range of spatial scales, *i.e.* , we have to model the magnetic field power spectrum.

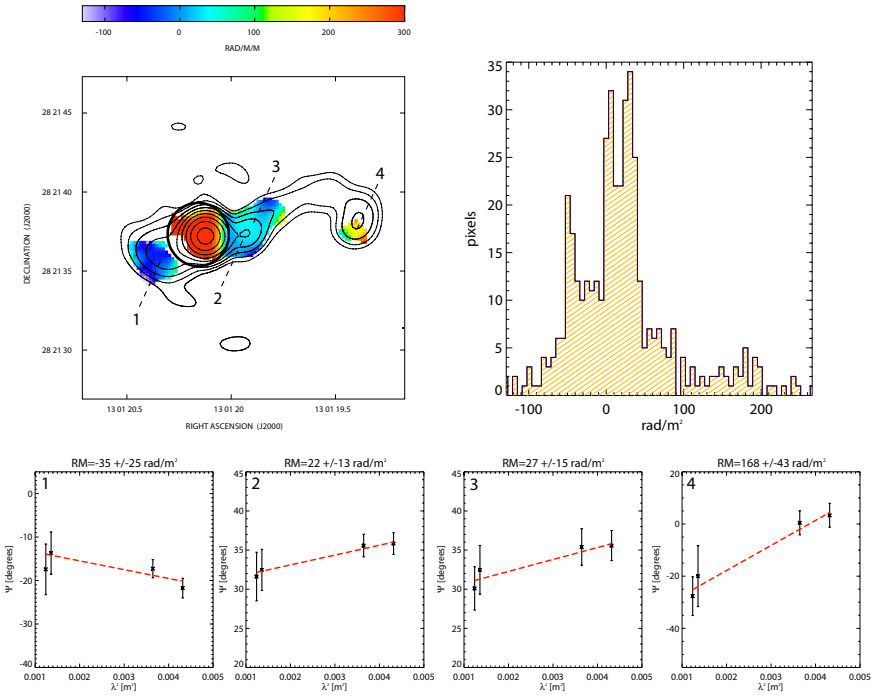

Figure 3.13: **5C4.127:** *Top left:* The *RM* image is shown in color along with total intensity radio contours at 4.935 GHz. Contours start at 3σ and increase by factors of 2. The circle indicates the area masked in the *RM* analysis. *Top right* distribution histogram of the *RM* values. *Bottom:* fits of polarization angle versus λ^2 in four representative pixels.

3.6 Conclusions

We have presented new VLA observations of seven sources in the Coma cluster field at multiple frequencies in the range 1.365 – 8.465 GHz. The high resolution of these observations has allowed us to obtained detailed *RM* images with 0.7 kpc resolution. The sources were chosen in order to sample different lines-of-sight in the Coma cluster in order to constrain the magnetic field profile. We have found that:

- the distribution of the *RM* derived for the sources are nearly Gaussian, in agreement with a Gaussian distribution of the magnetic field components. Deviations from this distribution are interpreted as due to missing information deriving from finite sampled area, that is the region of the cluster covered by the source emission.

- σ_{RM} and $\langle RM \rangle$ decrease with increasing distance from the cluster center, except for the source 5C4.74, that shows a high value of $\langle RM \rangle$. We argue that this may arise from its peculiar position southwest of the Coma cluster core,

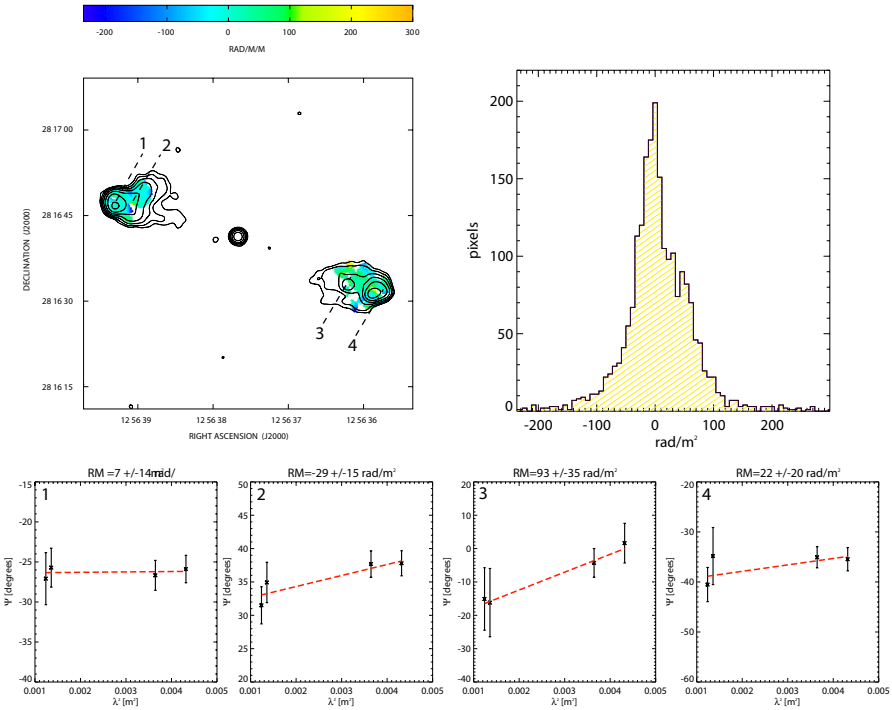

Figure 3.14: **5C4.42:** *Top left:* The RM image is shown in color along with total intensity radio contours at 4.935 GHz. Contours start at 3σ and increase by factors of 2. *Top right* distribution histogram of the RM values. *Bottom:* fits of polarization angle versus λ^2 in four representative pixels.

toward the NGC4839 group that is currently merging with the Coma cluster. These trends indicate that the magnetic field has a radial decline going from the center to the periphery of the cluster, in agreement with previous studies and with theoretical expectations.

- The $\langle RM \rangle$ is considerably different from 0 in the inner sources, indicating that the magnetic field fluctuates on scales larger than the source size.

- Small fluctuations of the RM, on scales of a few kiloparsec indicate that the ICM magnetic field has also components on small scales.

- The above trends indicate that a power spectrum for the magnetic field has to be considered in order to explain RM fluctuations on both small and large scales.

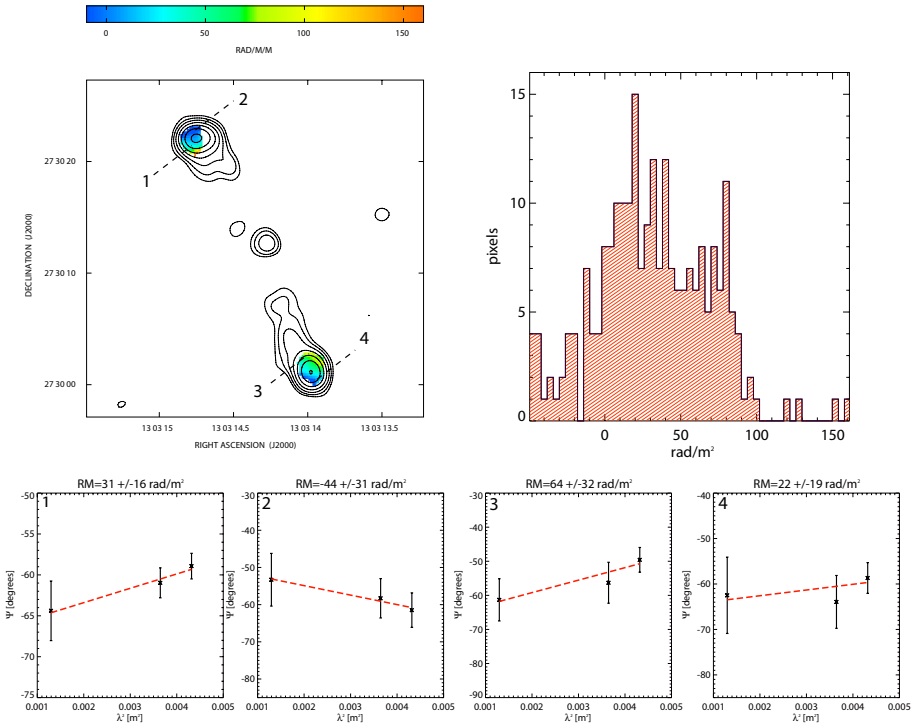

Figure 3.15: **5C4.152:** *Top left:* The *RM* image is shown in color along with total intensity radio contours at 4.935 GHz. Contours start at 3σ and increase by factors of 2. *Top right* distribution histogram of the *RM* values. *Bottom:* fits of polarization angle versus λ^2 in four representative pixels.

Chapter 4

The Coma cluster magnetic field: simulations and results*

4.1 Introduction

In this Chapter we will present the analysis of the magnetic field in the Coma cluster on the basis of the data presented in Chapter 3. The strategy to obtain the magnetic field model that best reproduces the observed data is the following: we have used the *Faraday* code (Murgia et al. 2004) to perform 2-Dim and 3-Dim simulations of magnetic fields with different power spectrum models, and varying the value of the central magnetic field strength and radial decline slope. From these different models, with the help of information available in the literature on the gas density distribution, we have derived synthetic RM images, that we have compared with the observed ones. Observational biases such as noise, beam convolution, and finite sampling of RM are taken into account in the analysis.
The study of the Coma cluster magnetic field through this new approach allows to put constraints on the magnetic field power spectrum, central intensity and radial decline slope. The results can then be compared with the estimates derived from equipartition and Inverse Compton Hard-X ray emission.

4.2 The magnetic field model

In order to set constraints on the magnetic field strength and structure in the Coma cluster, we adopted the approach suggested by Murgia et al. (2004). The magnetic

*Bonafede et al. 2010, A&A in press

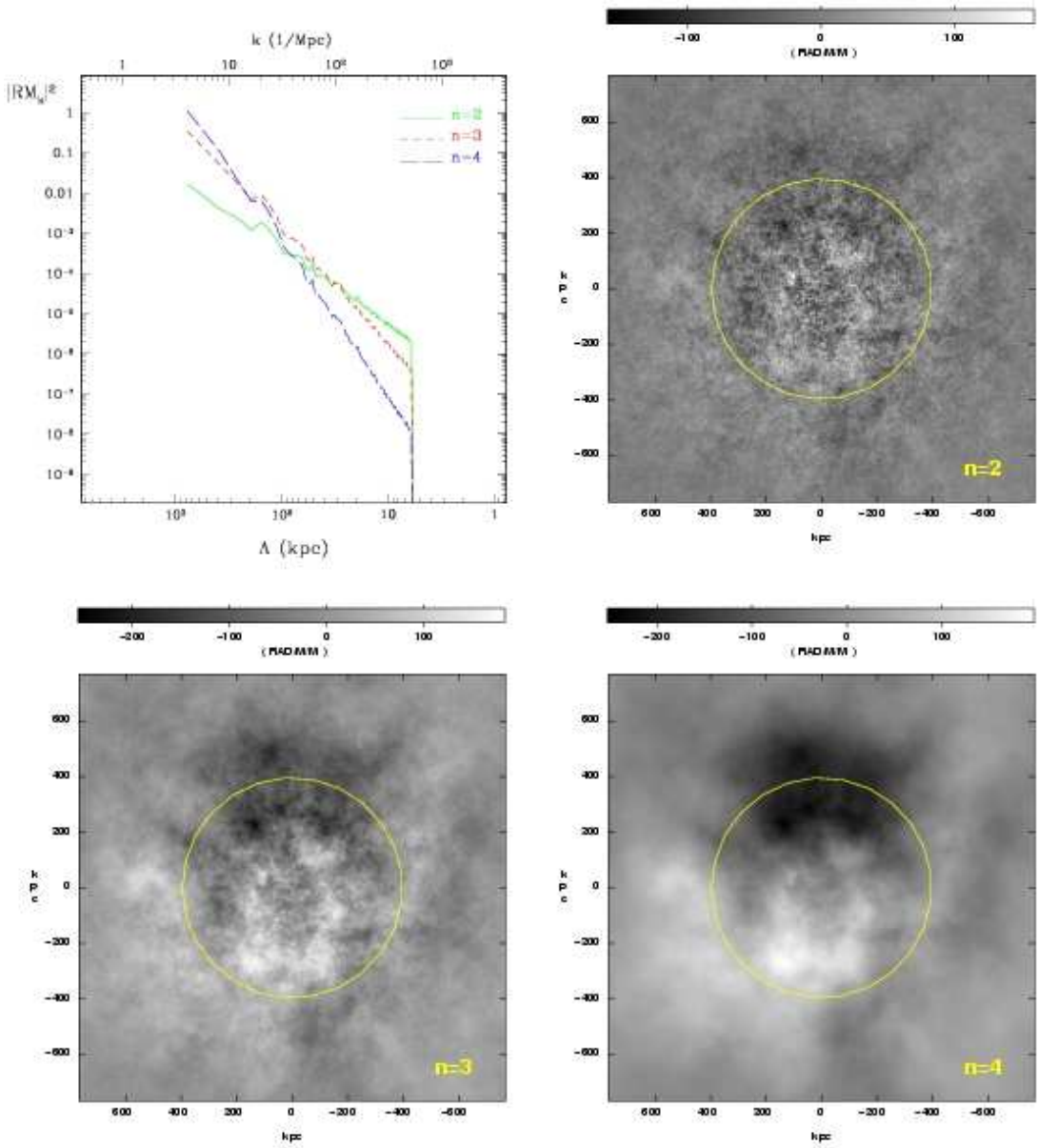

Figure 4.1: Simulated RM images for different values of the magnetic field power spectrum spectral index n. The three power spectra are normalized to have the same total magnetic field energy which is distributed over the range of spatial scales from 6 to 770 kpc. The average field at the cluster center is 1 μG. Each image shows a field of view of about 1.5 $\times$ 1.5 Mpc. The cluster core radius (indicated by the circle) is 400 kpc, and RM have been obtained by integrating up to $\sim$ 4 core radii. The two-dimensional power spectra of the simulated RM images are shown in the top left panel. They have the same slope as their parent magnetic field power spectra and they span an equivalent range of spatial scales. Figure taken from Murgia et al. (2004).

field is modelled as a 3-dimensional multi-scale model, and a radial decline of the magnetic field is accounted for as well.

4.2.1 The magnetic field power spectrum

The magnetic field is constructed by selecting a 3-Dim power spectrum for the vector potential A , and its components in the Fourier space: $\tilde{A}(k)$ accordingly. The amplitude of each component $\tilde{A}(k)$ is randomly extracted from a Rayleigh distribution:

$$P(A,\phi)dAd\phi = \frac{A}{2\pi|A_k|^2}exp(-\frac{A^2}{2|A_k|^2})dAd\phi \tag{4.1}$$

and the phase ϕ is uniformly distributed between $[0; 2\pi]$. We adopted a power-law power spectrum for the vector potential:

$$|A_k|^2 \propto k^{-\zeta} \tag{4.2}$$

The magnetic field components in the Fourier space are then obtained by the cross product:

$$\tilde{B}(k) = ik \times \tilde{A}(k). \tag{4.3}$$

Finally, the field components B_i in the real space are derived using 3-Dim Fast Fourier Transform (Press et al. 1986).
The resulting magnetic field is a multi-scale model with the following properties:

(i) $\nabla \cdot \mathbf{B} = 0$;

(ii) The magnetic field energy density associated with each component B_k is: $|B_k|^2 = C_n^2 k^{-n}$, $n = \zeta - 2$, where C_n^2 is the power spectrum normalization;

(iii) The assumed form of the vector potential results in a field whose components B_i have a Gaussian distribution, with $\langle B_i \rangle = 0$, $\sigma_{B_i} = \langle B_i^2 \rangle$;

(iv) B has a Maxwellian distribution, with $\langle B \rangle = 2\sqrt{\frac{2}{\pi}}\sigma_{B_i}$ and $\sigma_B = \sqrt{\frac{3\pi-8}{\pi}}\sigma_{B_i}$.

It follows that the magnetic field energy density averaged over a volume V is proportional to

$$\begin{aligned} \langle B \rangle^2 &\propto \frac{C_n^2}{V} \ln \frac{k_{max}}{k_{min}}, n = 3 \\ \langle B \rangle^2 &\propto \frac{C_n^2}{V} \frac{k_{max}^{3-n} - k_{min}^{3-n}}{3-n}, n \neq 3 \end{aligned} \tag{4.4}$$

We define $\Lambda = \frac{2\pi}{k}$ as the physical scale of the magnetic field fluctuations in the real space.

According to the chosen model for the magnetic field power spectrum, three parameters have to be determined: Λ_{min}, Λ_{max} and n. It is worth noting that a degeneracy arises between Λ_{max} and n (the higher n is the lower Λ_{max} is required). In fact, it can be easily seen from Fig. 4.1 (upper-left panel), that different models with different values of n can reproduce different values of RM with a proper choice of Λ_{max}: the higher n is, the lower Λ_{max} is required.

4.2.2 The magnetic field radial profile

There are several indications that the magnetic field intensity decreases going from the center to the periphery of a cluster. This is expected by magneto-hydrodynamical simulations (see *e.g.* Dolag et al. 2008) and by spatial correlations found in some clusters between thermal and non-thermal energy densities (Govoni et al. 2001).

We assume that the cluster magnetic field follows the thermal component radial distribution according to:

$$\langle \mathbf{B} \rangle (r) = \langle \mathbf{B}_0 \rangle \left(\frac{n_e(r)}{n_0} \right)^{\eta} \tag{4.5}$$

where $\langle \mathbf{B}_0 \rangle$ is the mean magnetic field strength at the cluster center.

In order to obtain the desired magnetic field radial profile we have operated directly in the real space. Strictly, this operation should be performed in the Fourier space, by convolving the spectral potential components with the shaping profile, before the cross product is formed. In fact, the convolution of the magnetic field power spectrum with the Fourier transform of the shaping function in the real space alters the power spectrum at the edges of the computational grid. We note however that in the case of Coma, the size of the cluster core radius is a considerable fraction of the simulated volume, and moreover, the size of the observed sources is much smaller than the cluster core radius, so that, as already proved by Murgia et al. (2004) these two approaches give negligible differences.

When the magnetic field profile is considered, two more parameters have to be determined: η and $\langle \mathbf{B_0} \rangle$. Another degeneracy arises here. In fact, since the RM is an integrated measure of the magnetic field strength, high values of $\langle \mathbf{B_0} \rangle$ and steep radial profile (*i.e.* high values of η) have the same effect as regards the RM, that

we would obtain for lower values of $\langle \mathbf{B_0} \rangle$ and flat radial profile (*i.e.* low values of η). Although this degeneracy cannot be entirely solved, the range of the degenerate parameters (B_0 and η) can be limited by observing several sources at different impact parameters, as obtained for the Coma cluster.

The adopted magnetic field model has then *a total of 5 free parameters:* Λ_{min}, Λ_{max}, n, η *and* $\langle \mathbf{B_0} \rangle$, *and is subject to two degeneracies:* Λ_{max}- n *and* η *and* $\langle \mathbf{B_0} \rangle$.
Fitting all of these five parameters simultaneously would be the best way to proceed, but it is not feasible here, due to the computational burden caused by the Fourier Transform inversion. Indeed we have to simulate a large volume $\sim 3^3$ Mpc^3 with a sub-kiloparsec pixel-size.
We proceed as follows: we perform 2-Dim simulations with different magnetic field power spectra in order to recover the RM statistical indicator that are sensitive to the magnetic field power spectrum (Sec. 4.4.1). From this analysis we derive the power spectrum that best reproduces the observations. We then perform 3-Dim magnetic field simulations varying the values of B_0 and η and derive the magnetic field profile that best reproduces the RM observations (Sec. 4.5.1).

4.3 Comparing observations and simulations

A tricky point when observations and simulations are compared is the correct evaluations of the errors and uncertainties that this process is subject to. The simulations we present in this work start from a random seed and generate 2-Dim and 3-Dim magnetic fields. From these fields simulated RM images are obtained, and then compared with those observed in order to constrain the magnetic field properties. It is worth noting that due to the random nature of the magnetic field, given a magnetic field model, the RM in a given position of the cluster varies depending on the initial seed of the simulation. It follows that different of the same model produce different values of $\langle RM \rangle$ and σ_{RM} at that position. Because of the limited area covered by RM observations, the random nature of the field cannot be neglected in our analysis.
We adopt the following approach to compare observations and simulations: once the simulated RM image is obtained for a source, it is convolved with a Gaussian function having $FWHM$ equal to the beam $FWHM$ of the observed image. The

simulated RM image is then blanked in the same way as the observed RM image. This ensures that simulations are subject to the same sampling bias that we have to deal with when obtaining the RM from observations. The comparison between the observed RM images and those simulated is performed with the χ^2 distribution, by computing:

$$\chi^2 = \sum_{i=1}^{7} \frac{(C_{i,obs} - \langle C_{i,sim} \rangle)^2}{Err^2_{C_{i,obs}}} \tag{4.6}$$

where i indicates the source, C_{obs} refers to a generic observed quantity, while $\langle C_{i,sim} \rangle$ is the same quantity averaged over the different equivalent numerical simulation that start with different random seeds, and $Err^2_{C_{i,obs}}$ refers to the error of C_{obs}.

4.4 Determining the magnetic field from RM observations

Here we describe how the magnetic field power spectrum has been investigated.

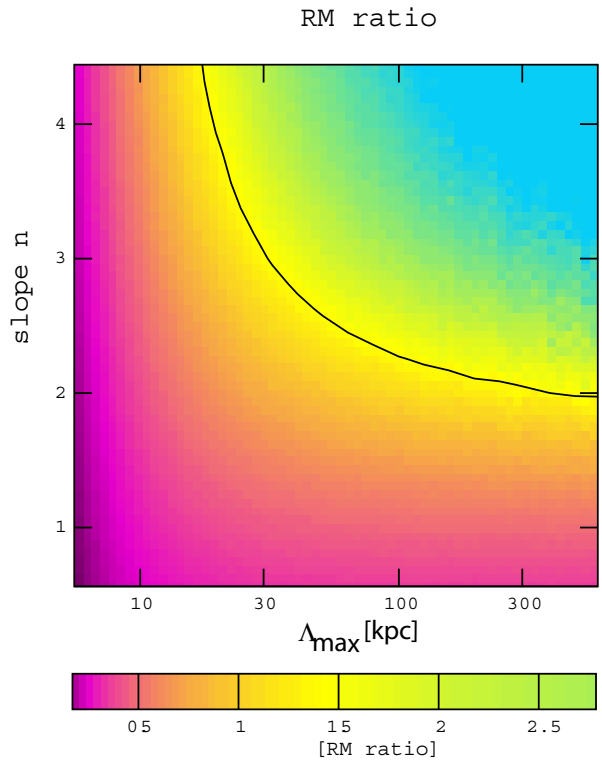

Figure 4.2: The RM ratio $|\langle RM \rangle|/\sigma_{RM}$ as a function of n and Λ_{max} computed on simulated RM images. The line refers to the mean values obtained by averaging the ratio of the sources.

4.4.1 Constraining the magnetic field power spectrum

Several observational quantities can be useful to constrain some properties of the magnetic field power spectrum. In particular:

- Both $\langle RM \rangle$ and σ_{RM} scale linearly with the magnetic field strength, while they have different trends with n and Λ_{max}, which are degenerate parameters. The ratio $|\langle RM \rangle|/\sigma_{RM}$ can thus be used to investigate the magnetic field power spectrum (see also Fig. 3 in Murgia et al. 2004).

- The minimum scale of the magnetic field fluctuation, Λ_{min}, affects the depolarization ratio (DP ratio) at two different frequencies (*i.e.* $DP^{\nu^2}_{\nu_1} = \frac{P_{\nu_1}/I_{\nu_1}}{P_{\nu_2}/I_{\nu_2}}$, see Eq. 2.19) and the σ_{RM}. Both $DP^{\nu_2}_{\nu 1}$ and σ_{RM} are in fact determined by the magnetic power on the small spatial scales. This parameter can be thus be derived by studying high resolution polarization images.

- It has been demonstrated that the magnetic field auto-correlation function is proportional to the RM auto-correlation function (Ensslin & Vogt 2003). Since the power spectrum is the Fourier transform of the auto-correlation function, it is possible to study the 3-Dim magnetic field power spectrum starting from the power spectrum of the RM images.

We simulated 2-Dim magnetic field models with different power spectra and compared simulated RM images and DP with the corresponding observable quantities. In these simulations the power spectrum normalization is set independently for each source[1]. The computational grid is 512×512 pixel^2 and the pixel-size was fixed to 0.2 kpc. This guarantees that each beam is represented by three pixels in the grid. The resulting field of view is then $\sim 100 \times 100$ kpc^2, that is enough to recover the projected size of the sources and to properly sample the large power spectrum scales. A Gaussian noise having $\sigma = Err_{fit}$ was added at the simulated images. Simulations were convolved with a Gaussian function having FMHM equal to the beam of the observations.

[1]In these 2-Dim RM simulations the radial profile of the magnetic field is not accounted for. This implicitly assumes that the mean magnetic field strength is not dramatically varying over the scale of the source. This is a reasonable assumption since the linear sizes of the sources at the Coma redshift are in fact much smaller that the cluster core radius.

The Λ_{max}-n plane

In order to illustrate the degeneracy existing between Λ_{max} and n, 2-Dim magnetic field models with different power spectra have been simulated. We allowed the parameter n to vary in the range $[0.5; 4.5]$ and Λ_{max} in the range $[5; 600]$ kpc, with steps of 0.06 and 9.3 kpc respectively. We derived simulated RM images for each combination of these parameters and calculated the RM ratio as:

$$RMratio = \frac{|\langle RM \rangle|}{\sigma_{RM}} \tag{4.7}$$

in a region of 15×15 kpc^2, comparable to the regions where RM has been observed. In Fig. 4.2 the values of the RM ratio for the simulated RM images is shown in colors, as a function of both n and Λ_{max}. The RM ratio was computed for the observed source that have a RM signal-to noise ratio >3 both for σ_{RM} and $\langle RM \rangle$, i.e for the sources 5C4.85, 5C4.81, 5C4.74 and 5C4.114. The resulting values are shown in Fig. 4.2 (black line).

The plot in Fig.4.2 shows what $\Lambda_{max} - n$ degeneracy means: the same value of the RM ratio can be explained with different power spectra. There are, as expected, two asymptotic trends. In fact, if the magnetic field power spectrum is flat (*e.g.* n <3), the bulk of the magnetic field energy is on the small scales, and thus the effect of increasing Λ_{max} is negligible after a certain threshold, that in this case is achieved for Λ_{max} ∼300 kpc. As the power spectrum steepens (n >3), the bulk of the energy moves to large scales, and thus as Λ_{max} increases, the energy content also increases sharply. This is the reason of the second asymptotic trend that is shown in the plot: as n increases Λ_{max} decreases faster and faster. As n approaches the value of ∼ 11/3 (Kolmogorov power spectrum), the observed data constrain Λ_{max} to be ∼20 - 40 kpc.

4.4.2 Structure function, auto-correlation function and Multi-Scale-Statistic

In order to constrain more precisely the estimate of the magnetic field power spectrum parameters indicated by the previous analysis we have investigated the statistical properties of the RM images individually. We have fixed $n = 11/3$, corresponding to the Kolmogorov power law for turbulent fields. This choice is motivated by both observational and theoretical works. Schuecker et al. (2004)

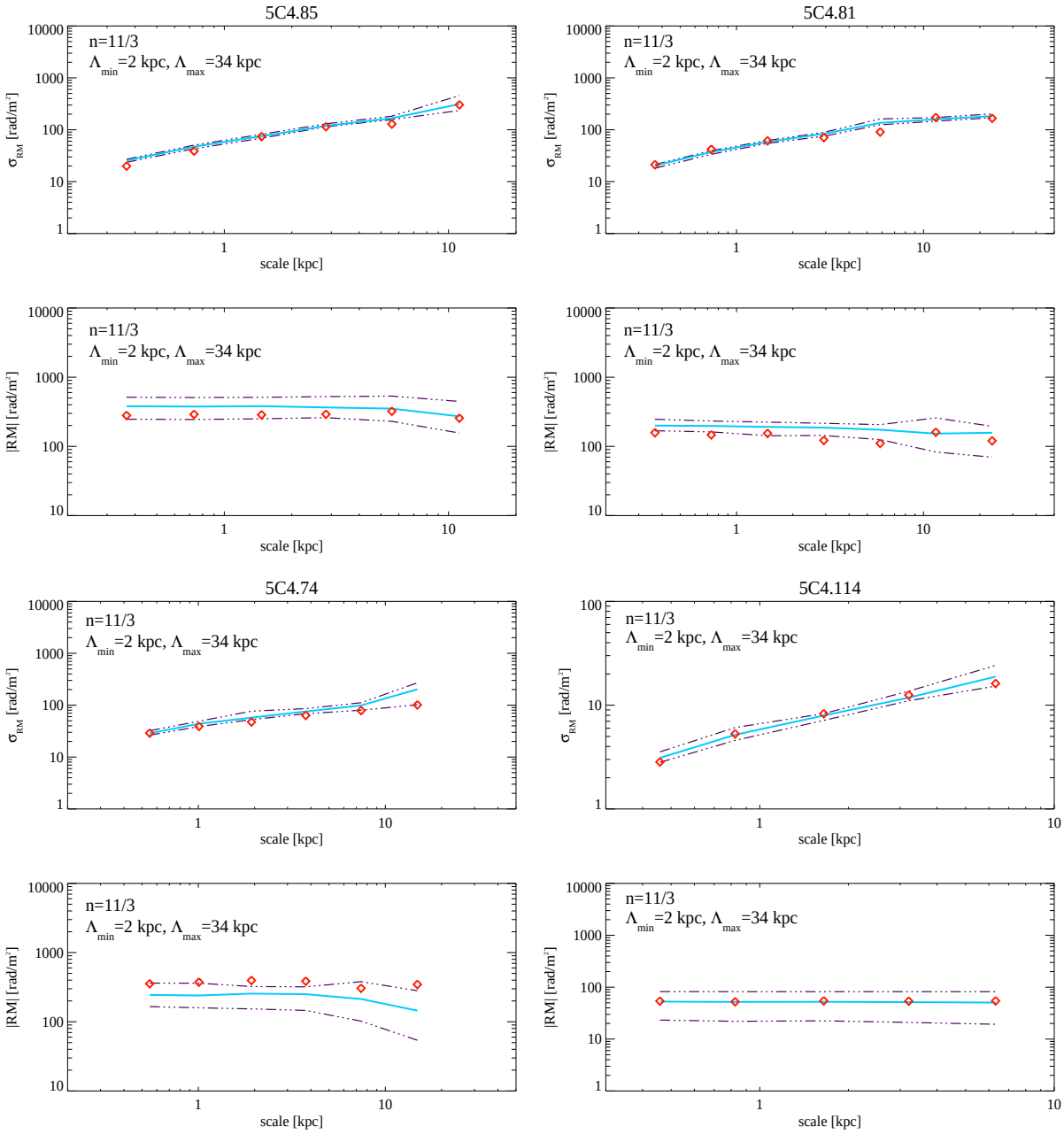

Figure 4.3: Fits to the RM images for the Kolmogorov power spectrum that best reproduces the observed RM (n=11/3, Λ_{min} =2 kpc, Λ_{max} =34 kpc) globally for the sources 5C4.85 and 5C4.81 used in the 2-Dim analysis (see Sec. 4.4.1). From top to bottom: fit to the σ_{RM} and $\langle RM \rangle$. Red diamonds represent the observed statistic, the cyan line represents the mean taken over ten different realizations of the same magnetic field power spectrum, and the blue lines represent the scatter in the simulations.

analyzed spatially-resolved gas pseudo-pressure maps of the Coma galaxy cluster deriving that pressure fluctuations in the cluster center are consistent with a

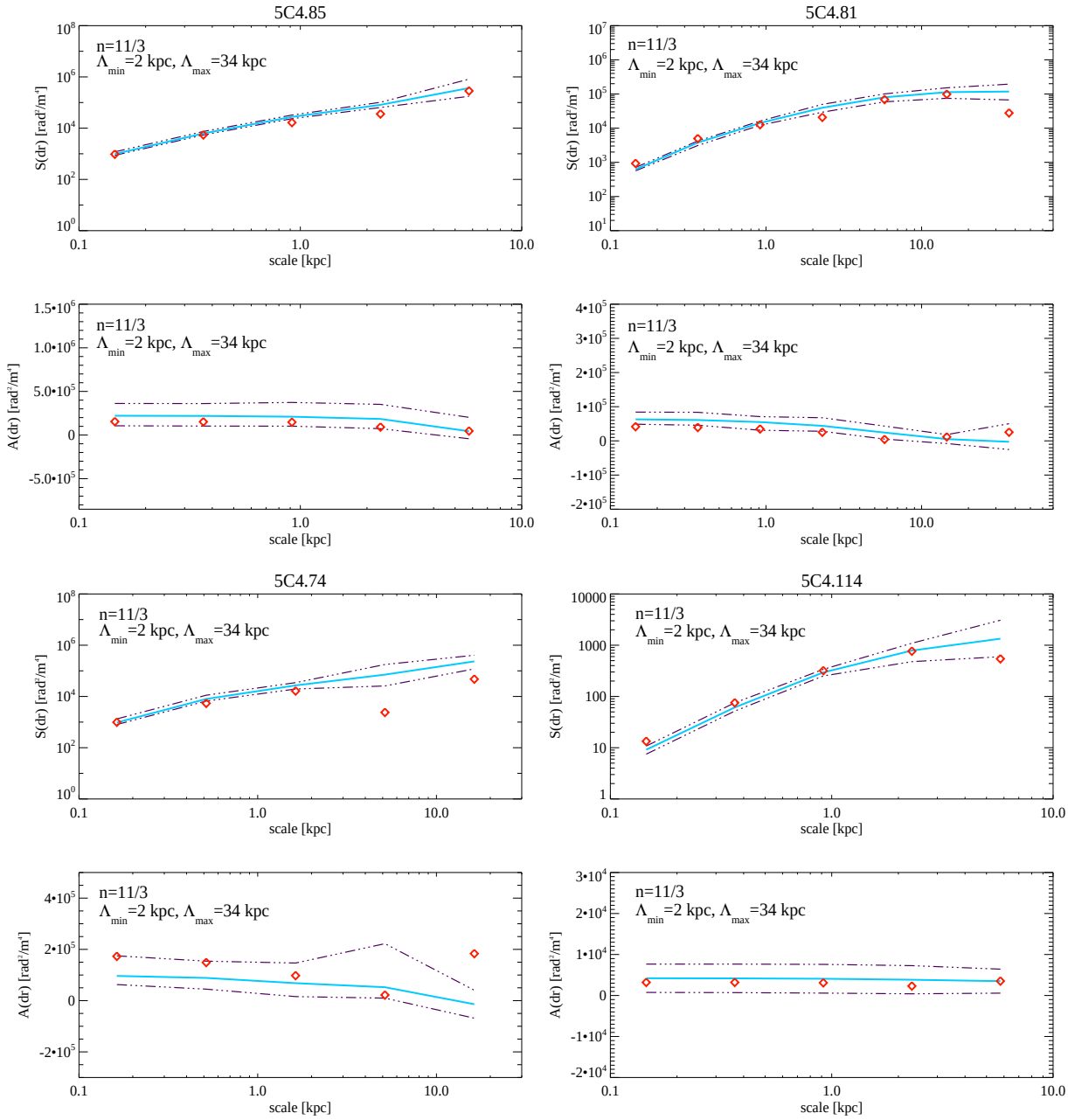

Figure 4.4: Fits to the *RM* images for the Kolmogorov power spectrum that best reproduces the observed *RM* (n=11/3, Λ_{min} =2 kpc, Λ_{max} =34 kpc) globally for the sources used in the 2-Dim analysis (see Sec. 4.4.1). Fit to the $S(r)$ (top) and $A(r)$ (bottom). Red diamonds represent the observed statistic, the cyan line represents the mean taken over ten different realizations of the same magnetic field power spectrum, and the blue lines represent the scatter in the simulations.

Kolmogorov-like power spectrum. Furthermore, cosmological numerical simulations have recently demonstrated that 3-Dim power spectrum of the velocity field is well

described by a single power law out to at least one virial radius, with a slope very close to the Kolmogorov power law (Vazza et al. 2009a, b).
The range of values of Λ_{max} is suggested by the previous analysis (see Fig. 4.2). In order to choose the best parameters in that range, and to find the best value for Λ_{min}, we simulated RM images and used two different statistical methods to compare the observed RM images to the simulated ones:

1. We calculated the auto-correlation function and the structure function of the observed RM images, and then compared them with the simulated RM images. The RM structure function is defined as follows:

$$S(dx, dy) = \langle [RM(x, y) - RM(x + dx, y + dy)]^2 \rangle_{(x,y)}, \tag{4.8}$$

   where $= \langle \rangle_{(x,y)}$ indicates that the average is taken over all the positions (x, y) in the RM image. Blank pixels were not considered in the statistics. The structure function $S(r)$ is then computed by radially averaging $S(dx, dy)$ over regions of increasing size of radius $r = \sqrt{dx^2 + dy^2}$. $S(r)$ is thus sensitive to the observable quantity σ_{RM} over different scales. The auto-correlation function is defined as:

$$A(dx, dy) = \langle [RM(x, y)RM(x + dx, y + dy)] \rangle_{(x,y)} \tag{4.9}$$

   Since $A(0) = \langle RM^2 \rangle = \sigma^2_{RM} + \langle RM \rangle^2$, the auto-correlation function is sensitive to both $\langle RM \rangle$ and the σ_{RM}.

2. We computed a Multi-Scale Statistic, namely we computed $\langle RM \rangle$ and σ_{RM} over regions of increasing size in the observed RM images and compared them with the same values obtained in the simulated images. The smallest region over which $\langle RM \rangle$ and σ_{RM} are computed corresponds to a box of 0.4×0.4 kpc size. The box side is then increased by a factor two until the full source size is reached. We note that this approach is sensitive to both $\langle RM \rangle$ and σ_{RM} over different spatial scales, and is thus a useful tool to discriminate among different power spectra. This indicator differs from the $S(r)$ and $A(r)$ in that as r increases, the number of pixels useful for computing the Multi-Scale Statistic increases, giving a robust statistical estimate on large scales.

For each source we simulated different power spectra varying Λ_{min} from 1 kpc to 5 kpc and Λ_{max} from 20 to 40 kpc. For every power spectrum and for each source we

realized ten different 2-Dim RM images, and compared the statistics ($S(r)$, $A(r)$ and Multi-Scale Statistic: MSS) with the observed ones by computing Eq. 4.6. This approach makes it possible to discriminate the best power spectrum model compatible with our data. In this 2-dim analysis we focused on the sources 5C4.85, 5C4.81, 5C4.74 and 5C4.114, whose RM images have signal-to-noise ratio >3. Each source was fitted separately. The total χ^2 was then computed by summing the individual values obtained for each source. The minimum value of the total χ^2_{tot} corresponds to the power spectrum model characterized by $\Lambda_{max} = 34$ kpc and $\Lambda_{min} = 2$ kpc. We show in Figs. 4.3 and 4.4 the structure function, the auto-correlation function, and the multi-scale statistic obtained for the Kolmogorov power spectrum model that best reproduces the observed RM images. In Sec. 4.5 similar plots obtained with other power spectrum models are shown.

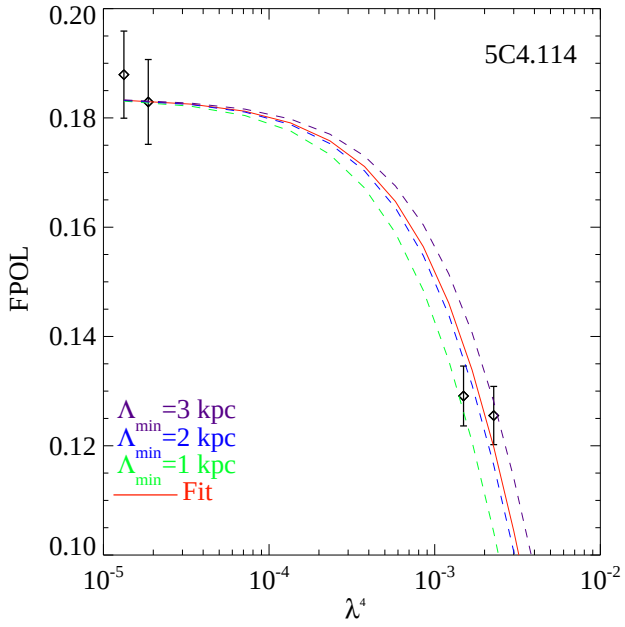

Figure 4.5: Fits to the Burn law. Points refer to observed data, while the red line is the fit obtained from observations. Dashed lines refer to the fits obtained from three different models, with different values of Λ_{min}, as reported in the bottom left corner of the plot.

Λ_{min} and Fractional polarization

It has been demonstrated (Burn 1966, see also Laing 2008) that when Faraday Rotation occurs the fractional polarization $FPOL$ can be related to the fourth

power of the observing wavelength λ according to the Burn law (see Eq. 2.22):

$$FPOL = \frac{P_\lambda}{I_\lambda} \propto exp(-k\lambda^4). \quad (4.10)$$

Since $FPOL$ is sensitive to the minimum scale of the power spectrum, Λ_{min}, Eq. 4.10 can be used to constrain it. We fitted Eq. 4.10 to our observations and to our simulations, performed with different values of Λ_{min}. These fits indicate that a Kolmogorov power spectrum with the best agreement with observations is achieved for $\Lambda_{min} \sim 2$ kpc, confirming the result from the previous analysis. As an example, we show in Fig. 4.5 these fits performed on the source 5C4.114, where the effect of depolarization is more appreciable, thanks to the 20 cm observations.

4.5 Structure Function and Multi-Scale Statistics with different power spectrum models

We discuss here other power-law spectral models that could be representative of the data presented in Chap. 3. Following the approach discussed in Sec. 4.4.1, we have obtained simulated RM images from different power spectrum models and compared them with observed data. The analysis is performed on the basis of the the structure-function, auto-correlation function and multi-scale statistics. We show in Fig. 4.6 the structure function, auto-correlation function and MSS derived from Kolmogorov power spectra that differ in the value of Λ_{max}, while in Fig. 4.7 the fits to the structure, auto-correlation functions and MSS for power spectrum models with $n = 2$, and different values of Λ_{max} are reported. We show only the plots obtained for the central source 5C4.85. These figures demonstrate how the RM data presented in this thesis are sensitive to different power spectrum models.
We note that Kolmogorov power spectra with Λ_{max} $\sim$100 and 10 kpc fail in reproducing the $\langle RM \rangle$. These trends can be easily understood since power spectrum models with $n > 3$ have most of the magnetic energy on large spatial scales, and thus small changes in Λ_{max} have a consistent impact on the resulting statistics. According to results presented in Sec. 4.4.1, the case Λ_{max} =20 kpc gives a reasonable fit to our data, although the best fit is achieved for Λ_{max} =34 kpc. In Fig. 4.7 similar fits obtained for power spectra models with $n = 2$ are shown. As indicated by the analysis performed in Sec. 4.4.1, in this case the best agreement with observations is achieved for Λ_{max} of order of hundreds kpc (see Fig. 4.2). We note that because of

the power spectrum degeneracy, it is possible to obtain a reasonable fit to our data. Indeed the case Λ_{max} =400-800 kpc can reproduce the MSS statistics, although they fail in reproducing the $S(r)$ trend on large spatial scales, indicating that a larger value of n is required.

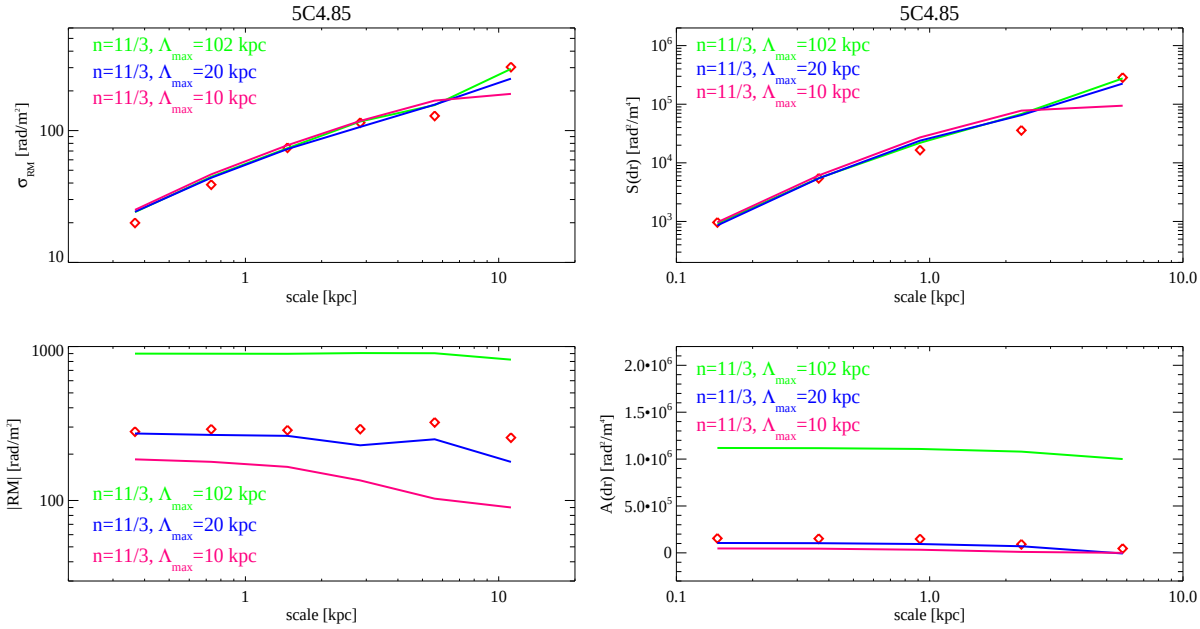

Figure 4.6: Fit to the RM images for different Kolmogorov power spectra for the central sources 5C4.85. The different models are indicated by different colors (see labels) *left*: fit to the σ_{RM} and $\langle RM \rangle$; *right*: fit to the $S(r)$ and $A(r)$. Red diamonds represent the observed statistics. Lines represent the value obtained by averaging 10 power spectra generated with different random seeds.

4.5.1 The magnetic field profile

The results obtained from the previous section indicate the power spectrum that is able to best reproduce the observed RM images. In order to investigate the magnetic field radial profile we simulated 3-dim Kolmogorov power spectra, with $\Lambda_{max} = 34$ kpc and $\Lambda_{min} = 2$ kpc, as derived from the 2-Dim analysis (Sec. 4.4.1). A computational grid of 2048^3 pixels was used, and the pixel-size was fixed to 0.5 kpc. This guarantees that the Nyquist criteria is satisfied for Λ_{min} and that fluctuations on scales $\sim \Lambda_{max}$ are also well represented in the cube. For each of these simulations Eq. 2.12 was integrated numerically, with a step of 0.5 kpc along the line of sight. The limits of the integral in Eq. 2.12 were $[0; 10r_c]$ for the cluster's sources 5C4.85

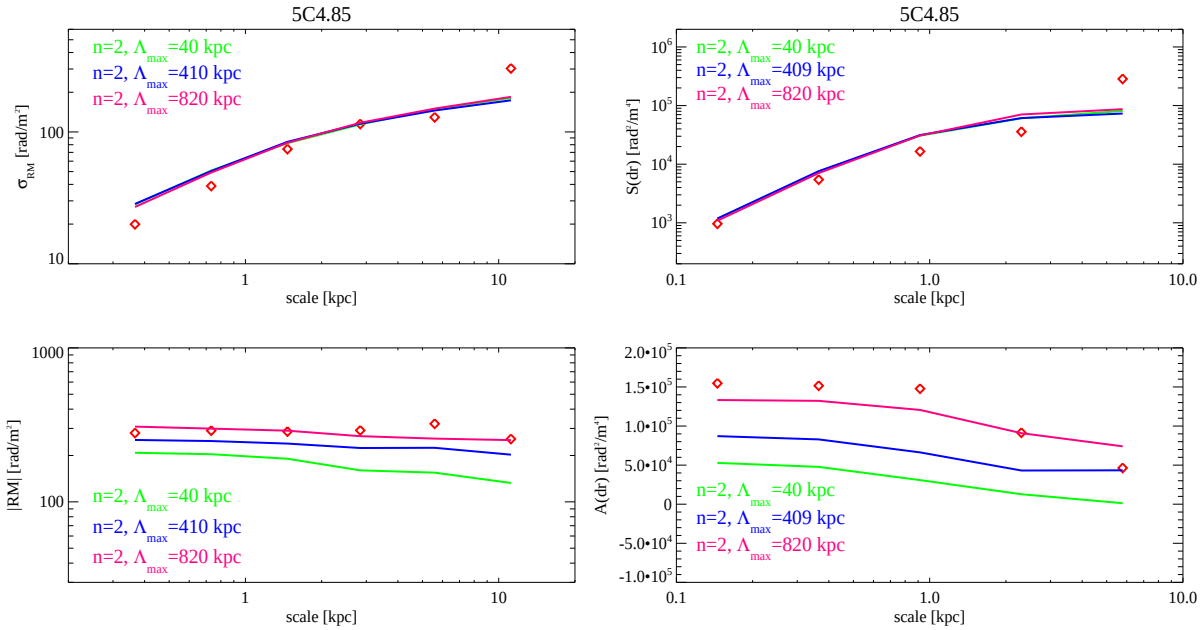

Figure 4.7: Fit to the RM images for different power spectra with $n = 2$ for the central sources 5C4.85. The different models are indicated by different colors (see labels) *left*: fit to the σ_{RM} and $\langle RM \rangle$; *right:* fit to the $S(r)$ and $A(r)$. Red diamonds represent the observed statistics. Lines represent the value obtained by averaging 10 power spectra generated with different random seeds.

and 5C4.81 and $[-10r_c; 10r_c]$ for the other sources in the background of the cluster. The simulated field of view covers an area of 1024×1024 kpc^2, thus the cube has been replicated to achieve a field of view that is large enough to reach the farthest source (5C4.152).

The integration was repeated by varying the parameter B_0 in the range [0.1; 11] μG, with a step of ~ 0.17 μG, and η in the range[-0.2; 2.5] with a step of 0.04. For each combination of B_0 and η a RM simulated image was thus obtained covering the full cluster area.

We extracted from this RM image seven fields, each lying in the plane of the sky in the same position of the observed sources, and having the same size of the observed RM images. The simulated RM images were convolved with a Gaussian beam having FWHM=0.7×0.7 kpc, in order to have the same resolution of the observations. Finally the simulated RM fields were blanked in the same way as the corresponding RM images.

The result of this integration is, for each combination of (B_0;η), a set of seven

simulated RM images, that are subject to the same statistical biases of the observed images.
This process was repeated 50 times, each starting from a different random seed to generate the magnetic field power spectrum model.
For each source and for each pair of values of (B_0;η) a simulated RM image was obtained for every realization of the same power spectrum model. The mean and the standard deviation of the $\sigma_{RM,sim}(B_0, \eta)$ was computed from the simulated RM images, and then the χ^2 was obtained (Eq. 4.6). The resulting χ^2 plane is shown in Fig. 4.8. The minimum value is achieved for B_0 =4.7 μG and $\eta = 0.5$, but the 1-σ confidence level of the χ^2 indicates that values going from B_0 =3.9 μG and $\eta = 0.4$, to B_0 =5.4 μG and $\eta = 0.7$, are equally representative of the magnetic field profile, according to the degeneracy between the two parameters. Magnetic field models with a profile flatter than $\eta < 0.2$ and steeper than $\eta > 1.0$ are excluded at 99% confidence level, for any value of $\langle B_0 \rangle$. Also magnetic field models with $\langle \mathbf{B_0} \rangle < 3.1 \mu$G and $\langle \mathbf{B_0} \rangle > 6.5$ μG are excluded at the 99% confidence level for any value of η. It is interesting to note that the best models include $\eta = 0.5$, the value expected in the case of a magnetic field energy density decreasing in proportion to the gas energy density (assuming a constant average gas temperature), and $\eta = 0.67$, expected in the case of a magnetic field frozen into the gas. In the latter case the corresponding value of $\langle \mathbf{B_0} \rangle$ is $\sim$5.2 μG.

The knowledge of the magnetic field strength and structure in the ICM has strong implications for models explaining the formation of diffuse radio sources like radio halos. Testing the different models proposed in the literature is beyond the scope of this work. We point out, however, that cosmological simulations recently performed by Donnert et al. (2009b) have shown that it is possible to test a class of these models once the magnetic field profile is known. In particular, we showed in that paper that secondary models fail in reproducing the radial profile of the Coma radio halo when the Coma cluster magnetic field profile is assumed.

4.5.2 Results excluding the source 5C4.74

The same procedure described above has been repeated excluding the source 5C4.74 (see Sec. 3.5). The minimum value for the χ^2 is again achieved with a model

characterized by B_0 =4.7 μG and η = 0.5. This is not surprising since the fit is computed based on σ_{RM}, and the source is sampled with only 10 beams. In order to investigate possible effects arising from the interaction of the Coma cluster with the NGC4839 group RM images of more sources in this region would be required.

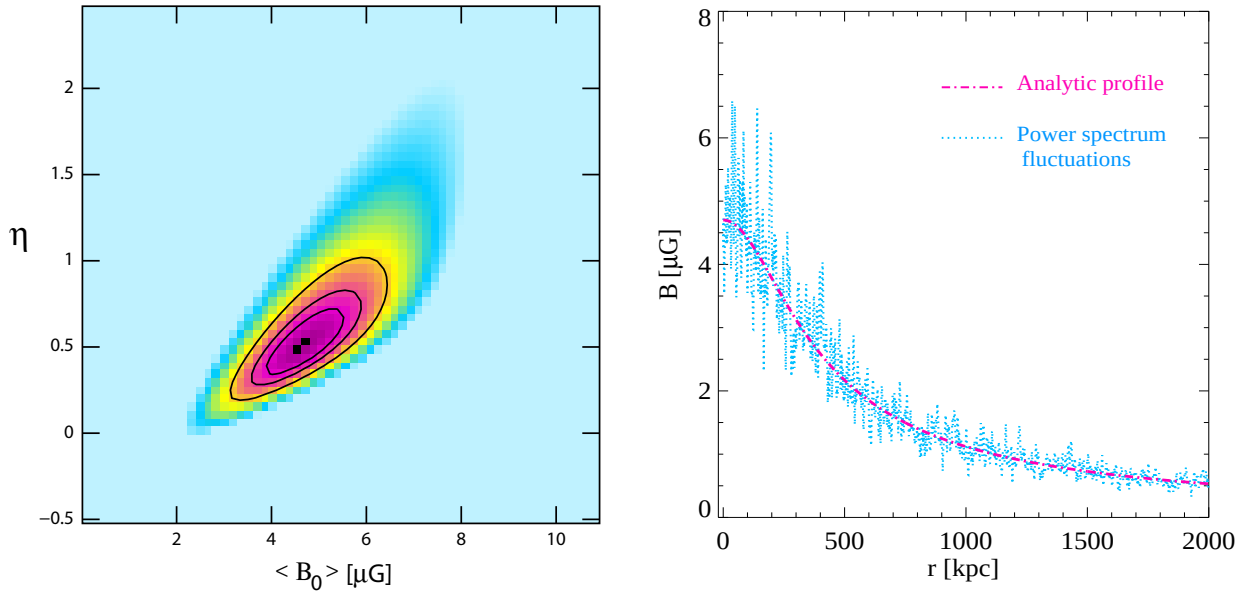

Figure 4.8: *Left*: χ^2 plane obtained by comparing simulated and observed σ_{RM}.*Right*: Profile of the best magnetic field model. magenta line refers to the analytic profile (Eq. 4.5), while the blue line refers to a slice extracted from the simulated magnetic field numerical model. Power spectrum fluctuations on the profile are shown.

4.6 Comparison with other estimates

In the literature there is a long-standing debate on the magnetic field strength derived from the RM analysis compared to the equipartition estimate and to the Inverse Compton hard X-ray emission. The discrepancy may arise from the different (but not incompatible) assumptions, and, moreover, are sensitive to the magnetic field on different spatial scales. Assuming the magnetic field models derived in the previous section, it is possible to derive an estimate that is comparable with equipartition values, and with the Inverse-Compton detection as well as with the upper limits derived from new hard X-ray observations. In order to obtain a value that is directly comparable with the equipartition magnetic field estimate, we have to derive the average magnetic field strength resulting from our RM analysis over the same volume assumed in the equipartition analysis, that is $\sim$1 Mpc^3. The magnetic

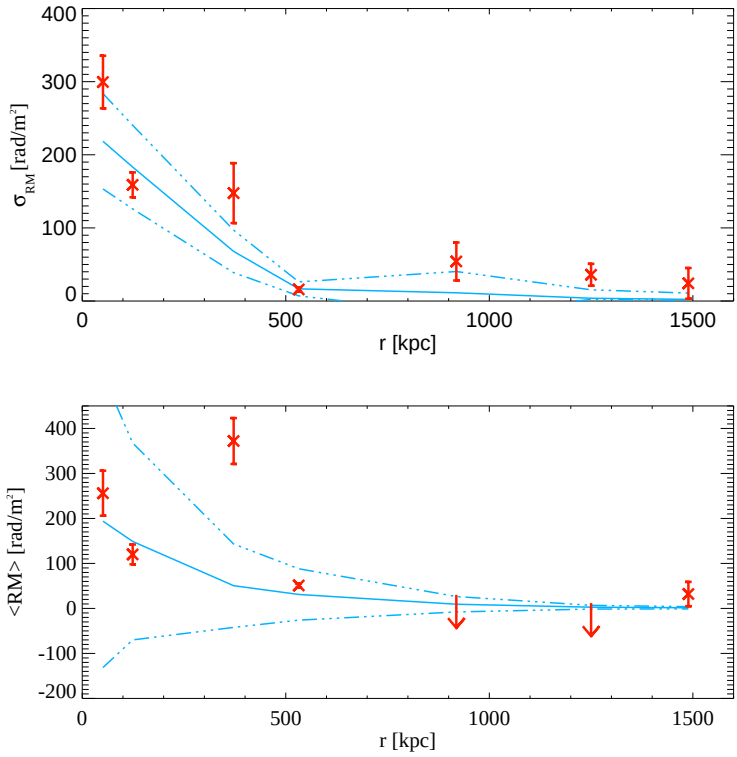

Figure 4.9: σ_{RM} and $\langle RM \rangle$ for the best model (cyan continuous line) and its dispersion (cyan dotted lines), given by the rms of the different random realizations. Observed points are shown in red.

field model resulting from our RM analysis gives an average magnetic field strength of $\sim$ 2 μG, consistent with the equipartition estimate derived from the radio halo emission (0.7 - 1.9 μG Thierbach et al. 2003), despite the different assumptions that these two methods require.

The Inverse Compton hard X-ray emission has been observed with the *Beppo Sax* satellite. Its field of view is $\sim 1.3°$, corresponding to $\sim 2.2 \times 2.2$ Mpc^2 at the Coma redshift. We computed the average value of the magnetic field over the same volume sampled by *Beppo Sax*. We obtained $\sim$0.75 μG when the best model is assumed, that is a factor four higher than the value derived from Hard-X ray observations (Fusco Femiano et al. 2004). We note however that models compatible with our data within 1-σ of the χ^2 give values slightly different, going from 0.9 to 0.5 μG. The steepest magnetic field model that is compatible with our data at 99% confidence level ($B_0 \sim 6.4$ μG, $\eta = 0.95$) gives 0.2 μG when averaged over the volume corresponding to the *Beppo Sax* field of view. Deeper Hard-X ray observations would be required to better compare the two estimates. The values computed here indicate however

that they can be reconciled. Recently, new hard X-ray observations of the Coma cluster have been performed with the new generation of satellites (see the work by Wik et al. 2009 using XMM and Suzaku data, Lutovinov et al. 2008 using ROSAT, RXTE and INTEGRAL data, Ajello et al. 2009 using XMM-Newton, Swift/XRT, Chandra and BAT data). These observations failed to find statistically significant evidence for non-thermal emission in the hard X-ray spectrum of the ICM, which is better described by a single or multi-temperature model. Given the large angular size of the Coma cluster, if the non-thermal hard X-ray emission is more spatially extended than the observed radio halo, both Suzaku HXD-PIN and BAT Swift may miss some fraction of the emission. These efforts have thus derived lower limits for the magnetic field strength, over areas smaller than the radio halo. The lower limit reported by Wik et al. (2009) is *e.g.* $\langle B \rangle > 0.2$ μG, that is compatible with our results.

4.7 Limits on the magnetic field profile from background radio sources.

Although several arguments (see Sec. 3.5.2) suggest that the main contribution to the observed RMs is due to the ICM, the best way to firmly avoid any kind of local contribution would be to consider only background radio galaxies in the analysis. This is however not trivial in general and not feasible here. In fact, sources located in the inner region of the cluster, at distances $\leq (1-2)r_C$ are fundamental to constrain the magnetic field strength and radial decline, so that a peculiar cluster where background bright and wide sources are seen in projection very close to the cluster center would be required. These conditions are not fulfilled in the case of the Coma cluster, even though it is a very nearby cluster, where several lines of sight can be inspected. We show in Fig. 4.10 (left panel) the χ^2 plane obtained by considering only the background radio galaxies: 5C4.74, 5C4.114, 5C4.127, 5C4.42 and 5C4.152. This plot shows that for every value of B_0 it is possible to find a value of η that can reproduce the observed data within 1-σ confidence level. In the same Fig. in the right panel we show the trends of σ_{RM} and $\langle RM \rangle$ as a function of r obtained for different value of B_0. They all lie within 1σ confidence level of the χ^2 plane. It is clear from this plot that the missing information at projected distances $r < 300$ kpc does not permit us to infer the magnetic field strength and radial decline in the

Coma cluster. Even unrealistic models where $\eta \leq 0$ cannot be ruled out when the two wide central sources are not considered. Future instruments such as SKA are expected to detect many more radio sources seen through a single cluster, possibly allowing this kind of analysis to be performed excluding cluster members.

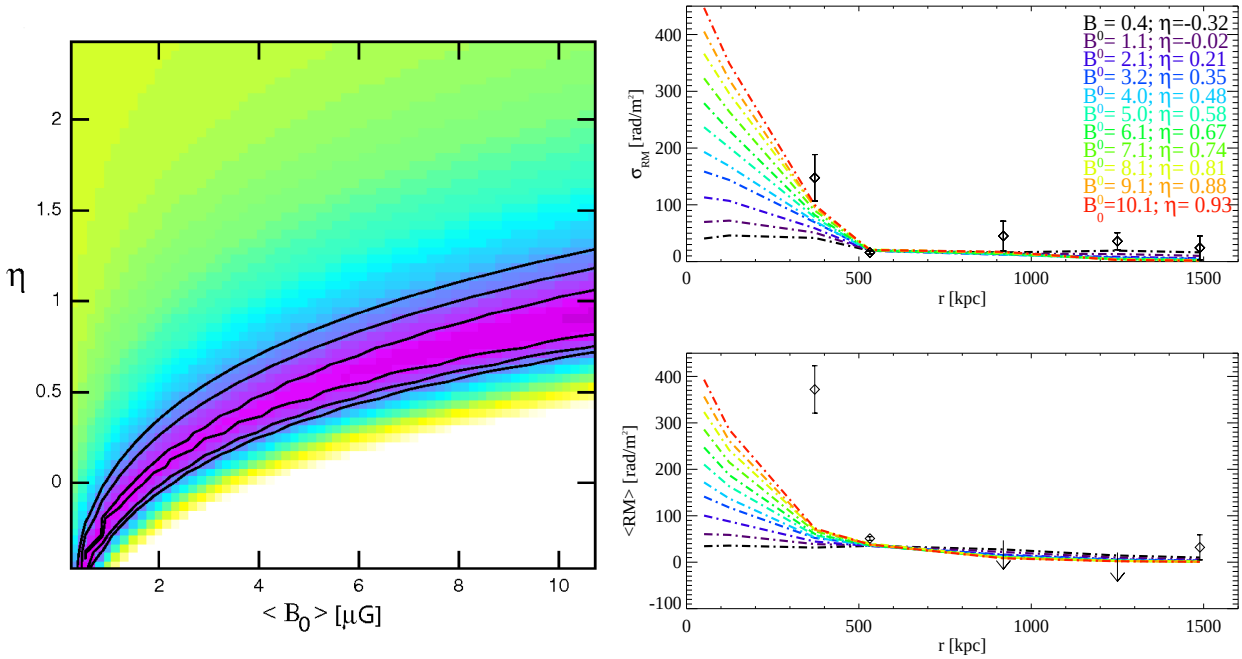

Figure 4.10: *Left:* χ^2 plane obtained by comparing simulated and observed σ_{RM} for background sources. Lines refer to 1,2 and 3-σ confidence level. *Right:* σ_{RM} and $\langle RM \rangle$ trends for different models that lie within 1-σ confidence level of the χ^2.

4.8 Conclusions

We have presented new VLA observations of seven sources in the Coma cluster field at multiple frequencies in the range 1.365 – 8.465 GHz. The high resolution of these observations has allowed us to obtained detailed RM images with 0.7 kpc resolution. The sources were chosen in order to sample different lines-of-sight in the Coma cluster in order to constrain the magnetic field profile. We used the numerical approach proposed by Murgia et al. (2004) to realize 3-dim magnetic field models with different central intensities and radial slopes, and derived several realizations of the same magnetic field model in order to account for any possible effect deriving from the random nature of the magnetic field. Simulated RM images were obtained, and observational biases such as noise, beam convolution and limited sampled regions were all considered in comparing models with the data.

Our results can be summarized as follows:

- the RM ratio and the DP ratio were used to analyze the magnetic field power spectrum. Once a Kolmogorov index is assumed, the structure-function, the auto-correlation function and the multi-scale statistic of the RM images are best reproduced by a model with $\Lambda_{max} = 34$ kpc and $\Lambda_{min} = 2$ kpc. We performed a further check to investigate the best value of Λ_{min} by fitting the Burn law (Burn 1966). This confirmed the result obtained from the previous analysis.

- The magnetic field radial profile was investigated through a series of 3-Dim simulations. By comparing the observed and simulated σ_{RM} values we find that the best models are in the range (B_0 =3.9 μG;η =0.4) and (B_0 =5.4 μG;η =0.7), the best fit being the one with B_0 =4.7 μG and η =0.5. It is interesting to note that the values η =0.5 and 0.67 are among those that best agree with observations. They correspond to models where the magnetic field energy density scales as the gas energy density, or the magnetic field is frozen into the gas, respectively. This is expected from a theoretical point-of-view since the energy in the magnetic component of the intra-cluster medium is a tiny fraction of the thermal energy. Values of B_0 >7 μG and <3 μG as well as $\eta < 0.2$ and $\eta > 1.0$ are incompatible with RM data at the 99% confidence level.

- The average magnetic field intensity over a volume of $\sim$ 1 Mpc^3 is $\sim$ 2 μG, and can be compared with the equipartition estimate derived from the radio halo emission. Although based on different assumptions, and although the many uncertainties relying under the equipartition estimate, the model derived from RM analysis gives an average estimate that is compatible with the equipartition estimate. A direct comparison with the magnetic field estimate derived from the IC emission is more difficult, since the Hard-X detection is debated, and depending on the particle energy spectrum, the region over which the IC emission arises may change. The model derived from RM analysis gives a magnetic field estimate that is consistent with the present lower limits obtained from hard X-ray observations. The values we obtain for our best models are still a bit higher when compared with the estimate given by Fusco

Femiano et al. (2004). It is worth to remind, as noted by several authors (see Sec. 4.6), that the IC estimate derived from Hard X-ray observations could be dominated by the outer part of the cluster volume, where the magnetic field intensity is lower, depending on the spatial and energy distribution of the emitting particles. Future Hard-X ray missions could help in clarifying this issue.

Chapter 5

Magnetic field in a high redshift system and connections with merging events: the case of MACS J0717+3745*

5.1 Introduction

Works on magnetic fields in clusters have, so far, focused on relatively nearby systems (z<0.4), with much less information being available for clusters at higher redshift. The studies that were mentioned in Chaps. 1 and 2 have been mainly performed in clusters at z≤0.1. An information that is missing in the literature regards the study of the magnetic field in higher redshift systems. Extending the redshift range of such studies is crucial because of their importance to the subject of the formation and evolution cosmic magnetic fields, and to investigate how the strength and structure of magnetic fields in clusters is connected to the dynamical history of such systems. MACS J0717.5+3745 is one of the most disturbed galaxy clusters known at any redshift. It belongs to the statistically complete sample of the twelve most distant MACS clusters (Ebeling et al. 2007) and it is among them the most promising candidate to the study of cluster magnetic fields. NVSS and FIRST images in fact reveal the presence of radio emission within the ICM, and in addition, X-ray and optical information allow to perform a detailed study of the thermal and non-thermal phenomena at work in the ICM during cluster collisions. In this chapter we present the study of the radio emission from this cluster. A

*Bonafede et al. 2009, A&A 503,707

new radio halo is discovered, it is the farthest ever observed, allowing to put new constraints of the presence of magnetic fields in the ICM. In addition polarization emission is detected from the radio halo, and the comparison with results obtained from numerical simulations allows us to derive the main properties of the magnetic field power spectrum. The magnetic field profile is also derived from the radio halo emission under some assumptions about its energy state and geometry, and the interactions between thermal and non-thermal components in this system are investigated thanks to X-ray observations.

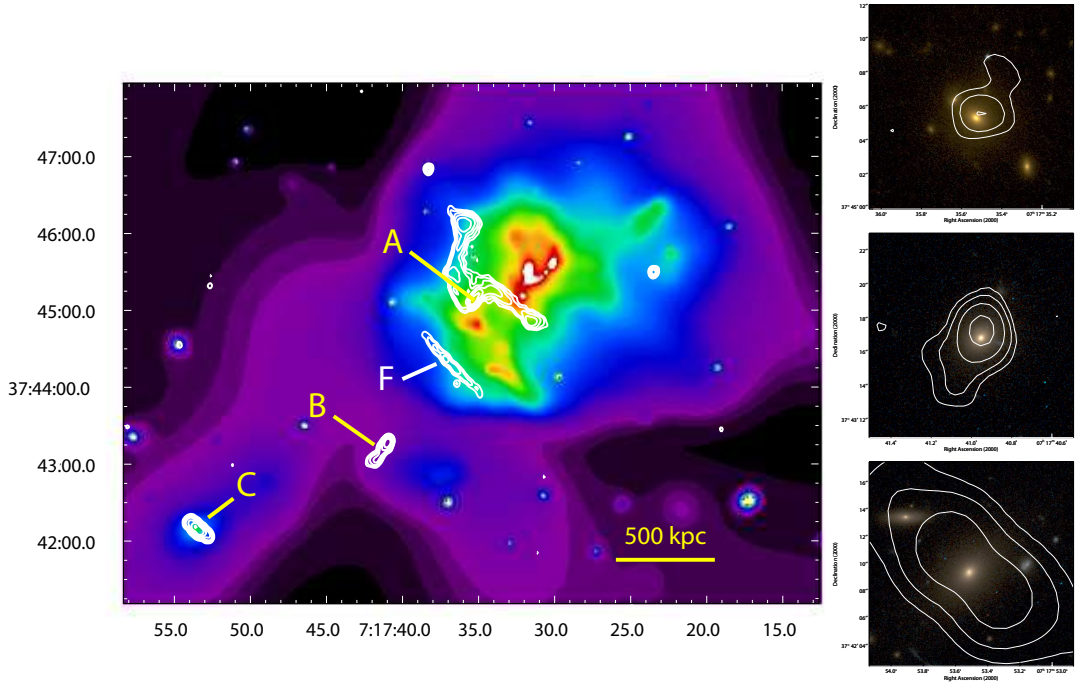

Figure 5.1: Image of the X-ray surface brightness of MACS J0717 as observed with Chandra in the 0.5–7 keV band, adaptively smoothed using the *asmooth* algorithm (Ebeling et al. 2006) requiring a minimal significance of 99% with respect to the local background. Contours show the emission from radio sources at 1.365 GHz. The size of the restoring beam is $5''\times4''$, and the rms noise is $\sigma \sim 3.0$ μJy/beam. The lowest contour level corresponds to 5σ, additional contours are spaced by factors of 2. The source labelled F is a foreground radio galaxy. The side panels show contours of the radio emission from sources A, B, and C (top to bottom), overlaid on optical images obtained with the Hubble Space Telescope (HST). For sources A and B, we show the emission at 8.460 GHz, where the restoring beam is $2.4''\times2''$, and the rms noise σ ~0.04 mJy/beam. The first contour is placed at the 3σ level; additional contours are spaced by factors of 2. Radio emission from source C is shown at 1.365 GHz, using the same contour levels as in the large image. The HST images were obtained with the Advanced Camera for Surveys (ACS), using the F555W and F814W filters (source A), and the F606W and F814W passbands (source B and C).

5.2 The cluster MACS J0717+3745

The cluster MACS J0717.5+3745 (MACS J0717; z=0.55) was discovered in the Massive Cluster Survey (MACS; Ebeling et al. 2001). It is part of the statistically complete sample of the twelve most distant MACS clusters, all of which lie at z>0.5 (Ebeling et al. 2007). In-depth optical and X-ray studies of the galaxy population and the ICM of MACS J0717 identified it as one of the most promising targets for studies of the physical mechanisms governing merger events (Ebeling et al. 2004; Ma et al. 2008, 2009).

5.2.1 Optical observations

The complex optical morphology of MACS J0717 was first noted by Edge et al. (2003), based on imaging in the V, R, and I passbands obtained with the University of Hawaii 2.2m telescope. Much deeper observations conducted since with SuprimeCam, the wide-field imager at the prime focus of the Subaru 8m telescope, firmly established MACS J0717 as a highly disturbed merger and led to the discovery of a 6-Mpc long filament leading into the cluster from the South-East (Ebeling et al. 2004). Spectroscopic observations of over a thousand galaxies in the field of MACS J0717 have been performed in order to probe its spatial and kinematic structure along the line of sight, and to characterize the galaxy population as a function of cluster environment (Ma et al. 2008). Finally, space-based observations with the Advanced Camera for Surveys (ACS) aboard the Hubble Space Telescope provided a high-resolution view of MACS J0717, including the interface region where the filament meets the dynamically most active central region of the cluster.

5.2.2 X-ray observations

With an X-ray luminosity of (2.74± 0.03)×10^{45} erg/s in the 0.1-2.4 keV energy band (Ebeling et al. 2007) MACS J0717 is one of the most X-ray luminous clusters known at z>0.5. The cluster was observed with the ACIS-I instrument aboard the Chandra X-ray Observatory for a total exposure time of 60 ks (ObsID 4200). A detailed study of the system's X-ray properties was performed by Ma et al. (2008, 2009). Their spatial description of the gas distribution uses a β-model (Cavaliere &

Fusco-Femiano 1976):

$$\rho_{gas} = \rho_0 \left[1 + \frac{r^2}{r_c^2}\right]^{\frac{-3\beta}{2}} \tag{5.1}$$

where ρ_{gas} is the gas density, r is the radial distance from the cluster center, and r_C is the cluster core radius. By fitting this model to the X-ray surface brightness data, they derived $\beta = 1.1 \pm 0.1$, $r_c = 92'' \pm 6''$ and $\rho_0 = 1.71 \pm 0.05 \times 10^{14} M_{\odot} Mpc^{-3}$. Ma and co-workers report the detection of X-ray emission from the filament and, for the main cluster, a very complex X-ray morphology, including dramatic variations in the intra-cluster gas temperature, with extreme values of 5 and over 20 keV (the average gas temperature quoted by Ebeling et al. (2007) is 11 keV). The authors' joint optical/X-ray analysis of all available data identifies the filament as the source of both continuous and discrete accretion of matter by the cluster from a south-easterly direction, and isolates four distinct subclusters participating in an ongoing triple merger. The X-ray emission from MACS J0717 and the cluster-filament interface is shown in Fig. 5.1.

Table 5.1: Radio observations

RA (J2000)	DEC (J2000)	ν (GHz)	Bandwidth (MHz)	Conf.	Date
07h17m35.0s	37d45′07″	1.365 - 1.435	25	B	16-DEC-07
07h17m35.0s	37d45′07″	1.485 - 1.665	25	B	24-DEC-07
07h17m35.0s	37d45′07″	4.885 - 4.535	50	C	24-MAR-08
07h17m53.0s	37d42′11″	4.885 - 4.535	50	C	20-APR-08
07h17m30.9s	37d45′30″	1.425	50	C	15-MAR-08
07h17m33.8s	37d45′20″	4.860	50	D	27-NOV-01
07h17m35.4s	37d45′07′	8.460	50	C	22-NOV-1998

Table 5.2: Radio observations

RA (J2000)	DEC (J2000)	ν (GHz)	ToS (Hours)	Restoring beam ″×″	rms noise (mJy/beam)
07h17m35.0s	37d45′07″	1.365 - 1.435	2.2	5×4	0.030
07h17m35.0s	37d45′07″	1.485 - 1.665	2.8	5×4	0.025
07h17m35.0s	37d45′07″	4.885 - 4.535	2.4	5×4	0.015
07h17m53.0s	37d42′11″	4.885 - 4.535	2.2	5×4	0.016
07h17m30.9s	37d45′30″	1.425	1.8	18×14	0.020
07h17m33.8s	37d45′20″	4.860	1.5	18×14	0.020
07h17m35.4s	37d45′07′	8.460	0.2	2.4×2	0.04

5.3 Radio observations and data reduction

Our detailed study of the radio emission arising from both galaxies and the ICM of this cluster is prompted by the work of Edge et al. (2003) who suggested the presence of a radio relic in MACS J0717 when analyzing data from the Faint Images of the Radio Sky at Twenty-cm (FIRST, Becker et al. 1995) survey. Since radio emission is indicative of the presence of a magnetic field, such observations are the most direct way to obtain information of this fundamental ingredient in the physics of the ICM. We investigate the radio emission from MACS J0717 with multi-frequency and multi-resolution VLA observations. Specifically, we performed new high-resolution observations in full-polarization mode. These observations focused on radio galaxies in the field, as well as on the candidate relic, to study their Faraday Rotation Measure. In addition, new low-resolution observations were performed to study the diffuse emission of the cluster. We also used archival VLA observations, both of high and low resolution, as specified below.

5.3.1 High-resolution observations

MACS J0717 was observed with the B array at four frequencies within the 20-cm band (1.365 GHz, 1.435 GHz, 1.485 GHz, and 1.665 GHz), and with the C array at two frequencies within the 6-cm band (4.535 GHz, and 4.885 GHz). The targets of these observations were the relic, the radio galaxy embedded in the candidate relic emission (labelled A in Fig. 5.1) and the radio galaxies labelled B and C in Fig. 5.1 detected at larger projected distance from the cluster center. Two separate pointings were necessary at 6 cm to avoid bandwidth and primary-beam attenuation. The source 0137+331 (3C48) was used as the primary flux-density calibrator, and the source 0521+166 (3C138) as an absolute reference for the electric vector polarization angle. The nearby source 0713+438 was observed at intervals of ∼20 min and used as phase calibrator. Calibration and imaging were performed with the NRAO Astronomical Image Processing System (*AIPS*), following standard procedures. Self-calibration was performed to refine antenna phase solutions, followed by a final gain and amplitude self-calibration cycle. Images of the total intensity (Stokes I), as well as of the Stokes parameters U and Q, were produced for each frequency separately. We then derived images of the polarized intensity $P = \sqrt{(Q^2 + U^2)}$ and of the polarization angle $\Psi = 0.5 \arctan(U/Q)$. These images were restored with a

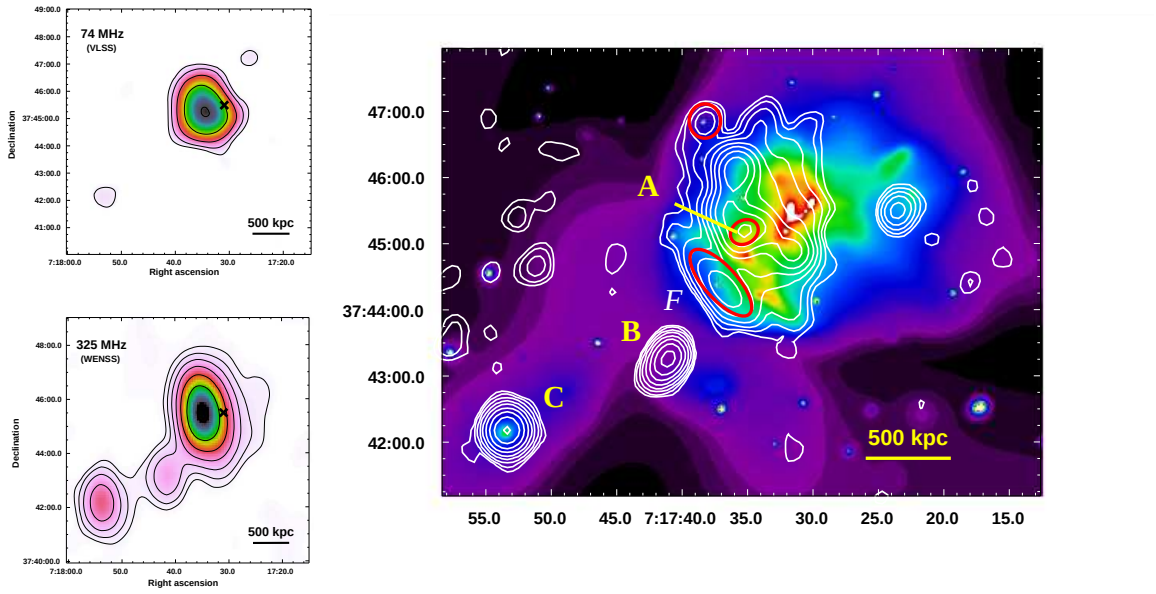

Figure 5.2: Radio emission from MACS J0717 at 74 MHz from the VLSS (top left), and at 325 MHz from the WENSS (bottom left). Contour levels start at 3σ (i.e. 0.24 Jy/beam for the VLSS image and 9 mJy/beam for the WENSS image) and are then spaced by factors of 2. The cross marks the X-ray center. See text for details. Right: Contours of the radio emission at 1.425 GHz and at low resolution, overlaid on a image of the X-ray emission as observed with Chandra (see caption of Fig. 1). Contour levels start at 9 mJy/beam (3σ); subsequent contour levels are spaced by factors of 2. The $FWHM$ of the restoring beam is $\sim 21'' \times 18''$. Circles and ellipse mark sources embedded in the radio-halo emission.

Gaussian beam of $FWHM = 5'' \times 4''$ which corresponds to a linear resolution of $\sim$32 kpc. In order to distinguish the relic emission from that of embedded radio sources we have retrieved from the NRAO archive a short ($\sim$ 10 min) observation performed at 8.460 GHz. Here the source 3C147 was used as primary flux-density calibrator, and the source 0741+312 was used as phase calibrator. Because of the smaller field of view, only the sources A and B are visible in the radio image. Observational details are reported in Tables 5.1 and 5.2.

5.3.2 Low-resolution observations

MACS J0717 was observed with the C array at 1.425 GHz in order to properly image the extended emission. The source 1331+305 (3C286) was used as primary flux-density calibrator, and also as an absolute reference for the electric vector polarization angle. The source 0713+438 was used as phase calibrator. Calibration and imaging were performed with the NRAO Astronomical Image Processing System

Table 5.3: Total and polarization-intensity radio emission.

Name	RA (J2000)	DEC (J2000)	dist kpc	ν GHz	S_{peak} (mJy/beam)	S (mJy)	P_{peak} (mJy/beam)
Source A	07h17m35.4s	+37d45'08″	450	1.365	8.3	22.2	0.3
				1.435	8.4	22.4	0.3
				1.485	7.7	20.0	0.2
				1.665	7.4	18.1	0.3
				4.535	2.3	4.7	0.2
				4.885	2.1	3.9	0.2
				8.460	0.5	0.7	
Source B	07h17m40.9s	+37d43'17″	1150	1.365	9.2	19.9	0.2
				1.435	9.3	18.8	0.3
				1.485	8.8	18.3	0.4
				1.665	8.8	18.3	0.4
				4.535	4.1	7.0	0.3
				4.885	3.8	6.4	0.2
				8.460	1.6	1.9	
Source C	07h17m53.7s	+37d42'11″	2140	1.365	10.0	32.8	0.1
				1.435	9.9	32.3	0.2
				1.485	9.6	30.5	0.2
				1.665	9.8	30.4	0.2
				4.535	5.4	17.2	0.5
				4.885	5.0	14.7	0.4

Col. 1: Source name; Col. 2, Col. 3: Pointing position (RA, DEC); Col. 4: projected distance from the cluster center; Col 5: Observing frequency; Col 6: Peak brightness; Col. 7: Flux density ; Col. 8: Peak of polarized flux

(*AIPS*), following standard procedures. In addition, we recovered from the VLA data archive an observation at 4.860 GHz. Here the source 0714+335 was used as phase calibrator. At both frequencies total-intensity maps (Stokes I) were produced using natural weighting and restored with the same beam, having $FWHM$ of $\sim$18″×14″, corresponding to $\sim$100 kpc. In order to study the diffuse polarized emission, I, Q, and U images were also produced from 1.425 GHz observations at low resolution ($FWHM$ $\sim$21$\sim$18″). Observational details are reported in Tables 5.1 and 5.2 .

5.4 Radio emission: the relic-filament structure and the radio galaxies

The presence of non-thermal emission associated with the ICM in MACS J0717 was first reported by Edge et al. (2003) who classified the emission as a relic. The wealth of radio data described in the previous section allows a multi-resolution and multi-frequency study of the radio emission arising from this cluster. Fig. 5.1 shows the

1.365 GHz data from VLA B-array observations in contours, overlaid on the X-ray surface brightness in colors. The radio data reveal a bright, filamentary structure whose central part is coincident with the relic discovered by Edge et al. (2003). In addition, several radio sources are detected. Those related to the cluster and the large-scale optical and X-ray filament are labelled A, B, and C, whereas the source labelled F is a radio galaxy in the foreground ($z = 0.1546$, Ma et al., in preparation). A proper study of the extended emission associated with the ICM needs to take into account possible contamination from radio galaxies embedded in the diffuse emission. This can be done with the help of high-resolution and high-frequency observations in which the extended emission is resolved out and too faint to be detected. Using 8.460 GHz observations we have identified one such embedded radio galaxy, labelled A in Fig. 5.1 and shown in a close-up view in the side panel of the same figure. This source is $\sim$70″ away from the cluster center in projection. It consists of a bright region, likely the core of the radio galaxy, with a spectral index of $\sim$0.7 between 1.465 GHz and 4.885 GHz, and an extended, more diffuse region extending toward the NW. The spectral index steepens up to ~ 2 with increasing distance from the core. The optical counterpart coincides with the radio core (Fig. 5.1) .
Moving out from the cluster center, two additional radio galaxies, labeled B and C in Fig. 5.1, are visible at all the observed frequencies. Both are located to the SE of the cluster's X-ray center, at projected distances of $\sim$ 180″ and $\sim$ 335″, respectively. We note their position along the X-ray and optical large-scale filament detected by Ebeling et al. (2004). Source C is the brightest cluster galaxy of the next cluster (also detected in the Chandra observation) that is going to merge with MACS J0717. In Table 5.3 we report the main radio properties of the identified radio galaxies at the observed frequencies. The optical counterparts of A, B, and C are all spectroscopically confirmed to lie at redshifts consistent with that of MACS J0717 proper.

5.5 The radio halo

Being sensitive to structure on larger angular scales, observations performed with the C array at 1.425 GHz and with D array at 4.860 GHz reveal the presence of an extended radio halo permeating the cluster volume around the filamentary structure visible at high resolution and discussed in the previous section. MACS J0717 is

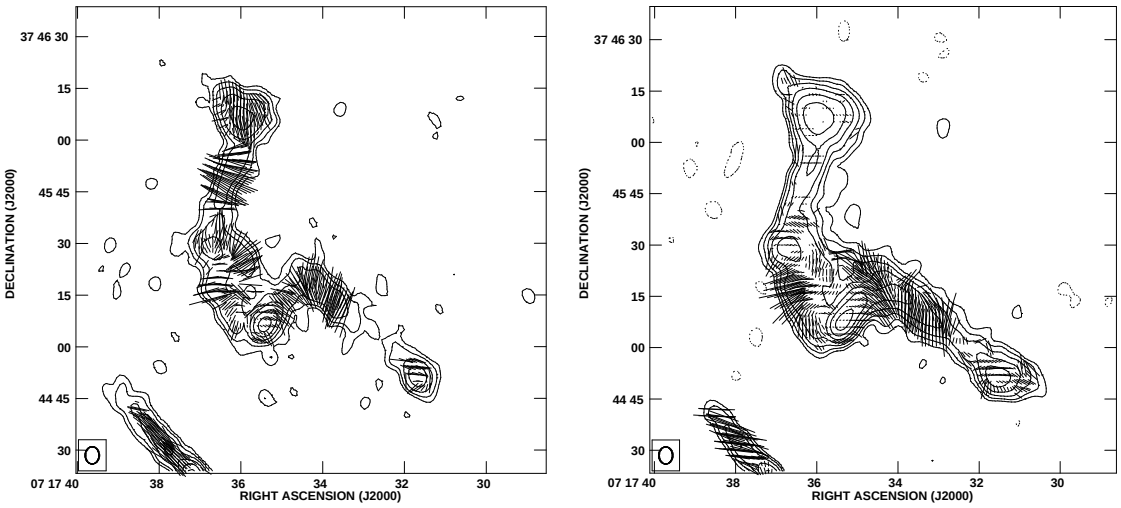

Figure 5.3: Polarized emission from MACS J0717 at 4.885 GHz (left panel) and at 1.365 GHz (right panel). Contours represent the total intensity. The $FWHM$ of the restoring beam is $5''\times4''$. The lowest contours shown are at –3σ and 3σ; subsequent contours are spaced by factors of 2. Lines represent the polarization vectors: line orientation indicates the direction of the E field, while line length is proportional to the polarization percentage. $1''$ corresponds to 3%.

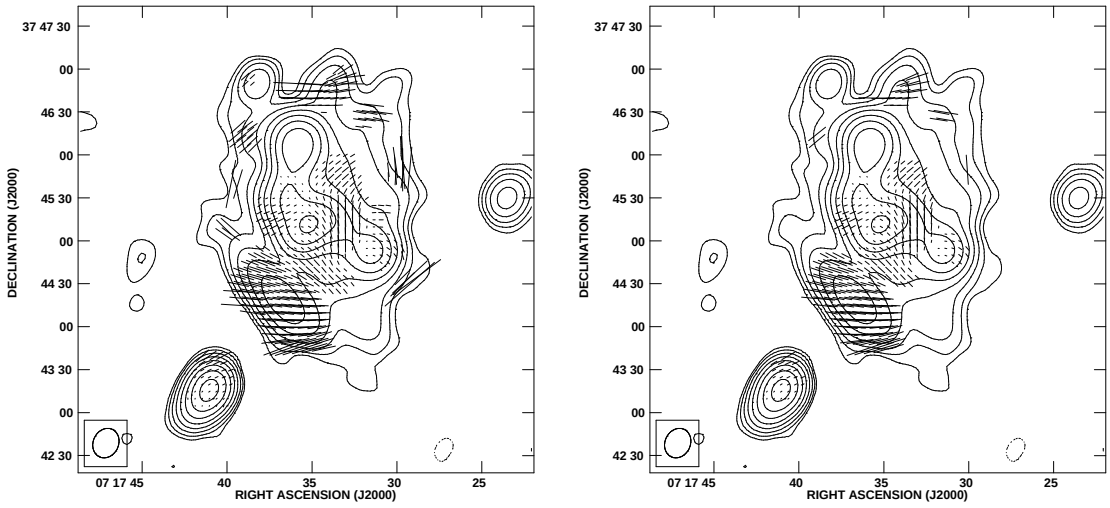

Figure 5.4: Polarized emission from the cluster at 1.425 GHz. Contours show to the total-intensity emission at the resolution of $21''\times18''$, starting at 3σ, with higher contour levels spaced by factors of 2. Lines refer to the E vectors. Their orientation represents the projected E-field not corrected for Galactic rotation. Their length is proportional to the fractional polarization: $1''$ corresponds to 1.3%. Fractional polarization pixels with a signal-to-noise ratio less than 3 (left) and 5 (right) were blanked (see text).

the most distant cluster in which a radio halo has been observed so far and its presence, together with the radio halo detected in the cluster CL0016+016 by Giovannini & Feretti (2000) at z=0.54, indicates that the ICM is already significantly magnetized at redshift z$\sim$0.5. The detection of yet more extended emission around the filamentary structure detected at higher resolution raises some questions about the nature and origin of the latter. This structure could either be a radio relic located at the cluster periphery, but appearing close to the cluster center when viewed in projection, or it could be a filamentary feature that is in fact part of the radio halo. We will further investigate these hypotheses with the help of additional information on the polarization and spectral index of the radio emission (see Secs. 5.7 and 5.8). In the following analysis, we will refer to this feature as the relic-filament in order to stress its uncertain nature.

In Fig. 5.2 the halo emission at 1.425 GHz is shown overlaid onto the cluster X-ray emission. The maximal angular extent of the halo at 1.425 GHz is $\sim$240$''$ in the NS direction, corresponding to a linear size of $\sim$1.5 Mpc. At 4.860 GHz only the brightest regions of the halo are visible, and its angular extent is reduced to $\sim$160$''$ (*i.e.* $\sim$ 1 Mpc).

As shown in the panels on the left of Fig. 5.2, the radio halo in MACS J0717 is also detected at 74 MHz in the VLSS (VLA Low Sky Survey, Cohen et al. 2007), and at 325 MHz in the WENSS (Westerbork Northern Sky Survey, Rengelink et al. 1997). The VLSS was performed with the B array at a resolution of 80$''\times$80$''$ and with an rms noise level of $\sim$0.08 Jy/beam, while the WENSS has a resolution of 54$''\times$54$''cosec(DEC)$, which translates into 54$''\times$84$''$ for the declination of MACS J0717. The apparent angular extent of the halo in the WENSS image is $\sim$280$''$, corresponding to $\sim$1.8 Mpc. Furthermore, faint radio emission that appears to connect the radio galaxies B and C with the central halo is detected at 325 MHz at 3 σ significance. We note that this region coincides with the large-scale filament funneling matter onto MACS J0717 that has been detected at optical and X-ray wavelengths by Ebeling et al. (2004) and Ma et al. (2009). The detection of radio emission in this area might indicate that the magnetic field is already present in the filament before the amplification due to the merger process has occurred. However, the feature is detected at 3σ significance and could simply be the result of blending of the two radiosources B and C at the low resolution of the 325 MHz data. Deeper

observations would be required to clarify this issue.
High-resolution observations were performed in full-polarization mode, as well as 1.425 GHz observations at low resolution. We are thus able to study the polarized emission in a wide range of resolutions, and, at high resolution, in a wide range of frequencies.

5.6 Polarized emission from the ICM

5.6.1 High-resolution images

The relic-filament is located $\sim 40''$ ($\sim$ 260 kpc in projection) SE of the main X-ray peak of the cluster. Its maximal angular extent is $\sim 130''$ at 1.4 GHz, corresponding to $\sim$ 830 kpc at the cluster redshift, and its orientation is $\sim 30°$. Its flux density (excluding the region covered by source A) is $\sim$83 mJy at 1.365 GHz, and $\sim$16 mJy at 4.885 GHz.
The relic-filament is polarized at all of the observed frequencies. Its mean fractional polarization is 8% at 1.365 GHz and increases to 17% at 4.885 GHz. These values are consistent with those found in other relics, as well as with the values found in the filament of the radio halo in Abell 2255 (Govoni et al. 2005). In Fig. 8.7 the E-vectors at 1.365 and 4.885 GHz are shown. We note that the polarization of the relic-filament is not uniform. Its northern part is strongly depolarized at 1.365 GHz. Its mean fractional polarization is a few percent at 1.365 GHz and increases to 20% at 4.885 GHz. Depolarization between 1.365 and 4.885 GHz also occurs in the southern part, as expected, but is less dramatic (the mean fractional polarization is $\sim$9% at 1.365 GHz and $\sim$16% at 4.885 GHz).

5.6.2 Low-resolution images

In order to reveal any extended emission from the radio halo, an image was produced using a Gaussian taper to down weight long-baseline data points in the UV plane. The image was then restored with a Gaussian beam of $FWHM$ $\sim 21'' \times 18''$ (see Fig. 5.2).
In order to investigate the presence of polarized emission from the radio halo we produced Stokes Q and U radio images following the same technique. We then derived the polarization angle image and the polarization intensity image without imposing any cut. From the polarization intensity image we derived the fractional

polarization image by dividing the polarization intensity image to the total intensity image, and we considered as valid pixels those whose signal-to-noise ratio was >3, and >5 in the output image. The cut on the final image, done on the basis of the signal-to-noise ratio, is done to get rid of possible spurious polarization. The resulting images are shown in Fig. 5.4. From them we can gather that there is a detection of polarization in the halo, mostly concentrated in one region in the center, and also strong at the edges, though this becomes weaker when the cut on the fractional polarization images are more severe.

From Fig. 5.4 we can also gather some indication that the radio emission detected at high resolution and previously classified as relic is likely a polarized filament belonging to the radio halo. We note, in fact that the polarized structure as revealed from the polarization vectors does not show any jump between the relic and the more extended part, but instead the E-vectors trace with continuity the brightest part of the radio halo. We refer, for comparison to the case of Abell 2256 (Clarke & Ensslin 2006). Here the polarized emission image marks a clear and sharp distinction between the radio halo and the radio relic. Thus, we report the polarization percentage values of the whole ICM emission (excluding only the contribution of source A). The mean polarization percentage at 1.425 GHz is ∼2-7%, (3-5σ detection) with lower value in the central part of the halo, that is ∼0.01-0.6% (3-5σ detection) and higher values at the edges, where it reaches a maximum value of ∼24-34% (3-5σ detection). We note that values reported here based on low-resolution observations might be affected by beam depolarization. Indeed, small-scale variations of the magnetic-field orientation are evident from high-resolution images (see Fig. 8.7). At 20 cm we get 1 radian of rotation for a RM of 25 rad/m^2 (see Eq. 2.10), thus for a 20″ beam the RM gradient is about 1 rad/m^2/″ to cause cancellation within the beam, and any reasonable ICM model could produce this. Therefore the mean polarization percentages should be considered lower limits.

5.7 Faraday Rotation from MACS J0717

As explained in Sec. 2.6, Faraday rotation is expected when synchrotron radiation passes through the magnetic ionized ICM, and if the cluster acts like an external Faraday screen useful information about the ICM magnetic field can be derived from the analysis of this effect (Eqs. 2.12, 2.22).

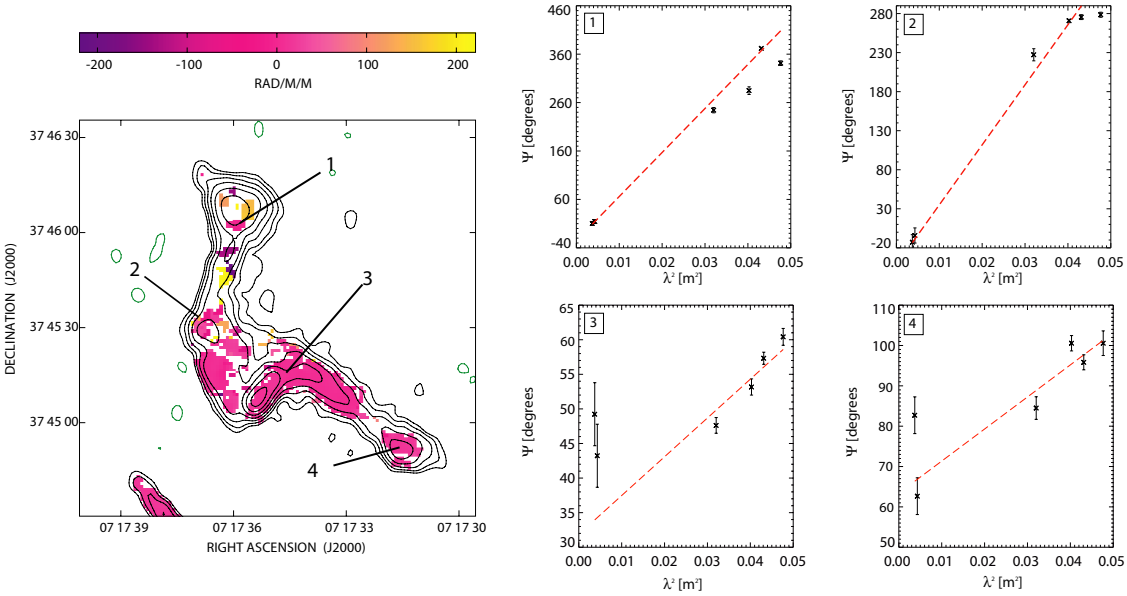

Figure 5.5: Left panel: Contours refer to the radio emission at 1.425 GHz. The restoring beam $FWHM$ is $5'' \times 4''$. The image represents the attempt to fit the Polarization Angle at the observed frequencies with the λ^2 law in the relic-filament region. Results from fits of a λ^2 law to the polarization angle are shown in the plots on the right. They refer to four random pixels located in different parts of the relic-filament and of the source A as indicated in the left panel.

The situation in this cluster could however be much more complicated that the drawn picture. If radiation is strongly affected by beam depolarization, or if the Faraday rotation is internal, Eq. 2.10 is not applicable (see Sec. 2.6.2). The large frequency range of our observations allows us to test whether a simple linear fit of the polarization angle versus λ^2 is consistent with our data.

5.7.1 Rotation Measure fits

We performed a fit of the polarization angle images as a function of λ^2 for the relic-filament, and for the sources B and C. We used the *Pacerman* algorithm developed by Dolag et al. (2005c). The algorithm solves the nπ ambiguity in low signal-to-noise regions exploiting the information of nearby reference pixels, under the assumption that the reference pixel is connected to the nearby areas as far as the polarization angle gradient is under a certain threshold in all of the observed frequency maps

Table 5.4: RM values for sources B and C

Name	$\langle RM_{obs} \rangle$ rad/m^2	$\langle RM_{crf} \rangle$ rad/m^2	Fit error (average) rad/m^2	N of beams
Source B	-130	-312	1	3
Source C	85	204	1	3

Col. 1: Source name ; Col 2: observed $\langle RM \rangle$;
Col 3: $\langle RM \rangle$ in the cluster rest frame;
Col. 4: fit error; Col 5: number of sampled beams

simultaneously (see Sec. 3.5). We considered as reference pixel those which have a polarization angle uncertainty smaller than 7 degrees, and fixed the gradient threshold to 15 degrees. Seven degree error of the polarization angle corresponds to 3σ level in both U and Q polarization maps simultaneously.
We note that some regions show a high polarized flux at 6cm while they are weakly polarized at 20cm. This could indicate that the Faraday rotation is higher in these regions, leading to higher depolarization in lower frequency observations. Excluding these regions would correspond to a bias toward low RM regions. So we decided to allow *Pacerman* to perform the RM fit if at least in 3 frequency maps the above mentioned conditions were satisfied.
Once the RM image is obtained, the Galactic contribution to the observed RM must be subtracted. We computed the average RM for extragalactic sources from the catalog published by Simard-Normandin et al. (1981). The cluster's galactic coordinates are: lon= 180.25° and lat= +21.05°. It results that in a region of 15°×15° centered on the cluster the Galactic contribution is $\sim 17 rad/m^2$. This value is also consistent with the $\langle RM \rangle$ that we find in our observations for the foreground galaxy F located at $07^h17^m37.2^s$, +37°44′21″ (J2000). Its $\langle RM \rangle$ is $15 \pm 3 rad/m^2$, with values going from -3 rad/m^2 to 28 rad/m^2.

RM fit in the relic-filament region

From the existing data we can only derive the position of the relic-filament in projection, but not where it lies with respect to MACS J0717 along the line of sight. It could be a foreground structure (case 1), a background structure (case 2) seen in projection, or a bright part of the radio halo neither behind or in front of the cluster (case 3). The polarization properties and the trend of the polarization angle

versus λ^2 can help in distinguish among these three situations, and we will discuss them in the following.

- **Case 1:** our galaxy acts like a Faraday screen, similarly to what we observe for the foreground source F, so we expect to obtain $RM \sim 15$s rad/m^2.

- **Case 2:** the ICM acts like a Faraday screen and the polarization angle rotates following Eq. 2.10.

- **Case 3:** the situation is more complicated. The trend of Ψ_{obs} versus λ^2 may result from complex geometries (see Burns 1966). In this case the rotation does not originate in an external Faraday screen, Eq. 2.10 does not hold anymore, and obtaining information about the magnetic field from Faraday rotation requires detailed knowledge of the ICM distribution and properties.

In Fig. 5.5 we show fits of Ψ_{obs} versus λ^2 obtained in the relic-filament region. The poor agreement between the data and the simple linear model suggests that the Faraday rotation is not occurring in a Faraday screen, thus favouring scenario (3) above. The observed trends of Ψ_{obs} versus λ^2 are also incompatible with internal Faraday rotation generated by a uniform slab (see Burn 1966). Although strong beam depolarization could affect the trend of Ψ_{obs} versus λ^2, present data favour the third scenario and suggest that the relic-filament is actually a polarized filament belonging to the radio halo and not a radio relic connected to a peripheral merging shock.

RM fit for the sources B and C

In Fig. 5.6 we show the *RM* image and plots of Ψ_{obs} versus λ^2 obtained with *Pacerman* for the two radio sources B and C. These plots confirm that, as expected, the *RM* observed here is due to an external Faraday screen. In Table 5.4 we report the observed RM for these sources (RM_{obs}) and the *RM* in the cluster rest frame (RM_{crf}), that is given by $RM_{crf} = RM_{obs} \times (1+z)^2$. Once the Galactic contribution is subtracted, we obtain $\langle RM_{crf} \rangle$ values of –312±1 rad/m^2 and 204±1 rad/m^2 for sources B and C, respectively. As source C is associated with the BCG of a satellite cluster embedded in the large-scale filament and visible in the X-ray image, its *RM* is representative of the properties of that cluster. There is no obvious concentration

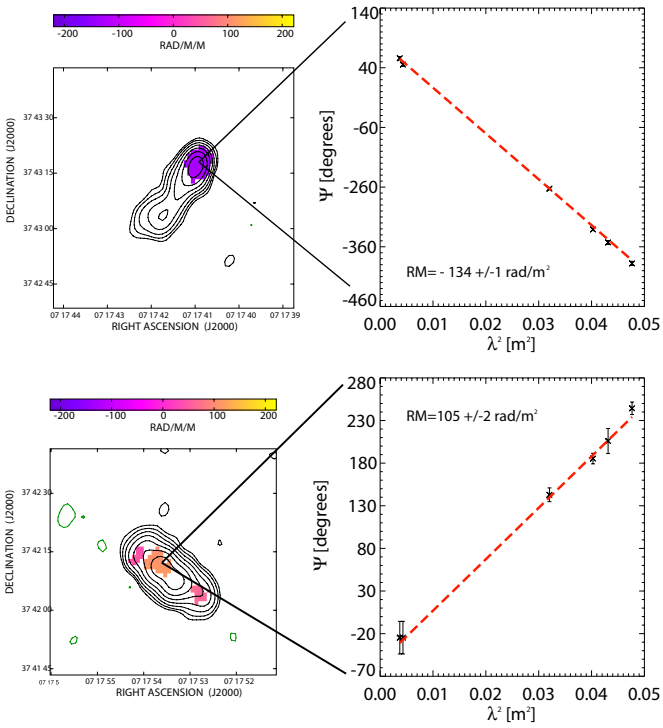

Figure 5.6: Left: Observed rotation measure images obtained for the source B (top panel) and C (bottom panel). Right panel: fit of the Polarization angles Ψ_{obs} versus λ^2, demonstrating that the Faraday rotation is occurring in a foreground screen. The fits are referred to a representative pixel in the two sources.

of X-ray emission around source B, which is also located along the optical and X-ray large-scale filament, but still within the virial radius of MACS J0717 proper. A crude estimate of the gas density here is $7\pm1\ 10^{-4}$ cm^{-3}. Deriving the magnetic field from RM using Eq. 2.12 requires knowledge of the correlation-length scale (Λ_B) of the magnetic field (see Murgia et al. 2004). The expectation value of the RM is in fact:

$$\langle RM^2 \rangle \propto \Lambda_B \int (n_e(l) B_{//}(l))^2 dl \tag{5.2}$$

We have then to make some assumptions on Λ_B, and to fix the limits of the integral in Eq. 5.2. If we assume that both gas and magnetic field are uniform on a scale Λ =1 Mpc (i.e. the projected distance from B to the center of the main cluster), and that Λ_B=1 Mpc as well, we derive $\langle B \rangle$ ~0.5μG. This value should be considered a lower limit to the magnetic field strength. In fact, if we assume Λ_B=200 kpc (the aproximate linear extent of source B), we obtain $\langle B \rangle$ ~1.2 μG. Although these estimates rely on several assumptions, the values of both the RM and of the magnetic

field obtained are still high compared to the values derived for sources located at similar distances from the cluster center (see e.g. Clarke et al. 2004, and Fig. 2.3). Our findings thus indicate that the magnetic field has already been amplified in these regions, possibly by energetic phenomena associated with the complex merging history of this cluster.

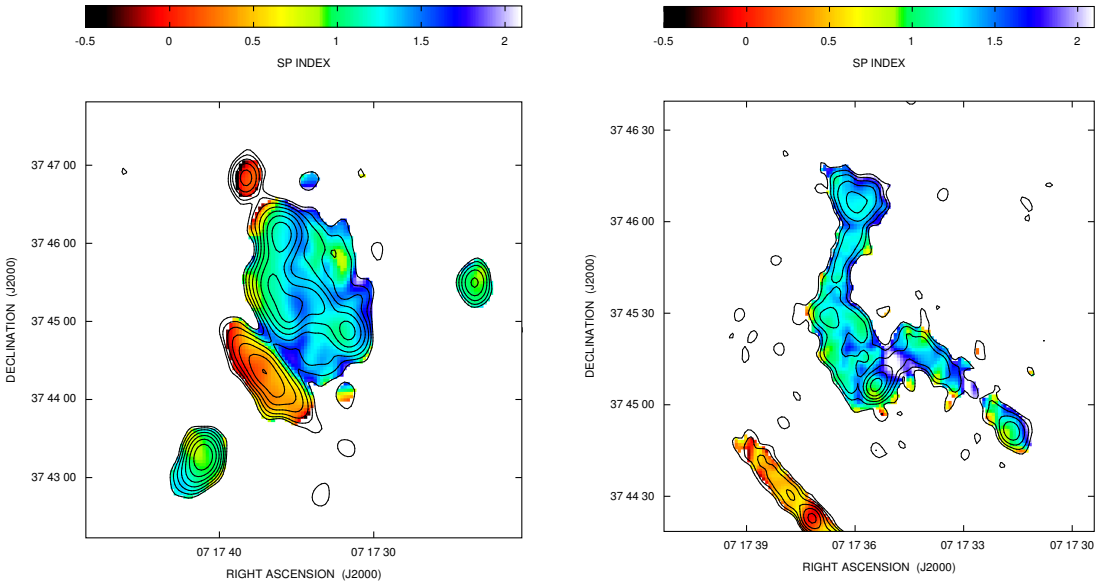

Figure 5.7: Left: spectral index image of the radio halo between 1.365 GHz and 4.885 GHz. Contours refer to the radio emission at 4.860 GHz. They start at 3σ and are then spaced by a factor of 2. The restoring beam $FWHM$ is $18''\times14''$. Right: spectral index image of the relic-filament between 1.365 GHz and 4.885 GHz. Contours refer to the radio emission at 4.885 GHz. They start at 3σ and are then spaced by a factor of 2. The restoring beam $FWHM$ is $5''\times4''$.

5.8 Spectral index analysis

The analysis of the spectral index is useful to determine the energetic spectrum of the emitting particles. In fact, it is well known that if the emitting particle energy distribution follows a power law $N(E) \propto E^{-\delta}$ the radio synchrotron spectrum will result to be a power law as well $S(\nu) \propto \nu^{-\alpha}$, with $\alpha = (\delta - 1)/2$.

We derived the spectral index image by comparing the high resolution images at 1.365 and 4.885 GHz and the low resolution images at 1.425 and 4.860 GHz. Spectral index images are shown in Fig. 5.7. They were obtained considering only pixels whose brightness is >3 σ at both frequencies. Images at the same resolution were

obtained using the same UV-range in order to avoid any effect due to their different sensitivity to the large angular structure.
We computed the global spectral index of the relic-filament by fitting the integrated brightness as a function of the frequency as:

$$LogS(\nu) = -\alpha Log(\nu). \tag{5.3}$$

We obtained $\alpha \sim 1.3 \pm 0.1$ for the relic-filament, from high resolution images, 1.27±0.02 for the radio halo once both the relic-filament and the embedded sources are masked, and 1.27±0.01 for the entire diffuse radio emission (*i.e.* masking the embedded sources only). The fits are shown in Fig. 5.8. We have to consider here that the halo emission observed at 4.680 GHz is likely affected by the Sunayev-Zeldovich effect, that causes a decrement of the radio emission at 4.860 GHz and consequently a steepening of the spectral index (see *e.g.* Liang et al. 2000).
The analysis performed in the previous Secs. indicates that the high resolution emission previously classified as relic is likely a bright region connected with the radio halo itself, rather than a peripheral radio relic. Also the spectral index analysis agrees with this hypothesis since the spectral index of the relic-filament alone, of the halo once the relic-filament is masked and of the entire ICM radio emission has the same value.
The analysis of the spectral index profile in the relic-filament offers another possibility to check this hypothesis. The spectral index study of radio relics has been performed so far on some clusters (see *e.g.* A2256, Clarke & Ensslin 2006; A3667, Roettgering et al. 1997; A2744, Orrú et al. 2007; A521, Giacintucci et al. 2008; A2345 and A1240, this thesis, Chap. 6), and all of the present theoretical models, as briefly explained in Sec. 1.3.2, require the presence of a shock wave that either accelerates the particles from the thermal pool to relativistic energies (Ensslin et al. 1998; Roettiger et al. 1999; Hoeft & Brueggen 2007) or compresses a region containing fossil radio plasma amplifying the magnetic field and re-energizing the particles so that they can emit radio wave again as proposed by Ensslin & Gopal-Krishna 2001. In both of these cases a spectral steepening across the relic main axis is expected if the relic is seen edge-on. The particles accelerated or energized by the shock wave lose rapidly their energy because of the combined effect of synchrotron and Inverse-Compton losses. Their particle energy spectrum will thus steepen rapidly giving rise to a radio spectrum that progressively steepens with the

Table 5.5: Radio Halo parameters

Freq GHz	Beam $''\times''$	Flux mJy	LLS Mpc
1.425	21×18	118±5	1.5
4.860	18×14	26±1	1.0
0.325	84×54	$1.2\pm0.5\times10^3$	1.8
0.740	80×80	$5.8\pm0.6\times10^3$	1.3

Data at 74 and 325 MHz refer to the radio emission from the cluster;
the contribution of embedded sources is not subtracted;
data at 1.425 and 4.860 GHz refer to the whole extended structure
excluding only the contribution of the embedded sources.

distance from the current location of the shock.

In order to investigate the presence of such a systematic trend, we integrated the radio brightness at each frequency (S_ν) in boxes of $\sim15''$ in width. The associated error is then given by $\sigma_{noise} \times \sqrt{N_{beams}}$, with σ_{noise} being the rms noise of the radio image, and N_{beams} the number of beams sampled in each box. The boxes are parallel to the relic main axis, and are shown in the inset of Fig. 5.9. The spectral index in each box was computed by fitting Eq. 5.3.

The value of α goes from 1.4±0.2 in the inner box to 1.1±0.1 in the outer box, with values of 1.2± 0.1 and 1.3±0.1 in the internal boxes. Its trend does not show a clear progressive steepening as in the case of the other relics cited above. Although we cannot exclude that this is due to ad-hoc projection effects, this result agrees with the hypothesis that the relic-filament is part of the more extended emission that is detected with low resolution observations, i.e. it is a bright filament belonging to the radio halo itself.

Thus, in the following analysis we will consider the flux emitted by the whole extended structure (low resolution emission +relic-filament), excluding only the contribution of the embedded sources. We will refer to this whole emission as halo.

5.8.1 Spectral index of the radio halo

The total flux of the radio halo at 1.425 GHz and at 4.680 GHz are ∼118 mJy and ∼26 mJy respectively. This makes MACS J0717 the most powerful radio halo ever observed. Its radio luminosity at 1.425 GHz, once the k-correction is accounted for, is in fact $\sim1.6\times10^{26}$ WHz^{-1}.

The total flux have been computed over the same area, excluding the regions where

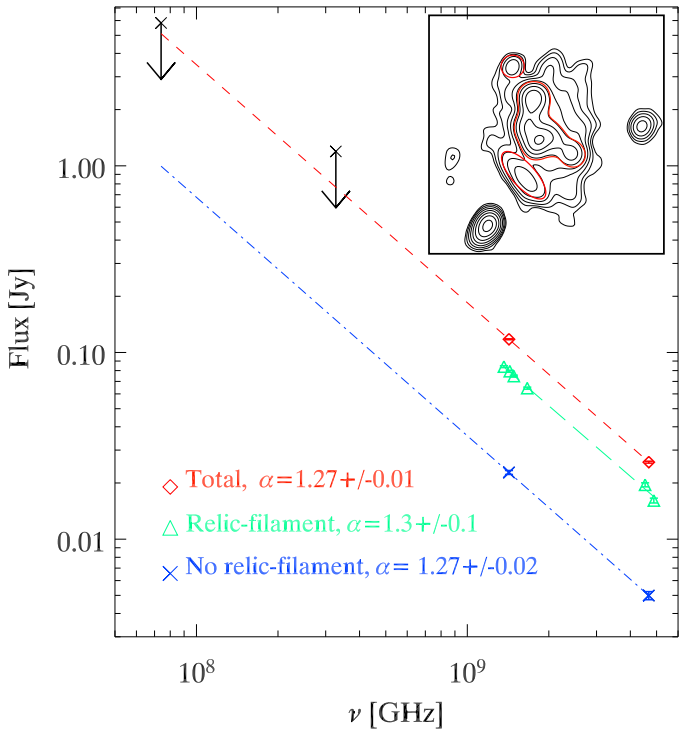

Figure 5.8: Global spectral index fit for the relic-filament (triangles), for the halo once the relic-filament is subtracted (crosses) and for the total ICM emission (diamonds) between 20 cm and 6 cm. Arrows represent the upper-limits derived from the VLSS and WENSS. Bars represent 3σ errors. In the inset thick lines illustrate the regions that have been masked in order to obtain the spectral index of the halo once the relic-filament is subtracted.

the embedded sources are present, so that these values underestimate the total flux of the radio halo and should be regarded as indicative estimates. Due to the low resolution of both the VLSS and the WENSS radio images, it is not possible to resolve the halo and the embedded sources as different radio components, so that the radio flux measured in those images can just be considered as upper limits to the halo spectrum. In Fig. 5.8 the flux density at the different frequencies are shown. 74 MHz and 325 MHz limits are consistent with the spectral index derived from the 1.425 and 4.680 GHz images.

The distribution of the spectral index is an important observable in a radio halo, since it depends on the shape of the electron spectrum and on the magnetic field in which they emit. Regions of flatter spectra indicate the presence of more energetic particles and/or higher value of the magnetic field strength. A systematic variation of the radio halo spectral index with radial distance from the cluster center is predicted by re-acceleration models (see *e.g.* Brunetti et al. 2001). In the re-

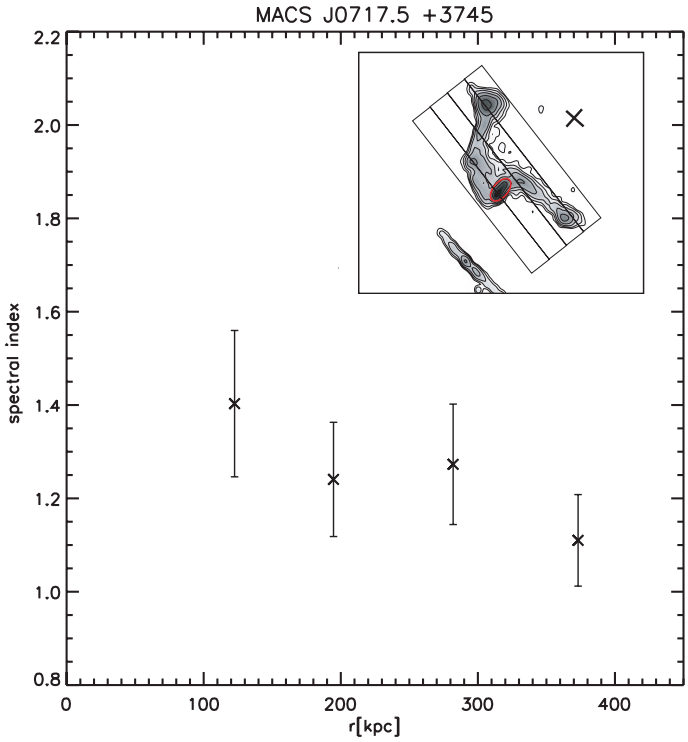

Figure 5.9: Spectral index profile between 1.365 and 4.885 GHz as a function of the distance from the cluster center. In the top right inset the displacement of the boxes is shown, the cross marks the location of the center.

acceleration scenario, in fact, particles are accelerated up to a maximum energy that is given by the balance between acceleration efficiency and energy losses. This results in a break in the spectrum emitted by these electrons. The break frequency depends on the acceleration efficiency and on the magnetic field strength, so that allowing for a decrease of the magnetic field strength with the radius, (see Sec. 5.9) a radial steepening of the radio spectrum is expected, even in the case of a radial constant acceleration efficiency (see Brunetti et al. 2001, Brunetti 2003, Feretti et al. 2003 and references therein). This radial steepening has been observed in some cases (see *e.g.* Feretti et al. 2004), while no steepening has been found in Abell 2744 (Orrù et al. 2006). Here it is tricky to derive such a trend since the cluster is in a very complex dynamical state. Ma et al. (2009) suggest that the most massive structure is located at RA$\sim 07^h17^m35''$, DEC$\sim 37^d45'00''$, that is not coincident with the X-ray brightest region. The halo at 1.425 GHz is more extended than at 4.680 GHz. In order to take this properly into account in the spectral index analysis, we integrated the brightness at 1.425 GHz and at 4.860 GHz in radial shells of $\sim 10''$ in width wherever the 1.4 GHz brightness is $> 3\sigma$. The associated error is then

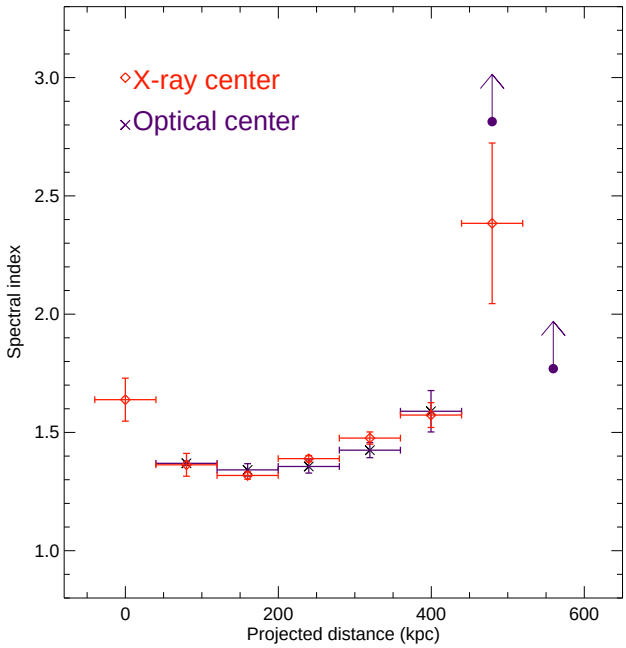

Figure 5.10: Spectral index profile of the radio emission observed at low resolution (including the extended emission and the relic-filament region) computed in spherical shells of 10″ in width. Crosses represent the profile when shells are centered on the X-ray brightness peak, diamonds represent the profile once the shells are centered on the optical integrated light concentration.

$\sigma \times \sqrt{N_{beam}}$. In those shells where the brightness is $>3\sigma$ in the 1.4 GHz image but $<3\sigma$ in the 4.680 GHz image only lower limits on the mean spectral index can be derived. We centered these shells on the X-ray cluster center and on the optical condensation peak. The spectral index profile is shown in Fig. 5.10. The flattest spectral index value is in the shell that is 150 projected kpc from either the X-ray and the optical center. Higher values of α are found in the shells with radial distances <150 kpc and >200 kpc. A radial steepening is thus detected centered on this point.

Spectral index - X-ray emission

Radio properties of radio halos are linked to the properties of the host cluster. This is directly demonstrated by several correlations that have been found between the radio power and the cluster X-ray luminosity (Bacchi et al. 2003), between the radio power and the thermal gas temperature (Liang et al. 2000), between the radio power and the total cluster mass (Govoni et al. 2001) and between the radio spectral

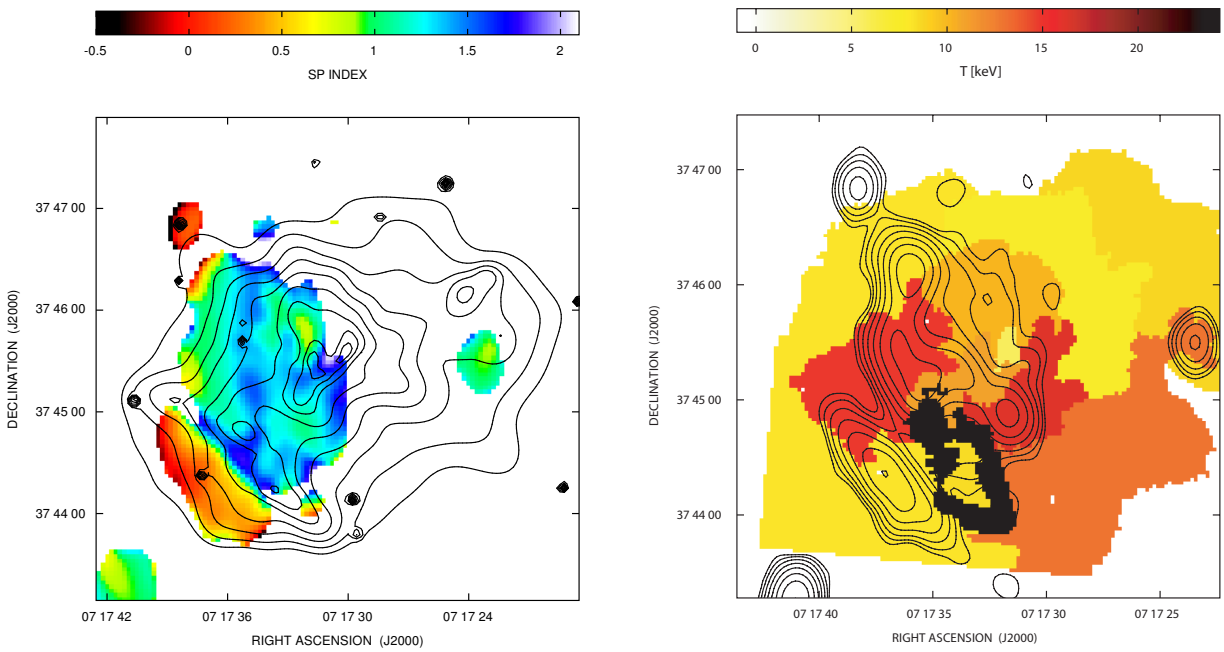

Figure 5.11: Left: Spectral index map overlaid onto X-ray contours. Contours refer to the Chandra X-ray emission in the 0.7-5 keV band. Contours start at 0.06 counts/s and are spaced by $\sqrt{2}$. Right: temperature map (from Ma et al. 2009) overlaid onto radio contours at 4.860 GHz. They start at 3σ and are then spaced by a factor of 2. The restoring beam $FWHM$ is $18'' \times 14''$.

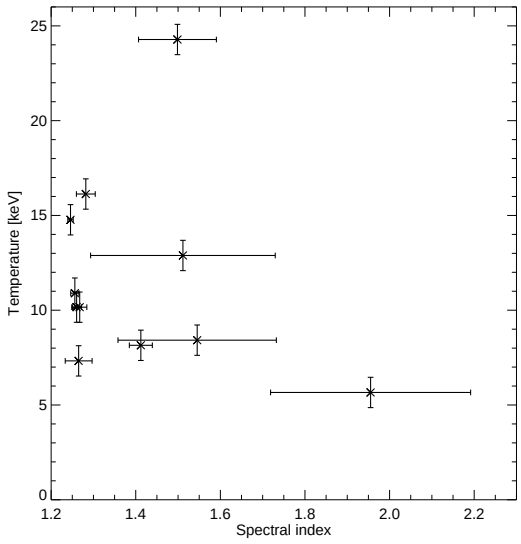

Figure 5.12: Temperature versus spectral index.

index and the thermal gas temperature (Feretti et al. 2004; Orrù et al. 2007). We will present in Chap. 8 a correlation between the radio halo integrated spectral index and the average X-ray gas temperature for a large sample of nearby radio halos (Giovannini et al. 2009). According to this correlation cold clusters (T $<$ 8 KeV) show steep radio spectra (average spectral index = 1.7), while hot clusters (T $>$ 10 KeV) show an average spectral index = 1.1 $-$ 1.2. The radio spectrum of present radio halo with $\alpha \sim 1.27$ confirms that flatter spectra are present in high temperature merging clusters, in agreement with expectations from radio halo re-acceleration models (Cassano 2009).

A spatial comparison of the spectral index image and the X-ray brightness image is shown in the left panel of Fig. 5.11. There is no clear correlation between the radio halo spectral index and the X-ray emission. We note however that a quite flat spectral feature is present in the NW region of the radio halo, close to one of the X-ray peaks. With the help of the temperature map (kindly supplied by C.J. Ma), we further investigate the anti-correlation between the spectral index of the radio halo and the ICM temperature. It is expected that flat spectrum regions have higher temperature, if a fraction of the gravitational energy, dissipated during mergers in heating thermal plasma, is converted into re-acceleration of relativistic particles and amplification of the magnetic field (see Chap. 1). In the right panel of Fig. 5.11 the temperature map is shown (Ma et al. 2009). A flatter region is detected in the NW part of the radio halo, where the mean temperature is 10.2$\pm$2.4 keV (Ma et al. 2009). However, in general, it is difficult to match the patchiness morphology of the temperature map with the spectral index map.

We also investigate the anti-correlation between the ICM temperature and the radio spectral index by computing the spectral index value in regions selected on the basis of their temperature. We used the temperature map obtained after the re-binning process (bottom panel of Fig. 2 in Ma et al. 2009). In Fig. 5.12 the temperature versus the spectral index is shown. We note that the coldest region is also characterized by the most steep spectrum, but in general from this plot we can gather that a correlation, if present, is weak in this cluster. We argue that it is due to projection effects.

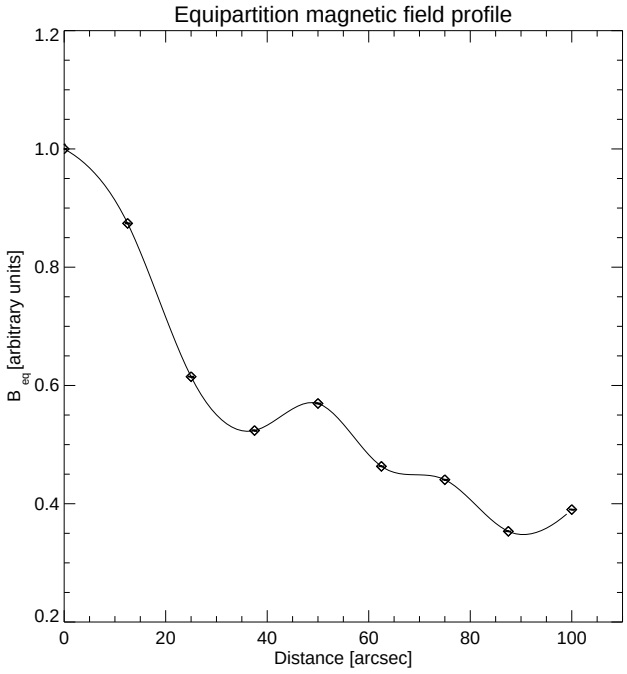

Figure 5.13: Equipartition magnetic field radial profile. It has been normalized to its central value. Regions where radio galaxies are present have been masked.

5.9 ICM magnetic field

The radio analysis performed so far can give important information about the magnetic field in this cluster.

Under the assumption that a radio source is in a minimum energy condition it is possible to derive an average estimate of the magnetic field strength in the emitting volume (Sec. 2.5). We indicate with γ the emitting particle Lorentz factor. The synchrotron luminosity is calculated from a low-energy cut-off of $\gamma_{min} = 100$ and $\gamma_{max} >> \gamma_{min}$ is assumed. We assume that the emitting particle energy distribution is well represented by a power-law $N(E) \propto E^{-\delta}$ with $\delta = 2\alpha + 1$ in this energy range. The volume of the halo is represented by an ellipsoid having the major and minor axis equal to the maximum and minimum linear extension of the relic, *i.e.* $\sim$1500 kpc and 1200 kpc respectively, and the third axis is assumed to be the mean between the major and the minor one. Under the assumption that magnetic field and relativistic particles fill the whole volume of the source and that the energy content in protons is the same as the one in electrons we find that the equipartition

magnetic field is $\sim$1.2 μG, in agreement with other values found in the literature.[1] Under equipartition conditions, if we assume that γ_{min} is constant with cluster radius we obtain that

$$j_\nu \propto B^{(\delta+5)/2} \tag{5.4}$$

where j_ν is the synchrotron emissivity at the frequency ν, B is the magnetic field modulus and δ is the slope of the particle energy distribution.
We used the deprojected brightness profile of the radio halo at 1.425 GHz and computed the equipartition magnetic field radial profile. This is shown in Fig. 5.13. The deprojected brightness profile was computed assuming spherical symmetry with respect to the radio peak brightness. The equipartition magnetic field decreases by a factor $\sim$2.5 from the center to the periphery of the cluster. If the cluster magnetic field decreases with radius as:

$$B(r) = B_0 \left[1 + \frac{r^2}{r_c^2}\right]^{\frac{-3\mu}{2}} \tag{5.5}$$

it is possible to reproduce the equipartition magnetic field profile assuming $\mu = 1.1$, i.e. assuming that the magnetic field profile scales as the gas density profile. Once μ is fixed, it is possible to derive the value of B_0 necessary to reproduce the magnetic field equipartition estimate. We obtain that B_0 =3 μG averaged over the halo emitting volume ($\sim$ 1.1 Mpc^3) can reproduce the equipartition magnetic field estimate. It must be stressed that many assumptions rely on the equipartition assumption, and as explained in Sec. 2.5 the equipartition estimate is critically dependent on the assumed value of γ_{min}, so that these estimates should be regarded with caution.

5.9.1 Contraints on the magnetic field power spectrum

The detection of polarized emission reveals important information about the magnetic field structure in this cluster. Radio halos are intrinsically polarized, since the synchrotron process generates linearly polarized emission. However, in the ICM the emitting plasma is mixed with the thermal one, so due to the Faraday Rotation

[1] Standard equipartition estimate, *i.e.* obtained computing the radio synchrotron luminosity in a fixed range of frequency (10 MHz - 10 GHz) would give B_{eq} $\sim$0.6μG. We report this value to compare this estimate with other given in the literature for other radio-sources. However it has been pointed out by Brunetti et al. (1997) that this approach is not self-consistent since electron energy corresponding to a fixed frequency depends on the magnetic field value.

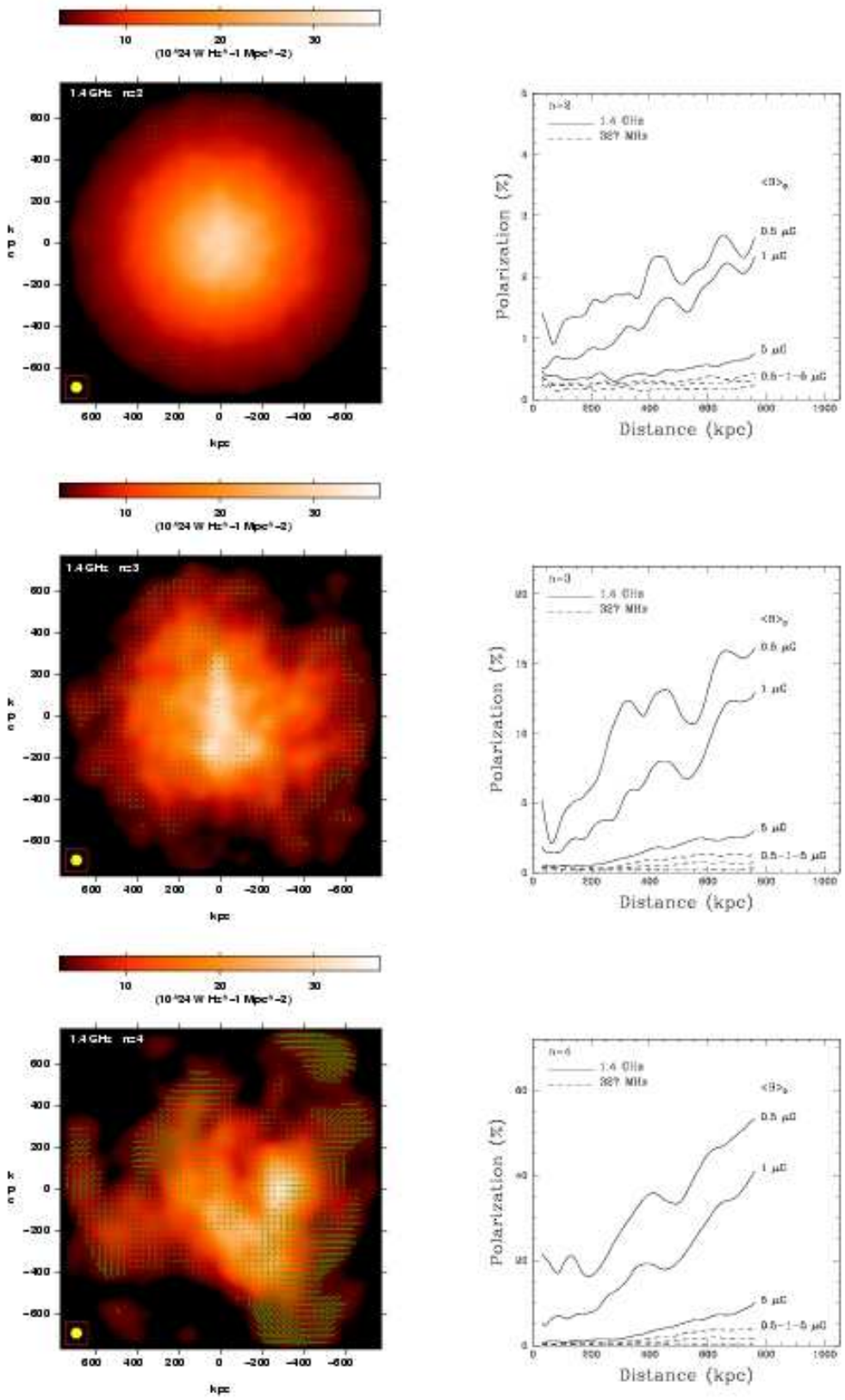

Figure 5.14: Simulated synchrotron halo emission. Left column: simulated halo brightness and polarization images at 1.4 GHz for different values of the magnetic field power spectrum slope and $\langle B_0 \rangle$ =1 μG. Vector lengths are propositional to the degree of polarization, 100% corresponds to 100 kpc on the sky. vector directions represent the **E** direction. Right: column: radially averaged profiles of the polarization percentage at different frequencies and for different values of $\langle B_0 \rangle$. Figure taken from Murgia et al. (2004)

significant depolarization may occur. Moreover, radio halos have a low surface brightness, and high resolution observations are often unable to detect them; if the magnetic field is tangled on scales smaller than the beam size, the observed emission will be further depolarized (beam depolarization). These two effects can explain why polarized emission from radio halos is usually non-detected.

The presence of polarized emission here indicates that the magnetic field fluctuates on scales as large as the beam, that is 130 kpc. Murgia et al. (2004) have demonstrated that if the magnetic field power spectrum[2] is steep enough (n>3) and the outer scale of the magnetic field fluctuation is larger than few hundreds kpc, it is possible to detect polarized emission from radio halos (see Fig. 5.14.

Radio halos are expected to be generated by re-acceleration of particles by Fermi II processes that occur in the ICM after merger events (see *e.g.* Cassano & Brunetti, 2005; Cassano, Brunetti & Setti, 2006). The energy is injected at large spatial scales and then a turbulent cascade is generated. This cascade converts the energy into motions at smaller and smaller scales until the dissipation scale is reached. The analysis performed on this cluster suggests that it could be in a young phase after the merger. The magnetic field is thus still ordered on sufficient large scale and its polarized emission can be detected even with low resolution observations.

5.10 Conclusions

In this chapter we have presented the study of the emission arising from the cluster MACS J0717+3745. The analysis of the radio polarized emission joint to the analysis of the total intensity radio and X-ray emission allows us to investigate non-thermal phenomena at work during merging episodes. The Faraday rotation arising from a bright filament within the cluster does not allow to derive firm constraints on the magnetic field profile and power spectrum as we have done in the Coma cluster (Chap. 4), nonetheless, information about the magnetic field in this complex systems have been derived, and a joint analysis between thermal and non-thermal emission has been performed.

The main result of this work is the discovery of a giant radio halo in a massive galaxy cluster at z$\sim$0.55. The radio halo of MACS J0717 is the most distant radio

[2]The magnetic field power spectrum is modelled as $|B(\Lambda)|^2 \propto \Lambda^n$, where Λ is the fluctuation scale in the real space and n is the power spectrum spectral index

halo ever observed and the most powerful one. Moreover, it is only the second halo for which polarized emission has been detected. We here summarize the results of our analysis:

- The cluster MACS J0717+3745 shows a complex radio morphology that reflects the complex dynamical state revealed by X-rays and optical studies.

- A powerful radio halo has been observed, emission from which is detected here for the first time at 1.425 and 4.680 GHz. With a radio power of $\sim 1.6 \times 10^{26}$ WHz^{-1} at 1.4 GHz, it is the most powerful radio halo ever observed. Its spectral index is steep (α =1.27$\pm$0.01), in agreement with results obtained for other radio halos found at lower redshifts. Our detection of diffuse radio emission from MACS J0717 at z=0.55 indicates that the ICM is already magnetized at this redshift.

- We argue that the bright radio emission visible in high-resolution images and previously classified as relic is more likely a bright, polarized filament connected with the radio halo. This feature, in fact, lies at the center of the cluster and of the radio halo. The trend of the polarization angle Ψ_{obs} versus λ^2 indicates that the Faraday rotation originates in a region where a morphologically complex mix of thermal and non-thermal gas is present, resulting in a poor match both with the λ^2 law expected in the case of a Faraday screen and with the simplified model expected in the case of a uniform slab. Although the effects of depolarization cannot be taken into account trivially, we find the most plausible scenario to be one in which this filamentary emission is embedded in the central cluster region. The radio emission from this filamentary structure is polarized at $\sim$8% at 1.365 GHz and $\sim$17% at 4.885 GHz, and the polarization image does not show any discontinuity between the radio halo and this relic-filament structure. The spectral-index profile further reinforces our interpretation since no clear steepening is observed across the main axis, as would be expected if the emission were caused by a peripheral shock wave. We also note that the mean spectral index of the relic-filament and of the radio halo are fully compatible within the small errors.

- Low-resolution polarization observations at 1.425 GHz have shown that the polarized emission is not confined to the bright relic-filament observed at high

resolution but extends to the innermost regions of the radio halo and to some regions in the outskirts. Following Murgia et al. (2004), this indicates that the power spectrum of the magnetic field is steep in this cluster, with a spectral index n>3, and that it must fluctuate on scales as large as ∼130 kpc.

- Under the equipartition assumption, we derived the magnetic-field profile of the radio halo and found it consistent with predictions based on the assumption that the magnetic-field profile scales as the gas-density profile. Once the radial decline is fixed, a central value of $\sim 3\mu$G can also account for the magnetic-field equipartition estimate.

- Finally, high RM values have been found for the source labelled with B in Fig. 5.1, that lies onto the filament detected in optical and X-ray data. The high value suggests that energetic phenomena associated with the complex dynamical history of this cluster may have amplified the magnetic field in this region.

Chapter 6

Magnetic field at the cluster periphery: double radio relics in Abell 1240 an Abell 2345*

6.1 Introduction

The presence of magnetic field at the cluster periphery is proved by radio relic emission. Although the origin of these sources is not understood yet, several models have been proposed to explain their origin and evolution. All of these models require the presence of shock waves, (merging or accretion shocks), that could be able to amplify the magnetic field and/or accelerate the emitting particles (see Sec. 1.3.2). A number of predictions are made by such models, regarding the radio relic morphology, spectral index, spectral index trend, and their polarization properties, that can be tested with radio observations. Understanding the origin of radio relics can help in understanding the role that shock waves have in the amplification of magnetic fields. We selected two clusters that are candidate to host two relics at their periphery: Abell 1240 and Abell 2345 and obtained VLA observations at 20 and 90 cm. We performed spectral index and polarization analysis and compared our results with expectations from theoretical models. The presence of double relics in these two cluster is confirmed by these new observations. The double relics in Abell 1240 show radio morphology, spectral index and polarization values in agreement with "outgoing merger shocks" models. One of the relics of Abell 2345, shows a peculiar morphology and spectral index profile, that are difficult to reconcile with present scenarios. We suggest a possible origin for this peculiar source.

*Bonafede et al. 2009, A&A, 494,429.

6.2 Radio relics and shock waves

Particularly interesting would be to explore the connection between merger shock waves and clusters with double relics, *i.e.* clusters hosting two relic radio sources located in the peripheral region and symmetric with respect to the cluster center. So far, a very small number of clusters with two double relics has been found. One of them is Abell 3667 (Röttgering et al. 1997; Johnston-Hollitt et al. 2002). Here, the cluster X-ray emission shows an elongated shape, interpreted as the merger axis of two sub-clusters, and relics are displaced symmetrically and perpendicular to the main axis. The X-ray, optical, and radio properties have been reproduced by a numerical simulation of a merger between clusters with mass ratio of 0.2 by Roettiger et al. (1999). We note, however, that not all of the predictions made by such simulations have been tested with available data. Apart from Abell 3667, double relics have been observed in Abell 3376 (Bagchi et al. 2006, Fig. 1.3) and interpreted as "Outgoing merger shock waves". Double relics have also been observed in RXCJ 1314.4-2515 (Feretti et al. 2005; Venturi et al. 2007), but no detailed study of the relic formation has been performed on this cluster so far. Two more candidates for hosting double relics are Abell 2345 (Giovannini et al. 1999) and Abell 1240 (Kempner & Sarazin 2001).

Spectral index analysis of both radio relics in the same cluster have not been performed so far. In Abell 3667, the spectral index image has been obtained for only one of the two relics, and no spectral index information are available for relics in Abell 3376. Only integrated spectral index information is available for the relics in RXCJ 1314.4-2515. Studying the spectral index and the polarization properties of relics offers a powerful tool for investigating the connection between double relics and outgoing shock waves originating in a merger event. In fact, theoretical models and numerical simulations make clear predictions on the relic spectral index trend and magnetic field properties (see Ensslin et al. 1998; Roettiger et al. 1999; Hoeft & Brüggen 2007).

Table 6.1: VLA observations

Source	RA (J2000)	DEC (J2000)	ν (MHz)	$\Delta\nu$ (MHz)	Conf.	Date	ToS (h)
Abell 2345	21 27 12.0	-12 10 30.0	325	3.125	B	16-AUG-2006	2.0
			325	3.125	C	08-DEC-2006	5.4
Abell 1240	11 23 37.0	43 05 15.0	325	3.125	B	05-AUG-2006	2.6
			325	3.125	C	08-DEC-2006	4.7
Abell 2345-1	21 26 43.0	-12 07 50.0	1425	50	C	08-DEC-2006	1.9
	21 26 43.0	-12 07 50.0	1425	50	D	09-APR-2007	1.0
Abell 2345-2	21 27 36.0	-12 11 25.0	1425	50	C	08-DEC-2006	2.0
	21 27 36.0	-12 11 25.0	1425	50	D	09-APR-2007	1.0
Abell 1240-1	11 23 25.0	43 10 30.0	1425	50	C	08-DEC-2006	1.8
	11 23 25.0	43 10 30.0	1425	50	D	12-APR-2007	1.0
Abell 1240-2	11 23 50.0	43 00 20.0	1425	50	C	08-DEC-2006	1.9
	11 23 50.0	43 00 20.0	1425	50	D	12-APR-2007	1.0
Abell 2345	21 26 57.2	-12 12 49	1490	50	AnB	02-NOV-1991	0.1

Col. 1: Source name; Col. 2, Col. 3: Pointing position (RA, DEC); Col. 4: Observing frequency;
Col 5: Observing bandwidth; Col. 6: VLA configuration; Col. 7: Dates of observation; Col. 8: Net time on source.

6.3 VLA radio observations

6.3.1 Total intensity data reduction

Observations were performed at the Very Large Array (VLA) at 20 cm in the C and D configuration and at 90 cm in the B and C configuration, to obtain the same spatial frequency coverage in the UV plane. Observations details are given in Table 6.1.

Observations at 20 cm (1.4 GHz) were pointed separately on the two relics in both of the clusters because of the smaller full width at half power of the primary beam. Observations of the cluster Abell 1240 were calibrated using the source 3C286 as the primary flux density calibrator[1]. The source 1156+314 was observed at intervals of about 30 min and used as phase calibrator. Observations of Abell 2345 were calibrated using the sources 3C48 as the primary flux density calibrator. Phase calibration was performed by observing the source 2137-207 at intervals of $\sim$ 30 min. We performed standard calibration using the NRAO Astronomical Imaging Processing Systems (*AIPS*). Cycles of phase self-calibration were performed to refine antennas phase solutions, followed by a final amplitude and gain self-calibration cycle.

In addition we recovered from the VLA data archive a short observation performed

[1]we refer to the flux density scale by Baars & Martin (1990)

with AnB array. The source 3C48 was used as primary flux density calibrator and the source 2121+053 was used as phase calibrator. We reduced and calibrated these data as explained above, and details are given in Table 6.1.

Observations at 90 cm (325 MHz) were performed in the spectral line mode, using 32 channels with 3.127 MHz bandwidth. This observing method avoids part of the VLA internal electronics interferences and allows us to remove radio frequency interferences (RFI) accurately. This also reduces bandwidth smearing, which is quite strong at low frequencies. Primary flux density and phase calibrators were the same sources as used in 1.4 GHz observations. Both 3C48 and 3C286 were also used for bandpass calibration. RFI are particularly strong at low radio frequency, so that an accurate editing was done channel by channel, resulting in a consistent flag of data. This in conjunction with bad data coming from EVLA antennas, results in a loss of ~ 40 % of observing time. We calibrated data following the "Suggestions for P band data reduction" by Owen et al. (2004). Afterwords the initial bandpass calibration channels from 1 to 4 and from 28 to 32 were flagged because of the roll-off of the bandpass. In the imaging procedure data were averaged to 8 channels. Imaging was done using the wide-field imaging technique to correct for non complanarity effects over a wide field of view. Twenty-five facets covering the main lobe of the primary beam were used in the cleaning and phase-self calibration processes. We also searched in the NVSS data archive for sources stronger than 0.5 Jy over a radius as large as 10°. These sources were included in the initial cleaning and self calibration steps.

Each (u,v) data set at the same frequency (but observed with different configurations) was calibrated, reduced, and imaged separately and then combined to produce the final images. Images resulting from the separate pointed observations at 1.4 GHz were then linearly combined to obtain a single image. We combined the data set and produced images at higher and lower resolutions (herein after HR images and LR images) giving uniform and natural weight to the data. For the purposes of the spectral analysis, the final images at 325 MHz and 1.4 GHz, were restored with the same beam (reported in Table 6.2 and 6.3) and corrected for the primary beam effects.

Table 6.2: Abell 2345

Source name	ν MHz	θ arcsec	σ_I mJy/beam	Fig.
Abell 2345-1 HR	1425	37 X 20	0.08	
Abell 2345-1 LR	1425	50 X 38	0.09	6.2, central panel
Abell 2345-2 HR	1425	37 X 20	0.09	
Abell 2345-2 LR	1425	50 X 38	0.09	6.2, central panel
Abell 2345 HR	325	37 X 20	1.7	
Abell 2345 LR	325	50 X 38	2.0	6.2, right panels
Abell 2345	1490	6X6	0.13	6.1, central panel

Col. 1: Source name; Col. 2: Observation frequency;

Col. 3: Restoring beam; Col. 4: RMS noise of the final images;

Col 5: Figure of merit.

Table 6.3: Abell 1240

Source name	ν MHz	θ arcsec	σ_I mJy/beam	Fig.
Abell 1240-1 HR	1425	22 X 18	0.04	6.6
Abell 1240-1 LR	1425	42 X 33	0.04	6.7,central panel
Abell 1240-2 HR	1425	22 X 18	0.04	6.6
Abell 1240-2 LR	1425	42 X 33	0.05	6.7, central panel
Abell 1240 HR	325	22 X 18	0.9	
Abell 1240 LR	325	42 X 33	1.0	6.7, left panels

Col. 1: Source name; Col. 2: Observation frequency;

Col. 3: Restoring beam; Col. 4: RMS noise of the final images;

Col. 5: Fig. of merit.

6.3.2 Polarization intensity data reduction

Observations at 20 cm (1.425 GHz) include full polarization information. Polarization data observed with the D array are not usable because of the bad quality of data of the polarization calibrator. The absolute polarization position angle was calibrated by observing 3C286 for both clusters in C configuration. The instrumental polarization of the antennas was corrected using the source 1156+314 for Abell 1240 and the source 2137-207 for Abell 2345.

Stokes parameters U and Q images were obtained. We then derived the polarization intensity image ($P = \sqrt{U^2 + Q^2}$), the polarization angle image ($\Psi = \frac{1}{2} arctan \frac{U}{Q}$) and the fractional polarization image ($FPOL = \frac{P}{I}$), with I the total intensity image. More details are given in Table 6.4.

Table 6.4: Total and polarization intensity radio images at 1425 MHz

Source name	θ arcsec	σ_I (mJy/beam)	$\sigma_{Q,U}$ (mJy/beam)	Fig.
Abell 2345-1	23 X 16	0.05	0.02	6.5, right panel
Abell 2345-2	23 X 16	0.07	0.02	6.5, left panel
Abell 1240-1	18 X 17	0.04	0.02	6.10, top panel
Abell 1240-2	18 X 17	0.04	0.01	6.10, bottom panel

Col. 1: Source name; Col. 2: Restoring beam;

Col. 4: RMS noise of the I image;

Col 5: RMS noise of the Q and U images

Col 6: Figure of merit.

Table 6.5: Abell 2345 and Abell 1240 properties

Source name	RA (J2000)	DEC (J2000)	z	scale (kpc/″)	F_X 10^{-12} erg/s/cm^2	L_X 10^{44} erg/s
Abell 2345	21 27 11.00	-12 09 33.0	0.1765	2.957	5.3	4.3
Abell 1240	11 23 32.10	43 06 32	0.1590	2.715	1.3	1.0

Col. 1: Source name; Col. 2, Col. 3: Cluster X-ray centre (RA, DEC);

Col 4: Cluster redshift; Col 5: arcsec to kpc conversion scale;

Col 6: Flux in the 0.1- 2.4 keV band (Abell 2345) and in the 0.5-2 keV (Abell 1249);

Col 7: X-ray cluster luminosity in the 0.1-2.4 keV band (Abell 2345) and in the 0.5-2 keV (Abell 1240);

Data from Böhringer et al. (2004) for Abell 2345

and from David et al. (1999) for Abell 1240, corrected for the adopted cosmology.

6.4 The Cluster Abell 2345

Optical information is available for this cluster, while little is known about its X-ray emission. General data are reported in Table 6.5. Weak gravitational lensing analysis has been performed by Dahle et al. (2002) and by Cypriano et al. (2004). Optical data cover the inner part of the cluster ($\sim 3' \times 3'$). They find that this cluster has a well-defined core dominated by a cD galaxy, and both the light and galaxy number density distributions have several peaks close to the central galaxy. The authors find that the projected mass distribution has the most prominent peak displaced from the central cD by $\sim 1.5'$, although a secondary peak is closer to the central cD. No information about the possible presence of a cooling flow associated with this galaxy is present in the literature. Dahle et al. (2002) conclude from their analysis that the cluster may be a dynamically young system. Cypriano et al. (2004) report the mass distribution derived from weak lensing analysis and find that the best fit to their data is a singular isothermal ellipsoid with the main axis oriented in the EW direction.

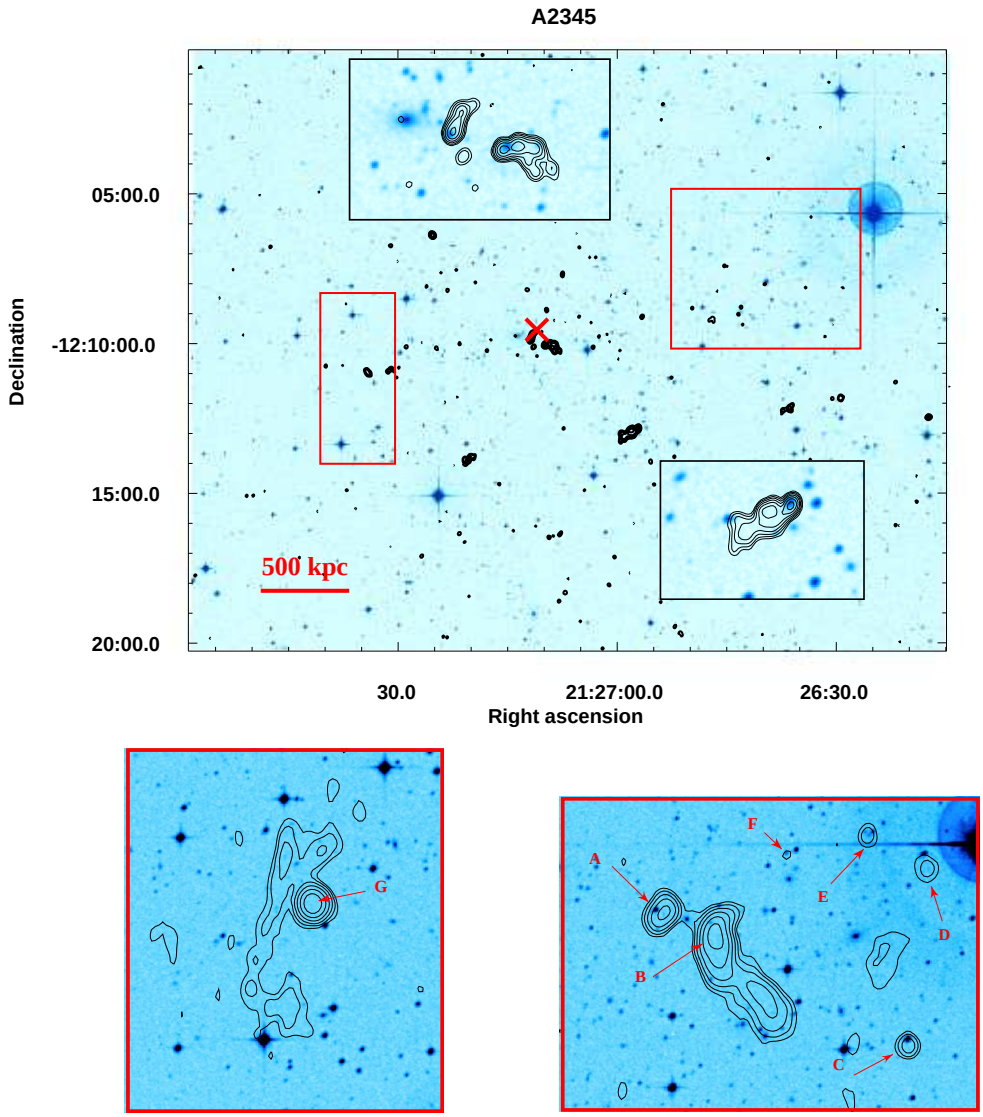

Figure 6.1: The cluster Abell 2345. In the center: DPOSSII optical emission (red band) in colors overlaid onto radio contours at 1.490 GHz. First contours are ± 0.4 mJy/beam, and they are then spaced by a factor 2. The beam in 6″×6″. Top inset shows the zoomed images of the central sources: the central cD galaxy and two radio galaxies are visible. Bottom inset shows the zoomed image of the southern radio source. Red boxes mark the region of the relics, completely resolved in the high-resolution image. In the left and right panels zoomed image of the red boxes is shown. Here colors represent the optical DPOSSII emission, while contours represent the relic radio emission at the resolution of 23″×16″. The relic A2345-1 is visible in the right panel, while A2345-2 is in the left panel. Contours start at ±0.15mJy/beam and are spaced by a factor 2. Red arrows indicate the position of the discrete sources embedded in the relic emission.

The radio emission of Abell 2345 is characterized by the presence of two relics

visible in the NVSS (Giovannini et al. 1999). Our new VLA observations confirm the presence of two regions where non-thermal emission is present at the cluster periphery, nearly symmetrical with respect to the cluster center. These new observations, together with the archive data, allow study of the cluster radio emission in a wide range of resolutions going from $\sim 6''$ to $\sim 50''$. Therefore, it is possible to separate the contribution of discrete sources whose emission is not related to the relic's physical properties. In Fig. 6.1 the radio emission of Abell 2345 at $6''$ resolution is shown overlaid onto the optical emission (taken from the Digitalized Palomar Sky Survey II, red band). Two central radio-tail sources are associated with optical galaxies in the cluster center. The central cD is visible in the optical image. Relics are not visible in this image because of the lack of short baselines. This confirms that the emission detected in lower resolution observations is indeed extended, and it is not due to the blending of discrete sources. In the same figure we also report the radio relic emission as detected by C array observations. The western relic (Abell 2345-1) is located at $\sim$ 1 Mpc from the cluster X-ray center, while the eastern relic (Abell 2345-2) is $\sim$ 890 kpc far from the cluster center (see Table 6.6).

There are several discrete sources close to the western relic, A2345-1, visible in the 1.4 GHz image. They are labeled with letters from A to F in the right panel of Fig.6.1. The sources A, C, D, E, and F could be associated with the optical galaxies visible in the DPOSSII image, whereas B does not have any obvious optical identification. Optical emission is present at $35''$ in the NE direction from the radio peak. This is greater than the error associated with the beam, that is only $6''\times 6''$ in the highest resolution image. We can then conclude that no optical counterpart of the B radio source is detected in the DPOSSII image. The sources D E and F are not visible in the 325 MHz image (see Fig. 6.2, top left panel). This is consistent with a radio source having a spectral index < 1.2[2]. There is only one discrete source near the relic A2345-2, labeled with G in the Fig.6.1 without any obvious optical identification. This source is also detected in the higher resolution image.

The whole extension of the relics is properly revealed by LR images (Fig. 6.2). The morphology of the relics is similar at 1.4 GHz and 325 MHz, although only the brightest regions can be seen at 325 MHz due to the higher rms noise level of these

[2]The spectral index α is derived according to $S_\nu \propto \nu^{-\alpha}$.

observations with respect to the 1.4 GHz ones. The total flux of the relics at the 2 frequencies, excluding the contribution of the discrete sources, are reported in Table 6.6, where the main physical parameters are summarized.
The relic A2345-1 shows an elongated shape at high resolution, while at lower resolution it shows a weaker wide emission extending in the western direction, *i.e.* toward the cluster outskirts. We note that this circular filamentary morphology is not seen in other double relic sources.

6.4.1 Spectral index analysis

We derived the spectral index image of the cluster's relics comparing the LR images at 1.4 GHz and 325 MHz. The rms noise of the images are reported in Table 6.2. Spectral index and spectral index noise images are shown in Fig. 6.2. They were obtained by considering only pixels whose brightness is $> 3\sigma$ at both frequencies. We note that relics are more extended at 1.4 GHz than at 325 MHz. This can be due to the different sensitivities at 1.4 GHz and 325 MHz. Confusion and RFI strongly affect the low-frequency image, where the noise level is significantly higher than the thermal noise. A consistent spectral index analysis has to consider the different extension at the two frequencies. In fact, as already pointed out by Orrú et al. (2007), if we compute spectral index analysis considering only regions that have a signal-to-noise ratio > 3 at both frequencies, we introduce a bias, since we are excluding a priori low spectral index regions, whose emission cannot be detected at 325 MHz. For instance, the relic A2345-1 radio brightness at 1.4 GHz decreases as the distance from the cluster center increases. The fainter region could be detected in the 325 MHz image only if its spectral index, α, were steeper than $\sim$1.8.
In both of the relics the spectral index is patchy. The spectral index rms is $\sigma_{spix} \sim$ 0.4 while the mean spectral index noise is $\langle Err_{spix} \rangle$ 0.1 for both relics. Thus, by comparing these two quantities, we can conclude that spectral index features are statistically significant.
Our aim here is to investigate whether there is a systematic variation in the relic spectral index with distance from the cluster center as found in other radio relics (*e.g.* 1253+275 by Giovannini et al. 1991; Abell 3667 by Röttgering et al. 1997; Abell 2744 by Orrú et al. 2007; Abell 2255 by Pizzo et al. 2008; Abell 521 by

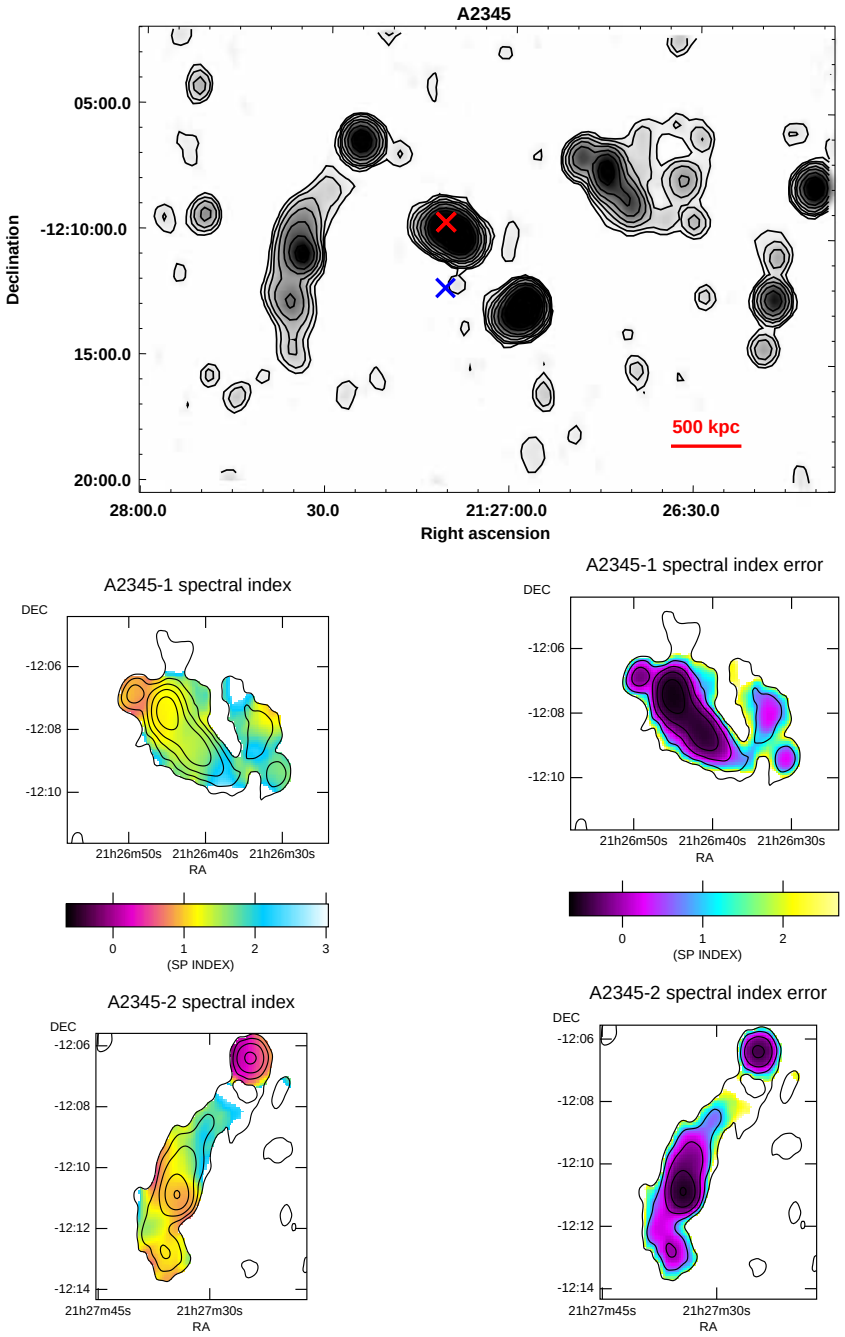

Figure 6.2: Top: the cluster Abell 2345 radio emission at 1.4 GHz. The beam is $50'' \times 38''$. Contours start at 3 σ (0.24 mJy/beam) and are then spaced by a factor 2. The cross marks the X-ray cluster center. Bottom: in the left panel colors represent the spectral index of the relic A2345-1 (top) and A2345-2 (bottom) superimposed over the radio emission at 325 MHz (contours). The beam is $50'' \times 38''$, contours start at 3σ (6 mJy/beam) and are then spaced by a factor 2. In the bottom right panel : Spectral index error image (colors) superimposed onto the emission at 325 MHz (contours are as above).

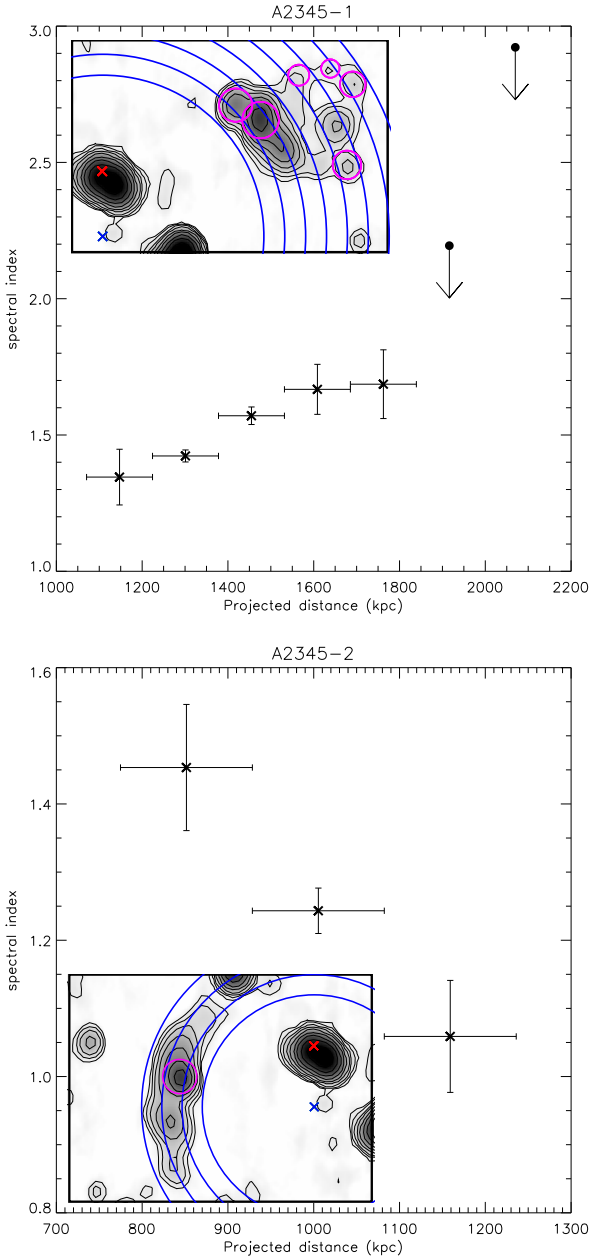

Figure 6.3: Spectral index radial trend of A2345-1 (top) and A2345-2 (bottom), computed in shells of $\sim 50''$ in width. It was computed excluding the contribution of the discrete sources. Crosses refer to spectral index values computed in shells where the mean brightness is $> 3\sigma$ at both 325 MHz and 1.4 GHz. Arrows are 3σ upper limits on the spectral index mean value (see text). The red cross refers to the cluster X-ray center, the blue cross refers to the center of the spherical shells. In the insets: displacement of the shells over which the mean spectral index were computed. Circles refer to the discrete sources embedded in the relic emission. The red cross refers to the cluster X-ray center, the blue cross is the center of the spherical shells.

Giacintucci et al. 2008).

To properly obtain the radial trend of the spectral index, we integrated the radio brightness at 325 MHz and 1.4 GHz in radial shells of $\sim 50''$ in width wherever the 1.4 GHz brightness is $> 3\sigma$, and then we computed the value of the spectral index in each shell. We excluded the regions where discrete radio sources are embedded in the relic emission (see insets in Fig. 6.4). The shells were centered in the extrapolated curvature center of the relic A2345-2, that is $2.6'$ south the cluster X-ray center. Shells are then parallel to the relics main axis. We computed the integrated brightness in each shell at 20 and 90 cm , and calculated the associated error as $\sigma \times \sqrt{N_{beam}}$, where σ is the image rms noise, and N_{beam} the number of beams sampled in the shell. In those shells where the brightness is $> 3\sigma$ in the 1.4 GHz image but $< 3\sigma$ in the 325 MHz image, only upper limits on the mean spectral index can be derived. The spectral index profiles thus obtained are shown in Fig. 6.4. These plots show that the spectral index in the relic A2345-1 increases with distance from the cluster center, indicating a spectral steepening of the emitting particles. The spectral index in each shell is rather high, going from $\sim$1.4 in the inner rim to $\sim$1.7 in the central rim of the relic. The spectral index trend derived for the outer shells is consistent with further steepening. The spectral index of the relic A2345-2 instead shows a different trend, going from $\sim$1.4 in the inner shell to $\sim$1.1 in the outer rim (Fig. 6.4).

6.4.2 Radio-X-ray comparison

No X-ray studies are present in the literature for this cluster. X-ray observations in the energy band $0.1 - 2.4$ keV were retrieved by the ROSAT all-sky survey (RASS) data archive. The total exposure time is of $\sim$ 4 ksec. After background subtraction, the event file was divided by the exposure map. We smoothed the resulting image with a Gaussian of $\sigma = 60''$. The resulting image is shown in Fig. 6.4.

The X-ray emission of this cluster is elongated in the NW-SE direction. Two bright regions are visible at $\sim 10'$ and $14'$ in N-W direction from the cluster center (referred to as X1 and X2, respectively). The galaxy J21263466-1207214 (RA =21h26m34.6s, DEC= -12d07m22s, z=0.178221) is close to the first one. Another bright region is present at $\sim 4'$ south of the cluster center (X3).

Data presented here allow an interesting comparison among cluster emission at

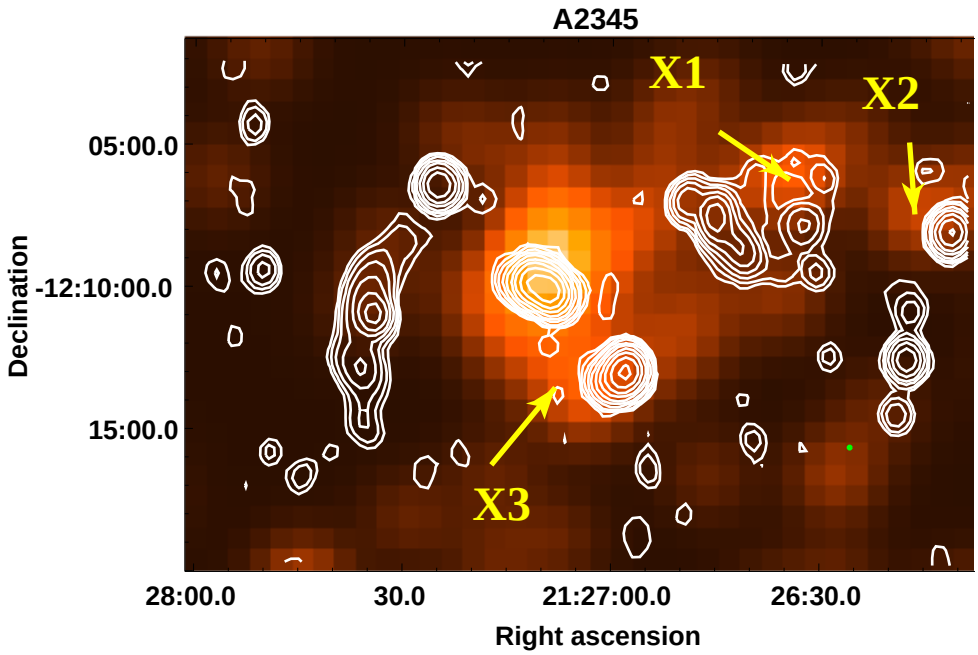

Figure 6.4: Abell 2345 X-ray emission (colors) in the energy band 0.1-2.4 keV from RASS. The image has been smoothed with a Gaussian of σ $\sim$60$''$; contours represent the radio image of the cluster at 1.4 GHz. The beam is 50$''\times$38$''$. Contours are 0.24 mJy/beam and are then spaced by a factor 2. Arrows mark the position of the X1 X2 and X3 regions.

different wavelengths. We note that mass distribution from weak lensing studies (Cypriano et al. 2004) is represented well by an ellipsoid with the major axis directed in the EW direction, and relics are found perpendicular to this axis. Consistently with the optical analysis, the X-ray emission is elongated in the NW-SE direction, indicating a possible merger along that direction, and relics are displaced perpendicular to that axis. In Fig. 6.4 the X-ray emission is superimposed onto radio contours. A2345-2 is located at the edge of the X-ray emission, as found in relics of Abell 3667 and A3376. A2345-1, instead, is located between eastern edge of the cluster and the X1 region, 10$'$ from Abell 2345 center, and its radio emission extends toward X1.

From the same figure, in the X3 region a narrow-angle tail radio galaxy is visible in radio images at every resolution (see Figs. 6.1 and 6.2). Although redshift is not available for this radio source, its structure favors a connection to the cluster and/or to the close X-ray peak. One possibility is that these X-ray multiple features are galaxy clumps interacting with Abell 2345.

Table 6.6: Abell 2345

Source name	Proj. dist kpc	LLS kpc	F_{20cm} mJy	F_{90cm} mJy	B_{eq} - B'_{eq} μG	$< \alpha >$
Abell 2345-1	340″=1000	390″= 1150	30.0±0.5	291± 4	1.0 -2.9	1.5±0.1
Abell 2345-2	300″=890	510″= 1500	29.0±0.4	188± 3	0.8 -2.2	1.3±0.1

Col. 1: Source name; Col. 2: projected distance from the X-ray centroid;

Col. 3: Largest linear scale measured on the 20 cm images.

Col. 4 and 5: Flux density at 20 and 90 cm;

Col. 6: equipartition magnetic field computed at fixed frequency - fixed energy (see Sec. 6.4.3);

Col. 7: mean spectral index in region where both 20 and 90 cm surface brightness is $> 3\ \sigma$

A self consistent scenario arises from this analysis, indicating that the cluster Abell 2345 could be undergoing multiple merger with X3 and X1 groups, and this could explain the peculiar properties of A2345-1. More sensitive and resolved X-ray observations in conjunction with optical studies are required to shed light on the connection between the radio emission of A2345, X1, X2, and X3.

6.4.3 Equipartition magnetic field

Under the assumption that a radio source is in a minimum energy conditions, it is possible to derive an average estimate of the magnetic field strength in the emitting volume (see Sec. 2.5). We assume that the magnetic field and relativistic particles fill the whole volume of the relics, and that energy content in protons and electrons is equal. We further assume that the volume of the relics is well represented by an ellipsoid having the major and minor axis equal to the largest and smallest linear scales visible in our images; we estimated the third axes to be the mean between the major and minor ones. The synchrotron luminosity is calculated from a low-frequency cut-off of 10 MHz to a high frequency cut-off of 10 GHz. The emitting particle energy distribution is assumed to be a power law in this frequency range ($N(E) \propto E^{-p}$), with $p = 2\alpha + 1$. We used the mean value of α =1.5 and 1.3 for A2345-1 and A2345-2, respectively, and found B_{eq} ∼1.0 μG in A2345-1, and 0.8 μG in A2345-2. These values are consistent with equipartition magnetic field found in other relics.

It has been pointed out by Brunetti et al. (1997) that synchrotron luminosity should be calculated in a fixed range of electron energies rather than in a fixed range of radio frequencies (see also Beck & Krause 2005). In fact, electron energy corresponding to a fixed frequency depends on the magnetic field value, and thus the integration

limits are variable in terms of the energy of the radiating particles. Given the power law of the radiating particles and the high value of the radio spectral index, the lower limit is particularly relevant here. We adopted a low energy cut off of γ_{min}=100 and assumed $\gamma_{max} >> \gamma_{min}$, obtaining $B'_{eq} \sim 2.9$ μG in A2345-1, and 2.2 μG in A2345-2. We derived the minimum nonthermal energy density in the relic sources from B'_{eq} obtaining U_{min} $\sim$8.1 and 4.3 10^{-13}erg/cm^{-3} for A2345-1 and A2345-2. The corresponding minimum non-thermal pressure is then $\sim$5.0 and 2.7 10^{-13}erg/cm^{-3}. We are aware that the extrapolation to low energies or frequencies could overestimate the number of low-energy electrons, leading to overestimating the equipartition magnetic field if a spectral curvature is present. We note that a detailed study of the radio spectrum on a wide frequency range is available for three peripheral relics: the one in Abell 786, in the Coma cluster (see Giovannini & Feretti, 2004 and references therein) and in Abell 521 (Giacintucci et al. 2008). In these relics a straight steep radio spectrum is observed. We also note that a low-frequency cut-off of 10 MHz and a magnetic field of $\sim$1μG imply a low-energy cut-off of γ_{min} $\sim$1500. Thus, if the spectrum of the emitting particles is truncated at γ >1500, both B'_{eq} and B_{eq} could overestimate the magnetic field strength. Future low-frequency radio interferometers such as LOFAR and after LWA ans SKA will likely shed light on this point. On the other hand, it is possible to derive an independent estimate of the magnetic field from X-ray flux due to inverse Compton scattering of CMB photons by relativistic electrons in the relic source. These studies have so far been performed on a small number of radio relics and have led to lower limits on the magnetic field strength: B >0.8μG in the relic 1140+203 of Abell 1367 (Henriksen & Mushotzky 2001); B >1.05μG in 1253+275 of the Coma cluster (Feretti & Neumann 2006); B >0.8μG in 0917+75 in Rood27 cluster (Chen et al. 2008); and B >2.2μG in the relic 1401-33 in the Abell S753 cluster (Chen et al. 2008). In these cases, the lower limits derived from IC arguments are consistent with equipartition estimates, thus indicating that the equipartition value could be used as a reasonable approximations of the magnetic field strength in relics.

6.4.4 Polarization analysis

Another important set of information about the magnetic field in the relics can be derived through the study of polarized emission. As previously mentioned, we could

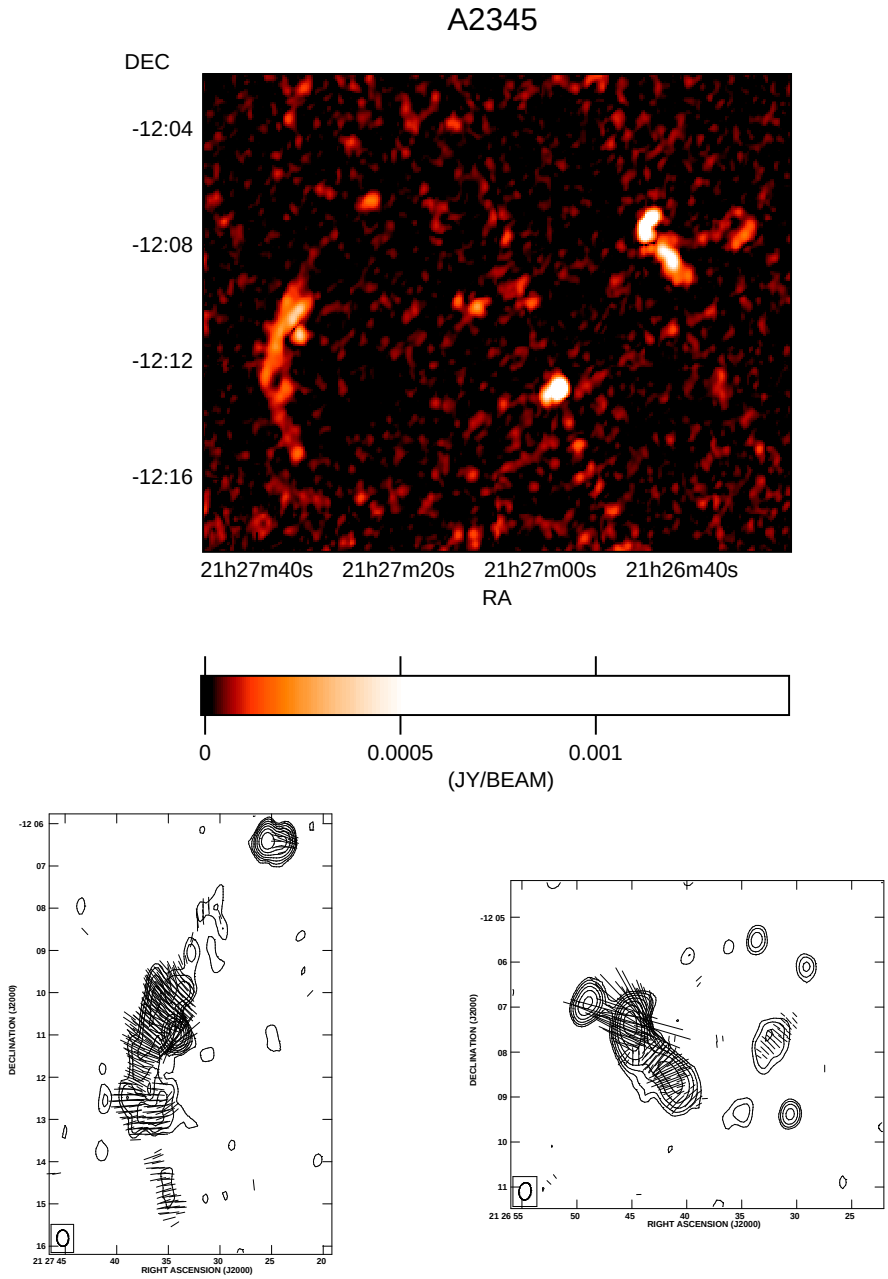

Figure 6.5: Abell 2345: Polarized emission of Abell 2345 at 1,4 GHz. In the top panel the polarized radio emission at 1.4 GHz is shown. The restoring beam is $23'' \times 16''$. Bottom: in the left and right panels contours refer to the radio image Abell 2345-2 and Abell 2345-1 (see Table 6.4 for details) respectively. Contours start from 3σ and are spaced by a factor 2. E vectors are superimposed: line orientation indicates the direction of the E field, while line length is proportional to the polarization intensity (Left panel: $1''$ corresponds to 5.5 μJy/beam; Right panel: $1''$ corresponds to 10 μJy/beam)

calibrate polarization only for observations at 1.4 GHz with the C array. The P radio image of the cluster is shown in Fig. 6.5. The noise achieved in the P, Q, and

U images (Table 6.4) are lower than those obtained in the total intensity image. In fact, total intensity images are affected by dynamical range limitation due to the presence of powerful radio sources near our target. These sources are not strongly polarized, so that P images are not affected by such limitation, and weaker polarized emission can be revealed. We note in fact that polarized radio emission of the relic A2345-2 reveals an arc-like structure that is more extended than in total intensity emission. The arc-like structure of this relic indicates that the shock wave, possibly responsible for the radio emission, has been originated $\sim 2.6'$ southern the present X-ray center.

The mean fractional polarization is $\sim 22\%$ in A2345-2, reaching values up to 50% in the eastern region. The relic A2345-1 shows a mean fractional polarization of $\sim 14\%$ with higher polarized region ($\sim 60\%$) in the northwestern part of the relic. The amount of fractional polarization allows us to estimate the level of order of the magnetic field in the source. Following Burn (1966), if we assume that the magnetic field is composed of an ordered component $\mathbf{B_o}$ plus a random isotropic component represented by a Gaussian with variance equal to $2/3B_r^2$, the ratio (B_r^2/B_o^2) can be derived by the ratio P_{oss}/P_{intr} (see Sec. 2.6.2 and Eq. 2.20). where P_{oss} is the observed fractional polarization, and P_i is given by Eq. 2.17. For the relic A2345-1, we obtain $B_r^2/B_o^2 \sim 4$, meaning that the magnetic energy density in the random component is four times higher than the one in the ordered component. For the relic A2345-2, instead, we obtain $B_r^2/B_o^2 \sim 2$. This indicates that the magnetic field in the region of the relic A2345-2 has a higher degree of order. We also have to consider possible beam depolarization, internal depolarization, and ICM depolarization, so that what we can conclude from this analysis is $B_r^2/B_o^2 < 4$ and < 2 in A2345-1 and A2345-2, respectively.

In A2345-1 the magnetic field is mainly aligned with the sharp edge of the radio emission, *i.e.* in the SW-NE direction. In the northern part of the relic, the E vectors rotate and in the NW part they are almost aligned toward the SW-NE direction. In A2345-2 the E vectors are perpendicular to the relic major axis, following the arc-like structure that is marginally visible in the total intensity image.

6.4.5 Results for Abell 2345

The presented analysis confirms that nonthermal emission is associated with the ICM of Abell 2345.

- The properties of the western relic, A2345-1 are quite peculiar. Indeed, its morphology is rather circular and filamentary, its brightness distribution is higher in the inner region of the relic, and its spectral index steepens toward the cluster periphery. Although the statistic is really poor, these features have not been found in other double relics so far. The level of polarization, the magnetic field direction mainly aligned with the sharp edge of the radio emission, and the value of the equipartition magnetic field instead agrees with other observed relics.

  Diffusive shock acceleration models predict a steepening of the radio spectrum towards the cluster center (*e.g.* Ensslin et al. 1998; Hoeft & Brüggen 2007) as a consequence of the electron energy losses after shock acceleration. It is worth mentioning here that theoretical predictions rely on some assumptions about the shock symmetry and the magnetic field structure that could be not representative of this specific cluster environment. Moreover, if the relic is not seen edge on, projection effects could further complicate the observed radio emission. Taking all of these into account, the observed spectral index trend of A2345-1 cannot be used as an argument to exclude an outgoing shock wave. We do, however, note that the position of A2345-1 is in between the main cluster and the possibly merging group X1. Thus we suggest the possibility that its radio properties could be affected by this ongoing merger. In particular, if the relic is seen edge on, and if the magnetic field strength is almost uniform in the relic region, the observed spectral index trend could be the sign of a shock wave moving inward, toward the cluster center. It could result from the interaction with X1. Detailed optical and X-ray observations would be needed to shed light on this point.

- The relic A2345-2 shows the classical feature of "elongated relic sources" also found in double relics of Abell 3667 and Abell 3376, as well as in single relic sources as 1253+275 (Andernach et al. 1984; Giovannini et al. 1991) and

A521 (Ferrari 2003; Giacintucci et al. 2008). It is located far from the cluster center, its spectral index is steep with mean value ~ 1.3 and steepens towards the cluster center, as expected by relic formation theories if the relic is observed edge on. The value of the equipartition magnetic field, the direction of the E vectors, and the detected level of polarization are consistent with previous observations of elongated relics and agree with expectations from theoretical models as well. The polarized emission image reveals the arc-like structure of the relic A2345-2. If we assume that the relic originated in a spherical shock wave, we can infer the propagation center of the shock by extrapolating the curvature radius of the relic. It turns out that the propagation center is $\sim 2.6'$, south of the present X-ray center of the cluster Abell 2345 (see Fig. 6.4).

This corresponds to a physical distance of 450 kpc at this redshift. From weak lensing analysis the galaxy velocity dispersion in this cluster results $\sim$900 km/s (Dahle et al. 2002; Cypriano et al. 2004). As we will see in Sect.6.6, the expected Mach number is of about 2.2 for this relic. Since the galaxy velocity dispersion is comparable to the sound speed in the ICM (see *e.g.* Sarazin 1988), a Mach number 2.2 corresponds to a velocity of $\sim$2000 km/s. The relic A2345-2 is $\sim$800 kpc far from the spherical-shock center. A shock wave with $M \sim 2.2$ travels this distance in ~ 0.4 Gyr (if the shock speed remains constant). Thus the merging between the two substructures should have occurred at $\sim$ 1200 km/s to explain the shift of the X-ray center in this scenario. This is a reasonable value for the cluster merger velocity.

Although a precise estimate should consider the amount of energy injected in the ICM as the shock wave passes through it, and despite the number of assumptions and approximations, we suggest that the relic indicates the position of the merger center as it was ~ 0.4 Gy ago. The time that the shock wave has taken to get the present relic position is the time that the sub-cluster has taken to get the current X-ray center position.

6.5 The Cluster Abell 1240

Little is known in the literature about this cluster. It is a rich cluster classified as Bautz-Morgan type III. In Table 6.5, general data about this cluster are reported.

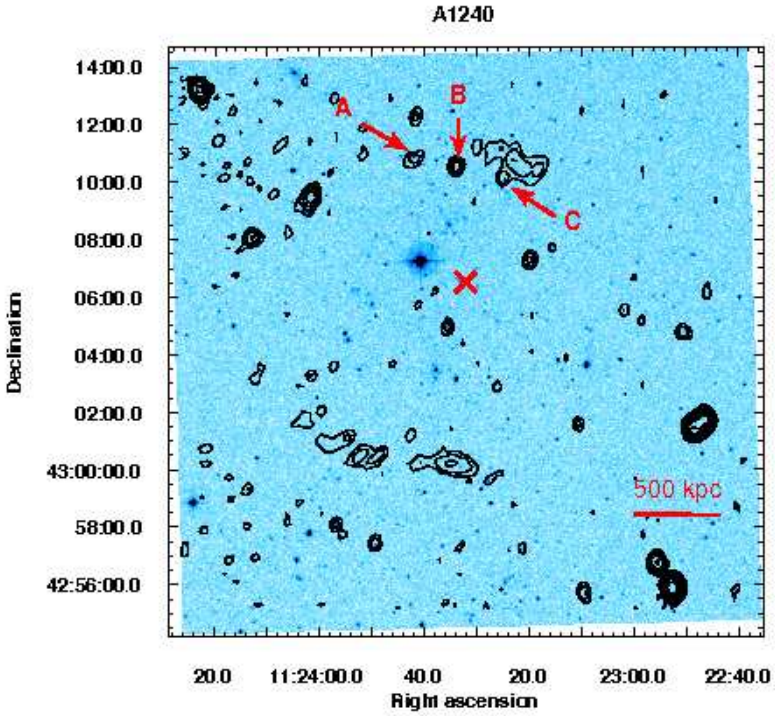

Figure 6.6: Abell 1240. Colors: Optical emission from DPOSSII (red band); Contours: radio emission at 1.4 GHz (HR image). Contours start at $\pm 3\sigma$ and are then spaced by 2. Red cross signs the X-ray center, labels refer to the discrete sources embedded in A1240-1.

Kempner & Sarazin (2001) have revealed the presence of two roughly symmetric relics from the Westerbork Northern Sky Survey (WENSS). From WENSS images, relics are visible at 2 and 2.5 σ level. Our VLA observation confirm the presence of two weak radio-emitting regions in the cluster's outskirts. The radio image of the cluster is shown in Fig. 6.6 (contours) overlaid on optical emission (from the DPOSSII, red band). The northern relic (A1240-1) is located at $\sim 270''$ from the cluster X-ray center. This distance corresponds to ~ 700 kpc at the cluster's redshift. This relic is mainly elongated in the EW direction, and its radio brightness decreases going from the western to the eastern parts of the relic (see Fig. 6.7). At 325 MHz, only the eastern brightest part is visible. This is likely due to the higher noise in the 325 MHz image. In fact from the mean brightness of the weaker part of the relic, we estimated that it should have a spectral index >3 to be detected at 325 MHz. Three radio sources are embedded in the relic emission, and are labeled with A, B, and C in Fig. 6.6. The sources A and B are not detected in the 325 MHz observations. This is consistent with spectral index values <1, as commonly found in radiogalaxies. A weak emission at 1.4 GHz links the A radio source at the relic

(see Fig. 6.7).
The southern relic (A1240-2) is located at $\sim 400''$ (1.1 Mpc) from the cluster X ray center. At 1.4 GHz, it is elongated in the EW direction extending $\sim 480''$. No discrete sources have been found embedded in the relic emission. Also in this case at 325 MHz, the relic's extension is reduced to $\sim 350''$ along the main axis, and only the brightest regions are visible at 325 MHz. The relic's physical parameters are reported in Table 6.7. The quantity are computed excluding the region where discrete sources (A,B, and C) are present.

6.5.1 Spectral index analysis

We report in Fig.6.7 the spectral index map and the spectral index map error for the relics of Abell 1240. They were obtained considering only those pixels that have a brightness $>2\sigma$ at both frequencies. Figure 6.7 shows that the spectral index image is patchy. The spectral index image rms, σ_{spix}, is ~ 0.3 and 0.4 for A1240-1 and A1240-2, respectively, while the mean of the spectral index error image, $\langle Err_{spix} \rangle$ is ~ 0.2 for both of the relics. We can then conclude that features in A1240-2 are statistically significant, while given the small difference between σ_{spix} and $\langle Err_{spix} \rangle$ in A1240-1, we cannot exclude that local features are a noise artifact in this case. In the relic A1240-2 a gradient is visible along the main axis of the relic, as found in Abell 2256 by Clarke & Ensslin (2006).
In Fig. 6.8 the radial spectral index trend is shown for A1240-1 and A1240-2. They were obtained as described in Sect. 6.4.1. Spherical shells are centered close to the X-ray cluster center and are parallel to the main axis of both relics.
Despite the small extension of the relics at 325 MHZ, it is still possible to derive some important results on the spectral index radial trends in these relics: in the relic A1240-1 the spectral index is steeper in the inner part of the relic and flatter in the outer part, as found in A2345-2 and predicted by "outgoing merger shock" models if relics are seen edge on (Roettiger et al. 1999; Bagchi et al. 2006). The same trend is consistent with the spectral index profile derived in A1240-2, although a firm conclusion cannot be derived from these data. We note, in fact, that errors and upper limit in the inner shell cannot exclude a constant spectral index or even an opposite trend.

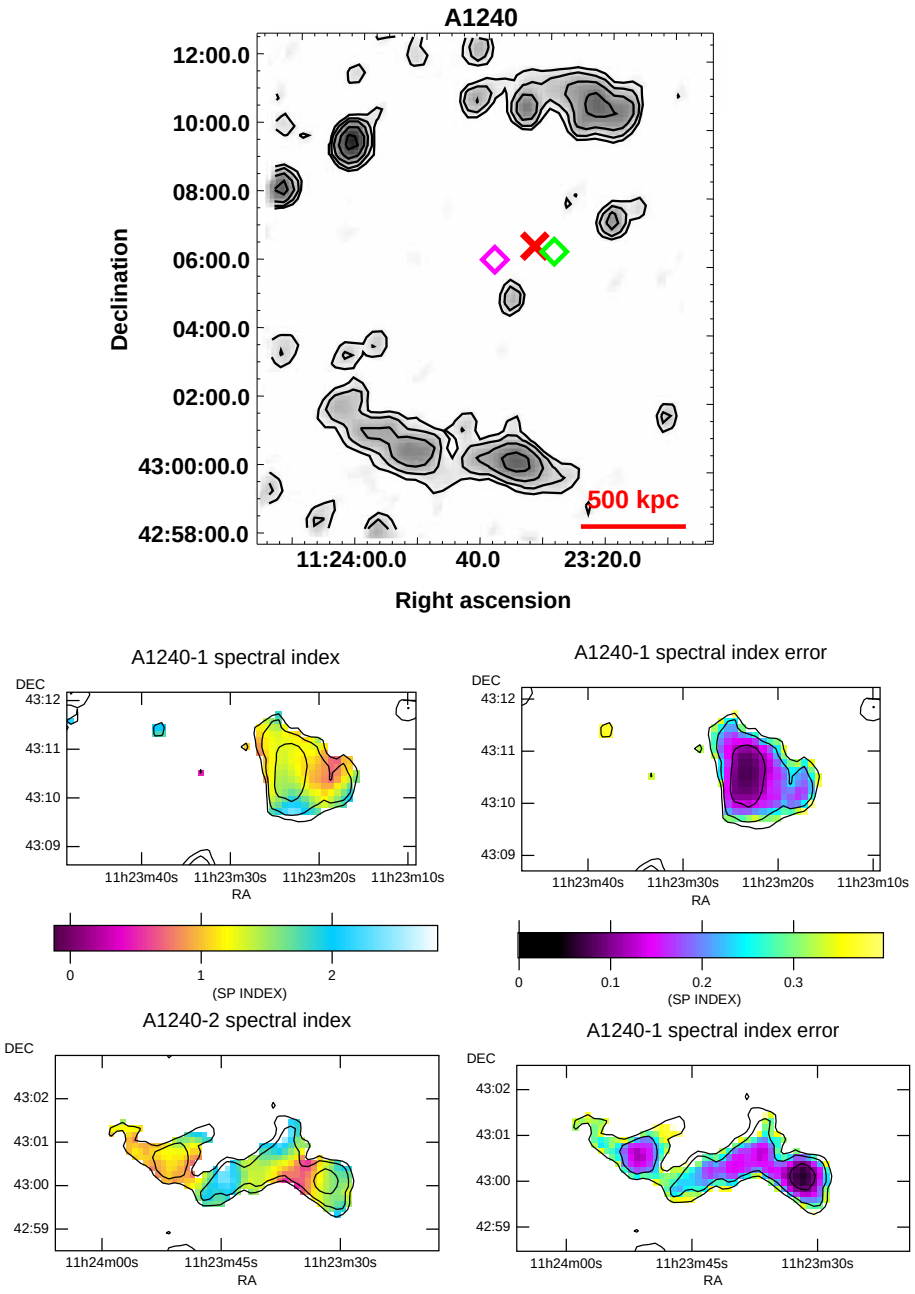

Figure 6.7: Top: the cluster Abell 1240 radio emission at 1.4 GHz. The beam is $42'' \times 33''$. Contours start at 3σ (0.13 mJy/beam) and are then spaced by a factor 2. The cross marks the cluster X-ray center. Bottom left: colors represent the spectral index of the relic A1240-1 (top) and A1240-2 (bottom) superimposed over the radio emission at 325 MHz (contours) The beam is $42'' \times 33''$, first contours are 2 σ (2 mJy/beam), 3σ and are then spaced by a factor 2. Bottom right: Spectral index error image (colors) superimposed onto the emission at 325 MHz (contours are as above).

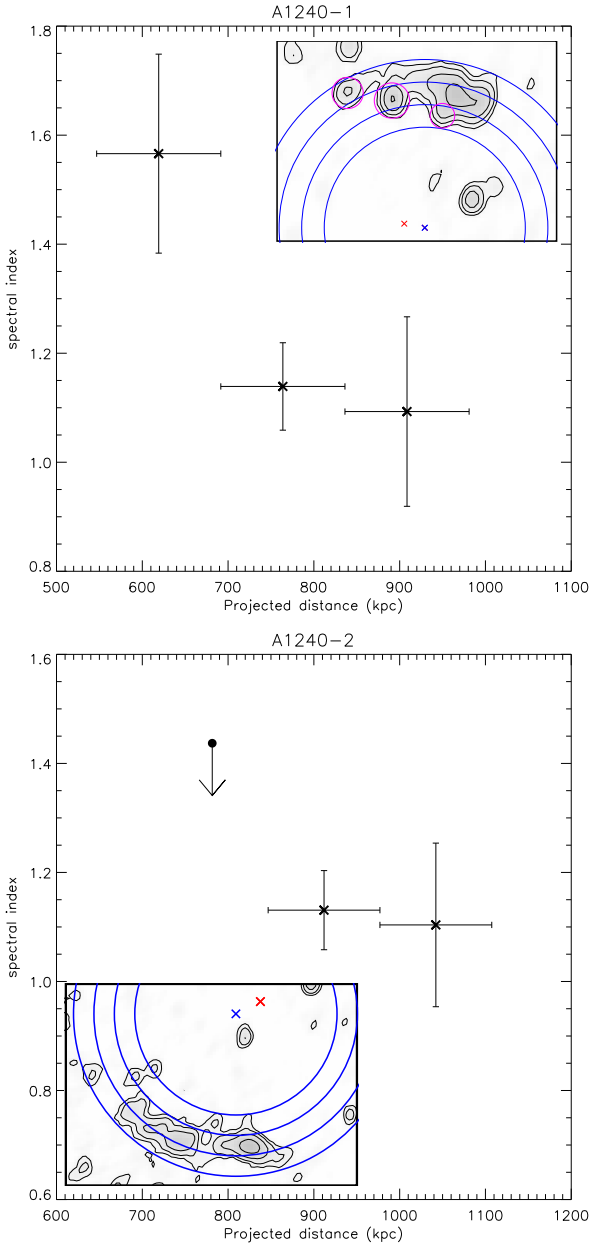

Figure 6.8: Spectral index radial trend of A1240-1 (top) and A1240-2 (bottom), computed in shells of $\sim 50''$ in width. It was computed excluding the contribution of the discrete sources. Crosses refer to spectral index values computed in shells where the mean brightness is $> 3\sigma$ at both 325 MHz and 1.4 GHz. Arrows are 3σ upper limits on the spectral index mean value (see text). In the inset: displacement of the shells over which the mean spectral index has been computed. Circles refer to the discrete sources embedded in the relic emission. The red cross refers to the cluster X-ray center, the blue cross is the center of the spherical shells.

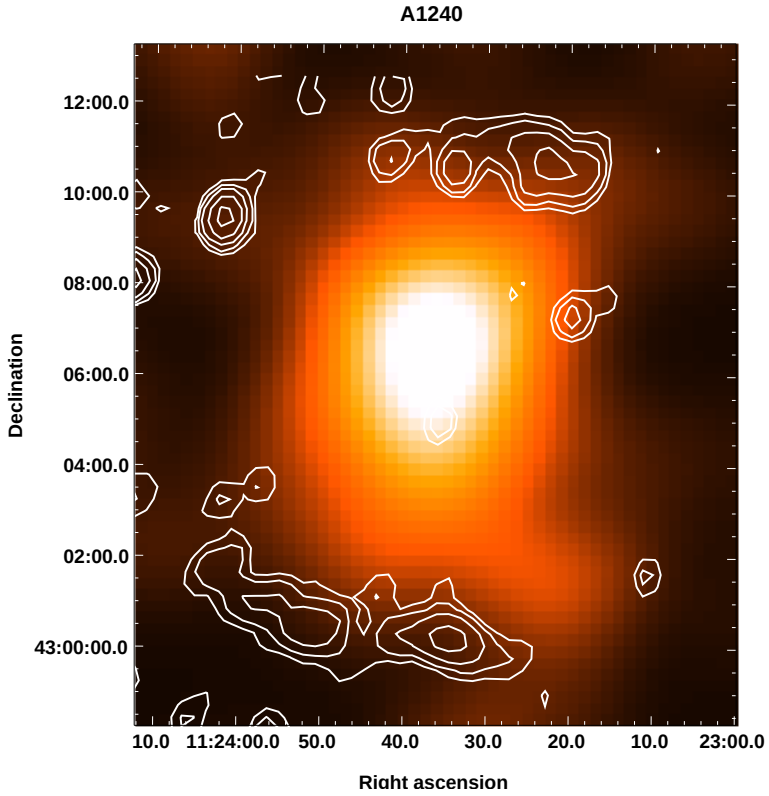

Figure 6.9: Colors: Abell 1240X-ray emission in the energy band 0.5-2 keV from ROSAT PSPC observations. The image has been smoothed with a Gaussian of σ ∼60″; contours represent the radio image of the cluster at 1.4 GHz. The beam is 42″×33″. First contour is 0.13 mJy/beam, other contours are then spaced by a factor 2.

6.5.2 Radio-X-ray comparison

We retrieved X-ray observations in the energy band $0.5 - 2$ keV from the ROSAT data archive. The cluster is $\sim 28'$ offset from the center of the ROSAT pointing. Observations were performed with the ROSAT PSPC detector for a total exposure time of $\sim$ 12 ksec. After background subtraction the event file was divided by the exposure map. We smoothed the resulting image with a Gaussian of $\sigma = 60''$.

The resulting image is shown in Fig. 6.9, where the X-ray emission of the cluster is superimposed onto radio contours. The X-ray emission of this cluster is elongated in the SN direction and shows a double X-ray morphology. As already stated by Kempner & Sarazin (2001) this morphology is consistent with a slightly asymmetric merger.

Relics are located at the edge of the X-ray emission. Their emission shows the characteristic elongated shape, and their main axis is perpendicular to the main

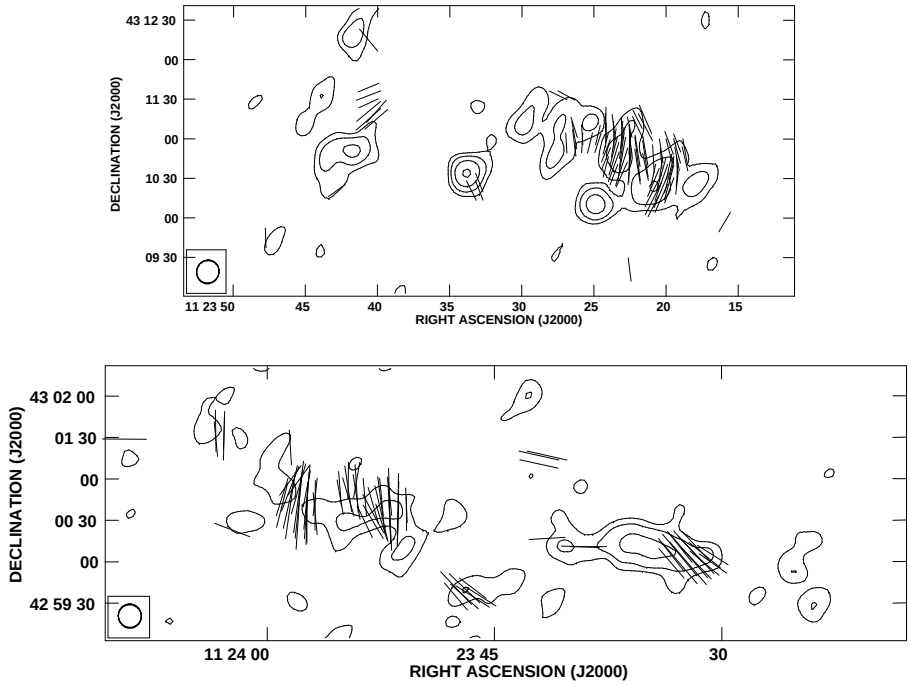

Figure 6.10: Top panel: A1240-1 radio emission at 1.4 GHz, lines represent the E vectors. The line direction indicates the E vector direction and the line length is proportional to the polarized flux intensity. 1″ corresponds to 3μJy/beam. The beam is 18″×18″. Contours start at 0.12 mJy/beam and are then spaced by a factor 2. Bottom panel: A1240-2 radio emission at 1.4 GHz. The line direction indicates the E vector direction and the line length is proportional to the polarized flux intensity. 1″ corresponds to 2μJy/beam. Contours are as above.

axis of the X-ray emission, as found in double relics of Abell 3367 and Abell 3376.

6.5.3 Equipartition magnetic field

Under the same assumptions explained in Sect. 6.4.4 , we calculated the equipartition magnetic field for the relics A1240-1 and A1240-2. Values obtained are reported in Table 6.7. We note that these values were computed considering the brightness of those pixels for which we have well-constrained information about the spectral index value, *i.e.* those regions whose emission is detected at both frequencies. Since the emission at 325 MHz is only detected in a small region of the relics, while relics are more extended at 1.4 GHz, the equipartition estimates refer to the same small regions, and different estimates could be representative of the wider relic emission detected at 1.4 GHz.

We derived the minimum nonthermal energy density in the relic sources from B'_{eq}

Table 6.7: Abell 1240

Source name	Proj. dist kpc	LLS kpc	F_{20cm} mJy	F_{90cm} mJy	B_{eq} - B'_{eq} μG	$< \alpha >$
Abell 1240-1	270″=700	240″= 650	6.0±0.2	21.0±0.8	1.0 -2.4	1.2 ±0.1
Abell 1240-2	400″=1100	460″= 1250	10.1±0.4	28.5±1.1	1.0 -2.5	1.3 ±0.2

Col. 1: Source name; Col. 2: projected distance from the X-ray centroid;

Col. 3: Largest linear scale measured on the 20 cm images.

Col. 4 and 5: Flux density at 20 and 90 cm;

Col. 6: equipartition magnetic field computed at fixed frequency - fixed energy (see Sec. 6.5.3)

Col. 7: mean spectral index in region where both 20 cm and 90cm surface brightness is $> 3\ \sigma$.

obtaining U_{min} ∼5.5 10^{-13}erg/cm^{-3} for A1240-1 and A1240-2. The corresponding minimum nonthermal pressure is then ∼3.4 and ∼3.5 10^{-13}erg/cm^{-3}. The consistency between magnetic field equipartition values and magnetic field lower limits derived by X-ray emission in other few clusters (see discussion in Sect. 6.4.3) indicates that equipartition magnetic field can be used as a reasonable approximation of the magnetic field in relics.

6.5.4 Polarization analysis

We obtained the polarized intensity images for the relics as described in Sect. 6.4.4. In Table 6.4 the parameters relative to the polarization images of the relics A1240-1 and A1240-2 are reported. In Fig. 6.10 the polarized emission of the two relics is shown. Observations performed with C array cannot reveal the weak extended emission, and thus only the most compact and bright regions are visible in this image. In these regions, the magnetic field is mainly aligned along the relic main axis in both of the relics. This is consistent with what has been observed in the relics of Abell 2345 and with what is expected from the models that explain the origin of these sources (*e.g.* Ensslin et al. 1998; Roettiger et al. 1999). The mean fractional polarization of A1240-1 is 26%, reaching values up to 70%. In the relic A1240-2 the mean fractional polarization is 29%, reaching values up to 70%. From Eq. **??** we derive that B_r^2/B_o^2 ∼1.4 and 1.2 respectively. Because of possible beam depolarization, internal depolarization and ICM depolarization, we conclude that B_r^2/B_o^2 <1.4 and <1.2. This means that the magnetic energy density in the random and ordered component is similar.

6.5.5 Results for Abell 1240

Our observations confirm the presence of two relics in Abell 1240 with a spectral index values as steep as $\sim$1.2 and $\sim$1.3. The spectral index trends derived for these relics indicate a radial flattening toward the cluster outskirts. This is the trend predicted by "outgoing merger shock" models. The double relics radio morphology and location are similar to the double relics found in Abell 3667 and Abell 3376.
The polarization level is high in both of the relics, although we have to consider that our polarization observations lack the weak extended regions that are probably less polarized. The magnetic field estimate achieved under the minimum total energy assumption reveals magnetic field on the order of μG at the cluster periphery in the relic regions, ordered on a Mpc scale, indicating a magnetic field amplification and ordering.

6.6 Discussion

We confirm the presence of double relics in the cluster Abell 1240. Their symmetry and properties strongly suggest a common origin of A1240-1 and A1240-2. In the cluster Abell 2345 we confirm the existence of two relics. However, while A2345-2 is a classic extended peripheral relic source similar to 1253+275, in the Coma cluster (see Giovannini et al. 1991 and references therein), A2345-1 shows a more complex structure. We suggest that its properties could be due to its peculiar position in between the cluster Abell 2345 and the possibly merging group X1, and thus affected by a more recent merger.
Several models have been proposed to explain the origin of radio relics. They can be divided into two classes, as reported in Sec. 1.3.2. The wealth of data presented in this Chap. allows to test the main predictions of such models.

6.6.1 Relics from merging shocks

The presence of double relics is particularly interesting in this scenario, since the shape, morphology, and properties of these extended structures strongly suggest shock waves propagating from the cluster center to the peripheral regions. Because of the short radiative lifetime of relativistic electrons, radio emission is produced close to the location of the shock waves. These models predict that the magnetic field is aligned with the shock front and that the radio spectrum is flatter at the

Table 6.8: Predictions from the shock acceleration model

Relic	α	M	R	P_2/P_1	T_2/T_1	$(B_2/B_1)_{isoP}$
Abell 2345-1	1.5±0.1	2.8±0.1	2.5±0.2	6±1	2.4±0.4	2.4±0.2
Abell 2345-2	1.3±0.1	2.2±0.1	2.9±0.2	9±3	3±1	3.0±0.5
Abell 1240-1	1.2±0.1	3.3±0.2	3.1±0.3	14±6	4±2	3.7±0.8
Abell 1240-2	1.3±0.2	2.8±0.3	2.9±0.4	9±3	3±2	3.0±0.5

Col. 1: Source name; Col 2: spectral index value;

Col. 3: Mach number;

Col 4: Shock compression ratio estimated from the radio spectral index;

Col. 5, 6: Pressure and temperature jump across the shock;

Col. 7: Magnetic field strength in the pre and post shock regions in the iso pressure case (see text)

shock edge, where the radio brightness is expected to decline sharply.

The shock compression ratio can be estimated from the radio spectral index α (assuming an equilibrium electron population accelerated and cooled at the same time, and assuming a polytropic index 5/3, see Drury 1983), as

$$R = \frac{\alpha + 1}{\alpha - 0.5}. \tag{6.1}$$

The pressure and temperature jumps across the shock can be estimated from the theory of shocks (Landau & Lifschitz 1966) as

$$\frac{P_2}{P_1} = \frac{4R - 1}{4 - R} = \frac{\alpha + 1.5}{\alpha - 1}; \frac{T_2}{T_1} = \frac{P_2}{RP_1}. \tag{6.2}$$

Here and later, the index 2 refers to down stream regions and 1 to up stream regions *i.e.* regions inside and outside the cluster shock front. These parameters are reported in Table 6.8. The Mach number of the shock can be estimated from the radio spectral index under some assumptions: if the emitting particles are linearly accelerated by shock, the spectral index of the particle energy spectrum p ($= 2\alpha + 1$) is related to the Mach number M of the shock through:

$$p = 2\frac{M^2 + 1}{M^2 - 1} + 1, \tag{6.3}$$

including the effect of particle aging (continuous injection and inverse-Compton energy losses, see *e.g.* Sarazin 1999). Mach number values we obtained are reported in Table 6.8. These values are lower than Mach number expected for accretion shocks (*e.g.* Bykov et al. 2008), and are instead consistent with those expected for weaker shocks due to merging of structures.

The spectral index trend clearly detected in A2345-2 and in both relics of Abell 1240

agrees with the predictions of this scenario. If relics are seen edge on, the flattest region, in the outer part of the relics, would correspond to the current shock location, indicating shock waves moving outward from the cluster center. As discussed in Sect. 6.4.5, A2345-1 shows a more complex radio emission. It could be affected by a more recent merger with the X1 group. It could trace a merger shock moving inward to the cluster center as a result of the Abell 2345 - X1 group interaction.

Magnetic field and merging shocks

The study of the magnetic field associated with the relics offers more opportunities to investigate the connection between relics and merger shock waves. First of all, the presence of relics itself indicates the existence of significant magnetic field at the cluster periphery on the Mpc scale. Furthermore, the detected level of polarization shows that the magnetic field in these regions is relatively ordered.

The effect of a shock wave passing in the ICM could be twofold: (i) order and compress a magnetic field that was randomly oriented before the shock passage or (ii) compress a magnetic field that was already ordered on the relic scale before the shock passage . This depends on the turbulence development at the cluster periphery, which could either give rise to a random field in the cluster outskirts (case i) or not (case ii). Little is known about this point from an observational point of view. Observational evidence from the gas pressure map of the Coma cluster (Schuecker et al. 2004) indicates the relevance of chaotic motions within the ICM. Cosmological numerical simulations (*e.g.* Bryan & Norman 1998; Sunyaev et al. 2003) suggest that the level of ICM turbulence is greater at increasing radial distances from the cluster center. If the simple Kolmogorov picture of incompressible fluid turbulence is assumed, this implies a more developed turbulence in the outermost region (since the decay time is L/σ, where L is the typical scale where the bulk of turbulence is injected, and σ is the rms velocity of turbulence).

Recently, Ryu et al. (2008), have argued that turbulence is very likely well developed in clusters and filaments, and not in more rarefied regions such as sheets and voids. On the other hand, Dolag et al. (2005a) suggest that the bulk of turbulence is injected in the core of galaxy clusters, thus implying a more developed turbulence in the innermost regions, compared to the outermost ones. The main limitation

of cosmological simulations is the lack of resolutions in low-density environments, which makes it difficult to distinguish whether the turbulent cascade is developed in these regions. Moreover, details of the conversion process of large scale velocity fields into MHD modes is still poorly understood. Thus, the overall picture seems still uncertain from the theoretical point of view.

In the case that the magnetic field in the cluster outskirts is randomly oriented before the shock passage (*i.e.* the turbulence is developed in the cluster outskirts) and that it has been amplified and ordered by the passage of the shock wave (case i above), the observed ratio B_r/B_o derived by polarization analysis (Sects. 6.4.4 and 6.5.3) could be used to estimate the magnetic field amplification due to the passage of the shock.

Following Ensslin et al. (1998), if the relic is seen at some angle δ >0 between the line of sight and the normal of the shock front, the projected magnetic field should appear perpendicular to the line connecting the cluster center and the relic. This is indeed what the polarization data presented here show. The magnetic field amplification, the observed integral polarization, and the preferential direction of the field revealed by the E vectors orientation could be derived, provided that δ and R, the shock compression factors, are known. The present data do not allow the angle δ to be inferred. Future X-ray and optical observations could reconstruct the merging geometry for these two clusters, as done, *e.g.* in Abell 521 by Ferrari et al. (2003, 2006). Despite this, if relics are only supported by magnetic pressure, the upstream and downstream fields are related by $(B_2^2/B_1^2)_{isoP} = P_2/P_1$ ("strong field" case in Ensslin et al. 1998). This ratio can be compared to the ratio derived by the polarization properties of the relics, under the assumption that B_2 corresponds to the ordered component of the field and B_1 to the random one. In Table 6.8, the $(B_2/B_1)_{isoP}$ ratio is reported for the relics in Abell 2345 and Abell 1240. These values are comparable to the observed ratio B_r/B_o derived by polarization analysis (Sects. 6.4.4 and 6.5.3).

Another indication of the magnetic field amplification in the relics may be obtained by comparing the magnetic field in the relic with the cluster magnetic field intensity expected at the relic location. Several works have shown that the properties of the magnetic field in galaxy clusters do not depend on the detailed structure of the assumed initial magnetic field (Dolag et al. 1999, 2002; Dolag & Stasyszyn 2009,

Donnert et al. 2008). Relics are located at 700-1100 kpc from the cluster center in Abell 2345 and Abell 1240. At these distances the cluster magnetic field strength is expected to be $\sim 10^{-1}\mu$G (see *e.g.* Dolag et al. 2008; Ferrari et al. 2008, Chap. 4). Equipartition magnetic field values are approximately μG (see Sects. 6.4.3 and 6.5.3), thus about 10 times higher. Despite the number of uncertainties and assumptions related to the equipartition estimate, this is consistent with the ratio $(B_2^2/B_1^2)_{isoP}$ and B_r/B_o.
Even if no firm conclusion can be obtained by this analysis, we can conclude that this picture is consistent with the presented observations.

6.6.2 Relics from adiabatic compression

Another model to explain the origin of cluster radio relics has been proposed by Ensslin & Gopal-Krishna (2001). This idea has been investigated with the help of 3-dimensional magneto hydro dynamical simulations by Ensslin & Brüggen (2002) and in a more realistic cosmological environment by Hoeft et al. (2004). In this scenario, cluster radio relics would originate by the compression of fossil radio plasma by a shock wave occurring in the process of large-scale structure formation. The expected high sound velocity of that still relativistic plasma should keep the shock from penetrating the radio plasma, so that shock acceleration is not expected in this model. The plasma gains energy adiabatically from the compression, and the magnetic field itself is amplified by this compression. If the electron plasma is not older than 2 Gyr in the outskirts of a cluster, they can emit radio waves again. Simulations performed by Ensslin & Brüggen (2002) show that the radio morphology of the resulting radio relic in the early stage after the shock passage is sheet-like. Then the formation of a torus is expected when the post shock gas starts to expand into the volume occupied by the radio plasma. Thus it is expected in this scenario that some correlation should exist between the morphology of the radio relic and its spectral index, which traces the time passed after the shock wave has compressed and re-energized the emitting particles. A2345-1 indeed shows a torus-like radio structure and a spectral index higher than A2345-2, A1240-1 and A1240-2, which exhibit a sheet-like structure. The simulations performed by Ensslin & Brüggen (2002) indicate that the compression of the radio plasma by the shock can be estimated from a cluster radio relic with a toroidal shape. Assuming the idealized

case of a initially spherical and finally toroidal radio cocoon, the compression factor is given by

$$R' = \frac{2r_{max}^2}{3\pi r_{min}^2}, \tag{6.4}$$

where r_{max} and r_{min} refer to the outer and inner radius of the torus. In the case of A2345-1, we assume that the observed torus-like structure can be described by taking $r_{max} \sim$ the LLS of the relic and r_{min} the thickness of the filament in the N-E part of the relic, as suggested by the same authors in the case of imperfect toroidal filamentary relics. With $r_{max} \sim 1$ Mpc, $r_{min} \sim 200$ kpc $R' \sim 5$ results. This is higher than the value of the maximum compression ratio for mono-atomic gas (which is 4); this would indicate that the radio plasma has a different equation of state, however, no conclusion can be drawn since Eq. 6.4 is based on assumptions that are too simplistic, in particular a spherical model for the compressed relic.

6.7 Conclusions

In this chapter we have presented 1.4 GHz and 325 MHz observations of Abell 2345 and Abell 1240. The presence of double relics in these cluster had been inferred by Giovannini et al. (1999) for Abell 2345 and by Kempner & Sarazin (2001) for Abell 1240 from NVSS and WENSS. We confirm the presence of two relics in each of these clusters. The detection of radio synchrotron emission at the cluster periphery testifies the presence of magnetic fields in the ICM at large distance from the cluster center, and allows to investigate possible scenarios for the amplification of magnetic fields in the process of structure formation. By combining 1.4 GHz and 325 MHz observations, we obtained the spectral index image of the diffuse radio emission. The study of the polarized emission at 1.4 GHz has been presented as well. The analysis of both the spectral index distribution and the polarization properties of relics allows several independent predictions of the relic formation models to be tested. We summarize the results from the presented analysis:

1. **A2345**: two relics have been detected in the cluster outskirts at both 1.4 GHz and 325 MHz. They are not perfectly symmetrical with respect to the cluster center; the normals to the relic main axis form an angle of $\sim$150°. A2345-2 is a classical peripheral relic, and A2345-1 is a peculiar relic with a torus-like

structure possibly related to a merging region.

2. **A1240**: relics are fainter than relics in A2345. Their extended emission is detected at 1.4 GHz, while only their brightest part is detected at 325 MHz. They are symmetrical with respect to the cluster center, and the angle between their normals is $\sim$180° as found in the other known double relics: Abell 3667, Abell 3376, and RXCJ1314.4-2515.

3. Relics are located at the edge of the X-ray emission of Abell 2345 and Abell 1240. The X-ray emission of Abell 2345 shows multiple substructures that could be galaxy groups interacting with A2345. Peculiar features of A2345-1 could arise from this multiple interaction, but only detailed X-ray and optical analysis could shed light on this point.

4. Relics in Abell 1240 are located perpendicular to the cluster main axis revealed by X-ray observations. The double X-ray morphology of the cluster is typical of merging clusters.

5. The average spectral indexes are steep. We found 1.5 $\pm$ 0.1 and 1.3 $\pm$0.1 for A2345-1 and A2345-2 and 1.2$\pm$ 0.1, 1.3$\pm$ 0.2 for A1240-1 and A1240-2.

6. The spectral index distribution in the relics is rather irregular and patchy, although a clear radial trend is present in the relics of these two clusters. A2345-2 spectral index ranges from $\sim$1.5 in the region closer to the cluster center to $\sim$1.1 in the outer rim. This trend is consistent with shock models predictions. The same trend is observed in both of Abell 1240 relics. A1240-1 spectral index ranges from $\sim$1.1 to $\sim$1.6 going from the outer to the inner rims, A1240-2 spectral index is also consistent with a similar trend (going from $\alpha <$ 1.5 in the inner rim to $\alpha \sim$ 1.1 in the outer one). An opposite trend is instead detected in A2345-1. Spectral index values are lower in the inner rim ($\sim$1.3) and increase toward the outer part of the relic reaching values $\sim$1.7. This trend

could be due to its peculiar position between two merging clumps.

7. The magnetic field, as revealed by polarized emission, is mainly aligned with the relic main axis. In Abell 2345 the polarized emission reveals the arc-like structure morphology of the relic A2345-2. Under equipartition conditions, values of $\sim$ 2.2 - 2.9 μG are derived. The field has been likely amplified, consistently with shock-model predictions.

These results have been discussed in the framework of relic formation models. The Mach numbers derived from the value of radio spectral index speak against the "accretion shock" scenario, since they are too small. Outgoing merger shock waves, proposed to explain double relic emission in Abell 3667 and A3376, could also work in Abell 1240 and Abell 2345. For the last cluster we suggest that the peculiar emission of A2345-1 could be explained by a shock wave moving inward, due to the interaction of the main cluster with the X1 group.
The toroidal shape of A2345-1 could be produced by adiabatic compression, however the available data and models do not allow a conclusive comparison.

Chapter 7

Cosmological simulations of magnetic fields in galaxy clusters*

7.1 Introduction

The evolution of magnetic fields in the ICM has been investigated in the past through cosmological simulations, performed with different numerical codes (see Sec. 2.3 and references therein). The comparison with observations is necessary to constrain the main magnetic field properties, and it is now feasible thanks to the progress that has been done in recent years. One key aspect is that, so far, large scale radio emission is mainly detected in very massive clusters. Such massive systems are not easily studied by numerical simulations, since the size of the density fluctuations responsible for the formation of massive halos is large, *i.e.* $\sim$ 20 Mpc/h, and statistically, a total volume of $\sim (100 Mpc/h)^3$ needs to be sampled by simulations in order to produce at least one cluster of mass $\sim 10^{15} M_{\odot}$/h. An important step for studying non-thermal phenomena is to perform simulations based on extremely large cosmological volumes, *e.g.* 1 Gpc side-length. Such large volumes cannot be simulated at the resolution reached by observations, so that re-simulation techniques have been developed. In this chapter we will present a study of the magnetic field in a sample of massive galaxy clusters re-simulated at high resolution in order to resolve scales comparable to those reached by observations.

*Bonafede & Dolag, in prep

7.2 The cluster set

7.2.1 The parent simulation

The clusters were selected from a large hydrodynamical simulation performed according to the 'concordance' ΛCDM cosmological model ($\Omega_\Lambda = 0.76$, $\Omega_0 = 0.24$, $h = 0.72$ and $\sigma_8 = 0.8$). The power spectrum for the primordial density fluctuations $P(k) \propto k^{-n}$ was characterized by $n = 0.96$. This simulation was carried out with the massively parallel TREE+SPH code *Gadget2* (Springel 2005) and consists of a periodic box of size 1 h^{-1} Gpc. The cluster identification was performed at $z = 0$ using a standard *Friend of friends* algorithm. The linking length was fixed to 0.15 the mean inter-particle separation between DM particles.
The cosmological box contains a large sample of 117 clusters having $M_{FOF} > 10^{14} h^{-1}$ $M_\odot$. The center of each cluster is placed at the position corresponding to the center of mass of the selected particles.. This large simulated cosmological box contains 64 clusters with $M_{FOF} > 10^{15}$ $M_\odot$/h at $z = 0$, offering thus a large sample of objects to investigate the magnetic field properties in massive clusters.

7.2.2 Cluster selection and Initial Conditions

Clusters were selected from the parent simulation on the basis of their mass only. We selected the 20 most massive objects among those with $M_{FOF} > 10^{15}$ $M_\odot$and re-simulated each of these clusters at higher resolution by using the *Zoomed Initial Conditions* (ZIC) code (Tormen et al. 1997). The setup of initial conditions was optimized to guarantee a volume around the cluster of $\sim$ 5-6 R_{vir} simulated at high resolution. This was obtained using the following iterative procedure: we started from analyzing the output of the DM-only parent simulation, and selected the particles in each cluster at distance <5 R_{vir} from the cluster center. These particles were traced back to their initial conditions. The corresponding Lagrangian region was enclosed in a box of side $L_{HR} \sim 62.5$ Mpc (High resolution HR region). The Volume occupied by the HR particles, V_{HR}, is only a fraction of the volume L_{HR}. Thus, in order to optimize the use of the HR particles, we modelled the occupation within the HR region by building the smallest ellipsoid that contains the HR particles. This ellipsoidal concave volume was re-sampled with a higher number of particles in order to obtain a mass resolution of $1 \times 10^9 M_\odot$/h for DM particles. The HR particles were perturbed according to the same density fluctuations of the

parent simulation , together with new fluctuations of higher frequency up to the Nyquist frequency. The amplitude of the fluctuations are given by the theoretical power spectrum $P(k)$ of the parent simulation, extended to higher k. In order to fully keep the cosmological context of the simulation the density and velocity field of the particles that fell outside the HR region (*i.e.* Low Resolution LR particles) were computed as follows: density and velocity of LR particles were interpolated onto a spherical grid with constant angular resolution: $d\theta$. The size of each cell, $dr = rd\theta$ was chosen to obtain approximately cubic cells through the sphere. The interpolation onto a spherical grid reduces the number of LR particles to the minimum necessary to preserve the large-scale tidal field of the original simulation. We used $d\theta = 1.5°$, corresponding to $\sim 2\times10^6$ particles, that guarantees an accurate sampling of the tidal field (see Tormen et al. 1997). By construction, as the distance from the HR region increases, dr increases too, and the mass of the LR particles increases accordingly. The gravitational softening, ϵ_{grav} was then modified as $\epsilon_{grav} \propto M^{-1/3}$. The sphere where LR particles are interpolated was taken as big as the size of the parent simulation, since reducing that size would correspond to exclude contributions in the initial fluctuations, loosing the large scale perturbation and changing the tidal field that the central object is subject to. The new initial conditions were finally traced back to a higher redshift, so that the *rms* of the particle displacement in the HR region is small enough to guarantee the validity of the linear theory. $z = 70$ was required for our choice of resolution. After generating the new IC at higher resolution, we run another DM-only re-simulation. This procedure was repeated iteratively until we found that none of the LR particles was entering in the HR region, because of the introduction of low-scale modes. Several runs were required for each cluster to avoid the presence of LR particles in the HR region while keeping the number of HR particles as low as possible.

The number of particles required in the HR region was 5-10 10^6 depending on the cluster dynamical state at $z = 0$ and on the number and mass of clusters interacting with the target one. One of the cluster initially selected by the *Friend of friends* algorithm as single massive clusters turned out to be a massive merging systems, where two clusters with mass $> 10^{15}$ $M_\odot$/h are merging at $z = 0$. In this cluster, the number of HR particles necessary to sample the merging region was $\sim 16\times10^6$. The final sample consists then of 21 massive clusters, comprising both isolated and

merging systems. HR particles have a mass of $\sim 10^9$ $M_\odot$/h. The cluster set is shown in Table 7.1. The virial mass of each cluster was defined as the mass contained within a radius encompassing an average density equal to the virial density, ρ_{vir} , predicted by the top-hat spherical collapse model. For the assumed cosmology it is $\rho_{vir} \sim 100\rho_c$, where ρ_c is the critical cosmic density (Eke et al. 1996). We report in that Table the mass of the DM halos with $M > 10^{14}$ $M_\odot$/h that are within 5 R_{vir} from the cluster center, as identified by the spherical overdensity criterion that we used.

Once the Initial conditions have been obtained, we added the baryonic component in the following way: we selected from the output of the DM run all of the particle that follow inside the R cleaned region of the target cluster. Each DM particle has been splitted in a pair of DM+gas particles. The pair DM-gas particle are shifted from each other preserving the center of Mass and of velocity and taking into account the mean inter-particle separation. The mass of DM and gas particle is then $1.0\times^9$ $M_\odot$/h and 0.16×10^9 $M_\odot$/h respectively. The gravitational softening length used is 5 kpc, which corresponds to the smallest SPH smoothing length reached in the dense centres of clusters. In lower density regions, the resolution is lower.

7.3 The Dianoga set

Once the initial conditions (IC) for high resolution simulations were set, clusters have been re-simulated including the gas-physics (Borgani et al., in prep). In order to study the main global properties of the clusters, simulations have been initially performed including non-radiative gas dynamics with standard viscosity ($\alpha_{visc} = 1$, see Springel 2005). We refer to these simulations as *ovisc* simulations. From the final snapshots of these simulations we derived the projected X-ray surface brightness images, by using a map-making algorithm (Dolag et al. 2005b) that allows us to project the predicted emission of every SPH particle along the line of sight considering an integration depth of $\pm$ 5 R_{vir} around the center of simulated clusters. We also computed the X-ray Luminosity and gas temperature inside the virial radius. These quantities are reported in Tab. 7.2, and the X-ray surface brightness images of the clusters are reported in Fig. 7.1. Clusters in different dynamical state belong to this sample, and consequently, the X-ray surface brightness images show quite different morphologies. Several clusters are disturbed in the very internal part,

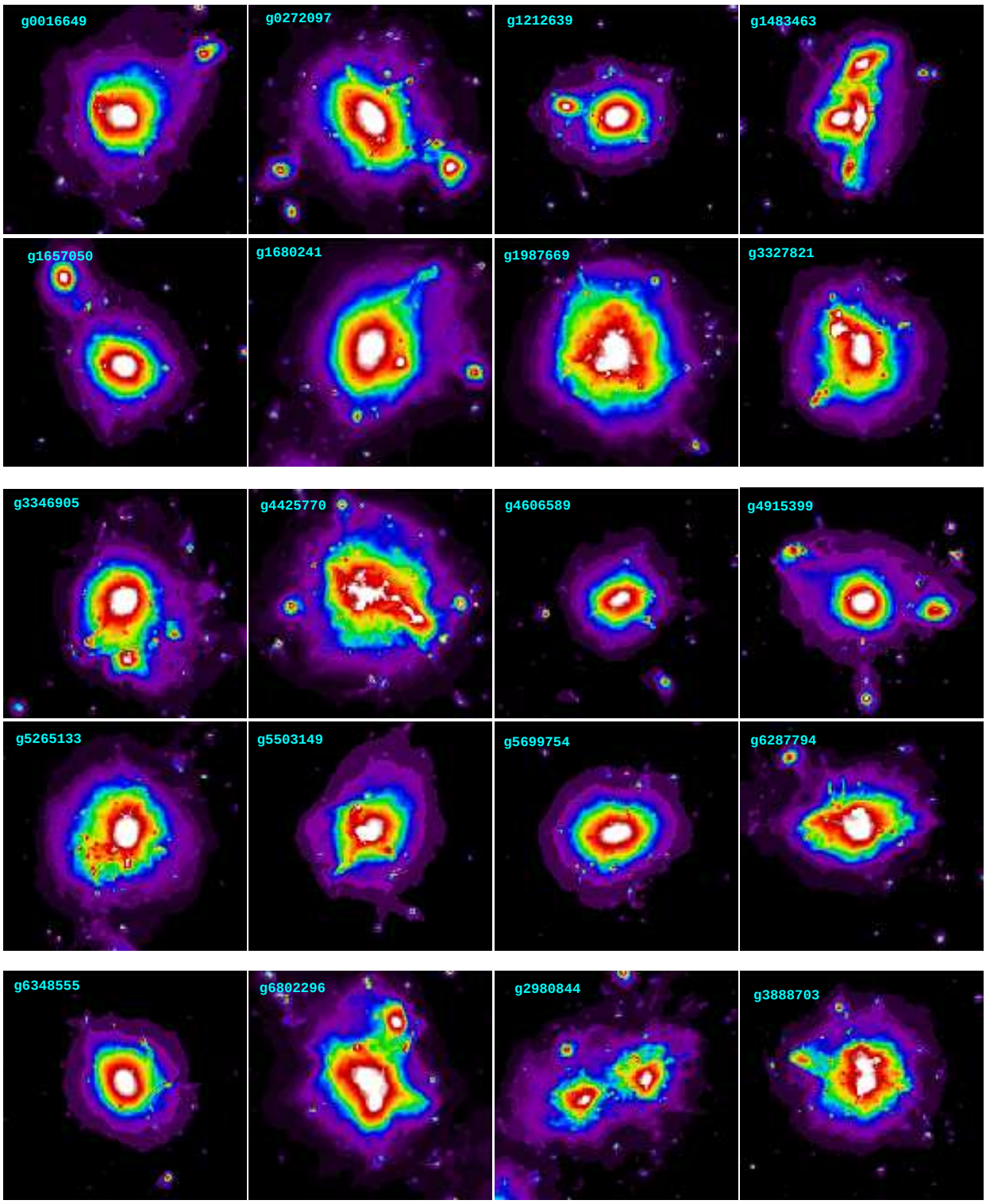

Figure 7.1: X-ray surface brightness of the cluster in the Dianoga sample. The side of each box corresponds to $\sim 2.2\ R_{vir}$

Table 7.1:

Cluster	R cleaned $[R_{vir}]$	M_{DM} $[10^9]M_\odot$/h	N of nearby clusters	M of nearby clusters $[10^{14}]M_\odot$/h
g0016649	5.2	1.618	1	1.4
g0272097	5.4	1.518	3	1.6,1.8,1.1
g1212639	5.3	1.49	2	5.4, 1.3
g1483463	5.4	1.482		
g1657050	5.0	1.537	4	7.6,2.2,2.2,1.7
g1680241	5.0	1.165	3	5.8, 2.7,1.5
g1987669	5.4	1.776	1	1.5
g2980844	5.3	1.993,1.170	4	5.1 ,4.8, 1.2, 1.1
g3327821	5.2	1.657		
g3346905	5.1	1.705	6	7.9,2.9,1.8,1.2,1.2,1
g3888703	5.3	3.163	1	1.1
g4425770	5.5	1.678	2	3.8, 2.8
g4606589	5.6	1.171	3	4.8,3.9,2.4
g4915399	6.0	1.557	3	3.1,1.3,1.3
g5265133	5.5	1.840	1	1.6
g5503149	5.2	1.385		
g5699754	5.5	1.813		
g6287794	5.1	1.356	1	7.8
g6348555	5.1	1.316	1	2.7
g6802296	5.2	1.067	2	6.8, 1.1

Col. 1: Cluster name; Col. 2: Number of virial radii cleaned by LR particles;

Col. 3: Mass of the DM component inside the virial radius;

Col 4: Number of nearby clusters within 5 R_{vir} with $M_{DM} > 10^14 M_\odot$/h

Col 5: Mass of the dark matter component of the nearby clusters.

indicating that a merger event has just occurred (*e.g.* g442578) , while other clusters have multiple peaks in the X-ray images, like *e.g.* g1483463. Note that this cluster, that was found to be isolated according to the spherical overdensity criterion based on DM particles, turned out to be a multiple merging system when the gas properties are analyzed. It is then necessary to investigate the gas properties in order properly identify the dynamical state of the clusters. In the sample there are also clusters that look more regular is shape, and clusters that are going to interact with a smaller halo, that is visible in the X-ray images (*e.g.* g0016649), and one ongoing merger event between two massive clusters (g2980844).

Since the physics that we include to follow the evolution of the gas particles does not consider several sources of heating (star formation, feedback, thermal conduction), and cooling, we will concentrate our analysis on cluster volumes where the gas

Table 7.2:

Cluster	M_{vir} [10^{15} $M_\odot$/h]	R_{vir} kpc	L_X [10^{45}] erg/s	T_{MW} [keV]	T_{spec} [keV]
g0016649	1.649	2521	4.10	6.1	3.7
g0272097	1.527	2453	3.60	5.0	2.4
g1212639	1.485	2430	6.30	6.0	3.9
g1483463	1.499	2438	4.40	3.8	2.4
g1657050	1.529	2455	5.34	5.6	2.6
g1680241	1.220	2271	1.89	5.1	2.6
g1987669	1.774	2585	3.15	6.2	3.0
g2980844	2.000	2707	2.58	5.6	2.2
g3327821	1.703	2549	5.06	6.2	3.7
g3346905	1.741	2569	4.60	6.6	3.7
g3888703	3.163	3133	10.5	8.7	4.3
g4425770	1.680	2537	2.01	4.7	1.9
g4606589	1.180	2247	2.45	5.6	2.5
g4915399	1.582	2484	4.87	5.5	3.1
g5265133	1.898	2647	4.95	5.6	3.3
g5503149	1.403	2382	8.10	8.0	5.4
g5699754	1.855	2626	8.95	8.4	5.9
g6287794	1.376	2366	6.61	6.9	4.0
g6348555	1.144	2346	7.21	6.6	4.9
g6802296	1.055	2165	1.86	3.5	1.8

Col. 1: Cluster name; Col. 2: Total mass inside R_{vir};

Col. 3: Virial radius;

Col 4: Estimated X-Luminosity in the band 0.1-10 keV

Col 5: Mean temperature (mass weighted); Col6: Mean Temperature (spectroscopic like).

All quantities are computed inside R_{vir}

density and temperature suggest that these processes are not dominant and the main physical driver is just the gravitational collapse. Such volumes are therefore expected to be fairly independent by more sophisticated physical implementations (*e.g.* Roncarelli et al. 2006).

7.4 Non-ideal MHD simulations

We want to study the magnetic field properties in large massive systems, evolving the baryonic components using the new MHD implementation in the *Gadget3* code by Dolag & Stasyszin (2009). This code combines the merely gravitational interaction of a dominant dark-matter component with the hydrodynamics of a magnetized gas to simulate the formation of magnetized galaxy clusters.

Our MHD simulations aim to follow the magnetic field through the turbulent

amplification driven by the structure formation process. We assumed an initially homogeneous magnetic field of 10^{-12}G co-moving, and evolved the magnetic field according to the induction equation:

$$\frac{\mathrm{d}\mathbf{B}}{\mathrm{d}t} = \nabla \times (\mathbf{v} \times \mathbf{B}) + \nabla \times (\eta_m \nabla \times \mathbf{B}). \tag{7.1}$$

The numerical implementation of this equation is not trivial, and in previous works it was usually assumed that the electric conducivity of the gas is infinite, ($\eta_m = 0$), so that the second term of the Eq. 7.1 vanishes, This assumption implies that the magnetic field is frozen into the gas. These assumptions, however, do not give reasonable results in our massive clusters. The magnetic field profiles resulting from ideal MHD simulation in fact do not match the slope inferred from observations and furthermore, the magnetic field in the cluster center is amplified up to high values (tens of μ G). Such high magnetic field would result in a very high magnetic energy at the cluster center. Simulations performed with different codes reach good agreement in predicting that the ratio of the bulk kinetic energy to the thermal energy has an upper limit of $\sim$15%. The energy in the magnetic field is then expected to be $\leq$ the kinetic energy. It is worth noting that all the MHD simulations performed so far have indicated that the magnetic field amplification increases when the resolution is improved. It is not surprising, then that the high resolution we have reached in these massive clusters needs that additional physics is included. As noted by Dolag et al. (2008), depending on the ICM resistivity, the magnetic field could suffer a decay that is so far neglected in all simulations.

We have extended the resistive MHD equation removing the ideal-MHD assumption, by assuming a spatially constant dissipation η_m. Using the constraint $\nabla \cdot \mathbf{B} = 0$, Eq. 7.1 can then be written as:

$$\frac{\mathrm{d}\mathbf{B}}{\mathrm{d}t} = (\mathbf{B} \cdot \nabla)\mathbf{v} - \mathbf{B}(\nabla \cdot \mathbf{v}) + \eta_m \nabla^2 \mathbf{B}. \tag{7.2}$$

so that the effect of a spatially constant η_m can be investigated

7.4.1 Test problems

The new implementation has been tested by solving numerically two test problems that we describe in the following:

One-dimensional slab

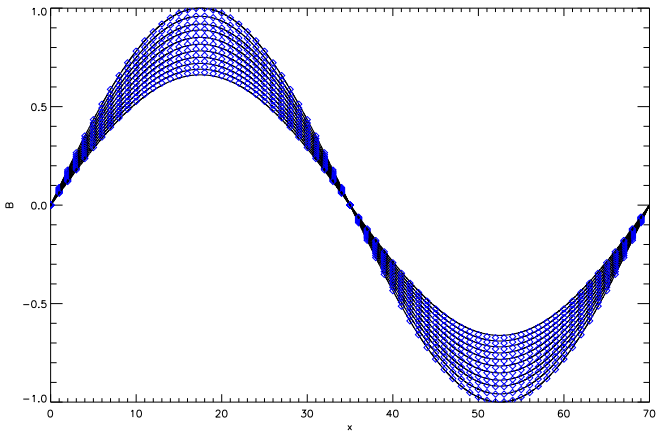

Figure 7.2: Comparison of the results from the simulations (diamonds) to the analytic solution (lines) at different output times. The magnetic resistivity η_m was set to 1 in this test.

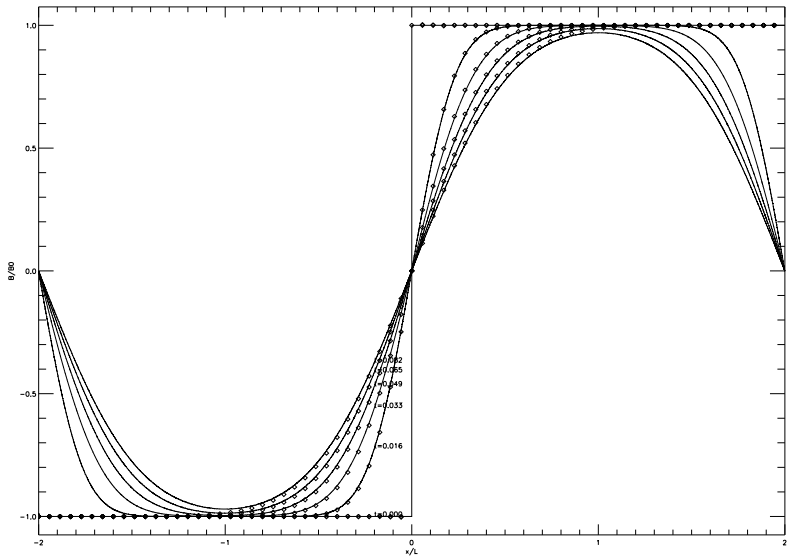

Figure 7.3: Comparison of the results from the simulations (diamonds) to the analytic solution (lines) at different output times. The magnetic resistivity η_m was set to 1 in this test.

We consider first a one-dimensional magnetic field ($\mathbf{B} = B(t)\hat{\mathbf{y}}$) in a one dimensional slab at rest with side length L. The induction equation reduces to

$$\frac{\mathrm{d}B}{\mathrm{d}t} = \eta_m \frac{\mathrm{d}^2 B}{\mathrm{d}x^2}, \tag{7.3}$$

which has the solution

$$B = exp\left(-\eta_m t \left(\frac{2\pi}{L}\right)^2\right) B_0 \mathrm{sin}\left(\frac{2x\pi}{L}\right) \tag{7.4}$$

Figure 7.2 shows the result of the numerical simulation (diamonds) compared to the analytic solution (lines) for various time steps, showing the very good match between the two.

Magnetic diffusion across a step

We consider here a case similar to the previous one, where the magnetic field is $\mathbf{B} = B(x,t)\hat{\mathbf{y}}$, a but now we include a step profile for the magnetic field of the form:

$$B(x,0) = \begin{Bmatrix} +B_0, & x > 0 \\ -B_0, & x < 0 \end{Bmatrix} \tag{7.5}$$

If the magnetic field is held fixed at two points ($\pm l$), so that

$$B(l,t) = -B(l,t) = B_0 \tag{7.6}$$

the solution of the diffusion equation is (see Wilmot-Smith et al. 2005)

$$B(x,t) = B_0 \frac{x}{L} + \frac{2B_0}{\pi} \sum_{n=1}^{\infty} \frac{1}{n} exp\left(\frac{-n^2\pi^2\eta_m t}{l^2}\right) sin\left(\frac{n\pi x}{l}\right) \tag{7.7}$$

Figure 7.3 shows the result of the numerical simulation (diamonds) compared to the analytic solution (lines) for various time steps. As can be seen the magnetic field diffuses very rapidly to the steady-state solution, $B(x) = B_0(x)/l$.

The results obtained from observations, in particular those obtained in Chap. 4 about the magnetic field central intensity and radial decline, and the large sample of massive galaxy clusters, permit now to test which is the most appropriate value of η_m to recover the observed magnetic field strength and radial profile.

7.5 Testing the effect of the magnetic diffusivity

In order to test the effect of different values of the magnetic field diffusivity we have selected from the initial sample a sub-sample of clusters that at $z = 0$ show

dynamical state similar to the Coma cluster, *i.e.* those clusters that appear to be interacting with a second group or cluster with a mass ratio 0.1-0.05 as reported for the Coma cluster by the analysis of Colless & Dunn (1996). We started simulating these clusters with different value of η_m, with the aim of finding the best value that can reproduce what observed in a real cluster. In Fig. 7.4 we show the gas density, temperature and magnetic field strength profile for the cluster g1987669. These plots show that including a magnetic diffusivity affects the thermodynamical properties of the cluster. Although the dynamical effect of a magnetic field of the order of $\sim$1-10 μG in the cluster cores is negligible, the overall effect of the magnetic force and pressure integrated over one Hubble time results in a change of the density and temperature profile. Moreover, the energy dissipated can be transported into heat, and it will be very interesting to investigate with future MHD radiative simulations how it can help in understanding the high density and low temperature profiles observed in the so-called "cool-core" of relaxed galaxy clusters. The higher η_m, the higher the cited effects are. The results of the simulations performed in this initial sub-sample show that a value of $\eta_m = 20$ seems to be the best choice to obtain a magnetic field strength in the cluster centre similar to the one observed in Coma.

7.6 Preliminary results and future perspectives

We have presented a new sample of massive clusters that we have re-simulated at high resolution by using the ZIC code (Tormen et al. 1997). We have followed the evolution of the gas by using a novel MHD implementation within the *Gadget3* code. The main result obtained with our new sample of massive galaxy clusters is that the inclusion in the induction equation of the diffusion term is necessary to reproduce the observed magnetic field profiles in galaxy clusters.

Even is the magnetic field energy is a tiny fraction of the thermal one, the effect of the magnetic force integrated over the cluster evolution may affect the gas density profile as well as the temperature profile.

We started to simulate the other clusters in the full-sample with $\eta_m = 20$. It is expected, by numerical simulations, that the magnetic field is amplified during the process of structure formation, not only because of the adiabatic compression of the gas, but also because of phenomena due to turbulence and shear-flows (see Chap. 2 and references therein). The magnetic field strength is however expected

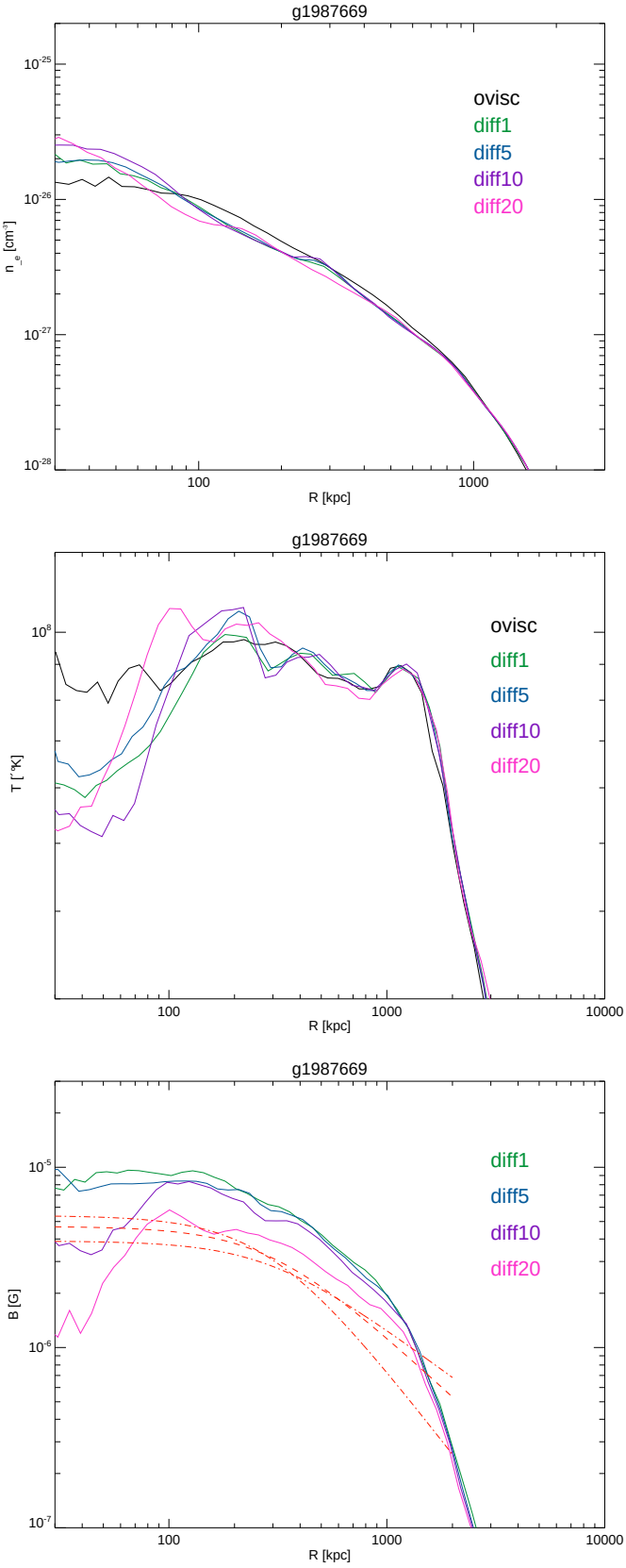

Figure 7.4: From top to bottom: density, temperature and magnetic field profile for the cluster g1987669 for different full MHD runs with different values of the diffusivity constant η_m. In the bottom panel the red dashed line refers to the best profile for the Coma cluster as derived by RM observations (see Chap. 4), while the dotted-dashed lines correspond to the steepest and flatter profiles that are consistent with RM data within 1σ of the χ^2.

to saturate in the core of massive galaxy clusters, but simulations performed so far in the literature could not properly investigate such high mass systems. Our fairly large sample of massive galaxy clusters represent now a powerful tool to study such effects with a statistical representative sample, and as a function of underlying ICM dynamics, as a response to the different dynamical histories of clusters. New radio instruments that are expected to become operative very soon, like LOFAR and EVLA, will dramatically increase our knowledge of the non-thermal components of galaxy clusters and their origin. Together with the next generation of radio telescopes (like LWA and SKA) with their improved wavelength coverage and sensitivity, these instruments will step into essentially unexplored territory. Therefore, theoretical predictions for the properties of the magnetic field in galaxy clusters are mandatory to interpret current and future observations as well as to shed new light on the interpretation of non thermal processes in galaxy clusters.

Chapter 8

Other results

8.1 Introduction

In addition to the results presented in this thesis, in the last years other important observational and theoretical works have given a contribution in understanding the large scale magnetic fields properties. In this chapter we will briefly present other results obtained from works done in collaboration with G. Giovannini, L. Feretti, F. Govoni, and M. Murgia.

8.2 Statistical study of nearby radio halos*

In collaboration with G. Giovannini, L. Feretti, Govoni, M. Murgia, F. Ferrari and G. Monti, we have performed a statistical study on all the nearby radio halos at $z < 0.4$, by collecting literature data as well as new and archive VLA observations. The final sample consists of 31 objects, that allow to draw some general properties and to test the correlations between between thermal and non-thermal components of the ICM (see Chap. 1). Here we summarize the main results obtained from the analysis of the cluster sample.

- Radio halos are usually located in the center of the cluster and show a regular morphology. In a few cases the radio structure is irregular and elongated. In particular in 4 clusters, namely Abell 851, Abell 1351, Abell 2218, Abell 1213 the radio emission is centrally located, but extended only on one side with respect to the cluster center (see Fig. 8.1). We interpret these structures as related to smaller and asymmetric cluster mergers.

*Giovannini, Bonafede, Feretti, Govoni, Murgia, Ferrari & Monti, 2009, A&A 507 1275

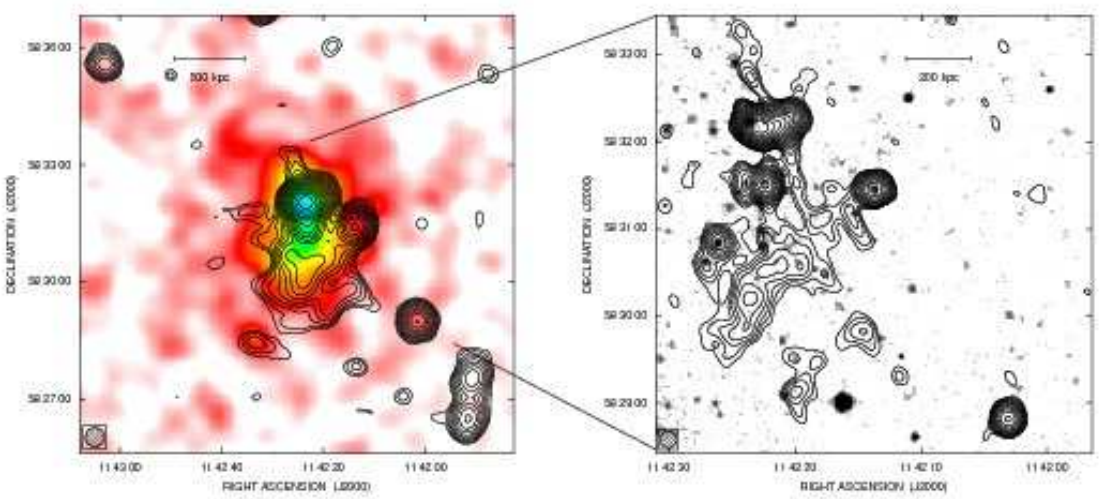

Figure 8.1: Left: radio contours of the extended halo in A1351 obtained with the VLA at 1.4 GHz combining data in C+D configuration. The HPBW is $30'' \times 30''$ and the noise level is 0.09 mJy/beam. The first contour level is drawn at 0.25 mJy/beam and the others are spaced by a factor $\sqrt{2}$. The contours of the radio intensity are overlaid onto the Rosat HRI X-ray image in the 0.1-2.4 keV band. The X-ray image has been smoothed with a Gaussian of $\sigma = 16''$. Right: radio contours obtained with the VLA at 1.4 GHz in C configuration of A1351. The HPBW of the radio image is $11'' \times 11''$ and the noise level is 0.06 mJy/beam. The first contour level is drawn at 0.15 mJy/beam and the others are spaced by a factor $\sqrt{2}$. The contours of the radio intensity are overlaid onto the optical image from the POSS2 red plate.

- A relic radio source is present in $\sim 30\%$ of clusters with a radio halo. This is in agreement with the relation between these two classes of sources and merger events.

- We find a good correlation between radio size and radio power for both small and giant radio halos (see Fig. 8.2). This result suggests a common origin and similar physical properties in small size and giant radio halos.

- From the power and size distribution with redshift of radio halos, shown in Figs. 8.3 and 8.4 we derive that known radio halos are homogeneously distributed in the observable region covered by the present radio telescopes. To investigate the presence of possible *different* radio halos, new instruments such as the Low Frequency ARray (LOFAR - NL), the Low Wavelength Array (LWA - US), the Australian Square Kilometre Array Pathfinder (ASKAP), and the Square Kilometer Array (SKA) are necessary. However we point out that observations with a better sensitivity as possible in the near future with the EVLA, could

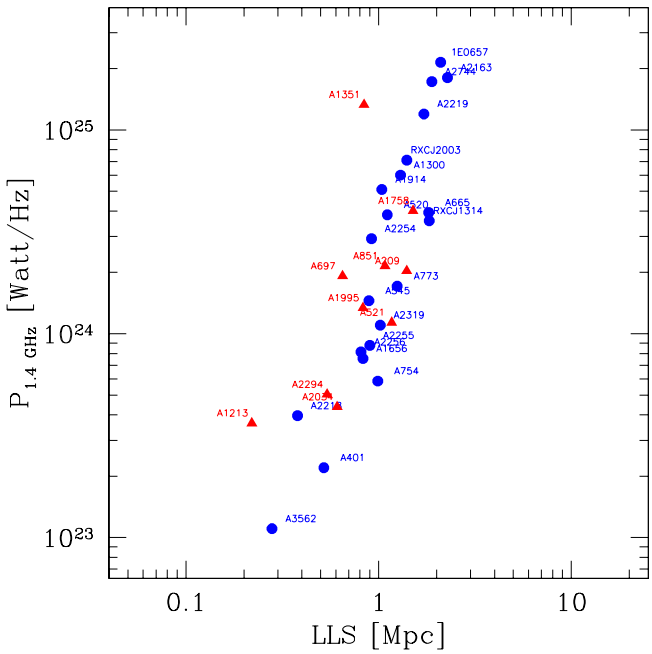

Figure 8.2: Total radio power at 1.4 GHz versus the largest linear size of radio halos in Mpc. New halos are represented by red triangles, while halos already known in literature by blue dots.

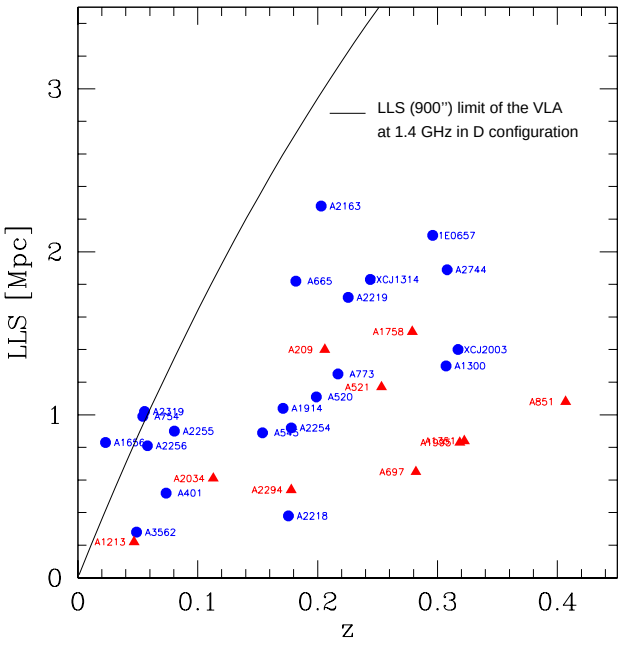

Figure 8.3: Largest Linear size of radio halos in Mpc versus z. The upper line corresponds to a radio halo with a size = 15′, the largest structure visible by VLA at 1.4 GHz in D configuration. Red triangles are new halos, blue dots are halos from literature data.

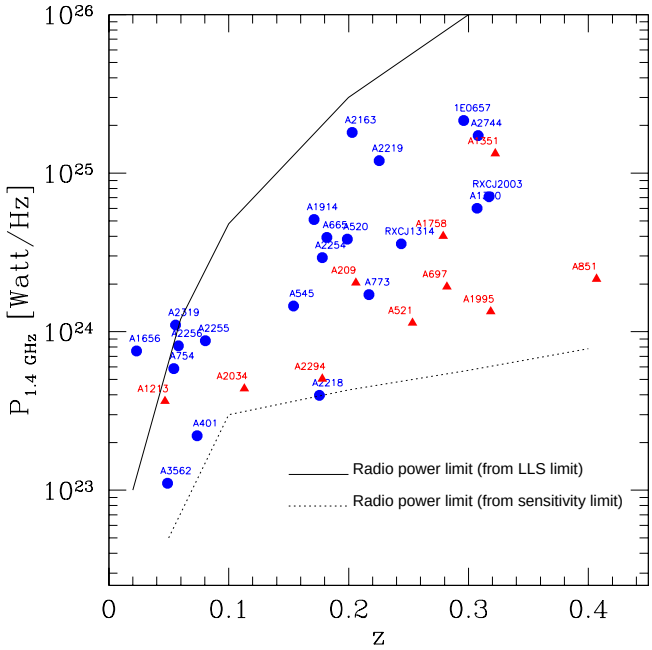

Figure 8.4: Total radio power at 1.4 GHz versus z. The upper continuous line corresponds to a halo linear size corresponding to 15', the upper limit for VLA observations at 1.4 GHz. The lower dotted line is from an average sensitivity limit assuming a standard VLA observation with an integration time of $\sim$ 3 hrs. Red triangles are new halos, blue dots are halos from literature data.

improve our knowledge of small and faint radio halos.

- The correlation between the spectral index of radio halo and the temperature of the host cluster is confirmed with a better statistics. The hotter the cluster, the flatter the radio halo spectral index is. This correlation favours the interpretation that turbulence is the mechanism responsible to supply energy to relativistic electrons.

- The correlation between cluster X-ray luminosity and radio power is confirmed with a better statistics (see Fig. 8.5). We note however the exception of the peculiar cluster A1213 where a diffuse radio emission is clearly present but the X-ray Luminosity is very low. We suggest that A1213 and a few other cases discussed in the literature (see e.g. Brown & Rudnick 2009) could represent a class of objects with an extended radio emission not clearly related to the cluster X-ray properties. The small number of these sources does not permit yet to discuss their properties.

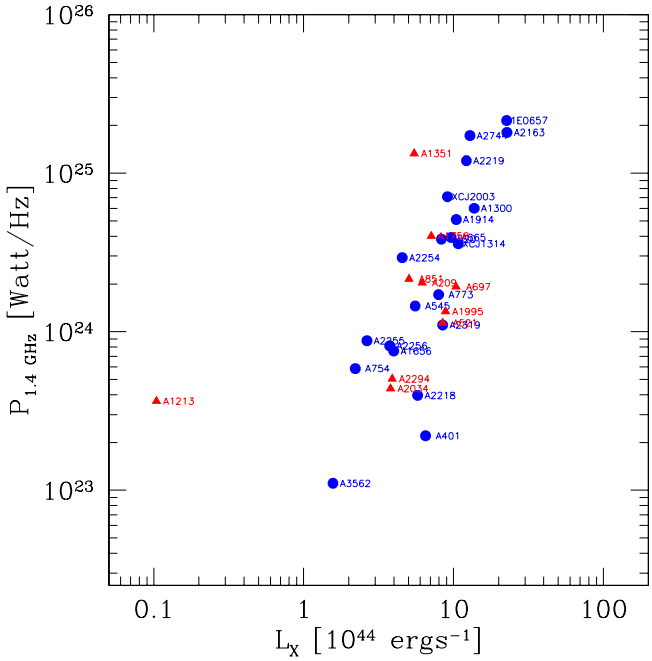

Figure 8.5: Cluster X-Ray Luminosity between 0.1 and 2.4 keV versus the total halo radio power at 1.4 GHz. Red triangles are new halos, blue dots are halos from literature data.

8.3 Beyond galaxy clusters: the diffuse radio filament ZwCl 2341.1+0000*

In recent years some evidences have been found of the existence of non thermal emission on scales even larger to those of radio halos and relics. For instance, bridges of radio emission have been observed in the region connecting the radio relic and the radio halo of the Coma cluster (Kim et al. 1989, Giovannini et al. 1990), and similar features have been observed also in Abell 2255 (Feretti et al. 1997), and Abell 2744 (Govoni et al. 2001). In addition, diffuse emission have been found at large distance from the cluster Abell 2255 (Pizzo et al. 2008), and Abell 2256 (van Weeren et al. 2009a).

In collaboration with G. Giovannini, L. Feretti, F. Govoni and M. Murgia, we studied the radio emission associated to the complex merging region detected in the ZwCl2341.1+0000 complex. This radio emission is 2.2 Mpc long, and Bagchi (2002) suggested its identification with the multi-Mpc scale filamentary network of galaxies in the ZwCl2341.1+0000 region at z = 0.27. This association was controversial, since more recent data obtained at lower frequencies (van Weeren et al. 2009c) revealed

*Giovannini,Bonafede, Feretti, Govoni & Murgia, 2010, A&A 511, L5

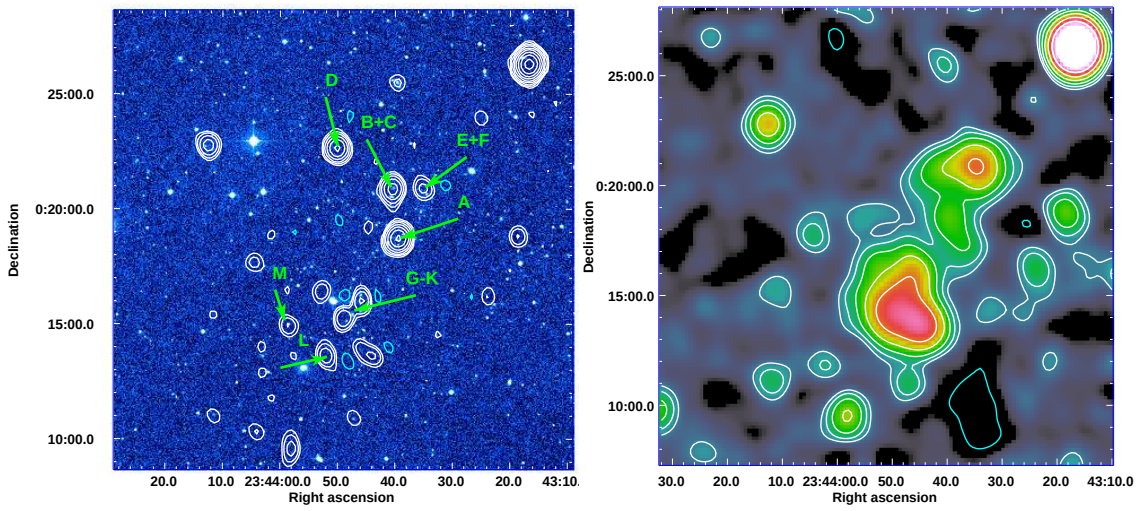

Figure 8.6: *Left:* The large scale galaxy distribution around ZwCl 2341.1+0000 is shown in colors. The optical image is from GSCII (Lasker et al. 2008). Contours of the radio emission from discrete sources (see text) are overlaid. The HPBW is $39'' \times 35''$. The first contour is drawn at 3σ level (0.15 mJy/beam). Following contours are spaced by a factor of 2. The first negative contour at 3σ level is displayed in cyan. Labels refer to the sources found by Van Weeren et al. (2009). *Right:* Colors and contours refer to the radio emission after the subtraction of the discrete sources. The HPBW is $83'' \times 75''$. The first contour is drawn at 3σ level (0.15 mJy/beam). Following contours are spaced by a factor of 2.

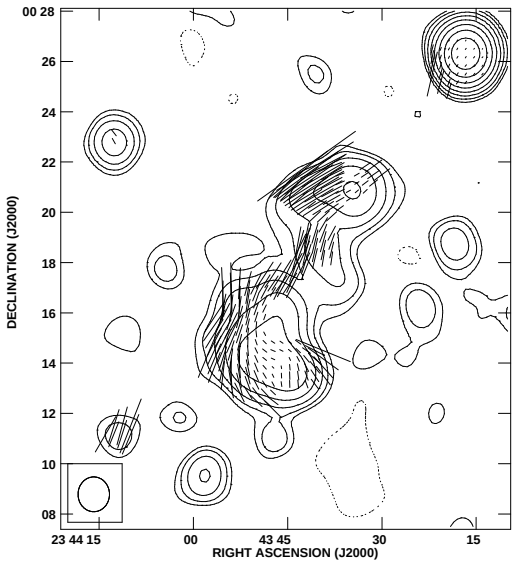

Figure 8.7: Polarized emission from ZwCl 2341.1+0000 at 1.4 GHz. Contours show the total-intensity emission at low resolution (see Fig. 8.6. Lines refer to the E vectors Their orientation represent the projected E-field not corrected for the galactic rotation. Their length is proportional to the fractional polarization: $1''$ corresponds to 0.2%.

only the two diffuse sources to the north and south of the cluster position which they classified as double radio relics. We have obtained deeper observations of this region to clarify the nature of this emission. The main results are summarized in the following:

- In the final image, obtained after the subtraction of discrete sources, (Fig. 8.6) an extended emission is detected, which is consistent with the result of Bagchi et al. (2002). Thanks to the better sensitivity of our image, the diffuse source is well defined. Its radio morphology is elongated, clearly following the distribution of the optical galaxies and of the X-ray emission, shown by van Weeren et al. (2009c). The regions of highest brightness are coincident with the two relics found detected at lower frequencies (van Weeren et al. 2009c).

- The total size of the diffuse emission is $\sim$ 2.2 Mpc. The measured total flux at 1.4 GHz is 28.5 mJy, corresponding to a radio power log $P_{1.4}$ = 23.66 W/Hz. The radio emission is irregular and decreases from the two bright outer regions toward the cluster center. A plateau of radio emission, at the level of about 0.6 mJy/beam is present at the location of the southernmost X-ray peak, detected by Chandra and published in Fig 1 of van Weeren et al. (2009c).

- We detect polarized emission from large areas of the diffuse radio source, both from the outer and the central regions (see Fig. 8.7). The polarized flux is more prominent in the eastern side of the extended source. Once the discrete sources have been subtracted, the total polarized flux is $\sim$2.4 mJy. The polarized percentage in the northern and in the southern bright regions is $\sim$15% and 8% respectively, while the mean fractional polarization in the central region is $\sim$11%. The polarization vectors are very regular and oriented toward the NE-SW direction in the northern source region. In the other regions they follow the eastern edge of the total intensity emission still showing some level of ordering.

The most natural interpretation is, as suggested by Bagchi et al. (2002), that this region is witnessing the process of a large scale structure formation, where cosmic shocks originated by a complex multiple merger are able to accelerate particles and amplify seed magnetic fields.

Conclusions

This PhD thesis has addressed several topics related to the intra-cluster magnetic field strength and structure and its connection with cluster thermo-dynamical properties. In this thesis the widespread existence of magnetic fields in the intra-cluster medium of galaxy clusters has been revealed, and the main properties of the magnetic fields, as well as its connection with thermal and non-thermal emission of galaxy clusters, have been studied. These topics have been investigated by using different methods and the results obtained by either the work presented here and other works recently published, permit to derive a more general picture regarding both the magnetic field properties and the origin of non-thermal emission. In the following the main results of this thesis will be summarized, and discussed together with recent results obtained either by works that we have collaborated to and recent literature results.

Results on cluster magnetic fields and radio emission

- **The magnetic field profile.**
  The magnetic field central strength and radial decline in the Coma cluster has been constrained by comparing RM images with numerical simulations of the magnetic field. The magnetic field central strength and radial decline slope have been constrained for the first time. The best model to reproduce the observed RM is the one with central magnetic field mean value of ~ 4.7 μG and radial decline slope $\eta = 0.5$ ($B(r) = \langle B_0 \rangle \left(\frac{n_e(r)}{n_0}\right)^{\eta}$). This is the slope expected for a magnetic field whose energy density decreases as the thermal gas energy density. In addition, our statistical analysis allows to exclude magnetic field profiles that have a central mean value $> 7\mu$G or $< 3\mu$G as well as magnetic field profiles with $\eta < 0.2$ and $\eta > 1$ at 99% confidence level.

- **Magnetic field power spectrum.**
  The magnetic field power spectrum ($|B_\Lambda|^2 \propto \Lambda^n$) has been studied in the Coma cluster through statistical analysis of the structure function and auto-correlation function of the RM images obtained for several sources in the Coma cluster field, and through the comparison with numerical simulations. We found that the magnetic field power spectrum is well represented by a Kolmogorov-like power spectrum, *i.e.* $n = 11/3$ with maximum scale of 34 kpc and minimum scale of 2 kpc. The detection of polarized emission in the cluster MACS J0717+3745 has allowed us to investigate the magnetic field power spectrum in this system. By comparison with numerical simulations we have found that the power spectrum spectral index n must be > 3 and that the maximum scale Λ_{max} must be of the order of hundreds kpc in order to produce the observed polarization percentage. The power spectra of these two clusters at different redshift and in different stages of their evolution is then consistent with a Kolmogorov-like slope. The maximum scale is instead different by one order of magnitude. We suggest a possible scenario where the system MACS J0717+3745, consisting of 4 sub-clusters participating in a triple merger event, is in a young phase after the merger, and the turbulence developed by such mergers has not yet had time to develop to smaller scales.

- **Magnetic field in a high-redshift system**.
  The magnetic field has been analyzed in the cluster MACS J0717+3745, at $z = 0.55$. We detected here the most distant and most powerful radio halo, and the second case after Abell 2255 where polarized emission has been detected. Together with the cluster CL0016 +0016 at z=0.54, this detection sets a new limit on the presence of magnetic field in the ICM at high z. The Faraday rotation of the radio emission has been analyzed. Here the orientation of the polarization plane does not follow the λ^2 law expected in the case of a Faraday screen, indicating that a more complex interaction between the thermal and non-thermal components of the ICM. The connection between thermal gas properties and radio emission have been investigated. We did not find any clear correlation between the radio spectral index distribution and the temperature distribution, but the average spectral index and temperature

follow the correlation that we have found for a large sample of clusters (Chap.8). The magnetic field profile has been derived under the equipartition assumption by using the deprojected surface brightness profile. We found $B_0 = 3\mu$G and $\eta = 1$.

- **Magnetic field at the cluster periphery.**
  The magnetic field at the cluster outskirts have been studied by analyzing the radio emission arising from the clusters Abell 1240 and Abell 2345. Spectral index and polarization analysis has been performed on these sources. The magnetic field, as revealed by the polarized emission, is mainly aligned with the relic main axis. In Abell 2345 the polarized emission reveals an arc-like structure morphology for one of the two relics that is not visible in total intensity image. Under equipartition assumptions values of $\sim$2.2-2.9 μG are derived. The field has been likely amplified, consistently with shock models predictions.

- **Evidence of magnetic field amplification in intergalactic filaments**
  The magnetic field in the intergalactic filament surrounding the system MACS J0717+3745 is revealed by the RM of a source that lies on the filament itself. The detected value of the RM indicates that a magnetic field is present in this filament, and has already been amplified in these regions, possibly by energetic phenomena associated with the complex merging history of this cluster. In collaboration with G. Giovannini, L. Feretti, F. Govoni and M. Murgia, we studied the radio emission associated to the complex merging region detected in the ZwCl2341.1+0000 complex. This radio emission is 2.2 Mpc long, and is associated to the optical filament, as firstly suggested by Bagchi et al (2002). Furthermore, we detected polarized emission from this intergalactic filament, at $\sim$11% level. This result shows that magnetic fields and relativistic particles are present also in filamentary structures (see Giovannini et al.2010 for further details).

- **ICM magnetic field from cosmological simulations**.
  The magnetic field in galaxy clusters has been studied also through cosmological MHD simulations. A sample of massive clusters has been re-simulated at higher resolution sing the SPH *Gadget3* code. The aim is to reach

length scale comparable to the resolution of the observations. The comparison between he magnetic profile obtained with ideal MHD and that derived for the Coma cluster indicates that a magnetic field dissipation is necessary to reproduce the observed strength of the magnetic field in the cluster core. The MHD implementation has been extended and a diffusivity constant η_m has been included. We have found that including the diffusion term in the induction equation is necessary to recover the observed strength of the magnetic field in galaxy clusters. The preliminary results that we have obtained so far indicate that the best value of η_m is of the order of 20.

- **Impact of radio relic formation models.**
  The results obtained for the relics in Abell 2345 and Abell 1240 have been discussed in the framework of relic formation models. The Mach numbers derived from the radio spectral index disfavour the accretion shock scenarios, being too small, while outgoing merger shock waves could have produced the observed radio properties of Abell 1240 and Abell 2345, although one of the relics of Abell 2345 presents peculiar features that need to be further investigated.

Open problems and future prospects

Magnetic field strength and structure: It is now well established that the ICM is magnetized. We have shown that, as first suggested by Jaffe (1980), different estimates derived from different methods can be reconciled by assuming realistic magnetic field models that take into account the magnetic field structure and radial decline. Understanding how the magnetic field is correlated with the thermal gas is still an open issue.

In addition to the results presented in this thesis, the ICM magnetic field has been investigated in the last three years in some more clusters. In Abell 2382 (Guidetti et al. 2008), RM data of two polarized cluster radio sources are consistent with a Kolmogorov like power spectrum characterized by $\Lambda_{max} \sim 35$ kpc. In this cluster the radial decline of the magnetic field has also been analyzed, and even if data could not exclude steep (*e.g.* $\eta = 1$) and flat (*e.g.* $\eta = 0$) profile slopes, the best agreement with observations was obtained for η =0.5, in agreement with what we have found in the Coma cluster. In Abell 665, assuming that the magnetic field power spectrum is

a power law with a Kolmogorov index and imposing a local equipartition of energy density between relativistic particles and field, the radio halo emission is found to be consistent with a central magnetic field strength of about 1.3 μG. To explain the azimuthally averaged radio brightness profile, the magnetic field energy density should decrease following the thermal gas density (*i.e.* $\eta = 0.5$). Very recently Kuchar & Ensslin (2009, submitted) have proposed a novel maximum a posterior method to estimate the magnetic field starting from RM images of diffuse sources. They applied this method to the source HydraA-north, finding a power spectrum that is consistent with the Kolmogorov slope, with scales going from 0.3 to 8 kpc. They also found that the magnetic field strength profile seems to follow the electron density profile with an index $\eta = 1$.

There is thus a general agreement that the magnetic field power spectrum in galaxy clusters is well represented by a Kolmogorov-like power spectrum, although the number of clusters for which this information is available is still very scarce. It is worth noting that the Kolmogorov theory is developed in homogeneous and isotropic environments, and when a magnetic field is included (Kraichnan's theory) it is not trivial to infer the power spectrum of the magnetic field, so that the above results about the magnetic field power spectrum, in agreement also with cosmological MHD simulations, need to be explained and may help in understanding this complicate phenomena.

Impact on radio halo and radio relics formation models: In the last years much work has been done in the literature regarding the properties of radio halos and relics. Apart from the works that we have presented in this thesis, halos have been studied with low frequency observations by other groups, both performing statistical analysis on cluster sample (Venturi et al. 2007, 2008; van Weeren et al, 2009b) and on individual objects (*e.g.* Pizzo et al. 2008, Brentjens 2008, Kale & Dwarakanath 2009, Giacintucci et al. 2008).

The results presented in this thesis in agreement with the above cited works, disfavour the secondary origin of the emitting particles and confirm some of the expectations of the re-acceleration models for the origin of radio halos.

Knowledge of the magnetic field strength and radial decline is fundamental in order to test different class of radio halo formation models. Coma is one of the most studied

clusters. It hosts the prototype of radio halos, so that it is the ideal candidate to make predictions for different radio halo formation theories (see *e.g.* Pfrommer & Ensslin 2004, Brunetti et al. 2001). The new results obtained from Faraday RM have been in fact used to test the predictions of hadronic models (Donnert et al. 2009). We have collaborated to the work performed by Donnert et al. (2009). Cosmological MHD simulations have been used to investigate the predicted properties of the radio halo in the Coma cluster, within the framework of the hadronic models. It results that the observed properties of the radio emission cannot be reconciled with the magnetic field profile derived from RM studies. The magnetic field in fact should be almost constant within ~ 1 Mpc, *i.e.* the region where the radio halo is observed to account for the observed radio brightness profile, the large extent of the observed radio halo, and its spectral steepening (Thierbach et al. 2003).

The correlation between the radio power and the X-ray cluster luminosity and the correlation between the radio halo spectral index and the cluster temperature, that we have confirmed with a large statistical sample of radio halos, reinforce the connection between merger event and radio emission, thus favouring the re-acceleration scenario.

There is thus a general consensus that the radio emission detected in halos and relics is linked to the cluster dynamical history, and the observed properties of radio halos seem to be consistent with the re-acceleration scenario, while the interpretation of the emission detected is radio relics is more controversial, since no clear connection between relic and shock front has been detected so far. The upcoming generation of radio telescopes, such as LOFAR and EVLA, and after LWA and SKA, will provide a lot of data to investigate the magnetic field properties and the origin of the radio emission.

Bibliography

[1] Ajello M., et al., 2009, ApJ, 690, 367

[2] Andernach H., Feretti L., & Giovannini G., 1984, A&A, 133, 252

[3] Baars, Jacob W.M. & Martin, Robert M. 1990, LIACo, 29, 293

[4] Bacchi M., Feretti L., Giovannini G., Govoni F., 2003, A&A, 400, 465

[5] Bagchi, J., Enßlin, T. A., Miniati, F., et al., 2002, New Astronomy, 7, 249

[6] Bagchi, J., Durret, F., Lima Neto, G.B., & Paul, S. 2006, Science, 314, 791

[7] Bartlett, J.G., 2006, astro-ph/0606241

[8] Beck R., Krause M., 2005, AN, 326, 414

[9] Becker R. H., White R. L., Helfand D. J., 1995, ApJ, 450, 559

[10] Bell A. R., Lucek S. G., 2001, MNRAS, 321, 433

[11] Belsole, E., Sauvageot, J.-L., Pratt, G.W., & Bourdin, H., 2005, Adv. Sp. Res., 36, 630

[12] Bicknell G. V., Cameron R. A., Gingold R. A., 1990, ApJ, 357, 373

[13] Blasi P., Colafrancesco S., 1999, APh, 12, 169

[14] Blumenthal G. R., Gould R. J., 1970, RvMP, 42, 237

[15] Böhringer, H. et al. 2004, A&A, 425, 367

[16] Bonafede A., Giovannini G., Feretti L., Govoni F., Murgia M., 2009a, A&A, 494, 429

[17] Bonafede A., et al., 2009b, A&A, 503, 707

[18] Bonafede A., Feretti L., Govoni F., Murgia M., Giovannini G., Dolag K., Taylor G. B., 2009c, RMxAC, 36, 303

[19] Bonafede A., Feretti L., Murgia M., Govoni F., Giovannini G., Dallacasa D., Dolag K., Taylor G. B., 2010, arXiv, arXiv:1002.0594

[20] Borgani, S., Murante, G., Springel, V., et al., MNRAS ,2004,348,1078

[21] Brentjens M. A., de Bruyn A. G., 2005, A&A, 441, 1217

[22] Briel U. G., Henry J. P., Boehringer H., 1992, A&A, 259, L31

[23] Brown, S., & Rudnick, L. 2009, AJ, 137, 3158

[24] Brüggen M., Ruszkowski M., Simionescu A., Hoeft M., Dalla Vecchia C., 2005, ApJ, 631, L21

[25] Brunetti G., 2003, ASPC, 301, 349

[26] Brunetti, G., Setti, G., & Comastri, A. 1997, A&A, 325, 898

[27] Brunetti G., Setti G., Feretti L., Giovannini G., 2001, MNRAS, 320, 365

[28] Brunetti G., Venturi T., Dallacasa D., Cassano R., Dolag K., Giacintucci S., Setti G., 2007, ApJ, 670, L5

[29] Brunetti G., Lazarian A., 2007, HiA, 14, 97

[30] Brunetti G., et al., 2008, Natur, 455, 944

[31] Bryan G.L. & Norman M.L. 1998, ApJ, 495, 80

[32] Buote, D.A., & Tsai, J.C., ApJ,1996,458,27

[33] Burn B. J., 1966, MNRAS, 133, 67

[106] Burn B. J. & Sciama, D. W., 1964, *Physics of Nonthermal Radio Sources*, NASA, SP-46, 139

[35] Burns J. O., Sulkanen M. E., Gisler G. R., Perley R. A., 1992, ApJ, 388, L49

[36] Burns J. O., Hallman E. J., Gantner B., Motl P. M., Norman M. L., 2007, hvcg.conf, 349

[37] Bykov, A.M., Dolag, K., & Durret, F. 2008, SSRv., 134, 119

[38] Byram E. T., Chubb T. A., Friedman H., 1966, Sci, 152, 66

[39] Carilli C. L., Taylor G. B., 2002, ARA&A, 40, 319

[40] Cassano R., 2009, arXiv, arXiv:0902.2971

[41] Cassano R., Brunetti G., 2005, MNRAS, 357, 1313

[42] Cassano R., Brunetti G., Setti G., 2006, MNRAS, 369, 1577

[43] Cavaliere A., Fusco-Femiano R., 1976, A&A, 49, 137

[44] Cavaliere A., Fusco-Femiano R., 1978, A&A, 70, 677

[45] Chen, C.M.H., Harris, D.E., Harrison, F.A., & Mao, P.H. 2008, MNRAS, 383, 1259

[46] Clarke T. E., Kronberg P. P., Böhringer H., 2001, ApJ, 547, L111

[47] Clarke, T.E., & Ensslin, T.A. 2006, AJ, 131, 2900

[48] Clarke T. E., 2004, JKAS, 37, 337

[49] Cohen A. S., Lane W. M., Cotton W. D., Kassim N. E., Lazio T. J. W., Perley R. A., Condon J. J., Erickson W. C., 2007, AJ, 134, 1245

[50] Colless M., Dunn A. M., 1996, ApJ, 458, 435

[51] Collins D. C., Xu H., Norman M. L., Li H., Li S., 2009, arXiv, arXiv:0902.2594

[52] Cowie L. L., Binney J., 1977, ApJ, 215, 723

[53] Cypriano, E.S., Sodré, L.J., Kneib, J.P., Campusano, L.E. 2004, ApJ 613 95

[54] Dallacasa D., Feretti L., Giovannini G., Venturi T., 1989, A&AS, 79, 391

[55] Dahle, H., Kaiser, N., Irgens, R.J., Lilje, P.B., & Maddox, S.J. 2002 ApJ 139 313

[56] David, L.P., Forman, W., & Jones, C. 1999, ApJ, 519, 533

[106] Dennison B., 1980, ApJ 239L, L93

[58] Diaferio A., 1999, MNRAS, 309, 610

[59] Diaferio A., Schindler S., Dolag K., 2008, SSRv, 134, 7

[60] Dolag, K., Bartelmann, M., & Lesch, H. 199, A&A, 348, 251

[61] Dolag, K., Schindler, S., Govoni, F., Feretti, L. 2001, A&A378, 777

[62] Dolag K., Bartelmann M., Lesch H., 2002, A&A, 387, 383

[63] Dolag K., Grasso D., Springel V., Tkachev I., 2004, JETPL, 79, 583

[64] Dolag K., Vazza F., Brunetti G., & Tormen G. 2005a, MNRAS, 364, 753

[65] Dolag K., Grasso D., Springel V., Tkachev I., 2005b, JCAP, 1, 9

[66] Dolag K., Vogt C., Enßlin T. A., 2005c, MNRAS, 358, 726

[67] Dolag, K., 2006, AN, 327, 575

[68] Dolag K., Bykov A. M., Diaferio A., 2008, SSRv, 134, 311

[69] Dolag K., Stasyszyn F., 2009, MNRAS, 398, 1678

[71] Donnert J., Dolag K., Lesch H., Müller E., 2009, MNRAS, 392, 1008

[71] Donnert J., Dolag K., Brunetti, G., Cassano, R. Bonafede, A. arXiv:0905.2418

[72] Dubois Y., Teyssier R., 2008, A&A, 482, L13

[73] Drury, R.O. 1983, Reports on Progress in Physics, 46, 973

[74] Ebeling H., Edge A. C., Henry J. P., 2001, ApJ, 553, 668

[75] Ebeling H., Barrett E., Donovan D., 2004, ApJ, 609, L49

[76] Ebeling H., White D. A., Rangarajan F. V. N., 2006, MNRAS, 368, 65

[77] Ebeling H., Barrett E., Donovan D., Ma C.-J., Edge A. C., van Speybroeck L., 2007, ApJ, 661, L33

[78] Edge A. C., Ebeling H., Bremer M., Röttgering H., van Haarlem M. P., Rengelink R., Courtney N. J. D., 2003, MNRAS, 339, 913

[79] Eilek J. A., Owen F. N., 2002, ApJ, 567, 202

[80] Eke V. R., Cole S., Frenk C. S., 1996, MNRAS, 282, 263

[81] Ensslin T. A., Biermann P. L., Kronberg P. P., Wu X.-P., 1997, ApJ, 477, 560

[82] Ensslin, T.A., Biermann, P.L., Klein, U., & Kohle, S. 1998, A&A, 332, 395

[83] Ensslin, T.A., & Gopal-Krishna 2001, A&A, 366, 26

[84] Ensslin, T.A., & Brüggen, M. 2002, MNRAS, 331, 1011

[85] Enßlin T. A., Röttgering H., 2002, A&A, 396, 83

[86] Ensslin T. A., Vogt C., Clarke T. E., Taylor G. B., 2003, ApJ, 597, 870

[87] Fabian A. C., 1994, ARA&A, 32, 277

[88] Felten J. E., Gould R. J., Stein W. A., Woolf N. J., 1966, ApJ, 146, 955

[89] Feretti, L., Dallacasa, D., Giovannini, G., Tagliani., A. 1995, A&A, 302, 680

[90] Feretti, L., Boehringer, H., Giovannini, G., Neumann, D. 1997 A&A, 317 432

[91] Feretti L., Giovannini G., Tordi M., Böhringer H., 1999, hxra.conf, 260

[92] Feretti L., Dallacasa D., Govoni F., Giovannini G., Taylor G. B., Klein U., 1999, A&A, 344, 472

[93] Feretti L., 2003, ASPC, 301, 143

[94] Feretti L., Orrù E., Brunetti G., Giovannini G., Kassim N., Setti G., 2004, A&A, 423, 111

[95] Feretti, L., Schuecker, P., Böhringer, H., Govoni, F., & Giovannini, G. 2005, A&A 444 157

[96] Feretti L., Neumann D. M., 2006, A&A, 450, L21

[97] Ferrari, C., 2003, "Multi-wavelength analysis of merging galaxy clusters", PhD Thesis

[98] Ferrari, C., Maurogordato, S., Cappi, A., & Benoist, C., 2003, A&A, 399, 813

[99] Ferrari, C., Arnaud, M., Ettori, S., Maurogordato, S., & Rho, J., 2006, A&A, 446, 417

[100] Ferrari C., Govoni F., Schindler S., Bykov A. M., Rephaeli Y., 2008, SSRv, 134, 93

[101] Finoguenov A., Henriksen M. J., Miniati F., Briel U. G., Jones C., 2006, ApJ, 643, 790

[102] Furlanetto S. R., Loeb A., 2001, ApJ, 556, 619

[103] Fusco-Femiano R., dal Fiume D., Feretti L., Giovannini G., Grandi P., Matt G., Molendi S., Santangelo A., 1999, ApJ, 513, L21

[104] Fusco-Femiano R., et al., 2000, ApJ, 534, L7

[105] Fusco-Femiano R., Dal Fiume D., Orlandini M., Brunetti G., Feretti L., Giovannini G., 2001, ApJ, 552, L97

[106] Fusco-Femiano, R. 2004, Ap&SS, 294, 37

[107] Fusco-Femiano, R., et al. 2004 ApJ, 602L, 73

[108] Fusco-Femiano R., Landi R., Orlandini M., 2007, ApJ, 654, L9

[109] Garrington S. T., Conway R. G., 1991, MNRAS, 250, 198

[110] Garrington S. T., Leahy J. P., Conway R. G., Laing R. A., 1988, Natur, 331, 147

[111] Giacintucci S., et al., 2008, A&A, 486, 347

[112] Giovannini, G., Kim, K. T., Kronberg, P. P., Venturi, T. 1990 Proceedings of the 140th. IAU Symposium, Kluwer Academic Publishers, Editors, R. Beck, P.P. Kronberg, R. Wielebinski; p. 492

[113] Giovannini, G., Feretti, L., & Stanghellini, C. 1991, A&A, 252, 528

[114] Giovannini, G., Tordi, M., & Feretti, L. 1999, New Astron., 4, 141

[115] Giovannini G., Feretti L., 2000, NewA, 5, 335

[116] Giovannini G., Feretti L., 2002, HiA, 12, 513

[117] Giovannini, G., & Feretti, L. 2004, Journal of the Korean Astronomical Society, Proceedings of the 3rd Korean Astrophysics Workshop "Cosmic Rays and Magnetic Fields in Large Scale Structure", Pusan, Korea, August 2004, eds. H. Kang & D. Ryu, 37, 1

[118] Giovannini G., Bonafede A., Feretti L., Govoni F., Murgia M., Ferrari F., Monti G., 2009, A&A, 507, 1257

[119] Giovannini G., Bonafede A., Feretti L., Govoni F., Murgia M., 2010, A&A, 511, L5

[120] Gitti M., Brunetti G., Setti G., 2002, A&A, 386, 456

[121] Gitti M., Schindler S., 2004, A&A, 427, L9

[122] Gitti M., Ferrari C., Domainko W., Feretti L., Schindler S., 2007, A&A, 470, L25

[123] Goldshmidt O., Rephaeli Y., 1993, ApJ, 411, 518

[124] Govoni F., Feretti L., Giovannini G., Böhringer H., Reiprich T. H., Murgia M., 2001, A&A, 376, 803

[125] Govoni, F., & Feretti, L. 2004, IJMPD, 13, 1549

[126] Govoni F., Murgia M., Feretti L., Giovannini G., Dallacasa D., Taylor G. B., 2005, A&A, 430, L5

[127] Govoni F., Murgia M., Feretti L., Giovannini G., Dolag K., Taylor G. B., 2006, A&A, 460, 425

[128] Govoni F., Murgia M., Markevitch M., Feretti L., Giovannini G., Taylor G. B., Carretti E., 2009, A&A, 499, 371

[129] Guidetti D., Murgia M., Govoni F., Parma P., Gregorini L., de Ruiter H. R., Cameron R. A., Fanti R., 2008, A&A, 483, 699

[130] Guo F., Oh S. P., 2008, MNRAS, 384, 251

[131] Grasso D., Rubinstein H. R., 2001, PhR, 348, 163

[132] Hayakawa A., Hoshino A., Ishida M., Furusho T., Yamasaki N. Y., Ohashi T., 2006, PASJ, 58, 695

[133] Heinz S., Brüggen M., Young A., Levesque E., 2006, MNRAS, 373, L65

[134] Henriksen, M., & Mukshotzky, R. 2001, ApJ, 553, 84.

[135] Henry J. P., Finoguenov A., Briel U. G., 2004, ApJ, 615, 181

[136] Hoeft, M., Brüggen, M., & Yepes, G. 2004, MNRAS, 347, 389

[137] Hoeft, M., & Brüggen, M. 2007, MNRAS, 375, 77

[138] Jaffe, W.J., Apj, 1977,,212,1

[139] Jaffe, W.J., ApJ, 1980, 241, 925

[140] Jeltema, T.E., Canizares, C.R., Bautz, M.W., & Buote, D.A., ApJ,2005,624,606

[141] Johnston-Hollitt, M., Clay, R.W., Ekers, R.D., Wieringa, M.H., & Hunstead, R. W. 2002 IAUS 199, 157

[142] Johnston-Hollitt M., Ekers R. D., 2004, astro, arXiv:astro-ph/0411045

[143] Kaiser, N., MNRAS, 1986, 222, 323

[144] Kempner, J.C., & Sarazin, C.L. 2001, ApJ, 548, 639

[145] Kempner J. C., David L. P., 2004, ApJ, 607, 220

[146] Kempner, J.C., et al. 2004, in "The riddle of cooling fows in galaxies and clusters of galaxies", T. Reiprich, J. Kempner & N. Soker (eds.), published electronically at http://www.astro.virginia.edu/coolingflow/

[147] Kim, K.-T., Kronberg, P. P., Giovannini, G., Venturi, T. 1989 Nature 341, 720

[148] Kim, K. T., Kronberg, P. P., Dewdney, P.. E., Landecker, T. L. 1990, ApJ, 335, 29

[149] Kim K.-T., Kronberg P. P., Tribble P. C., 1991, ApJ, 379, 80

[150] Kravtsov, A. V., Vikhlinin, A., & Nagai, D. 2006, ApJ, 650, 128

[151] Kronberg P. P., Lesch H., Hopp U., 1999, ApJ, 511, 56

[152] Laing R. A., 1988, Natur, 331, 149

[153] Laing R. A., Bridle A. H., Parma P., Murgia M., 2008, MNRAS, 391, 521

[154] Lawler J. M., Dennison B., 1982, ApJ, 252, 81

[155] Landau L.,D. & Lifshitz, E.M. 1966, Fluid Mechanics, (Pergamon Press Ltd.)

[156] Liang H., Hunstead R. W., Birkinshaw M., Andreani P., 2000, ApJ, 544, 686

[157] Longair M. S., 1981, heaa.book

[158] Lutovinov A. A., Vikhlinin A., Churazov E. M., Revnivtsev M. G., Sunyaev R. A., 2008, ApJ, 687, 968

[159] Ma C.-J., Ebeling H., Donovan D., Barrett E., 2008, ApJ, 684, 160

[160] Ma C.-J., Ebeling H., Barrett E., 2009, ApJ, 693, L56

[161] Markevitch, M. 1998, ApJ, 504, 27

[162] Markevitch M., Gonzalez A. H., David L., Vikhlinin A., Murray S., Forman W., Jones C., Tucker W., 2002, ApJ, 567, L27

[163] Mazzotta P., Giacintucci S., 2008, ApJ, 675, L9

[164] Mehlert D., Saglia R. P., Bender R., Wegner G., 2000, A&AS, 141, 449

[165] Miller N. A., Hornschemeier A. E., Mobasher B., Bridges T. J., Hudson M. J., Marzke R. O., Smith R. J., 2009, AJ, 137, 4450

[166] Murgia, M. et al. 2004, A&A, 424, 429

[167] Murgia M., Govoni F., Markevitch M., Feretti L., Giovannini G., Taylor G. B., Carretti E., 2009, A&A, 499, 679

[168] Nagai D., Kravtsov A. V., Vikhlinin A., 2007, ApJ, 668, 1

[169] Neumann D. M., Arnaud M., 2001, A&A, 373, L33

[170] Neumann D. M., Arnaud M., 1999, A&A, 348, 711

[171] Orrú, E., Murgia, M., Feretti, L., et al. 2007, A&A, 467, 943

[172] Owen, F.N., Brogan, C.L., & Clarke T.E. 2004, published electronically at http://www.vla.nrao.edu/astro/giudes/p-band/p-reduction/

[173] Pacholczyk, A.G. 1970, Radio astrophysics, (Freeman Eds.)

[174] Perley R. A., Taylor G. B., 1991, AJ, 101, 1623

[175] Petrosian V., 2001, ApJ, 557, 560

[176] Petrosian V., Bykov A., Rephaeli Y., 2008, SSRv, 134, 191

[177] Pizzo, R.,F.,de Bruyn, A.,G., Feretti., L., & Govoni, F. 2008, A&A, 481L 91

[178] Pfrommer C., Enßlin T. A., 2004, JKAS, 37, 455

[179] Pratt, G. W., Böhringer, H., Croston, J. H., et al. 2007, A&A, 461, 71

[180] Ramella M., et al., 2007, A&A, 470, 39

[181] Rees M. J., 2006, AN, 327, 395

[182] Rengelink R. B., Tang Y., de Bruyn A. G., Miley G. K., Bremer M. N., Roettgering H. J. A., Bremer M. A. R., 1997, A&AS, 124, 259

[183] Rephaeli Y., 1977, ApJ, 218, 323

[184] Rephaeli, Y., Gruber, D., & Blanco, P., 1999,ApJ, 511,21

[185] Rephaeli Y., Gruber D., 2003, ApJ, 595, 137

[186] Rephaeli Y., Gruber D., Arieli Y., 2006, ApJ, 649, 673

[187] Rephaeli, Y., Nevalainen, J., Ohashi, T., & Bykov, A., 2008, SSR

[188] Ricker, P.M, & Sarazin, C.L. 2001, ApJ, 561, 621

[189] Roncarelli M., Moscardini L., Tozzi P., Borgani S., Cheng L. M., Diaferio A., Dolag K., Murante G., 2006, MNRAS, 368, 74

[190] Rordorf C., Grasso D., Dolag K., 2004, APh, 22, 167

[191] Roettiger, K., Burns, J.O., & Stone, J.M. 1999, ApJ, 518, 603

[192] Rosati, P., Borgani, S., & Norman, C. 2002, ARAA, 40, 539

[193] Röttgering, H.J.A., Wieringa, M.H., Hunstead, R.W., & Ekers, R.D. 1997, MNRAS, 290, 577

[194] Rudnick L., Blundell K. M., 2003, ApJ, 588, 143

[195] Ruzmaikin A. A., Sokoloff D. D., 1979, A&A, 78, 1

[196] Ryu, D., Kang, H., Hallman, E., & Jones, T. W. 2003, ApJ, 593, 599

[197] Ryu D., Kang H., Cho J., & Das S. 2008, Science, 320, 909

[198] Sarala S., Jain P., 2001, MNRAS, 328, 623

[200] Sarazin, C.L. 1988, X-ray emission from clusters of galaxies, (Cambridge University Press)

[200] Sarazin, C.L. 1999, ApJ, 520, 529

[201] Schekochihin A. A., Cowley S. C., Dorland W., Hammett G. W., Howes G. G., Quataert E., Tatsuno T., 2007, arXiv, arXiv:0704.0044

[202] Schneider P., 2006, kbls.conf, Presented at the KITP: Blackboard Lunch Series, Oct 2, 2006, Kavli Institute for Theoretical Physics, University of California, Santa Barbara

[203] Schuecker P., Finoguenov A., Miniati F., Böhringer H., Briel U. G., 2004, A&A, 426, 387

[204] Sijacki, D., Springel, V., Di Matteo, T., & Hernquist, L. 2007, MNRAS, 380, 877

[205] Simard-Normandin M., Kronberg P. P., Button S., 1981, ApJS, 45, 97

[206] Sokoloff D. D., Bykov A. A., Shukurov A., Berkhuijsen E. M., Beck R., Poezd A. D., 1998, MNRAS, 299, 189

[207] Solovyeva, L., Anokhin, S., Feretti, L., et al. 2008, A&A 484 621

[208] Springel V., 2005, MNRAS, 364, 1105

[209] Subramanian K., Shukurov A., Haugen N. E. L., 2006, MNRAS, 366, 1437

[210] Sunyaev, R. A., Norman, M. L., & Bryan, G. L. 2003, AstL 29, 783

[211] Taylor G. B., Govoni F., Allen S. W., Fabian A. C., 2001, MNRAS, 326, 2

[212] Taylor G. B., Fabian A. C., Allen S. W., 2002, MNRAS, 334, 769

[213] Taylor G. B., Perley R. A., 1993, ApJ, 416, 554

[214] Thierbach,M., Klein, U., Wielebinski, R. 2003, A&A, 397, 53

[215] Tormen G., Bouchet F. R., White S. D. M., 1997, MNRAS, 286, 865

[216] Tribble P. C., 1991, MNRAS, 250, 726

[217] Valdarnini, R., 2003, MNRAS ,339,1117

[218] Vallee J. P., Kronberg P. P., 1975, A&A, 43, 233

[219] Vallée J. P., 2004, NewAR, 48, 763

[220] van Weeren, R.J., Intema, H.T., Oonk, J.B.R., et al. 2009a A&A, 508, 1269

[221] van Weeren, R.J., Röttgering, H.J.A., Bagchi,J., et al. 2009b A&A, 506, 1083

[222] van Weeren R. J., et al., 2009c, A&A, 506, 1083

[223] Vazza F., Brunetti G., Kritsuk A., Wagner R., Gheller C., Norman M., 2009, A&A, 504, 33

[224] Vazza F., Gheller C., Brunetti G. arXiv:0910.1925v1

[225] Venturi, T., Giacintucci, S., Brunetti, G., et al. 2007, A&A 463 937

[226] Venturi T., Giacintucci S., Dallacasa D., Cassano R., Brunetti G., Bardelli S., Setti G., 2008, A&A, 484, 327

[227] Véron-Cetty M.-P., Véron P., 2001, A&A, 374, 92

[228] Vladimirov A., Ellison D. C., Bykov A., 2006, ApJ, 652, 1246

[229] Völk H. J., Atoyan A. M., 2000, ApJ, 541, 88

[230] Vogt C., Enßlin T. A., 2003, A&A, 412, 373

[231] Vogt C., Enßlin T. A., 2005, A&A, 434, 67

[232] Werner N., Durret F., Ohashi T., Schindler S., Wiersma R. P. C., 2008, SSRv, 134, 337

[233] Wik D. R., Sarazin C. L., Finoguenov A., Matsushita K., Nakazawa K., Clarke T. E., 2009, ApJ, 696, 1700

[234] Wilmot-Smith A. L., Priest E. R., Hornig G., 2005, GApFD, 99, 177

[235] Willson M. A. G., 1970, MNRAS, 151, 1